Università degli Studi di Napoli "Federico II"

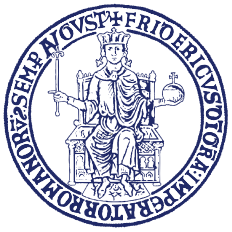

Doctoral Thesis

An improved preliminary design methodology for aircraft directional stability prediction and vertical tailplane sizing

Author:
Danilo Ciliberti

Supervisor:
Prof. Luigi De Luca

Tutor:
Prof. Fabrizio Nicolosi

A thesis submitted in fulfillment of the requirements for the degree of Doctor of Philosophy

in the

Design of Aircraft and Flight technologies research group
Department of Industrial Engineering

March 31, 2016

Declaration of Authorship

I, Danilo CILIBERTI, declare that this thesis titled, "An improved preliminary design methodology for aircraft directional stability prediction and vertical tailplane sizing" and the work presented in it are my own. I confirm that:

- This work was done wholly or mainly while in candidature for a research degree at this University.
- Where any part of this thesis has previously been submitted for a degree or any other qualification at this University or any other institution, this has been clearly stated.
- Where I have consulted the published work of others, this is always clearly attributed.
- Where I have quoted from the work of others, the source is always given. With the exception of such quotations, this thesis is entirely my own work.
- I have acknowledged all main sources of help.
- Where the thesis is based on work done by myself jointly with others, I have made clear exactly what was done by others and what I have contributed myself.

Signed:

Date: *March 31, 2016*

"*Essentially, all models are wrong, but some are useful.*"

George E. P. Box

UNIVERSITÀ DEGLI STUDI DI NAPOLI "FEDERICO II"

Abstract

Scuola Politecnica e delle Scienze di Base
Department of Industrial Engineering

Doctor of Philosophy

An improved preliminary design methodology for aircraft directional stability prediction and vertical tailplane sizing

by Danilo CILIBERTI

This work deals with the development of a new preliminary design method for aircraft directional stability and vertical tail sizing. It is focused on regional turboprop aircraft because of their economic advantage over regional jets on short routes, for the increasing oil price, and because of the market needs of new airplanes in the next 20 years. The focus on aircraft directional stability is due to the significant discrepancies that classical semi-empirical methods, as USAF DATCOM and ESDU, provide for some configurations, because they are based on NACA wind tunnel tests about models not representative of an actual transport airplane. This work exploits the CFD to calculate the aerodynamic interference among aircraft parts for hundreds configurations of a given layout, providing a useful method in aircraft preliminary design. A wind tunnel investigation involving about 180 configurations has validated the numerical approach. The innovation of the work concerns the numerical and experimental parametric study on the static directional stability of a model representative of the regional turboprop aircraft category and the direct measurement of the vertical stabilizer aerodynamic forces in the wind tunnel, in addition to the force and moments acting on the whole model. In this way, useful data about aerodynamic interference have been extracted from experimental tests, which are in good agreement with the results of numerical simulations.

Acknowledgements

A PhD research work is not an easy task, especially one involving both numerical and experimental activities. It requires the support of enthusiastic people, without which it would not have the same value.

First of all, I would like to express my gratitude to Prof. Fabrizio Nicolosi for giving me the possibility to fulfill this ambitious task. It all started when I still was un undergrad and his research group needed a passionate student to investigate semi-empirical methods about directional stability and vertical tail sizing, and eventually to develop an entire new method through the application of CFD!

Despite the inherent difficulties, this work was quite straightforward thanks to Pierluigi Della Vecchia, which trained me to be at the same time as practical and rigorous as possible. This approach avoided many difficulties and brought, I think, interesting results.

Elia Daniele, Salvatore Corcione, and Vincenzo Cusati, in rigorous alphabetical order, also helped me this work. In particular, the presence of Pierluigi, Salvatore, and Vincenzo throughout my entire PhD study provided an inestimable teamwork, which I hope to carry on for a long time.

Special thanks to Prof. Agostino De Marco for his not-only-technical advices. Also, I would like to thank the technician Antonio Alfano and the students Gennaro Zolfo and Nicola Bochicchio, who helped me in the last phase of this path and without them I would have had hard times.

Last, but not least, my deep appreciation goes to my parents Salvatore and Patrizia, and to my love Valeria, to which this thesis is dedicated. Without their encouragement, presence, and patience from the very first day, I probably would not have made it.

Contents

List of Figures

List of Tables

List of Abbreviations

AIAA	**A**merican **I**nstitute of **A**eronautics and **A**stronautics
BRICS	**B**razil, **R**ussia, **I**ndia, **C**hina, and **S**outh Africa
CAD	**C**omputer **A**ided **D**esign
CFD	**C**omputational **F**luid **D**ynamics
CIS	**C**ommonwealth of **I**ndependent **S**tates
CNC	**C**omputer **N**umerical Control
CPU	**C**entral **P**rocessing **U**nit
CRM	**C**ommon **R**esearch **M**odel (NASA)
DAF	**D**esign of **A**ircraft and **F**light technologies research group
DII	**D**ipartimento di **I**ngegneria **I**ndustriale
DAPCA IV	**D**evelopment and **P**rocurement **C**ost of **A**ircraft, Version **IV**
DES	**D**etached **E**ddy **S**imulation
DOC	**D**irect **O**perating **C**osts
DPW	**D**rag **P**rediction **W**orkshop
EASA	**E**uropean **A**viation **S**afety **A**gency
ESDU	**E**ngineering **S**cience **D**ata **U**nit
ETW	**E**uropean **T**ransonic **Wind** tunnel
FAA	**F**ederal **A**viation **A**uthorities
GDP	**G**ross **D**omestic **P**roduct
HiLiftPW	**H**igh **L**ift **P**rediction **W**orkshop
IEA	**I**nternational **E**nergy **A**gency
LES	**L**arge **E**ddy **S**imulation
m.a.c. or **mac**	**m**ean **a**erodynamic **c**hord
MATLAB	**MAT**rix **LAB**oratory (a MathWorks® software)
NACA	**N**ational **A**dvisory **C**ommittee for **A**eronautics
NASA	**N**ational **A**eronautics and **S**pace **A**dministration
OEI	**O**ne **E**ngine **I**noperative
OECD	**O**rganisation for the **E**conomic **C**o-operation and **D**evelopment
OPEC	**O**rganization of the **P**etroleum **E**xporting **C**ountries
RANS	**R**eynolds **A**veraged **N**avier-**S**tokes
RJ	**R**egional **J**et (aircraft category)
SCoPE	**S**istema **Co**perativo **P**er **E**laborazioni Scientifiche Multidisciplinari
SA	**S**palart-**A**llmaras (turbulence model)
SI	**S**ystème **I**nternational d'Unités
TP	**T**urbo**P**rop (aircraft category)
USAF DATCOM	**U**nited **S**tates **A**ir **F**orce **DAT**a **COM**pendium
VEDSC	**V**ertical tail **D**esign **S**tability and **C**ontrol

List of Symbols

Æ	Aspect ratio
A_F	Vertical tail (fin) aspect ratio (ESDU)
A_h	Horizontal tail aspect ratio (DATCOM)
A_T	Horizontal tail aspect ratio (ESDU)
A_v	Vertical tail aspect ratio (DATCOM)
$A_{v(f)}$	Vertical tail aspect ratio due to the fuselage
$A_{v(hf)}$	Vertical tail aspect ratio due to the fuselage and horizontal stabilizer
B	Compressibility parameter
C_{D0}	Zero-lift drag coefficient
$C_{D\text{e}}$	Effective profile drag coefficient
$C_{L_{\alpha_v}}$	Vertical tail lift curve slope
$C_{L_{\alpha_F}}$	Vertical tail (fin) lift curve slope (ESDU)
$C_{\mathcal{L}_\beta}$	Rolling moment coefficient derivative
C_{N_β}	Yawing moment coefficient derivative
$C_{N_{\delta_r}}$	Yawing moment coefficient due to rudder deflection derivative
C_{Y_β}	Sideforce coefficient derivative
D_f	Fuselage diameter
H_E	Engineering hours
H_M	Manufacturing hours
H_T	Tooling hours
J_B	Body correction factor (ESDU)
J_T	Horizontal tail correction factor (ESDU)
J_W	Wing correction factor (ESDU)
K_{F_v}	Fuselage to vertical tail aerodynamic interference factor (VeDSC)
K_{H_f}	Horizontal to fuselage aerodynamic interference factor (VeDSC)
K_{H_v}	Horizontal to vertical tail aerodynamic interference factor (VeDSC)
K_{V_f}	Vertical tail to fuselage aerodynamic interference factor (VeDSC)
K_{W_f}	Wing to fuselage aerodynamic interference factor (VeDSC)
K_{W_v}	Wing to vertical tail aerodynamic interference factor (VeDSC)

$\mathcal{L}$	Rolling moment
L_f	Fuselage length
M	Mach number
N	Yawing moment
Q	Number of aircraft produced in 5 year
R_E	Engineering cost rate
R_M	Manufacturing cost rate
R_T	Tooling cost rate
Re	Reynolds number
S	Wing planform area
S_{exp}	Exposed area
S_F	Fin planform area (ESDU)
S_{front}	Fuselage frontal (cross-sectional) area
S_v	Vertical tailplane planform area
S_{wet}	Wetted area
T	Engine thrust
V	Airspeed
W_e	Aircraft empty weight
W_f	Fuselage weight
W_{to}	Aircraft takeoff weight
W_v	Vertical tailplane weight
Y	Sideforce
$2r$	Fuselage depth in the region of vertical tail (DATCOM)
b	Wing span
b_F	Fin span (ESDU)
b_h	Horizontal tail span
b_T	Horizontal tail span (ESDU)
b_v	Vertical tail span
b_{v1}	Vertical tail span starting from fuselage centerline
c_{man}	Manufacturing cost
c_{mat}	Materials cost
d_{BF}	Body width at fin root quarter-chord station (ESDU)
d_f	Fuselage diameter
d_{fv}	Fuselage height at vertical tail aerodynamic center
h_{BF}	Body height at fin root quarter-chord station (ESDU)
h_{BW}	Body height at wing root quarter-chord station (ESDU)
h_F	Fin span (ESDU)

k_h	Factor to account empennage relative size (DATCOM)
k_v	Factor to account tail-fuselage relative size (DATCOM)
l_v	Vertical tail longitudinal moment arm
$\dot{m}$	Air flow
p	Weight penalty
r_f	Fuselage radius
z_f	Fuselage height
z_{ftc}	Fuselage tail-cone height
z_h	Horizontal tail location on the vertical tail
z_v	Vertical tail vertical moment arm
z_w	Wing height in fuselage
Δ	Difference of a quantity
Λ	Sweep angle
α	Angle of attack
β	Angle of sideslip
ϵ_{sb}	Solid blockage
λ	Taper ratio
κ	Section lift-curve to theoretical thin-section slopes ratio
μ	Air dynamic viscosity
ρ	Air density
θ	Fuselage upsweep angle

Dedicated to my Family and my Love

Chapter 1

Introduction

About this work This work focuses on the aerodynamic design of large regional turbopropeller transport aircraft. There are several reasons for this choice: first of all there is the field expertise of the Design of Aircraft and Flight technologies research group, where the author is working; the international co-operation with aviation companies, especially those involving propeller-driven aircraft; an interesting and challenging aviation market where short routes and oil price are key concern.

This work makes use of the *Système International d'Unités* (SI) whenever possible, except for those methods taken from reference that use the British imperial units.

Each chapter starts with a bulleted list called *Synopsis*, which gives the reader an idea of the content.

Synopsis

- ✈ Aircraft industry and airlines business are risky and expensive
- ✈ Gross Domestic Product growth will be dominated by emerging countries in the next 20 years
- ✈ Gross Domestic Product is strictly correlated to air travel
- ✈ Oil price is predicted to rise, although the 2015 drop
- ✈ Regional air traffic is dominated by jetliners, but turboprops still necessary, especially on short routes
- ✈ New turboprops will be produced for replacements and new deliveries
- ✈ Typical large regional turboprop aircraft are presented

- ✈ A simple method to evaluate aircraft Direct Operating Costs is applied
- ✈ Some remarks about the methods that will be presented are given
- ✈ The thesis layout is presented

1.1 Regional air transport market outlook

Developing a transport airplane requires nearly ten years and it costs millions (perhaps more than one billion) dollars from conceptual design to entry into service, not to mention airline operations. An additional time is necessary to get beyond the break-even line, that is get positive cumulative cash flows, recovering the initial investment. The aircraft continues to be produced for some decades, while derivatives are developed. Once delivered, it will operate for 10-40 years. For these reasons, the aircraft industry has a very high business risk. From the airlines point of view, the risk is also affected by economic, social, geopolitical, and environmental factors, including privatization, deregulation, fuel price, and pollution [1].

1.1.1 World economics

Since the year 2004, the world Gross Domestic Product (GDP) growth has been driven by emerging countries, although the so-called developed, western countries still provide the biggest GDP value, but with a weak growth (Figure 1.1 and 1.2). In the next 20 years, that is by 2035 at time of writing, North America and Europe will remain the largest economies, while South Asia and China will be the fastest growing economies [2, 3].

These outlooks forecast that mature markets will slow down this grow rate: for the emerging countries it will be around 6 %, for the western countries it will be around 2 %, and the world GDP grow rate will be nearly 3.1 % (Figure 1.3 and 1.4).

The correlation between world GDP and air travel is clear (Figure 1.5 and 1.6), but for the regional air traffic is more complex, because of its dual role: feeding (connectivity to a wider range of destination) and point-to-point (day-return possibility, mid-day travel opportunity) services. Regional traffic growth rate is also influenced by network structure and maturity [2].

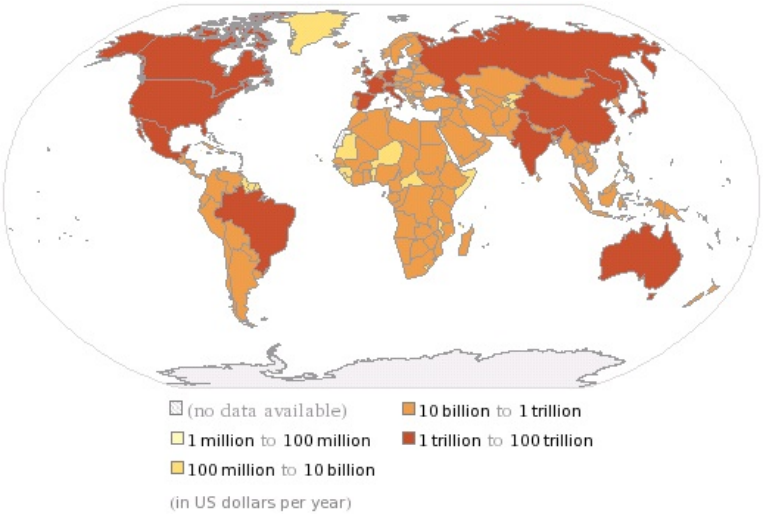

FIGURE 1.1: World GDP in 2015 [4].

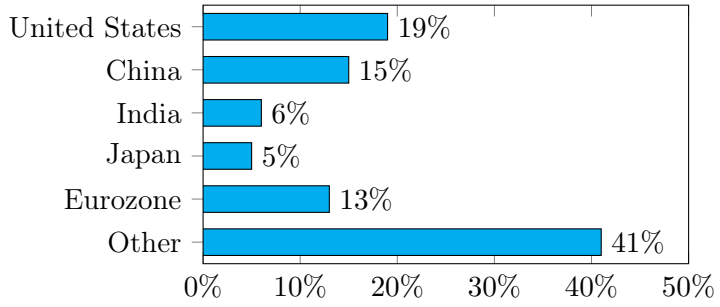

FIGURE 1.2: Proportion of global GDP in 2013 [5].

FIGURE 1.3: World GDP in 2035 [5].

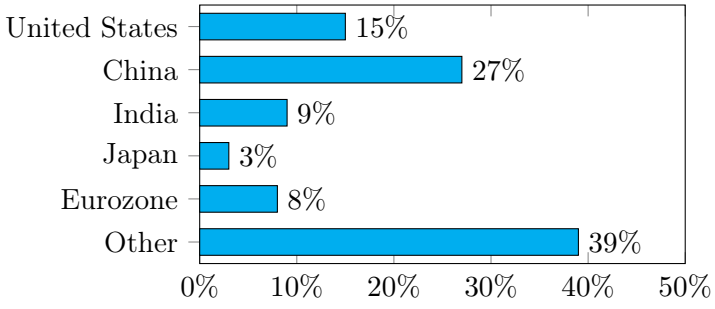

FIGURE 1.4: Proportion of global GDP in 2035 [5].

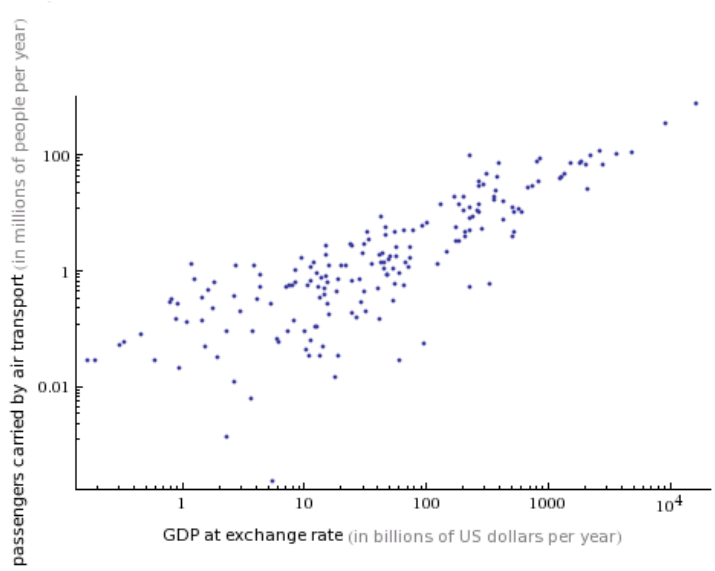

FIGURE 1.5: Passengers carried by air transport vs GDP [6].

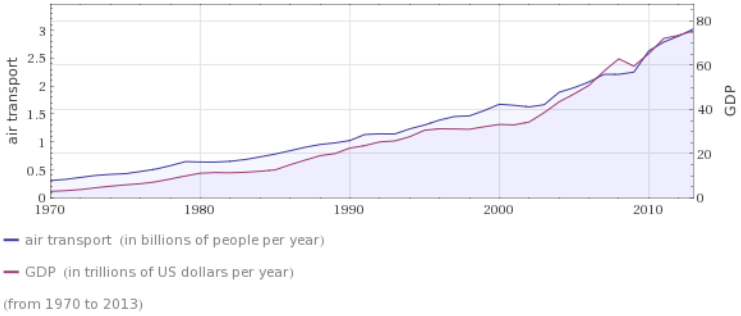

FIGURE 1.6: Air transport and GDP from 1970 [7].

1.1.2 Oil price

The following quotation has been taken from Ref. [1].

> In the airline industry, a sector of the transportation industry, changing fuel prices has a direct effect on profits. Spot prices of Brent Crude, an international index for oil prices, dropped 57 %, from $111.80/barrel in June of 2014 to $47.76/barrel in January of 2015, due to decreased demand in Europe and emerging economies, increased supply from shale oil in the United States and increased production of crude oil in non-OPEC countries, and deferment of OPEC production quotas in November of 2014. The average annual price also dropped from $108.56 in 2013 to $99.00 in 2014. The price of jet fuel (USA, spot price) also dropped by 48 %, from $2.88/gallon in June of 2014 to $1.50 in January of 2015. The average annual price also sank 6.8 %, from $2.92 in 2013 to $2.78 in 2014.
>
> Demand for crude oil before 2000 was mostly for consumption in developed countries. After 2000, increased demand was accompanied by economic development of Asian countries, especially the rapidly developed China, and other BRICS countries. Because of this, according to the IEA, demand for crude oil from non-OECD countries, as a fraction of global demand, increased from 37 % in 2000 to 49 % in 2013. Further development of emerging economies is expected in the future, and these countries shall continue to lead global demand for crude oil.
>
> After the year 2000, following strong global demand and rising prices, the amount of crude oil supplied grew from 77.3 million barrels/day in 2000 to 91.4 million barrels/day in 2013. Notably, the amount supplied from non-OPEC oil producing countries has increased dramatically, rising by 8.1 million barrels/day from 2000 to 2013. This is due to Russia and other CIS countries recovering from the production downturn following the collapse of the Soviet Union, development of deep-sea oil fields in South Africa and Brazil, and the development of shale oil fields in North America. In contrast, the amount supplied from OPEC countries has raised 5.9 million barrels/day.
>
> In the short term, the balance of supply and demand has broken down, leading to the downturn of Worldwide Market Forecast 2015-2034 crude oil prices, but it is expected that the excess supply of crude oil will eventually be resolved, and prices will rise again. In the long term, although there will be reduced demand due to energy saving technology and improved energy saving awareness, there will also be increased demand for crude oil following economic recovery and geopolitical causes, so crude oil prices will remain in an upward trend.

In summary, jet fuel price follows the international index for oil price (Brent), see Figure 1.7, which remains volatile and is forecasted to increase in the long term, although the drop in 2015. Future oil prices are lower than predicted in the 2014 market outlook, but the trend is still to increase (Figure 1.8). This will impact airliners fleet decisions [3].

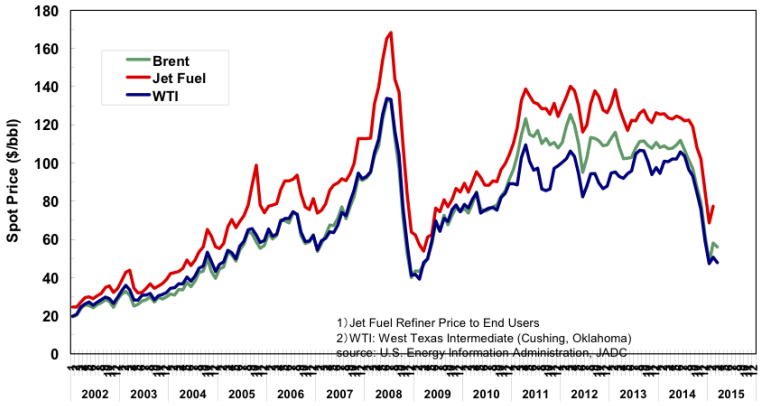

FIGURE 1.7: Relationship between crude oil and jet fuel price [1].

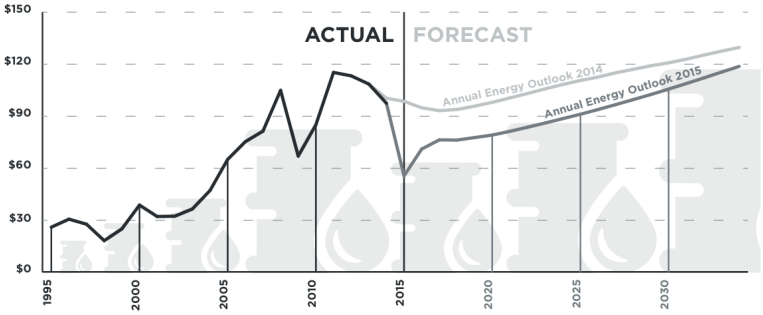

FIGURE 1.8: Price of crude oil in 2013 US dollars [3].

Fuel cost is the key concern for airlines because of its value and volatility. Fuel cost actually drives between 40 % and 50 % of cash operating cost depending on stage length, business model, and aircraft type. Fuel consumption is highly related to the aircraft aerodynamics, structural efficiency, and powerplant technology, which are improved more and more. Also, concerns in flight operations through trajectory optimization are made, where new satellite

based navigation systems are available[1]. This cost pressure is paramount to airlines aircraft choice as it can generate millions of US dollars savings [2].

As a matter of fact, fuel price has a strong relationship with turboprop preference in regional aircraft market. The ATR forecast assumes an oil barrel price of $106 average for the decade 2014-2023 and for an average price of $114 for the decade 2024-2033 [2].

1.1.3 The regional turboprop aircraft market for the next 20 years

The turboprop airliner market has experienced a considerable revival since 2004, as high fuel prices and a need to cut operating costs have resulted in regional carriers acquiring turboprops in significant numbers [8]. In the last 10 years, fast developing markets in Asia, Latin America, and Africa have pushed the growth of air travel, especially for turboprop transport aircraft. It was the beginning of a strong recovery in turboprop sales, where orders/backlogs were the highest ever made (more than 1400 new turboprops ordered in the last 10 years with 82 % of market share, see Figure 1.9), with a backlog of more than 370 turboprops at the end of May 2014. Today Asia Pacific, North America, and Europe represent about 60 % of the world passenger scheduled turboprop fleet, see Figure 1.10 [2].

Airlines have recognized that the turboprop aircraft is the most profitable way to operate short-haul sectors. One of the principal advantages of the twin-engine turboprop over the regional jet is its lower fuel consumption and economics on short-haul connections (Figure 1.11) [2].

The current regional aircraft fleet amounts to around 7200 units (30-120 seats), of which 40 % are turboprops. The average age of this fleet is 15 years (19 years for turboprops and 11 years for regional jets) [2].

The in service passenger turboprop airplane fleet will decrease from 3459 units in 2014 to 3273 units in 2034. Demand for new airplanes will be 2740 units with a total value of 54 billion US dollars (at 2014 list prices). However, routes that require a minimum level of aviation services or regionally specific routes (routes to isolated islands, etc.) are supposed to need turboprops, even if they are low in demand. Airplanes with 15 to 19 seats are expected

[1]The advent of satellite navigation improves the situation for pilots and also saves 30 miles of travel per flight when taking more direct approach paths to Juneau, Alaska. Source: Progress reported on NextGen air traffic control. `http://www.aiaa-aviation.org/Notebook.aspx?id=28697`, August 2015.

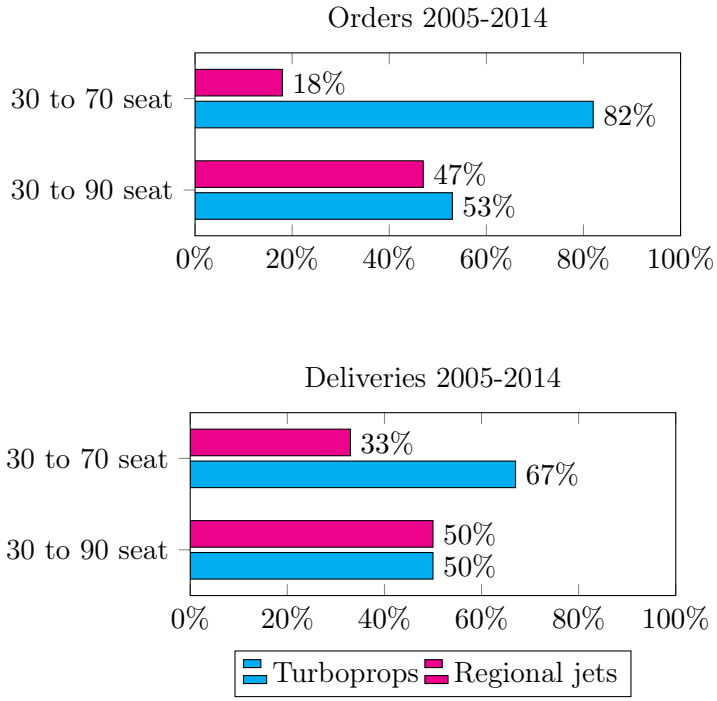

FIGURE 1.9: Regional aircraft orders and deliveries for the past 10 years [2].

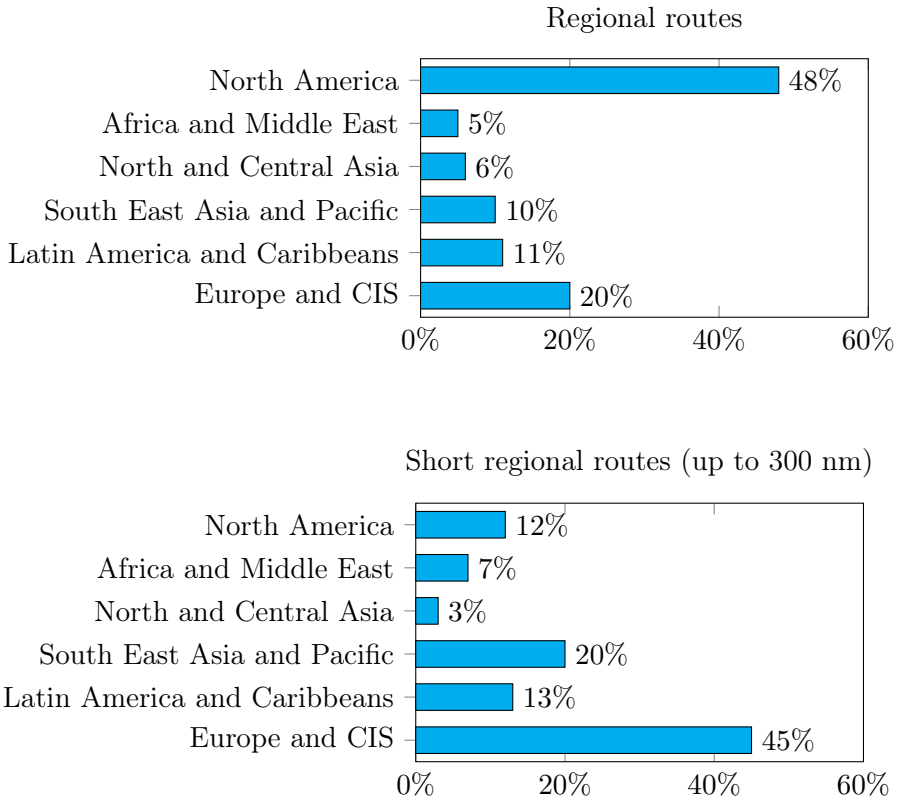

FIGURE 1.10: Regional routes around the world [2].

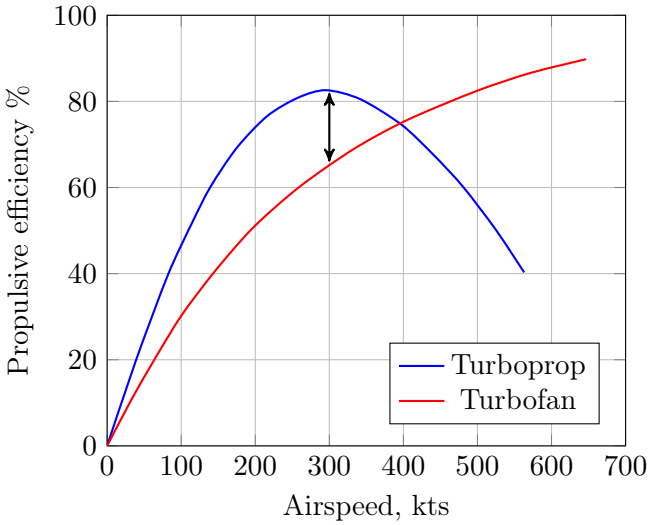

(A) Turboprop is optimized for speed around 300 kts.

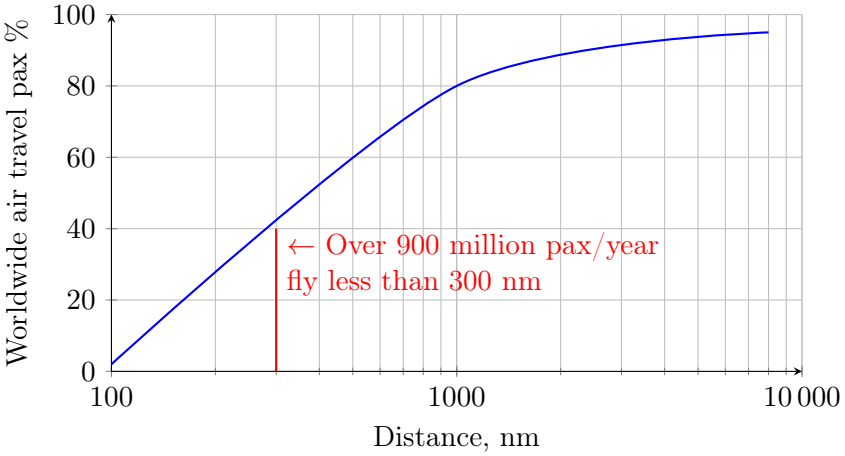

(B) Short haul: a big market essential to air transport.

FIGURE 1.11: Turboprop advantages over regional jet [2].

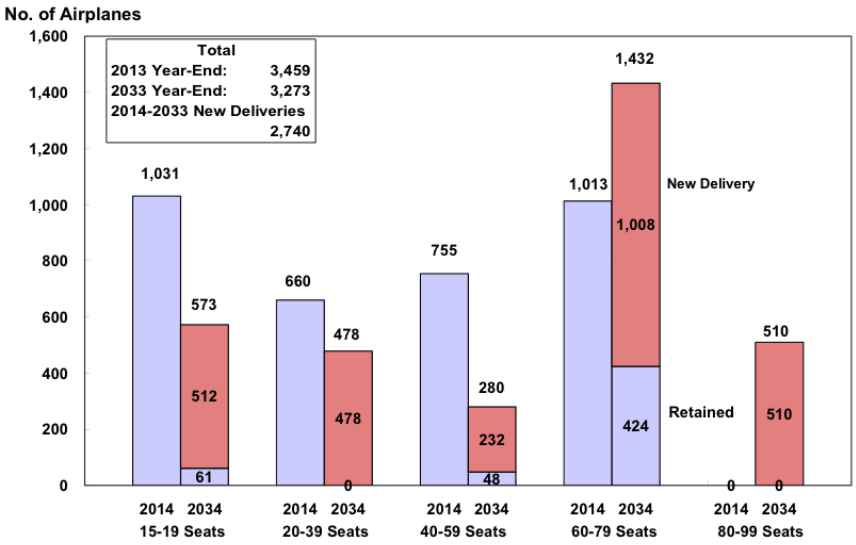

FIGURE 1.12: Passenger turboprop fleet and delivery forecast by seat category [1].

to continue to be operated on those routes; it is expected that 512 units will be delivered. The largest demand will be for airplanes with 60-79 seat class amounting to 1008 units. Regionally, as with passenger jets, the Asia-Pacific region will have the largest demand for passenger turboprop airplanes at 911 units [1].

Seventy-seaters, such as the ATR-72 and the Bombardier Q400, are currently the turboprops of choice for most operators. ATR and Bombardier are each exploring the prospect of developing a 90-seat turboprop, but both companies are displaying some hesitation in launching such an effort [8].

The difficulty to build a new turboprop (or a derivative of an existing model) and penetrate the market is due not only to the large amount of capital needed, but also to the competition with land transport on short-haul routes and regional jets over long-haul routes. Probably, a further rise in fuel price or a technological breakthrough can accelerate this process. For this reason, the demand of 90+ seat turboprop aircraft is expected to be 510 units in the next 20 years [1], see Figure 1.12.

Forecast International predicts that a total of 3867 regional aircraft (both jetliners and turboprops) will be produced from 2014 through 2023. As calculated in constant 2014 US dollars, the value of this production is

estimated at $127.9 billion. This involves production of regional aircraft types for civil use only and significant production of such aircraft for military use is excluded [8].

The regional aircraft market is still and will be mostly dominated by jetliners. Over the 2014-2023 time period, turboprops will account for 45.54 % of regional aircraft production and 25.34 % of production value, that is $32.42 billion [8].

The ATR forecast scenario for the next two decades is more optimistic (Figure 1.13), providing:

- the need for 3400 new turboprops;
- a $80 billion market value;
- an increasing demand for larger turboprops (70+ passengers);
- 60 % growth, 40 % replacement, 65 % from fast developing economies.

This prediction is based on aging aircraft, small turboprop retirement, increased turboprop demand, permanently rising fuel prices, greater environmental constraints, and airspace/airports congestion. Finally, more than 250 000 monthly frequencies are operated on short-haul sectors by regional jets, a large quantity of them unprofitably [2].

There is also a trend to increase the seats capacity across all fleet segments, in both turboprop and regional jet categories. Demand for regional transports continues to shift upward in favor of ever-larger-capacity aircraft. Aircraft with 20 to 100 seats have experienced the greater shift to larger aircraft (Figure 1.14). A good synthesis has been made by Bombardier Commercial Aircraft [3].

> Commercial airlines are profitable and growing. The industry continues to evolve to manage growth, volatile fuel prices, and increasing competition. Most new 60 to 150-seat aircraft deliveries to mature aviation markets will replace retiring aircraft fleets. In emerging markets, demand for air travel is growing with increasing GDP and an expanding middle class. Lower oil prices may permit airlines to delay the replacement or retirement of less efficient aircraft types, but in the long-term, fuel efficiency will remain a key driver of airline fleet decisions. Economic and technological obsolescence, as well as environmental regulations, are expected to drive aircraft retirements throughout the forecast.

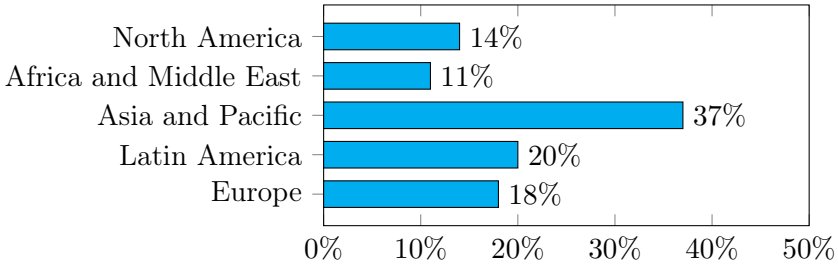

(A) Global turboprop forecast by country.

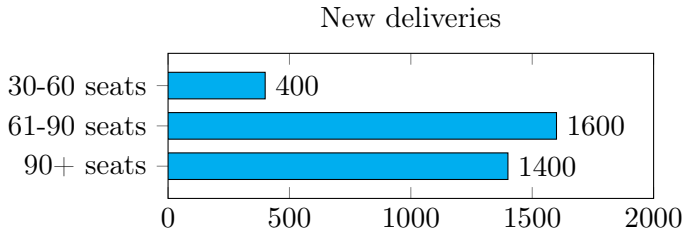

(B) Global turboprop forecast by seat category.

FIGURE 1.13: ATR turboprop market forecast (2014-2033) [2].

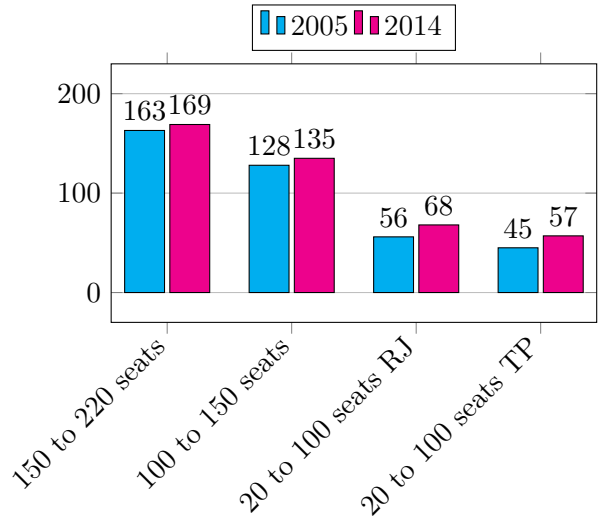

(A) Average seats per departure.

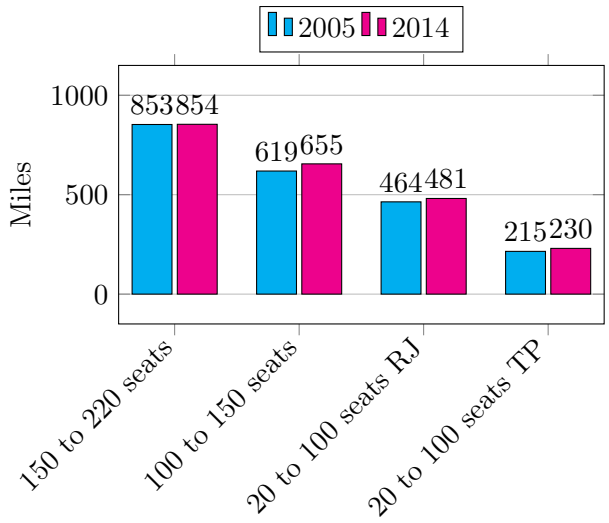

(B) Average seat per stage length (miles).

FIGURE 1.14: Bombardier market outlook [3].

1.2 Regional turboprop aircraft

A typical large turboprop aircraft (with about 70 seat) has a maximum take-off weight W_{to} from 23 to 28 tons, with a an empty weight W_e slightly bigger than 50 % W_{to} (about 13-17 tons). Figure 1.15 shows the ATR-42 three-view. In Figure 1.16 the ATR-72 and the Bombardier Q-400 pictures are shown, whose main characteristics are reported in Table 1.1.

Both aircraft have a straight tapered high-wing configuration, with about 60 m^2 to 70 m^2 planform area and about 27 m to 30 m wing span, that is an aspect ratio $\mathcal{AR} \approx 12$. A high-wing configuration provides an easy cabin access and a better aircraft clearance. To guarantee take-off from not prepared runways, a low-wing configuration is penalized due to an increased foreign object damage and propeller strike risks. The tail surfaces have similar geometrical characteristics both in terms of configuration and dimensions. T-tail configuration has been adopted for both airplanes, with the tailplane to wing area ratio S_h/S very close to 0.20 for both the horizontal and vertical tailplanes. Also, the fuselage slenderness ratio L_f/D_f is similar for both aircraft, between 10 and 12. Both airplanes have a dorsal fin to increase directional stability at high sideslip angles.

The airframe structures are made of high strength aluminum alloy. This choice is primary due to reliability and low maintenance and construction costs. The ATR-72 has the wing and the fuselage built of light aluminum alloy. ATR declared that composite materials constitutes 20 % of the aircraft empty weight and extended their application to the empennage. Bombardier declared the use of composite panels on radome, nose equipment bay, wing-fuselage fairings, tailcone, dorsal fin, and horizontal stabilizer leading edge. Steel structural alloy are used in the landing gear for both the aircraft [9]. The ATR-72 provides a short main landing gear located in a pod beneath the fuselage, whereas the main landing gear of the Q-400 deploys from the engine nacelle.

From all the above-mentioned considerations it is possible to identify the main features of large turboprop transport aircraft (referred to the nowadays market leaders aircraft):

- high-wing;
- T-tail;
- slender fuselage;

- wing mounted engines;
- easy cabin access for both passengers and baggage;
- reliability, low maintenance and manufacturing costs.

As highlighted in Ref. [9], future turboprop aircraft design should provide more reliable, environment friendly, low noise emission, and lower maintenance and operative costs airplanes. Thus, next generation turboprop aircraft should have:

- advanced avionics:
- full glass cockpit;
- fly-by-wire controls;
- enhanced cabin comfort.

It is quite apparent that an aircraft of this category must have a very accurate design in order to satisfy the above mentioned requirements. In particular, the aerodynamic design of these aircraft involves many aspects that must be assessed and addressed thoroughly in the design phase. In the following sections, the characteristic components of a regional turboprop aircraft are presented.

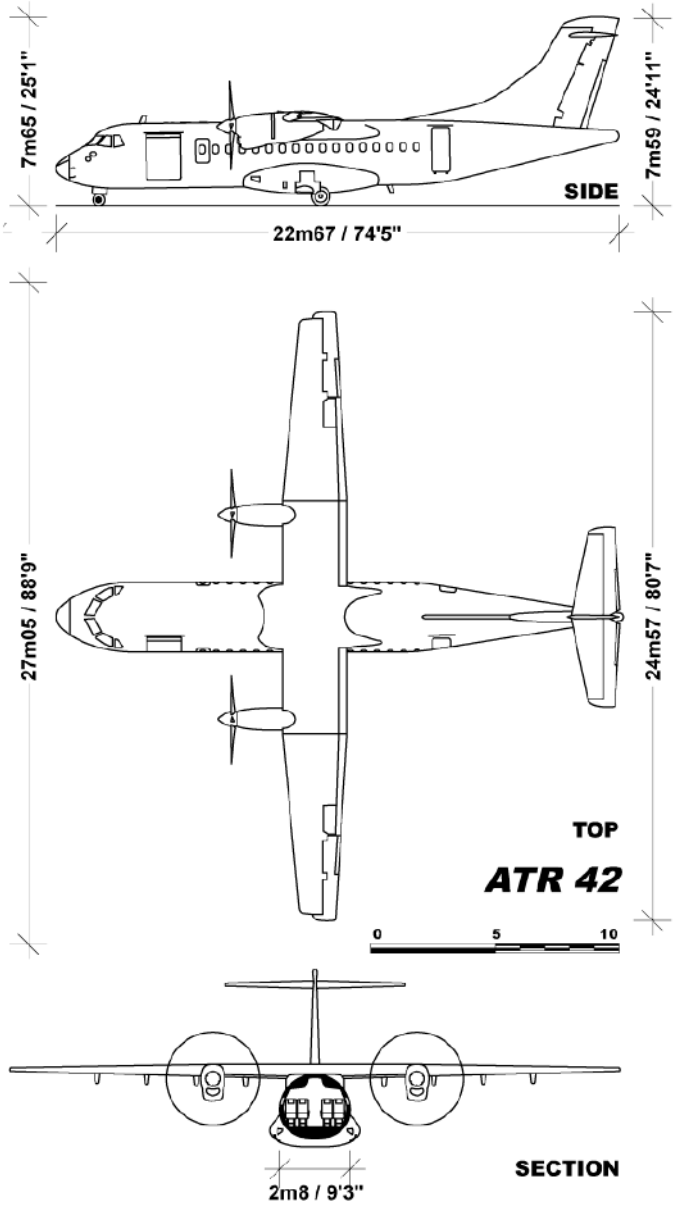

FIGURE 1.15: ATR-42 three-view. ©User:Julien.scavini / Wikimedia Commons / CC-BY-SA 3.0.

(A) ATR-72. Adrian Pingstone / Wikimedia Commons / Public Domain.

(B) Bombardier Dash 8 Q-400. Pedro Aragão / Wikimedia Commons / CC-BY-SA 3.0.

FIGURE 1.16: Typical regional turboprop aircraft.

TABLE 1.1: Large turboprop aircraft main characteristics.

	ATR-72	Dash 8 Q-400
Crew	2+2	2+2
Passengers	70	78
Takeoff mass, kg	23 000	27 995
Empty mass, kg	12 850	17 148
Fuselage length, m	27.17	32.81
Fuselage slenderness ratio	10.10	12.20
Wing		
Planform area, m^2	61.00	63.08
Span, m	27.05	28.42
Aspect ratio	12.0	12.1
Root airfoil thickness	18 %	18 %
Tip airfoil thickness	13 %	12 %
Horizontal tail		
Planform area, m^2	12.00	14.56
Span, m	8.10	7.85
Aspect ratio	4.4	4.3
Tail-to-wing area ratio	0.20	0.23
Tail volume coefficient	1.13	1.96
Vertical tail		
Planform area, m^2	12.00	14.13
Span, m	4.34	4.28
Aspect ratio	1.57	1.30
Tail-to-wing area ratio	0.20	0.22
Tail volume coefficient	0.10	0.13
Performance		
Cruise speed, km/h	511	648
Service ceiling, m	7620	6250
Range, km	2666	2400
Rate of climb, m/s	9.38	– – –
Take-off distance, m	1223	1350

1.2.1 The turboprop engine

The turboprop engine is a gas turbine engine where all the useful power output is transmitted by a shaft, driving an unducted fan or propeller. A scheme of the turboprop engine is shown in Figure 1.17. The low pressure turbine drives a large propeller through a speed reduction gearbox. The thrust T is generated by accelerating a large air mass flow:

$$T = \dot{m}\Delta V \tag{1.1}$$

where $\dot{m}$ is the air flow ($\mathrm{kg\,s^{-1}}$) and ΔV is the difference between the jet exhaust speed and aircraft speed (assuming the nozzle is not choked).

With respect to the turbojet (or the turbofan) engine, the turboprop engine accelerate more air at a lower velocity, delivering more thrust for a given fuel consumption (or lower fuel consumption for a given thrust). However, because of the low jet velocity, thrust lapses quickly as flight speed is increased. For this reason, and for compressibility effects on the propeller blades, the this kind of engine cannot be used in high-speed applications [10]. See again Figure 1.11a for reference, where it is apparent that large turboprop aircraft are very efficient between 250 and 350 kts.

1.2.2 Fuselage

The preliminary general arrangement of an aircraft is closely tied up with the fuselage, whose main dimensions should be laid down in some detail. In fact, the fuselage represents such an important item in the total concept that its design might well be started before the overall configuration is settled. It should be designed "from the inside outwards", and the skin should envelop the payload in such a way that the wetted area is minimum, thus avoiding breakaway of the airflow as far as possible. A typical layout for large turbopropeller transport aircraft is shown in Figure 1.18.

About 30 % of zero lift drag of the ATR-72 (34 % for a 90-seat turboprop) is due to the fuselage [9, §1.3]. Aircraft cruise performance, such as maximum flight speed or fuel consumption, are mainly dependent from the zero lift drag coefficient C_{D_0} and they could be improved with an accurate aerodynamic design. Moreover, aircraft longitudinal and directional stability characteristics are strictly related to the fuselage contribution, thus an accurate estimation

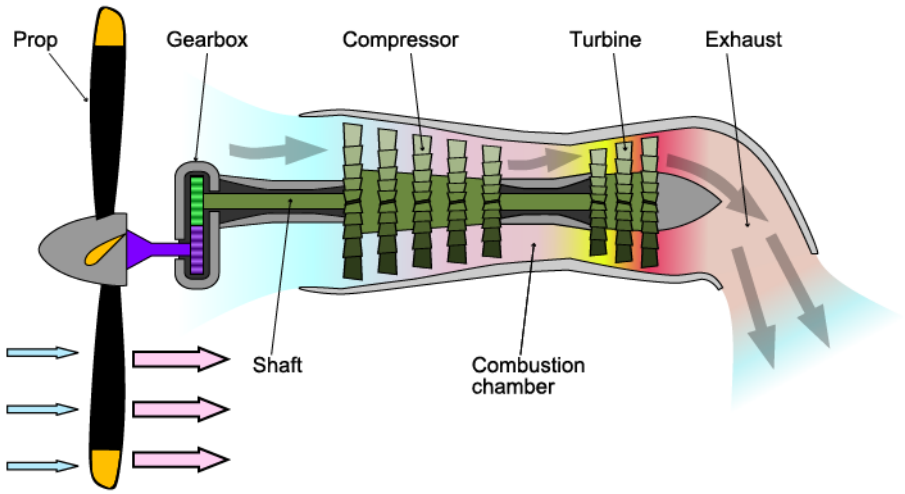

FIGURE 1.17: Turboprop engine schematics. ©User:Emoscopes / Wikimedia Commons / CC-BY 2.5.

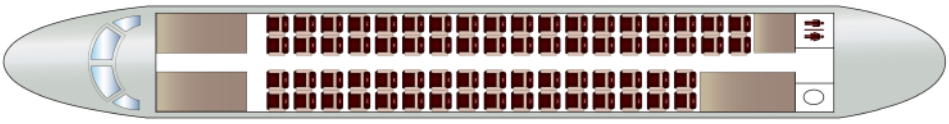

FIGURE 1.18: Example of fuselage layout. Reproduced from Ref. [11].

of the latter could lead to a better tailplane design and aircraft stability characteristics.

1.2.3 Vertical tail

As highlighted by aeronautic engineering textbooks [12–17], the vertical tailplane (Figure 1.19) must provide aircraft directional equilibrium, stability, and control in all flight conditions. Landing in a strong crosswind or takeoff with one engine inoperative (OEI) are critic conditions defined by authorities [18, 19] that are usually employed in the preliminary sizing of the vertical tailplane, in which the aerodynamic interference of other aircraft components (wing, fuselage, and horizontal tailplane) must be accounted for, otherwise

(A) Cessna 172 empennage. ©User:Elliebutton408 / Wikimedia Commons / Public Domain.

(B) Airbus A400M vertical tail. Photo by the author. Flickr / All rights reserved.

FIGURE 1.19: Examples of aircraft vertical tail.

it could lead to a heavier and more costly component (if oversized) or to insufficient directional stability (if undersized).

Minimum control speed V_{MC} is the calibrated airspeed, at which, when the critical engine is suddenly made inoperative, it is possible to maintain control of the airplane with that engine still inoperative, and maintain straight flight with an angle of bank of not more than 5° [18, §25.149]. The *airborne* minimum control speed may not exceed 1.13 times the reference stall speed (defined in Ref. [18, §25.103]), hence *it affects the take-off field length*, which must be kept as low as possible, otherwise payload could be reduced on short runways. Details may be found in the interesting article wrote by Horlings [20]. Here it is sufficient to say that, in OEI condition, the vertical tail has to counteract the airplane asymmetrical thrust. Forces and moments acting on the airplane in OEI conditions are shown in Figure 1.20, whereas a

preliminary vertical tail surface sizing can be outlined with the chart shown in Figure 1.21. The propeller-driven engine generates a thrust which decreases with airspeed, while the yawing moment of the vertical tail may be expressed as (details in Perkins and Hage [16, §8.3])

$$N_v = \frac{1}{2}\rho V^2 S b \, C_{N_{\delta_r}} \delta_r \tag{1.2}$$

$$C_{N_{\delta_r}} = C_{L_{\alpha_v}} \tau_r \frac{S_v}{S} \frac{l_v}{b} \eta_v \tag{1.3}$$

where (signs are omitted):

$C_{N_{\delta_r}}$ is the *rudder control power*

$C_{L_{\alpha_v}}$ is the lift curve slope of the vertical tail

τ_r is the rudder effectiveness $\frac{\partial \beta}{\partial \delta_r}$

$\frac{S_v}{S}\frac{l_v}{b}$ is the *vertical tail volume coefficient*

η_v is the dynamic pressure ratio.

Details on vertical tail sizing are given in Section 3.1 and Section 3.2. Basically, semi-empirical methods provide a way to calculate aircraft directional stability and control by including the effects of wing, fuselage, and horizontal tail in the $C_{L_{\alpha_v}}$ term. The rudder control power may be approximated as

$$C_{N_{\delta_r}} = C_{N_{\beta_v}} \tau_r \tag{1.4}$$

where the *static stability derivative* $C_{N_{\beta_v}}$ includes the above-mentioned effects. Thus, the calculation of directional control authority can be calculated, at least in a first approximation, from the directional static stability derivative. The method developed by the author, discussed in Chapter 5, tries to give a more accurate estimate of the aircraft C_{N_β}, providing an alternative to the methods described in Chapter 3. Equation 1.4 is an approximation because the effects of aerodynamic interference are not the same of the static stability case, as will be shown in Chapter 7.

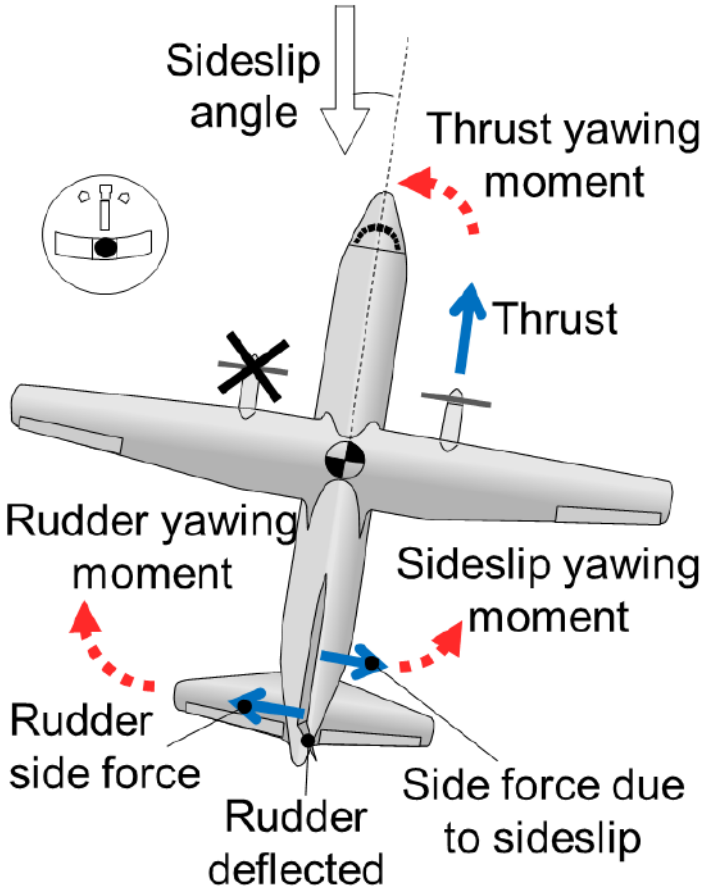

FIGURE 1.20: Most important forces and moments acting on the airplane while using the rudder to counteract the asymmetrical thrust and while keeping the wings level. Notice a sideslip cannot be avoided for balance of side forces: the drag is not minimal, rate of climb not maximal. ©Harry Horlings / Wikimedia Commons / CC-BY-SA 3.0.

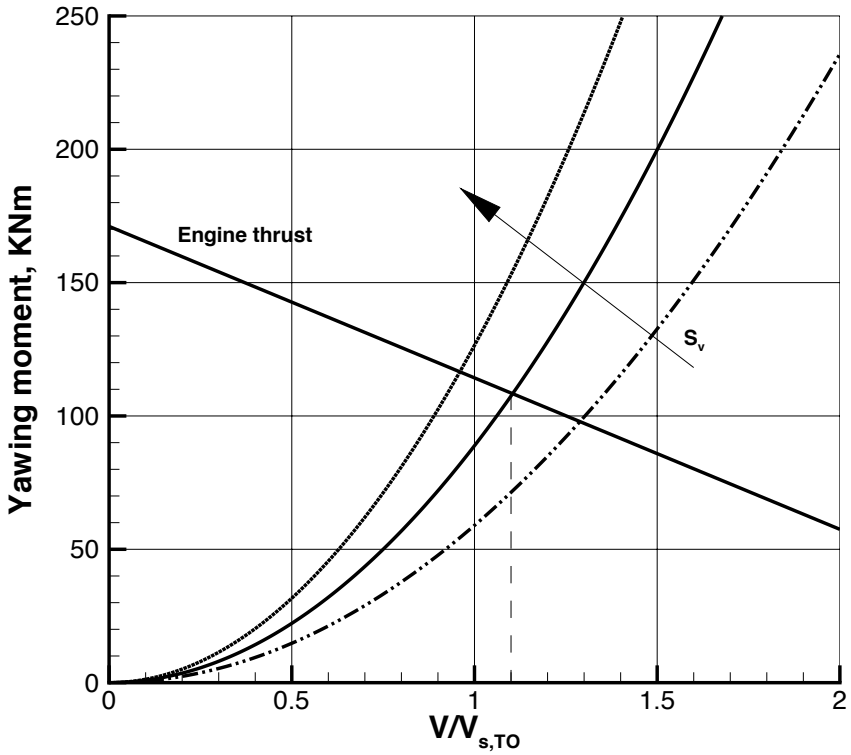

FIGURE 1.21: Chart to preliminary select the vertical tail area S_v according to airborne minimum control speed limit.

1.2.4 Drag breakdown

Della Vecchia [9, §1.3] evaluated the drag for a typical regional turboprop transport aircraft like the ATR-72. The method is discussed in Section 3.3. Here, the approach has been applied to a 90 seats turboprop transport, with the following results: the fuselage provides 81 drag counts[2] and it is the most influent drag source, followed by the wing, interference drag, and nacelle, as reported in Figure 1.22.

However, if some drag sources are included in the items which produce them, the drag breakdown slightly change in proportion. If:

- base drag, upsweep, and windshield are included in the fuselage;
- interference drag is added to wing, because of the wing-fuselage and wing-nacelle junction;
- gaps are divided and assigned to wing, nacelle, and empennage;

it results that fuselage is responsible for the 34 % of aircraft drag, followed by the wing (32 %) and other components, see Figure 1.23.

It has been shown [9, §1.3] that, for a large turboprop transport aircraft, there is an increase of 1 knot maximum cruise speed for every 2.5 drag counts less. A 15 drag count reduction provides 3 % fuel saving on a 200 miles stage length.

[2] 1 drag count = 0.0001

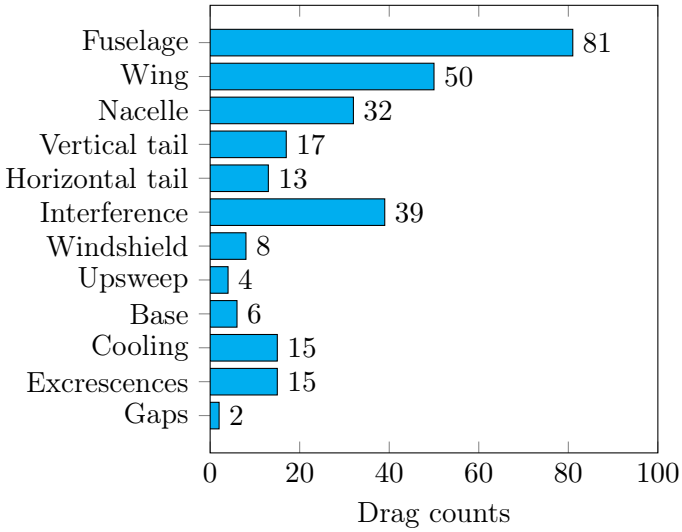

FIGURE 1.22: Turboprop drag source.

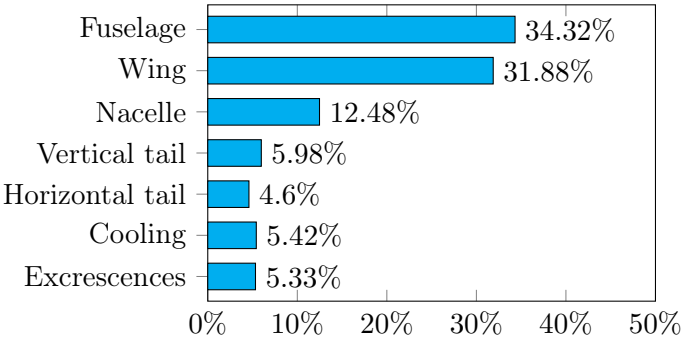

FIGURE 1.23: Turboprop drag breakdown.

1.3 Direct operating costs (DOC)

Direct operating costs (DOC) are associated with flying and direct maintenance of the aircraft (fleet). These include the engineering, manufacturing, materials, spares, avionics, and engine that form the total aircraft price. Depreciation, insurance, and interest rates (loan repayments) form the standing charges that must be accounted for. Maintenance of the engine, of the airframe, and overhead must be provided to upkeep the aircraft. Flight operations costs can be divided in crew cost, fuel/oil cost, and airport fees [21, Chap. 12].

1.3.1 A simple method to evaluate DOC

A very simple DOC estimation has been found in Ref. [22]

$$\mathrm{DOC} = c_{\mathrm{man}} + pW_e \tag{1.5}$$

where c_{man} are the manufacturing costs, p is a weight penalty, W_e is the aircraft empty weight. The manufacturing costs are defined as follows by Ref. [12, §18.4.2]

$$c_{\mathrm{man}} = 0.9(H_E R_E + H_T R_T + H_M R_M + c_{\mathrm{mat}}) \tag{1.6}$$

where H_E, H_T, and H_M are the engineering, tooling, and manufacturing hours respectively, whereas R_E, R_T, and R_M are the engineering, tooling, and manufacturing cost rate in \$/hr respectively, defined in Table 1.2. Following the modified DAPCA IV[3] model proposed by Raymer [12, §18.4.2], the engineering, tooling, and manufacturing hours are calculated

$$H_E = 4.86\, W_e^{0.777} V^{0.894} Q^{0.163} \tag{1.7}$$

$$H_T = 5.99\, W_e^{0.777} V^{0.696} Q^{0.261} \tag{1.8}$$

$$H_M = 7.37\, W_e^{0.820} V^{0.484} Q^{0.641} \tag{1.9}$$

where W_e is the aircraft empty weight in lb, V is the aircraft max cruise speed in kts, Q is the number of aircraft produced in 5 years.

[3] Development and Procurement Cost of Aircraft, Version IV.

TABLE 1.2: Labour cost rate in 2012 USD.

R_E	115 \$/hr
R_T	118 \$/hr
R_M	98 \$/hr

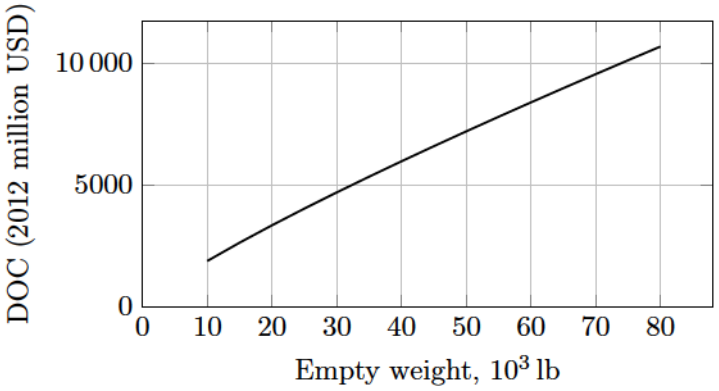

FIGURE 1.24: DOC as function of aircraft empty weight. $V = 280$ kts, $Q = 450$.

The material cost is calculated as follows (assuming a structure mainly made-up of aluminum alloy)

$$c_{\text{mat}} = 22.1\, W_e^{0.921} V^{0.621} Q^{0.799}. \tag{1.10}$$

This model ignores costs of avionics, furnishings, and similar, but includes the fuel cost in the weight penalty p, which is very difficult to estimate. Ref. [22] suggests 1500 to 2000 €/kg for an A350 aircraft, whereas the original proposed range was between 45 and 380 €/kg. Several calculations made by the author revealed that realistic results are obtained for a large turboprop transport aircraft if the weight penalty factor p is close to 3000 \$/lb. Figure 1.24 shows the results of our model for a given value of V and Q.

To check the validity of the approach, the proposed model has been applied to the ATR-72. Assuming:

$V = 280$ kts

$Q = 450$ (see Ref. [23])

$W_e = 27\,500\,\text{lb}$

$p = 3000\,\$/\text{lb}$

flight hours/year/aircraft = 3000

seats = 70

the model provides the following DOC:

$3231\,\$/\text{hr}$

$11.54\,\$/\text{nm}$

$0.16\,\$/\text{seat/nm}$

whereas Ref. [11] provides a DOC of $2944\,\$/\text{hr}$. The approach here developed overestimates the reference value, but results are consistent.

The calculation is repeated for a 90+ seats regional turboprop aircraft, assuming:

$V = 330\,\text{kts}$

$Q = 125$ (see Ref. [1])

$W_e = 43\,200\,\text{lb}$

$p = 3000\,\$/\text{lb}$

flight hours/year/aircraft = 3500

seats = 90

the model provides the following DOC:

$8160\,\$/\text{hr}$

$24.73\,\$/\text{nm}$

$0.27\,\$/\text{seat/nm}$

The cruise speed has increased, as the number of passengers, the empty weight, and the flight hours per year per aircraft. However, the production rate has decreased according to the market forecast (Section 1.1.3). It can be shown that, if the production rate and the flight hours per year per aircraft are kept constant, the DOC per seat per nautical mile is just $\$\,0.01$ over that of the ATR-72.

1.3.2 Effects of vertical tail size and fuselage diameter on performance and DOC

This work mainly deals with *vertical tail* and *fuselage*, with the aim to improve the prediction of aircraft directional stability and performance in the early phase of aircraft design. It is interesting to evaluate how the variation in size of these components may affect the aircraft operative costs.

It should be apparent that an increase in aircraft component size leads to an increase in drag, weight, and operating costs. A bigger tail provides a better stability (if desired) and a larger fuselage provides more comfort. How much more an airline is going to pay for these design decision (bigger tail, larger fuselage), with respect to a baseline value?

Similarly, if the tail size is reduced, but the design provides the same amount of directional stability, by simply adopting a different preliminary design approach that better evaluates the aerodynamic interference among aircraft components, and the same manufacturing technology is employed; or the fuselage contribution to the zero-lift drag is decreased by reducing the wetted area because of a shorter nose and tailcone, while keeping the same seats number and comfort level; how much the airline is going to save on operating costs because of the different preliminary design approach? This section tries to answer these questions, by performing a simple tradeoff study.

From literature [12, 24] it is known that the zero-lift drag coefficient C_{D_0} (in the approximation of the parabolic drag polar) is directly proportional to the aircraft wetted area S_{wet}. From Ref. [9] it has been adopted the relationship 2.5 drag counts $\Leftrightarrow$ 1 knot of max cruise speed. The influence of the wetted area $S_{v,\text{wet}}$ on aircraft structural (empty) weight W_e must be accounted too. A very simple formulation taken from Ref. [12, §15.2] states that:

$$W_v = 5.5\, S_{v,\text{exp}} \tag{1.11}$$

$$W_f = 5.0\, S_{f,\text{wet}} \tag{1.12}$$

where the weights W_v and W_f of the vertical tail and fuselage respectively are expressed in lb, and S_{exp} is the exposed projected area of the vertical tail, directly proportional to its planform area S_v, expressed in ft^2. The following

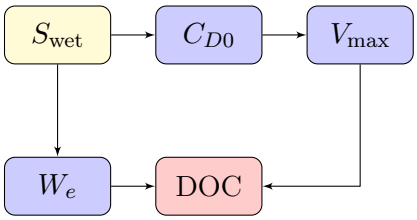

FIGURE 1.25: Flow chart, from wetted area to direct operating costs.

approximations are considered:

$$S_{v,\text{exp}} = 0.9\, S_v \tag{1.13}$$

$$S_{f,\text{wet}} = 0.9\, \pi D_f L_f \tag{1.14}$$

where D_f and L_f are the fuselage diameter and length respectively, expressed in ft.

A flow chart resuming the relationship between wetted area and direct operating costs is shown in Figure 1.25.

The effects of a 10 % variation of the vertical tail planform area and 10 % fuselage diameter variation of a 90-seats turboprop aircraft are here investigated. As previously stated, assuming a large turbopropeller aircraft of 33 tons (72 000 lb) of maximum takeoff weight, 60 % of which is empty weight (43 200 lb), 500 units to be produced in the next 20 years (125 in 5 years), 330 kts max cruise speed, 3000 \$/lb weight penalty, and 3500 flight hours per year per aircraft, the remainder of the data is reported in Table 1.3. The zero lift drag coefficient C_{D_0} is calculated with the method reported in Roskam [24, Part VI, Chap. 4], its effect on max cruise speed $V_{\max}$ is calculated with the relationship proposed in Ref. [9, §1.3], and performance results about cruise are reported in Table 1.4. The application of the simple DOC model proposed in Sec. 1.3 provides the final results of Figure 1.26.

According to Figure 1.25, both structural weight W_e and max cruise speed $V_{\max}$ influence DOC, but $V_{\max}$ is often a design requirement and should not be implemented as a parameter in an optimization loop. In fact, the inital calculation made by the author, assuming a variable $V_{\max}$ with C_{D_0}, in the case of +10 % S_v and hence a *heavier* tailplane, lead to a slight *decrease* of the DOC, an unexpected result. This is due to the combined effects of weight and airspeed changes in the engineering, tooling, and manufacturing

TABLE 1.3: Input data for DOC calculation of a 90-seats turboprop aircraft.

Parameter	Symbol	Baseline	+10 %	–10 %
Vertical tail				
Planform area	S_v, ft^2	194	214	174
Wetted area	S_{wet}, ft^2	366	403	330
Structural weight	W_v, lb	959	1055	863
Fuselage				
Diameter	D_f, ft	11.3	12.5	10.2
Length	L_f, ft	98.3	-	-
Wetted area	S_{wet}, ft^2	3147	3461	2832
Structural weight	W_f, lb	15 734	17 307	14 161

hours, which decreased because of the max airspeed reduction. Eventually, the effect of $V_{\max}$ should be accounted in the weight penalty p too, because of different fuel consumption, but it was too difficult to estimate correctly. Thus, the final results of Figure 1.26 are based on a constant max cruise speed of 330 kts.

It may be concluded that the variation of ±10 % vertical tail size are negligible to aircraft direct operating costs (order of the 3 $/hr to 5 $/hr), but the effect of 10 % diameter (or wetted area) variation has the significant impact of about ±245 $/hr per aircraft.

One may object that, since a sensible variation in vertical tail size does not affect the aircraft direct operating costs, the development of a new method of aerodynamic preliminary design may be not worth the effort. In truth, the primary objective of this work is not to reduce (at least not directly) the DOC of a regional turboprop aircraft, but to investigate the application of the Computational Fluid Dynamics (CFD) in preliminary aircraft design by parametric studies and to *provide a reliable tool to get a designer more confident in the early stage of aircraft conceptual design.* This may affect the development costs (hence the engineering hours H_E in Equation 1.6), since the *numerical simulations and wind tunnel tests hours could be reduced.*

TABLE 1.4: Drag and performance evaluation for a 90-seats turboprop aircraft.

	C_{D_0}	$V_{\max}$, kts
Baseline	0.0279	330.0
$+10\%\, S_v$	0.0281	329.2
$-10\%\, S_v$	0.0277	330.8
$+10\%\, D_f$	0.0291	325.2
$-10\%\, Df$	0.0267	334.8

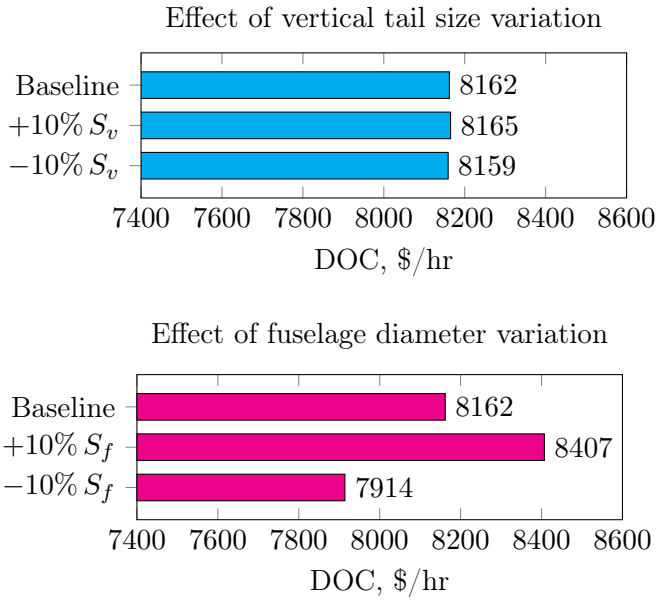

FIGURE 1.26: Results of DOC analysis on a 90-seats turboprop aircraft.

1.4 Thesis objective and layout

This section concludes the introduction chapter. The focus on the regional turboprop transport is due to "economic" reasons that now should be clear. The "academic" motivation is to provide a more reliable preliminary design method for aircraft directional stability and vertical tail sizing. This topic has been pushed by the fact that semi-empirical methods employed in aircraft design:

1. are based on models that *do not* represent actual transport airplanes;
2. *do assign* all the aerodynamic interference effects on the vertical tail;
3. *may* consequently oversize or undersize aircraft directional stability and control surfaces.

These items are deeply treated in the following chapters.

Chapter 2 discusses the aerodynamics of the vertical stabilizer and of the fuselage, with the mutual aerodynamic interference effects among aircraft components. The main works that describe these effects are presented. The content is divided in two main sections: vertical tail and fuselage. Each of them presents both a technical and historical review. The technical reports presented constitute the base of the semi-empirical methods discussed in the next chapter. It is noted that the models investigated experimentally are quite different from actual transport airplanes.

Chapter 3 presents conceptual and preliminary design methods applied in aircraft directional stability and control prediction. The major focus is given to the vertical stabilizer, since historically all the aerodynamic interference effects have been assigned to it, hence the methods dealing with fuselage contribution to aircraft directional stability give essentially the same results of the isolated fuselage. Some applications are provided about a reference aircraft and parametric studies are presented, highlighting discrepancies between different methods. Again, it is noted that the presented methods have been developed from a database of results based on models that are not similar to a modern transport aircraft.

Chapter 4 describes the application of computational fluid dynamics to aircraft design, stability, and control. After a discussion about the historical background, the advantages and drawbacks of several methods, and a comparison with the wind tunnel testing technique, the approach taken in this

thesis is described and several test cases are presented. Test cases are used to validate the approach and consist in replicating the experimental results of technical reports, by simulating the same models in a CFD environment, including recent models as the wing-body model of the AIAA 2nd High Lift Prediction Workshop and the Tecnam P2012 multi-role aircraft. Finally, lessons learned in CFD simulation are discussed, enabling confidence in its use as a tool for aircraft design process.

Chapter 5 presents the new approach, taken by the author, to develop a new method to calculate aircraft directional stability and apply it to vertical tail sizing. Essentially, it is a parametric study of hundreds of configurations to investigate the effects of the aerodynamic interference among aircraft components. Here, the advantage of using CFD as a design tool is apparent, since the contribution of each airplane part to directional stability can be calculated from the numerical analyses and compared with those of the other components. Thus, *CFD is not used to get absolute results, but to evaluate the mutual aerodynamic interference.* Results of the numerical analyses are collected to define aerodynamic interference factors that characterize the new preliminary design method. At the end, a guided procedure to apply the new approach is illustrated.

Chapter 6 deals with wind tunnel testing. The reason to perform an experimental investigation is to validate the developed method, since the numerical analysis alone is not sufficient to provide enough trust in the new approach. The model tested is the same of the numerical analyses and its design for manufacturing is deeply described. Following, the wind tunnel facility, its instrumentation, the setup, and preliminary tests are presented. Next, the wind tunnel test campaign and results are discussed.

Chapter 7 presents the conclusion and introduces related future research topics: aerodynamic interference effects about aircraft directional control, non-linear effects at high angles of sideslip, dorsal fin, compressibility effects and swept wings.

Chapter 2

Aerodynamics and genesis of semi-empirical methods

Synopsis

✈ The aerodynamics of the vertical tail and of the fuselage is presented

✈ The aerodynamic interference among aircraft components is discussed

✈ Several NACA reports about these effects are described

✈ These results have been collected in semi-empirical methods

Semi-empirical[1] methods are (simple) mathematical models of a physic phenomenon, based on both theoretical assumptions and on experiments. In conceptual and preliminary aircraft design they provide valuable data, even if the aircraft layout has not been sketched yet. They have the advantage to be simple and rapid to compute, especially on electronic spreadsheets, allowing very rapid manual design of experiments and optimization. However, they cannot be very accurate, because the exact shape of the aircraft is unknown, as well as the aerodynamics, structures, and flight performance. They are used to get a good starting point for further analyses. Examples are the preliminary aircraft weight estimation by statistical data about similar airplanes and the initial sizing of wing area and thrust to weight ratio (or

[1]Empirical. *Adjective.* Definition: derived from experiment, experience, and observation rather than from theory or logic. Source: Collins English Dictionary, 2006.

Semi-empirical. *Adjective.* Definition: partly empirical; especially: involving assumptions, approximations, or generalizations designed to simplify calculation or to yield a result in accord with observation. Source: Merriam-Webster. `http://www.merriam-webster.com/dictionary/semiempirical`, August 2015.

power loading for propeller driven aircraft) – known as *design point* – by statistics, simple aerodynamics, and flight mechanics: the final values of aircraft takeoff, empty, and fuel weight, wing planform area, and powerplant takeoff thrust (or power) will not be very different from those determined in the first phase of aircraft design [12–16].

This work mainly deals with the aerodynamics of vertical tail and fuselage, with the aim to improve the prediction of aircraft directional stability. Considering the extent of the matter, almost the totality of the work is presented for the incompressible, steady aerodynamics. The effect of compressibility is accounted into aerodynamic coefficients, it has not been investigated on aerodynamic interference.

2.1 Vertical tail, directional stability and control

2.1.1 Phenomenology

Generally speaking, the aircraft empennage performs three functions:

1. it provides a state of equilibrium (*trim*) in each flight condition;
2. it provides static and dynamic *stability*;
3. it enables aircraft *control*.

Typical arrangements have been shown in Figure 1.19. Tail surfaces sizing and shaping is almost exclusively determined by stability and control considerations. Normally they operate at only a fraction of their lift capability since, for the reasons stated above, they must be far away from stall condition.

A vertical tail, which provides *directional* stability and control, is usually made up of two parts: a fixed wing, called *stabilizer* or *fin*, and a plain flap, the *rudder* (Figure 2.1a). The stabilizer provides directional stability, whereas the rudder is the directional control surface. There is a large variety of tail shapes, often denoted by the letters whose shapes they resemble in front view [15], for instance T, V, H, Y (see Figure 2.1b):

- the standard configuration with roots of both horizontal and vertical surfaces attached directly to the fuselage is *structurally convenient*. The aerodynamic interference with the fuselage and horizontal tail increases the effectiveness of the vertical tail. However large areas of

the tails are affected by the converging fuselage flow, which can reduce the local dynamic pressure;

- a T-tail is often chosen to move the horizontal tail away from engine exhaust and to reduce aerodynamic interference. The vertical tail is in his most effective configuration, since the horizontal tail acts as an *end-plate*. The disadvantages of this arrangement include increased tail aerodynamic loads, potential flutter problems, and wing deep-stall;

- V-tails combine functions of horizontal and vertical tails. They are sometimes chosen because of their increased ground clearance, reduced number of surface intersections, or novel look, but require mixing of rudder and elevator controls and often exhibit reduced control authority in combined yaw and pitch maneuvers;

- H-tails or twin tails use the vertical surfaces as endplates for the horizontal tail, increasing their effectiveness and thus saving vertical tail span. Sometimes are used on propeller aircraft to reduce the yawing moment associated with propeller slipstream impingement on the vertical tail, but more complex control linkages and reduced ground clearance discourage their more widespread use;

- Y-shaped tails have been used when the downward projecting vertical surface can serve to protect a pusher propeller from ground strikes.

The problem of directional stability and control is to ensure that the airplane will tend to remain in equilibrium at zero *sideslip*[2] and to provide a control to maintain zero sideslip during maneuvers that introduce moments tending to produce sideslip [16, §8.1]. Although a tailless airplane is realizable, like a flying wing, whose directional stability is given by the swept wing and pushing propellers or an active control of the lateral control surfaces, the vertical tailplane is the main component of directional stability.

From the dynamic point of view, the role of the vertical tail is to provide *yaw damping*. If the vertical tail volume coefficient (combination of tail area and distance from the wing, see Section 3.1.1) is too small, for a given dihedral effect or lateral stability, the aircraft tends to oscillate in yaw as the pilot gives rudder or aileron inputs. This tendency is called *dutch roll* (see Figure 2.2) and makes precise directional control difficult [25].

[2] Angle between the relative wind and the aircraft longitudinal plane of symmetry.

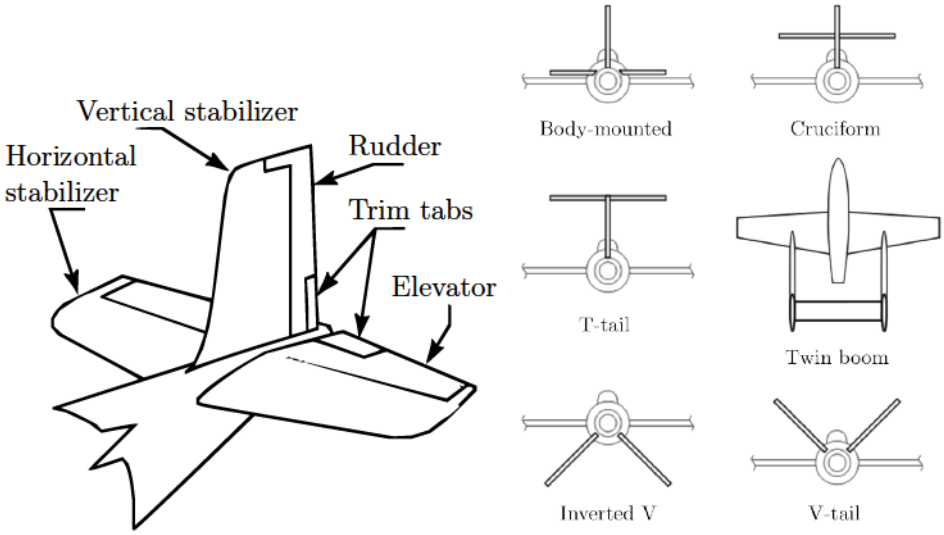

(A) Tail components definition. (B) Tails types. ©User:Steelpillow

FIGURE 2.1: Geometry of various tail arrangements.

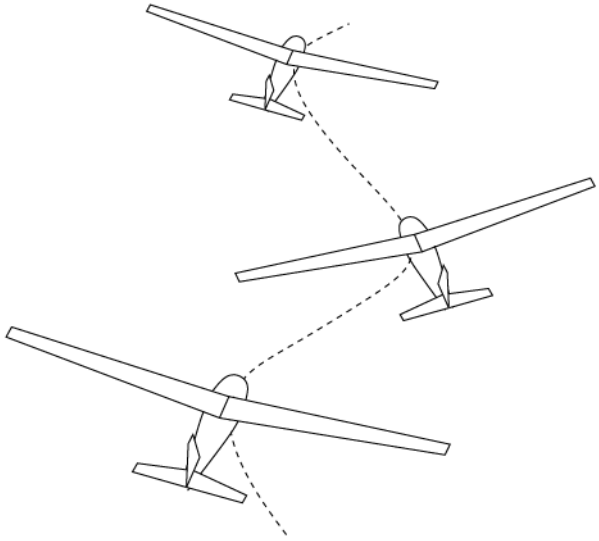

FIGURE 2.2: Dutch roll oscillation tendency from insufficient vertical tail volume. Reproduced from Ref. [25].

Extreme flight conditions often set design requirements for tail surfaces, like minimum control speed with one engine inoperative or maximum cross-wind capability: stability and control must be ensured even at very large angles of sideslip, up to 25° [17, §30]. These conditions are stated by the Federal Aviation Authorities (FAA) [19, §25.171] in the USA and by the European Aviation Safety Agency (EASA) [18, §25.171] in Europe.

Design of vertical tailplanes depends on the type of airplane (and so the flow regime), engine numbers and position, wing-fuselage and horizontal tail position [14, §9.1]. These factors affect the *stability derivatives*, i.e. the variation of aerodynamic coefficients with the independent variable, the angle of sideslip β. It is somewhat complicated since it involves asymmetrical flow behind the wing-fuselage combination and lateral cross-control[3].

The following design requirements can be formulated for vertical tailplanes [17, §30]:

1. they shall provide a sufficiently large contribution to static and dynamic stability, that is the sideforce derivative of the isolated vertical tail

$$C_{Y_{\beta_v}} = C_{L_{\alpha_v}} \frac{S_v}{S} \tag{2.1}$$

has to be determined. The vertical tail directional stability derivative $C_{N_{\beta_v}}$, that is the yawing moment coefficient due to sideslip, depends from the coefficient just defined. If a high lift gradient is desirable, the aspect ratio A_v should be the largest possible with the minimum sweep angle Λ_v. See Figure 2.3 for reference.

2. The same can be stated for sufficient control capability. Moreover control should be possible with acceptable control torque

$$\mathcal{M}_h = \frac{1}{2}\rho V^2 C_h S_c \bar{c}_c \tag{2.2}$$

which depends on control surface area S_c and chord $\bar{c}_c$ behind the hinge line, dynamic pressure $\frac{1}{2}\rho V^2$, and hinge moment coefficient C_h. See Perkins and Hage [16, §8.4] for details on directional control forces.

[3]Lateral control is provided by ailerons, but side forces on vertical planes also cause a rolling moment, which is a rotation about the aircraft longitudinal axis.

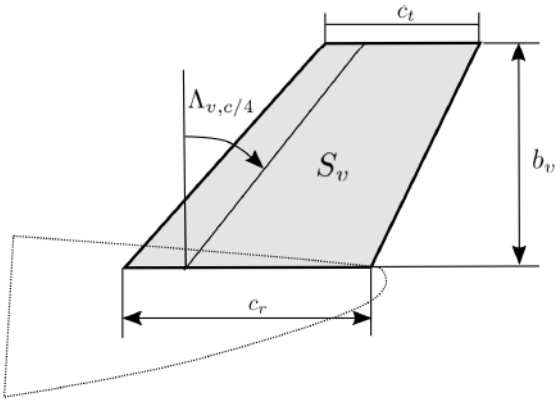

FIGURE 2.3: Vertical tail planform. Definitions of taper ratio and aspect ratio.

3. High angles of sideslip (up to 25°) can be reached and this condition is more serious when flying in possible icing conditions. In this case a low aspect ratio is required and sweep is beneficial, delaying the stall at higher angles of sideslip, but reducing the lift gradient $C_{L_{\alpha_v}}$.

4. Equilibrium has to be achieved in all flight conditions. This leads to specific requirements on tail surface areas and on the maximum lift coefficient with various amount of control surface deflection and should include the effect of ice roughness.

5. A high aspect ratio has an adverse effect on weight. Also, for T-tails the flutter analysis requires extra care.

6. Excessive taper ratio λ_v may lead to premature tip stall. On the other hand, tapering leads to lower weight.

Thus a compromise in high lift gradient and low aspect ratio and taper ratio must be considered. Conceptual design guidelines are presented in Section 3.1.1.

The aircraft directional stability provided by the vertical tail is influenced by the fuselage cross-flow encountered in sideslip, by the horizontal tail position and size, by the wing-body wake and the sidewash effect. Directional control is also influenced by the aerodynamic interference generated by a rudder deflection. Non-linear effects at high angles of sideslip may require the installation of a dorsal fin.

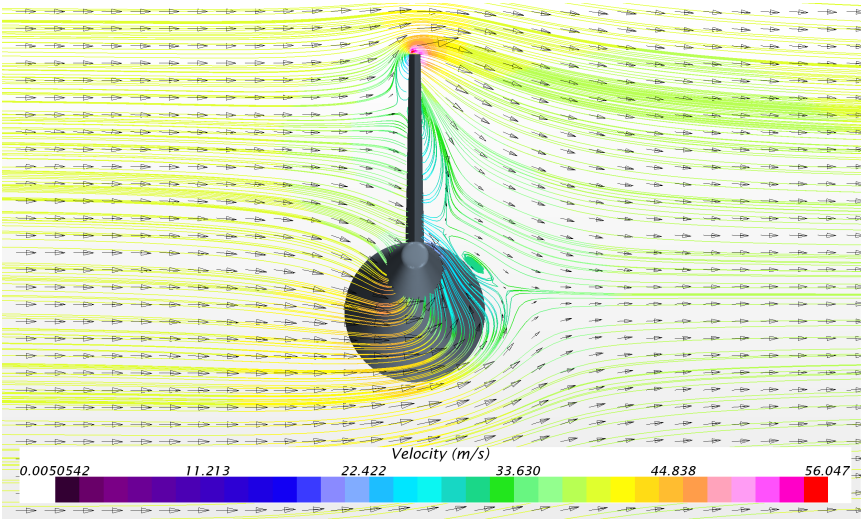

FIGURE 2.4: Effect of the fuselage on the vertical tail: acceleration of the flow at the root of the vertical tail.

Effect of the fuselage

A body in sideslip exhibits a flow characteristic similar to a cylinder in an airflow. For potential flow the peak local velocity occurs at the top at the cylinder and is equal to twice the free-stream cross-flow velocity. Actually, separation exists on the leeward side, reducing the peak velocity from the potential-flow value. Anyway, the velocity decays to the free-stream cross-flow value with distance from the body surface. Thus, tail-body combinations with large bodies and small tails have a greater effectiveness per unit area than combinations with large tails and small bodies and this trend is exhibited by test data. The fuselage *directly* alters the vertical tail incidence because of the cross-flow around the body, see Figure 2.4. The vertical tail itself causes a load carry-over from the tail onto the body that increases the effectiveness of the former [26, §5.3.1.1].

Effect of the horizontal tail

The presence of a horizontal panel in the vicinity of a vertical panel causes a change in the pressure loading of the latter if the horizontal panel is at a height where the vertical panel has an appreciable gradient, i.e. at a relatively high or

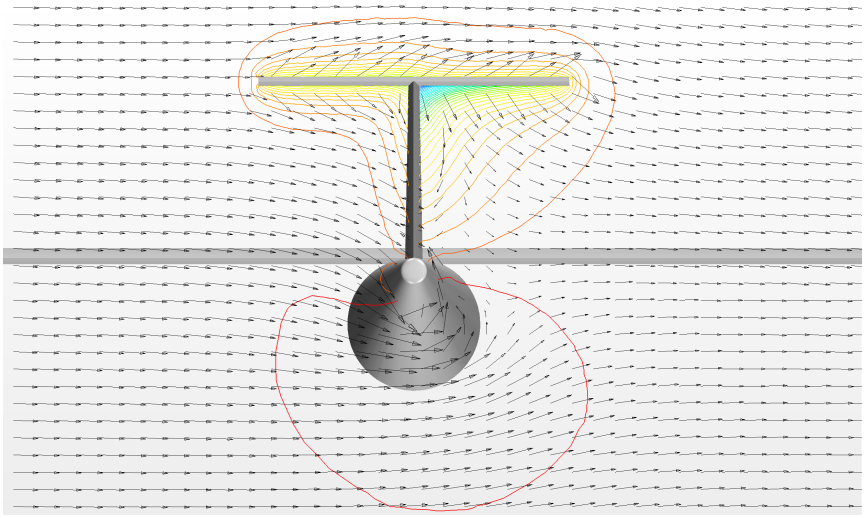

FIGURE 2.5: Effect of the horizontal tail on the vertical tail: the *end-plate* effect.

low position, see Figure 2.5. Test data substantiate the greater effectiveness of horizontal panels in these positions and the relative ineffectiveness of a horizontal panel at the midspan position on the vertical panel. At subsonic speeds the vehicle body and horizontal tail affect the flow on the vertical tail in such a way as to increase the effectiveness of the vertical tail. This phenomenon, known as the *end-plate effect*, is represented by an effective change in panel aspect ratio required to give the same lift effectiveness as the actual panel in the presence of the other vehicle components. Aerodynamic interference also exists among the vertical tail, the body, and any forward lifting surface [26, §5.3.1.1].

Effect of the wing

For a wing-body combination there are two contributions to the sidewash present at a vertical tail: that due to the body and that due to the wing. The sidewash due to a body arises from the side force developed by a body in yaw. As a result of this side force, a vortex system is produced, which in turn induces lateral-velocity components at the vertical tail. This effect, analogous to the downwash in the longitudinal plane, indirectly affects the incidence of the vertical tail because of the generation of the vortex system. This

sidewash from the body causes a destabilizing flow in the airstream beside the body. Above and below the fuselage, however, the flow is stabilizing. The sidewash arising from a wing in yaw is small compared to that of a body. The flow above the wake centerline moves inboard and the flow below the wake centerline moves outboard. For conventional aircraft the combination of the wing-body flow fields is such as to cause almost no sidewash effect below the wake center line [26, §5.3.1.1]. See Figure 2.6. The analyses presented in Chapter 5 do not always agree with these statements. The general trend shows an increase of vertical tail effectiveness in sideslip by lowering the wing on the fuselage and reducing its aspect ratio $\mathcal{AR}$.

Effect of the rudder

The aerodynamics of the directional control surface mainly involves the fuselage and the horizontal stabilizer. For a large turboprop aircraft the mutual effects between the wing and the rudder are negligible, because of their distance [27].

Even without cross-winds, a rudder deflection provides cross-flow on the fuselage. In fact, the deflection of the rudder creates a *local sideslip angle* due to the pressure change on the surfaces of the vertical tailplane and to the circulation induced by the vertical tail lift. This leads to an asymmetric streamlines path only near the tail, as shown in Figure 2.7, which in turn increases the control derivative $C_{N_{\delta_r}}$ due to the favorable aerodynamic interference. Thus, the local cross-component of the velocity on the rear part of the fuselage is accelerated like the flow past of a cylinder, increasing the vertical tail angle of attack close to its root and consequently the lift force generated [27].

The horizontal tailplane acts as end-plate if mounted on the fuselage or on the tip of the vertical tail (Figure 2.8), although the effect is reduced because the cross-flow induced by a rudder deflection without cross-winds is less intense than that generated by the aircraft in sideslip. If the horizontal tail is body-mounted, the end-plate effect seems independent from the vertical tail aspect ratio [27]. Yet, these effects are dependent on the rudder span and chord ratio (i.e. the ratio between the rudder chord and the stabilizer chord).

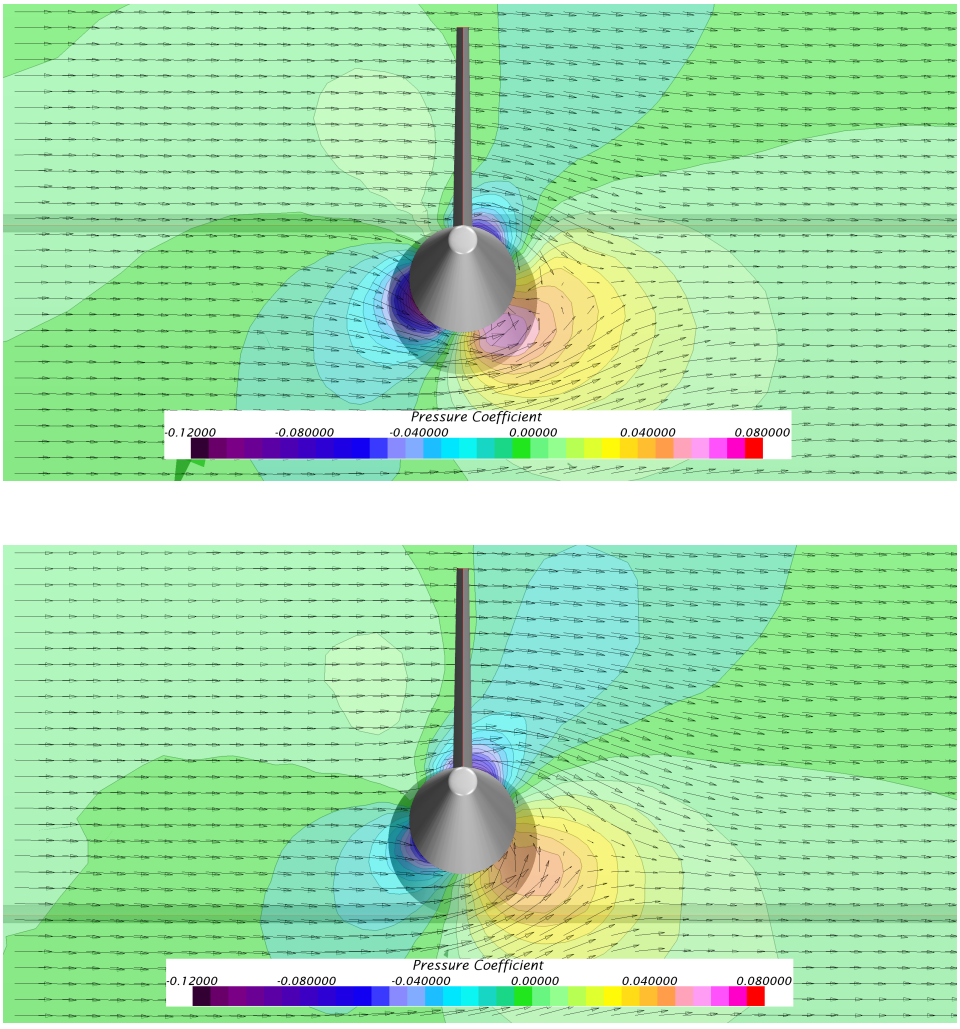

FIGURE 2.6: Effect of the wing on the vertical tail.

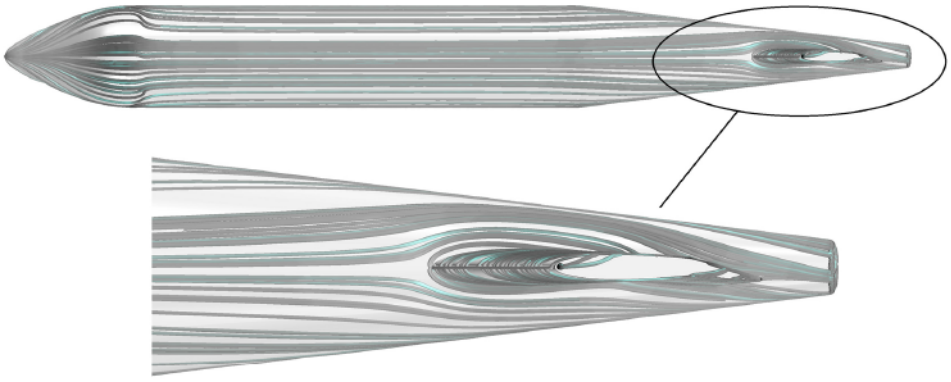

FIGURE 2.7: Streamlines showing the asymmetric flow path in the rear part of the fuselage.

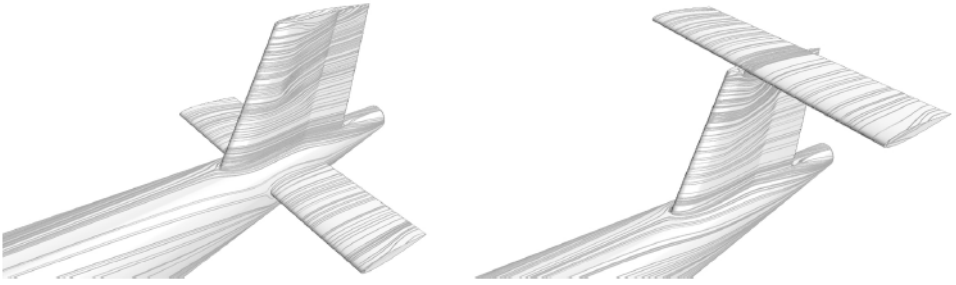

FIGURE 2.8: Streamlines around empennage for body-mounted and tip-mounted horizontal stabilizer configurations.

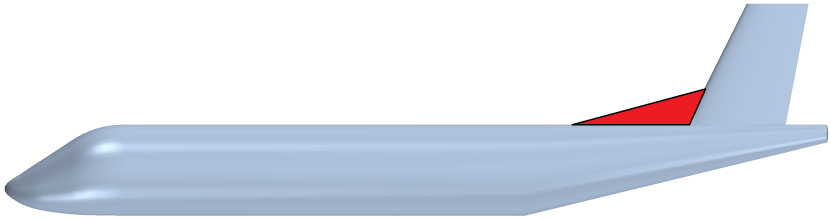

FIGURE 2.9: A dorsal fin is essentially a triangular flat plate installed at the root of the vertical stabilizer.

Effect of the dorsal fin

A dorsal fin is essentially a triangular flat plate installed at the root of the vertical stabilizer, see Figure 2.9. The dorsal fin is applied to delay the stall of the vertical tailplane to unattainable sideslip angles. In the case of reversible controls, i.e. for general aviation airplanes, the dorsal fin is installed to prevent the rudder lock phenomenon [16, §8.4]. This happens when the rudder angle required to keep a given sideslip angle coincides with the rudder floating angle, see Figure 2.10. In this case, the pedal force required to keep that angle is zero. Since the pilot was exerting a pedal force to reach that angle, when the force gradient reduces and the force required becomes null, he will inadvertently push the pedal to the end stop. In this case, the pilot must provide a strong force on the pedal in the opposite direction, since the force gradient has reversed and it is highly increased, that is the rudder seems locked [16, §8.4]. Even without reversible controls, modern transport airplanes (both turboprops and jetliners) may have a dorsal fin, because control forces must be limited.

The dorsal fin provides extra lift at high angles of sideslip, when the vertical tail begins to stall, in a manner similar to the vortex lift generated by delta wing of very low aspect ratio. The flow field around the empennage is swept by two vortex generated by the dorsal fin intersection with the fuselage (*primary vortex*) and with the vertical tail (*secondary vortex*), see Figure 2.11. Because of its extension on the aircraft body, a dorsal fin may affect the directional stability characteristic of the fuselage. Generally speaking, a dorsal fin short in height, but long in chord, will affect more the fuselage than the vertical tail. The combination of dorsal fin chord (length) and height

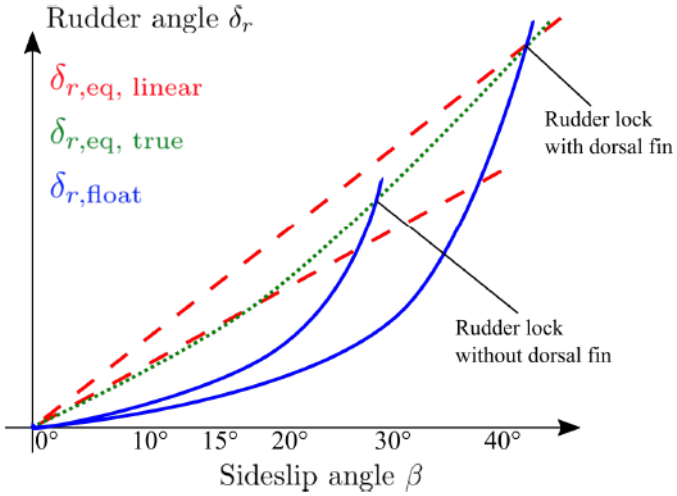

FIGURE 2.10: Rudder lock phenomenon: when the rudder float angle (stick free) approaches the rudder equilibrium angle for a given sideslip angle, the rudder hinge moment, and hence the pedal force, decreases to zero then reverses. A dorsal fin delays this effect to unattainable sideslip angles.

determines its planform area, aspect ratio, and sweep angle. The former is directly related to the size of the dorsal fin and its contribution to directional stability, whereas the latter is related to the generation of vortices and tail stall, together with the aspect ratio.

Several authors [13, 16, 17, 28–32] described the advantage of a dorsal fin, but very few provided data that could be used in aircraft preliminary design. Usually, several dorsal fin planforms are investigated in the wind tunnel in late phase of aircraft design. Obert et al. [17, §32] provided data about some test on the Fokker F-27, whereas Barua, Sousa, and Scholz [32] collected a large amount of geometric data and provided a statistical method to size a dorsal fin.

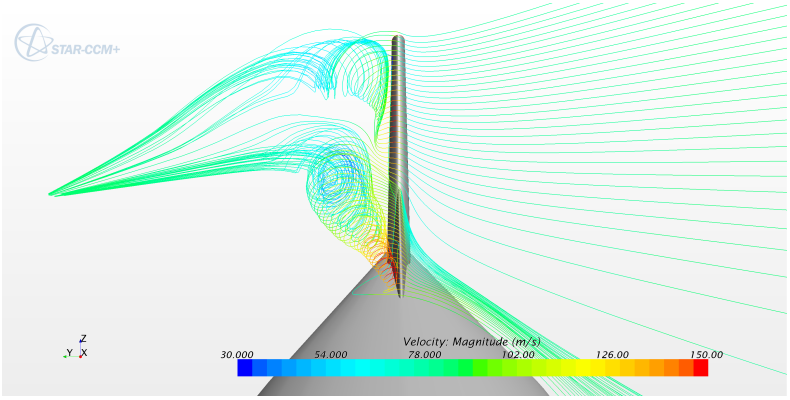

(A) Front view.

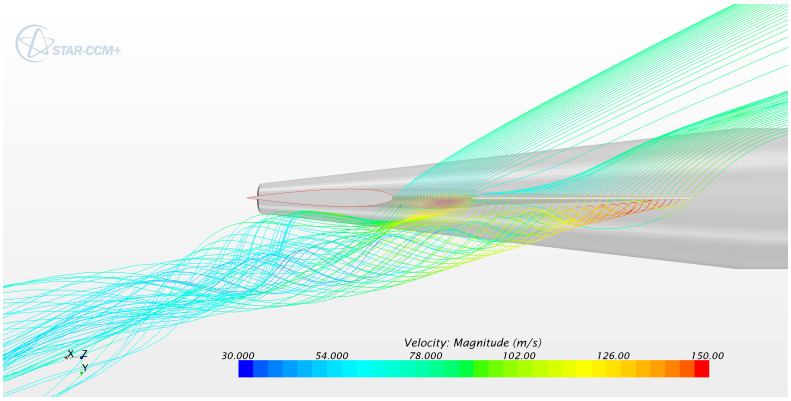

(B) Top view.

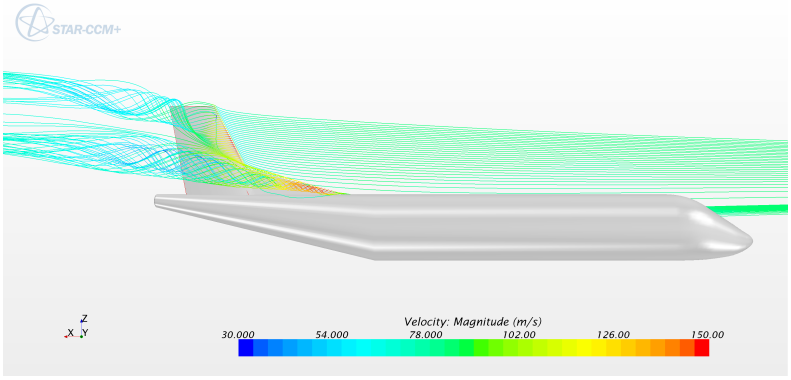

(C) Side view.

FIGURE 2.11: Dorsal fin aerodynamics.

2.1.2 A historical review

From the '30s to the '50s, in the USA, the National Advisory Committee for Aeronautics (NACA) provided useful results about the directional stability on isolated vertical tailplanes, partial and complete aircraft configurations, through many wind tunnel tests. These results were summed up in a method of analysis completely reported and described in the USAF DATCOM[4] by Finck [26]. The investigations were focused to separate the effects of fuselage, wing, and horizontal tail from the isolated vertical tail. From the early years to the '50s, many geometries have been tested, i.e. rectangular, elliptical and swept wings, symmetrical and unsymmetrical airfoils, slender bodies with rounded or sharp edges, tails of different aspect ratio and size [33–37].

However, these geometries are quite different from the actual transport airplanes. The aim of the early tests was to gain a certain knowledge on the mutual interference among aircraft components [33] and on the physics of the problem of directional stability and control [34], while later tests were focused to improve stability and maneuverability of high speed combat airplanes [36].

Investigations about the wing-body system

The aerodynamic interference of the wing-fuselage system on the vertical tail has been investigated by Bamber and House [35] in 1939. The three-view of the aircraft model tested is reported in Figure 2.12. The general trend reveals an increase in sideforce due to sideslip coefficient $C_{Y_{\beta_v}}$ and yawing moment derivative $C_{N_{\beta_v}}$ by moving the wing from high to low position in fuselage (Figure 2.13, respectively right and middle charts), excepts for the fin-off combination where there is a minimum for the mid wing position (without the fin, the model investigated in Ref. [35] has double symmetry, see again Figure 2.12). This trend holds when wing dihedral, flaps, and angle of attack have changed, although different values have been achieved for each combination. The rolling moment derivative $C_{\mathcal{L}_{\beta_v}}$ decreases and changes sign as the wing is moved downward (Figure 2.13, left chart). The effect of the

[4]United States Air Force Data Compendium: a collection, correlation, codification, and recording of best knowledge, opinion, and judgment in the area of aerodynamic stability and control prediction methods, with the purpose to provide a systematic summary of methods for estimating basic stability and control derivatives, organized in such a way to be self-sufficient. For any given flight condition and configuration the complete set of derivatives can be determined without resort to outside information [26].

angle of attack on $C_{N_{\beta_v}}$ is very small, hence it can be neglected (Figure 2.14). Recant and Wallace [38] provided experimental data on sidewash angles at the tail and came to similar conclusions, highlighting that much of the sidewash was produced by the interference between wing and fuselage and that the vertical tail on a low-wing model could stall at a smaller angle of yaw than the tail on a high-wing model. These works did not consider the horizontal tail.

Investigations about the tail-body system

An interesting approach to evaluate the fuselage effect on the vertical tail (without horizontal tail) was taken by Queijo and Wolhart [36] in 1950: an *effective* aspect ratio $A_{v_{\text{eff}}}$ was defined and compared with the ratio of vertical tail span b_v to the fuselage diameter d_f at the longitudinal location of the vertical tail aerodynamic center (shortly: *tail span per body depth*) and parameterized for various tail-fuselage combinations (Figure 2.15). The tail effectiveness increased as the ratio b_v/d_f decreased, that is as the vertical tail became small compared to the fuselage. Theory (based on the assumption that the body acts as an endless plate at the base of the vertical tail) suggested a non-linear increase of the effective aspect ratio with the above mentioned ratio. The scatter in experimental data is bigger for low value of the b_v/d_f ratios and two different trend lines are drawn for two aspect ratios. Similar tests were conducted by Michael Jr [39], which provided data about stability derivatives and location of the vertical tail center of pressure for many configurations.

Before 1950 only tests about untapered planforms were performed. Brewer and Lichtenstein [37] found that results could not be extended to swept planforms. The model used for the investigations [36, 37] was designed to permit tests of the wing alone, fuselage alone, or the fuselage in combination with any tail configuration, with or without the wing. Again, it is remarked that in the work done by Queijo and Wolhart [36] the horizontal tail is not present (Figure 2.16).

Investigations about empennage configurations

The effect of size and position of horizontal tail was studied by Brewer and Lichtenstein [37] in 1950, see Figure 2.17. The vertical tail-fuselage combination was frozen and the effective lift curve slope of the isolated

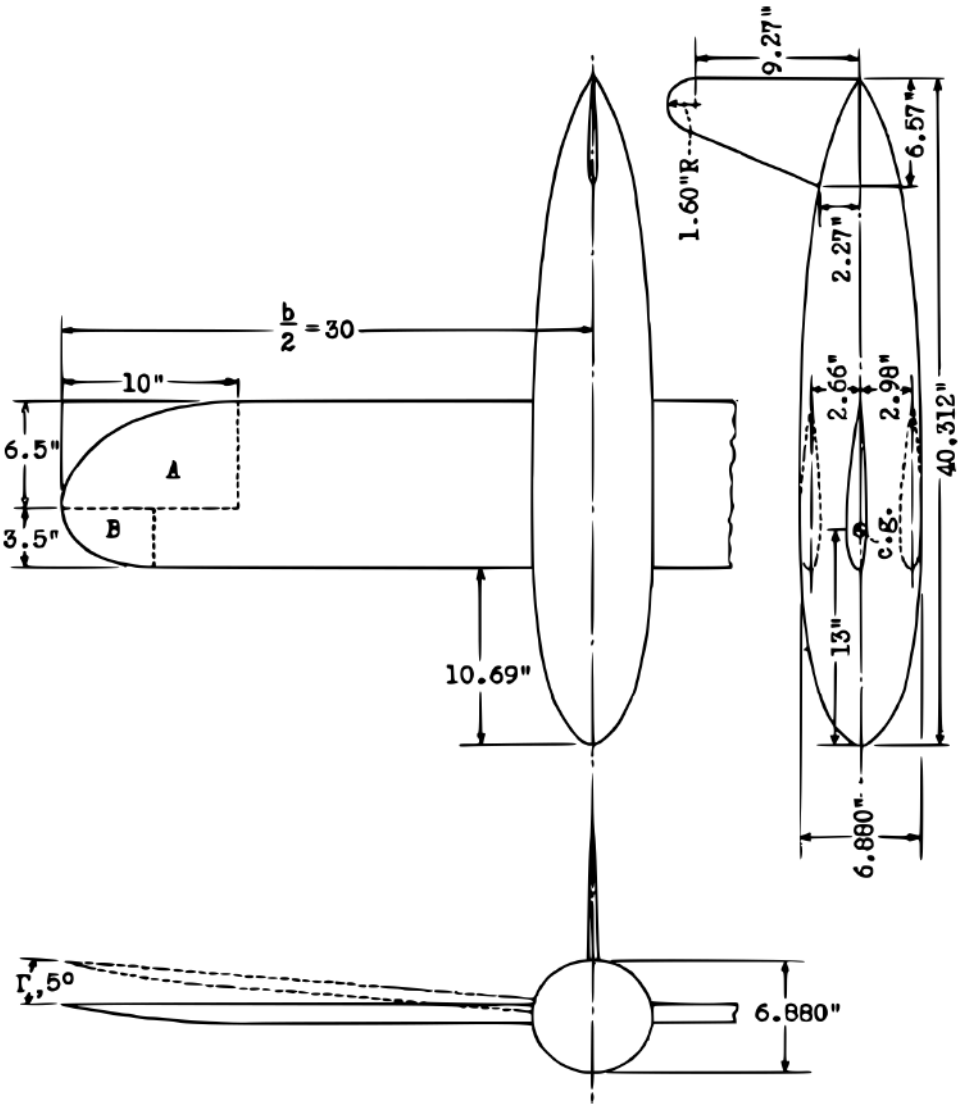

FIGURE 2.12: Geometries of the NACA TR-730. Reproduced from Ref. [35].

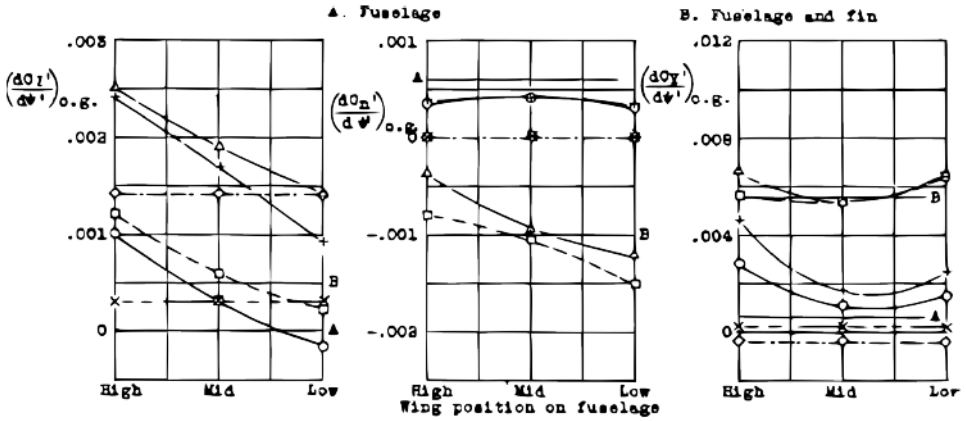

FIGURE 2.13: Some results of the NACA TR-730. Reproduced from Ref. [35].

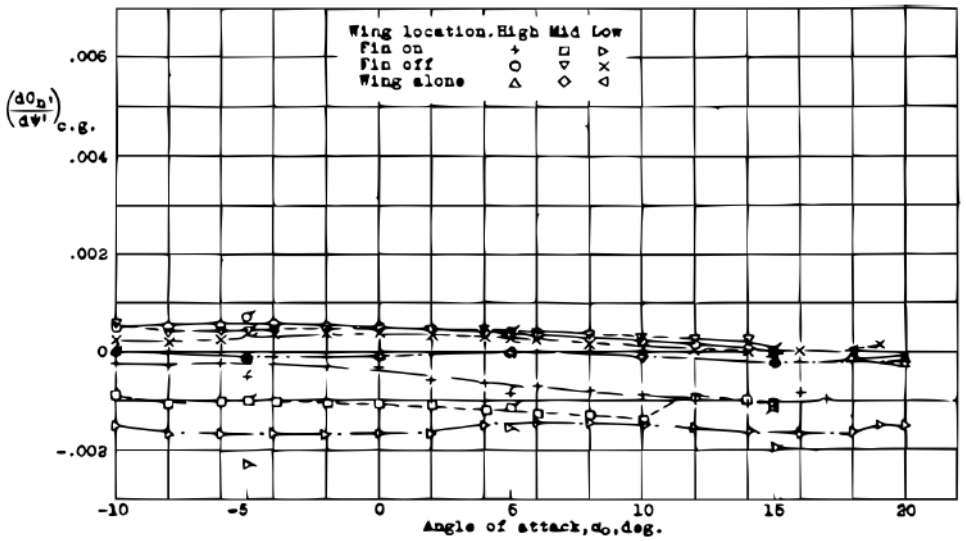

FIGURE 2.14: Insensitivity of the stability derivative C_{N_β} to angle of attack. Reproduced from Ref. [35].

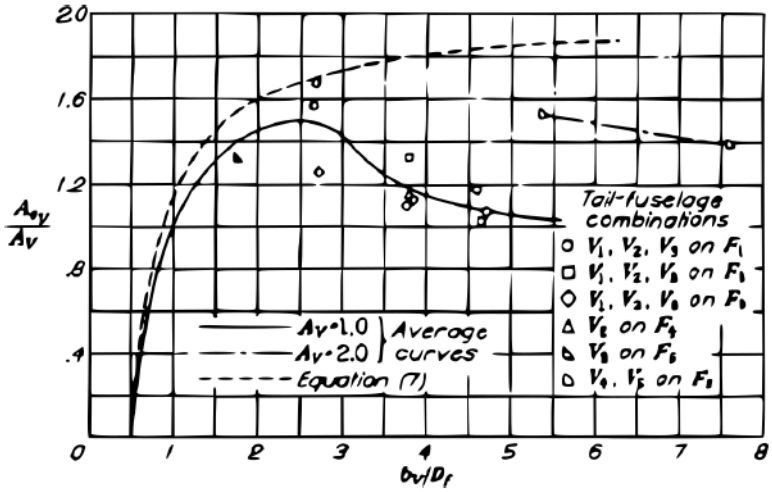

FIGURE 2.15: Effective aspect ratio of vertical tails as influenced by the fuselage ($\alpha = 0°$). The dashed line is referred to the equation derived from theory. Reproduced from Ref. [36].

vertical tail was calculated, as shown in Figure 2.18. The experimental lift curve slope is about 13 % higher than that predicted by theory. Indeed, according to the lifting surface theory, the gradient of the lift coefficient against the angle of attack curve is linear with aspect ratio for planforms with low aspect ratio, see Figure 2.19. According to Obert et al. [17, §32], for $A_v < 1.5$ the following relation holds

$$C_{L_{\alpha v}} = 0.0274\, A_v \quad \left[\text{deg}^{-1}\right]$$

where

$$A_v = \frac{b_v^2}{S} \tag{2.3}$$

so that the lift generated by the vertical tail is

$$L = 0.0274\alpha\,(\text{deg})\,\frac{\rho V^2}{2}\,b_v^2 \tag{2.4}$$

and this leads to the conclusion that, for most vertical tail surfaces, at a given fin angle of attack, the side force is only dependent on the fin height (tail span b_v) and planform is of secondary importance [17, §32].

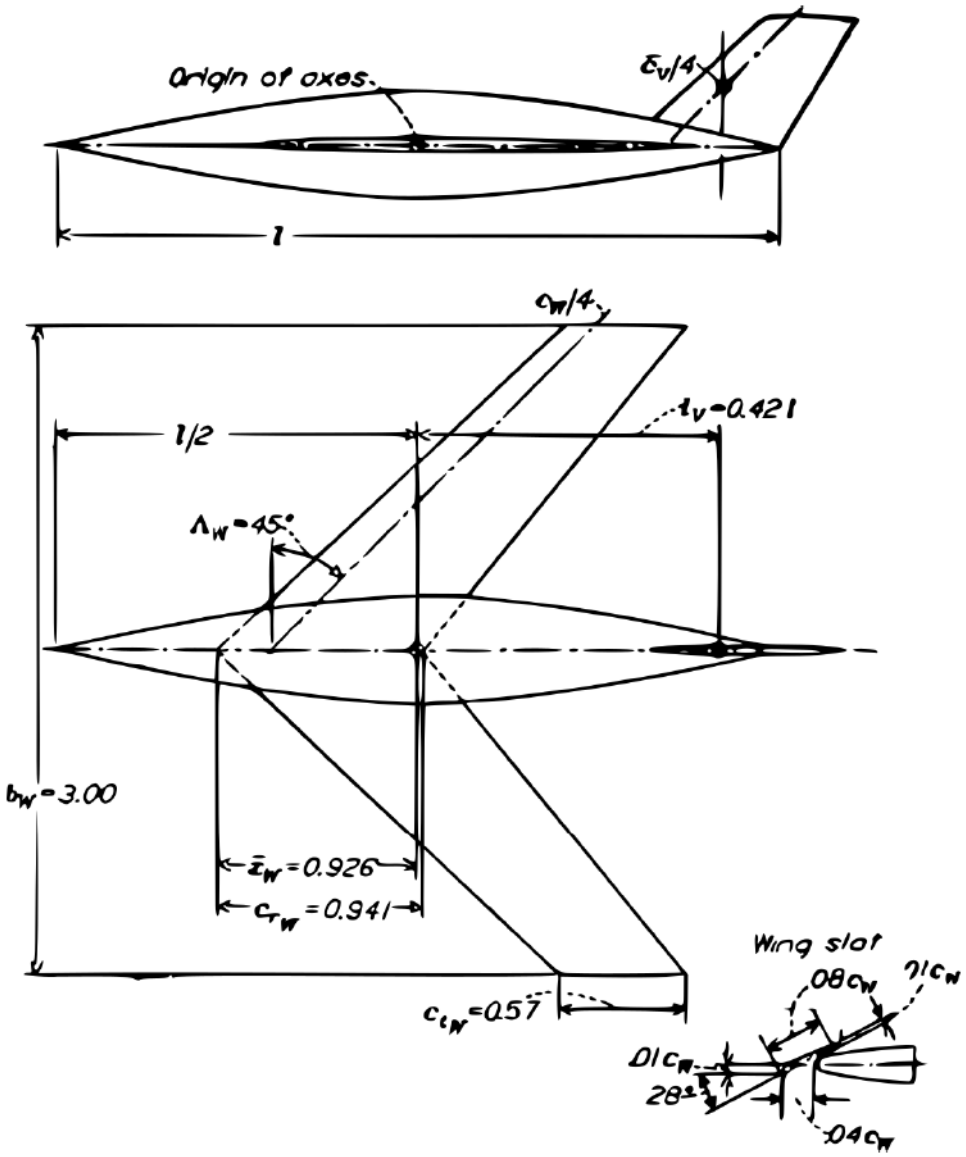

FIGURE 2.16: Geometries of the NACA TR-1049. All units are in feet. Reproduced from Ref. [36].

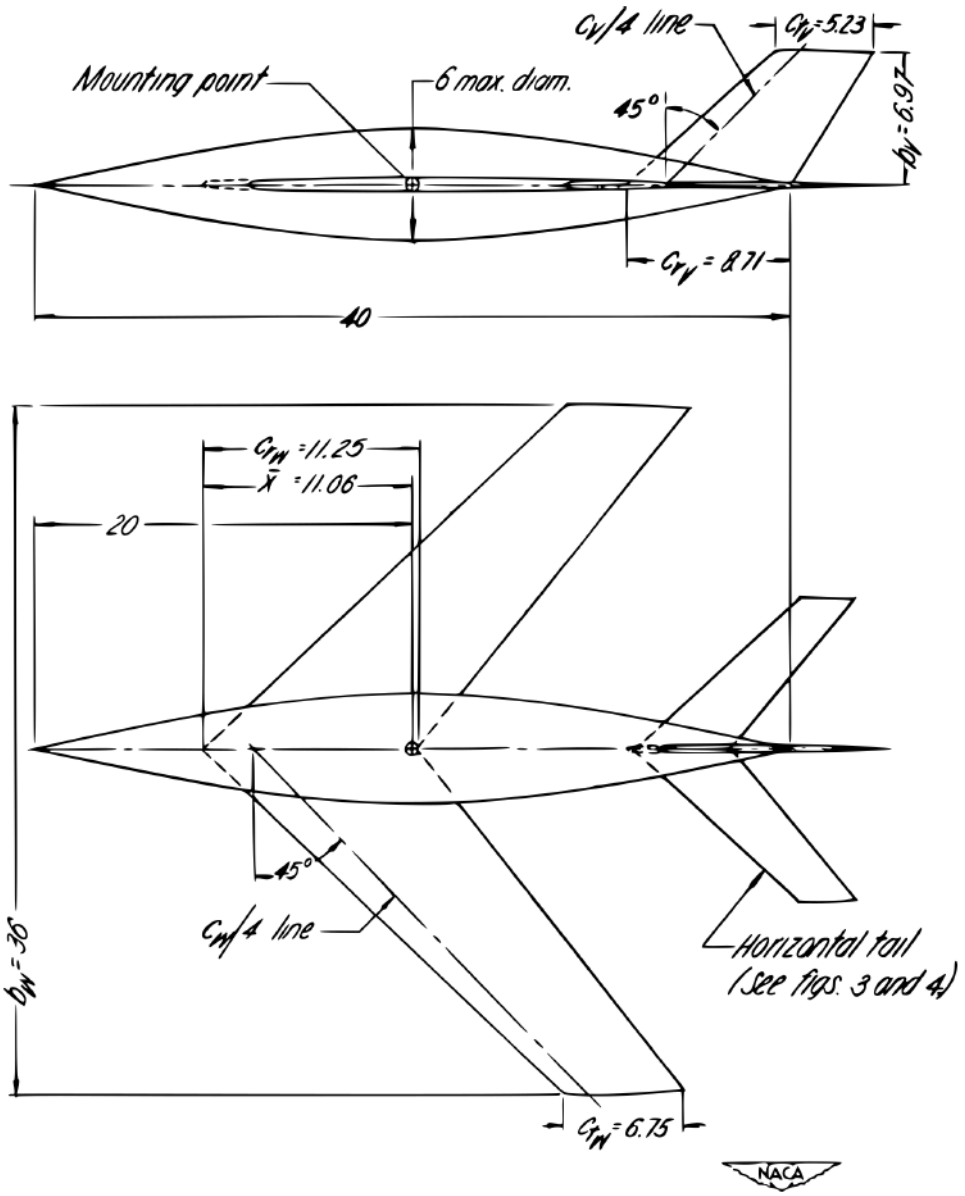

FIGURE 2.17: Geometries of the NACA TN-2010. All units are in inches. Reproduced from Ref. [37].

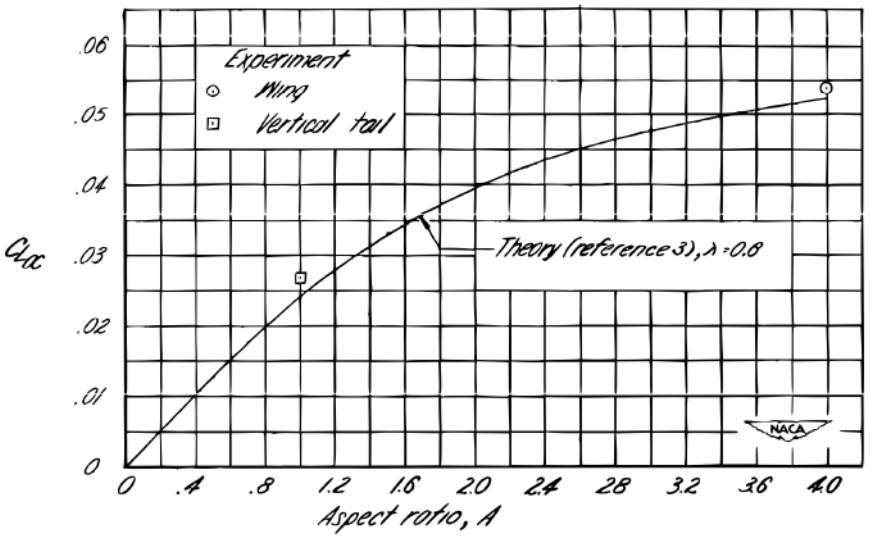

FIGURE 2.18: Comparison with theory of experimental lift curve shapes. Wing and vertical tail, $\alpha = 0°$. Reproduced from Ref. [37].

Results of the work by Brewer and Lichtenstein [37] show that the effect of the horizontal tail can be positive for stability if it is moved upward and rearward on the vertical tail or if positioned on the body, for low angles of attack (see configurations of Figure 2.20). At high angles of attack flow separation and the wing induced downwash can highly affect the stability, although positive effects can be obtained moving the horizontal tail forward and upward. Anyway, the vertical tail effectiveness is maximum when the horizontal tail is located on its root or tip, see Figure 2.21. This is the so-called *end-plate effect* investigated by several authors, including Katzoff and Mutterperl [40], Murray [41], and Riley [42]. This effect increases with the horizontal tail area, as shown in Figure 2.22.

The total effective aspect ratio was found to be function of the ratio of the effective aspect ratio in presence of fuselage (wing off) with horizontal tail on and horizontal tail off (Figure 2.21), corrected for the horizontal surface over vertical surface ratio S_h/S_v (Figure 2.22).

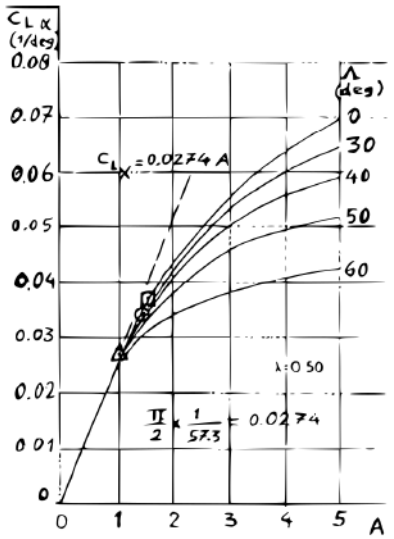

FIGURE 2.19: Vertical tail lift curve slope. Reproduced from Ref. [37].

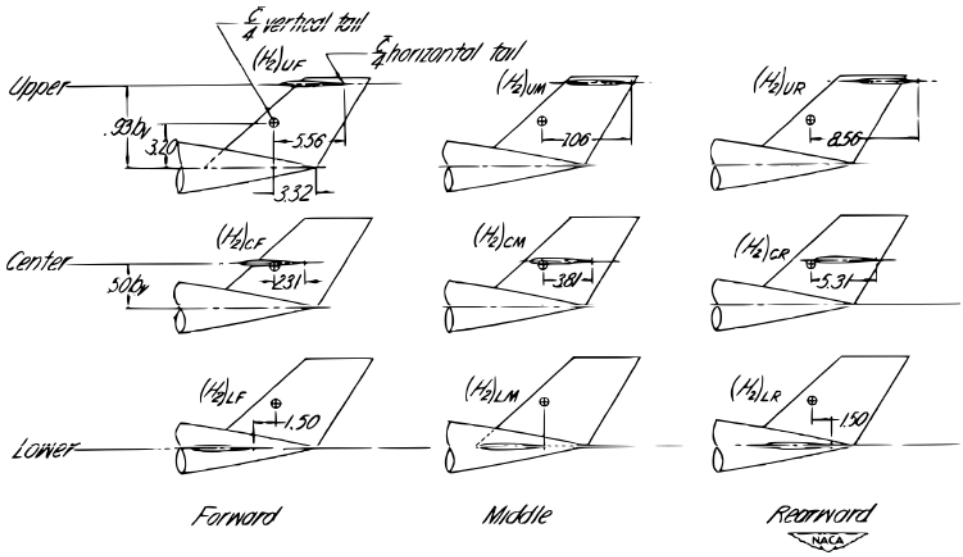

FIGURE 2.20: Vertical tails analyzed in the NACA TN-2010. Reproduced from Ref. [37].

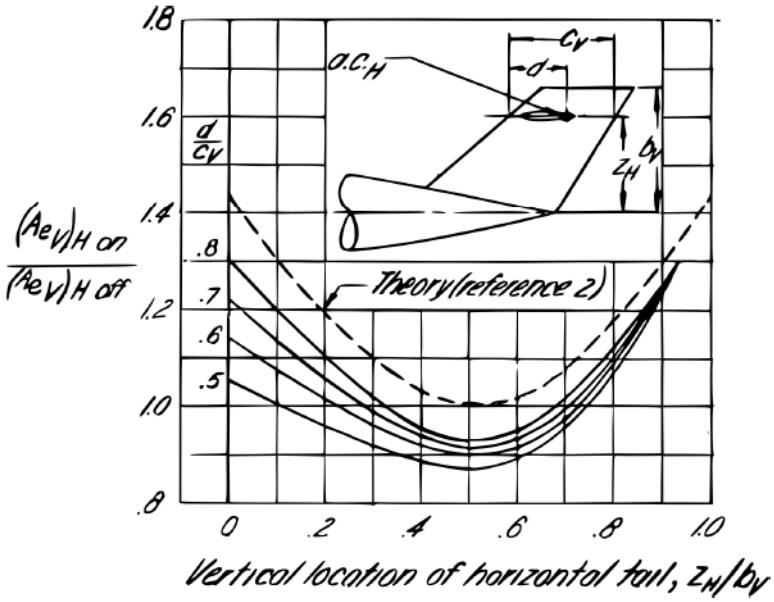

FIGURE 2.21: Variation of effective vertical tail aspect ratio with horizontal tail position, $\alpha = 0°$, wing off. Reproduced from Ref. [37].

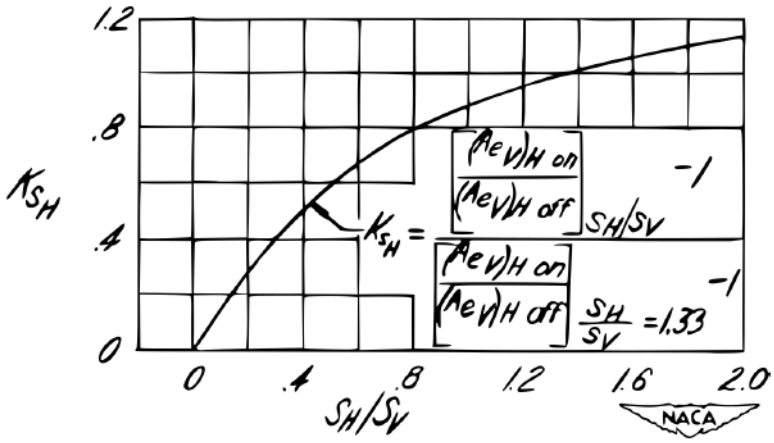

FIGURE 2.22: Effect of the horizontal tail area on vertical tail effectiveness in sideslip. Reproduced from Ref. [37].

Conclusive remarks

All these issues were included in the USAF DATCOM, as will be clearly described in Chapter 3. It is here remarked that the DATCOM method has been mainly developed on the geometries previously presented, i.e. elliptical bodies, swept wing and tails. Apart from the NACA, in the UK, the Engineering Science Data Unit (ESDU) proposed an alternative method to compute the vertical tailplane contribution to directional stability in presence of body, wing, and horizontal tailplane, described by Gilbey [43]. This method contemplates conventional geometries, an almost circular fuselage, and a constant sidewash. It is a synthesis of experimental analyses done by NACA, British Aerospace, SAAB, and others, from the '40s to the '70s, linked together with potential flow theory where data were highly scattered. The theory at the base is found in the work of Weber and Hawk [44], dating back to 1954, who assumes that a fin-body-tailplane combination at incidence (or sideslip) develops a vortex system that induces a constant velocity distribution along the wing span. Here the term *wing* is used as generic lifting surface, since the vertical fin in fuselage is considered as a wing with a cylinder at its root. Load distribution is computed in the Trefftz-plane (located far downwind for high aspect ratio wings) once the induced velocity is known. The latter is calculated from the wing characteristics as planform, sweep angle, and wing section lift curve slope. The method is described in detail in Chapter 3.

2.2 Fuselage aerodynamic design

The main characteristics of a fuselage are as follows:

- it contains and protect (from climatic factors and noise) the *payload*, which must be carried a certain distance at a specified speed;
- it provides fast loading and unloading capability;
- it houses the cockpit and provides good pilot visibility;
- it is the structural member that connects together the other aircraft components (wings, empennage, undercarriage and, in some cases, engines and externals storage);
- it includes systems as avionics, air conditioning, pressurization, etc.

The conceptual aircraft design must provide the main dimensions of the fuselage in some details. From a given set of requirements to which the above mentioned features must comply, the fuselage design might be started even before the overall configuration is settled [14, §3.1.1].

The fuselage shape may be streamlined or not, according to the aircraft mission. As a matter of fact, aerodynamic drag is an important factor, since the fuselage contribution varies from 25 % to 50 %. In Section 1.2.4 it has been stated that for a regional turboprop this value is around 30 %. However, the influence of weight, manufacturing, safety, comfort, together with aerodynamics, determines the DOC, which dictates, among other issues not always controlled by the designer, the success of an aircraft. An example of DOC calculation that involves the fuselage has been given in Section 1.3.

The cross-section shape strongly depends on the nature of the payload and the mission. The fuselage of a cargo aircraft may not require pressurization (however for long range airplanes that fly at high altitude the cockpit must be pressurized) or heating, but its structural design is complicated by large cutouts to allow sufficient space for rapid (un)loading of large payloads. An example of fuselage with squared cross-section is the Short SC-7 Skyvan, which is a short-haul, unpressurized airplane, shown in Figure 2.23. A large turboprop freighter recently introduced, the Airbus A400M, is shown with the rear cargo door opened in Figure 2.24.

For a passenger transport aircraft, the fuselage shall provide accommodation and comfort for the passengers, including: sufficient seat pitch, galleys,

FIGURE 2.23: Short SC-7 Skyvan. ©Mark Harkin / CC-BY 2.0.

FIGURE 2.24: Airbus A400M. Image courtesy of Biagio Giuliano.

and lavatories; sufficient space for cabin crew and services; emergency exits, ruled by authorities, see for instance Ref. [18, §25.807]; pressure, heat, humidity, and noise within acceptable levels.

The fuselage volume must be well exploited. For large turboprop airplanes, a circular cross-section is often chosen, because of easy of production and low fatigue loads due to the pressurization cycles. For larger airplanes, as long range jetliners, the fuselage cross-section may be composed of belly-shaped segments, usually with a flattened bottom, to account for cargo containers, which are of standard size. A clear example of a circular cross-section is given in Figure 2.25. The advantages of the circular cross-section are further stated in the following:

- by eliminating corners, the flow will not separate at moderate angles of attack or sideslip;
- when the fuselage is pressurized, a circular fuselage can resist the loads with tension stresses, rather than the more severe bending loads that arise on non-circular shapes;
- structural design and manufacture are considerable simplified;
- it is possible to obtain an efficient internal layout with little loss of space;
- the flexibility of the seating arrangement is improved;
- aircraft derivatives by fuselage *stretching* is facilitated.

Thus, a fuselage should be designed "from the inside outward" and the skin should envelop the load in such a way that the wetted area is minimum, avoiding breakaway of the airflow as far as possible [14, §3.1.2]. A slender fuselage involves low pressure drag, provided that the after-body does not induce flow separation due to big upsweep angles and blunt edges. However, a slenderness ratio L_f/D_f bigger than, say, 12-15 may result in stiffness and weight problems. Details on fuselage design for a variety of aircraft classes are given in Refs. [13, 14, 21, 24]. The aerodynamics of the fuselage and of the wing-fuselage system is discussed in the next section.

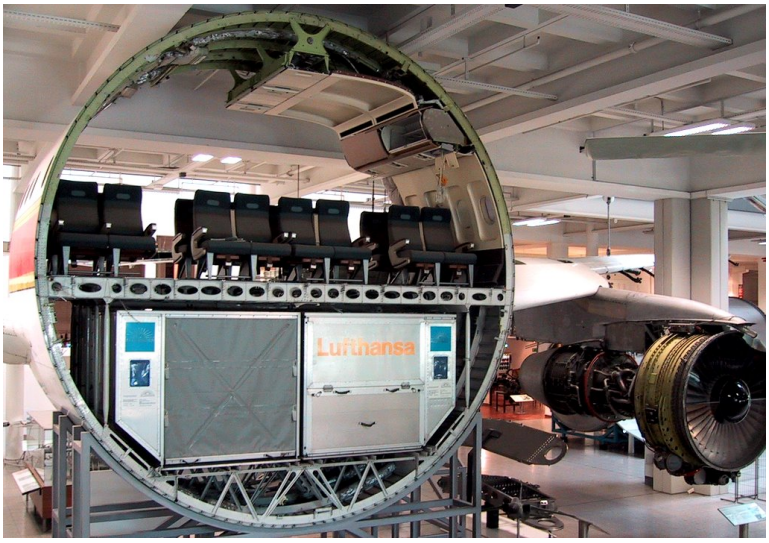

FIGURE 2.25: Airbus A300 fuselage cross-section. ©User:Asiir / Wikimedia Commons / CC-BY-SA 2.5.

2.2.1 Phenomenology

Even if this work is focused on aircraft directional stability, this section dedicated to the fuselage also illustrates concepts about aerodynamic drag of fuselage components and longitudinal (in)stability for the following reasons:

- the author would like to give an overview of the aerodynamics of the fuselage;
- the aerodynamic drag is the primary factor governing fuselage shape for a given layout (i.e. wing and tail configuration, pax number, etc.);
- for an axisymmetric body, the phenomenology in pitch is the same in sideslip;
- the discussion about wing-fuselage interference is useful to highlight differences between longitudinal and directional flow conditions.

Similar considerations apply to the contents of Section 2.2.2.

The fuselage alone

The aerodynamics of the fuselage is that of a slender body of a given cross-section (usually almost circular), which has a lift variation typical of a wing of small aspect ratio, a drag coefficient function of the square of the angle of attack, and a linear pitching moment coefficient variation with the angle of attack, as shown in Figure 2.26. Since the fuselage has the main function to carry the payload, it should provide the least possible drag [45, §5.1].

The aerodynamics of the fuselage at high angles of attack is qualitatively described in Figure 2.27, where the streamlines around an axisymmetric body with a slenderness ratio $L_f/D_f = 7$ show the evolution of the flow field. Vortices are shed from the upper side because of the flow breakdown.

The aerodynamic drag of a fuselage of a transport aircraft is typically due to friction. According to USAF DATCOM [26, §4.2.3.1], the zero-lift drag of a non-axisymmetric fuselage can be calculated with good approximation by methods developed for bodies of revolution, provided that the axial area distribution is the same. Although this approximation may be acceptable for a conceptual design, the effects of fuselage nose (fore-body) and tail (after-body) shapes may be accounted for preliminary design and aerodynamic optimization.

Effect of the windshield

The fuselage nose includes the cockpit and must allow for pilots accommodation, instrument panels, and part of the avionics. For a transport aircraft, the visibility is provided by the *windshield*, which must be inclined by at least 15° from the longitudinal axis, according to certification authorities [18, §25.775]. Hoerner [46, §13.1] showed that the C_{D0} based on frontal window area increases from 0.006 to 0.031, according to the shape of the windshield and its installation on the fuselage. The typical turboprop aircraft has a nose like that of the ATR-72, shown in Figure 1.16a, whereas a smoother shape has been realized on the Bombardier Dash 8 Q-400, shown in Figure 1.16b. Della Vecchia [9, §3.5] has shown by numerical analysis that the standard nose configuration can be optimized to a shape very similar to the Q-400 aircraft, see Figure 2.28, decreasing the fuselage C_{D0} based on wing planform area from 88 to 85 counts. Torenbeek [14, §3.5] suggested that the nose should have a length/diameter ratio from 1.5 to 2.0 to have a good compromise between friction and pressure drag.

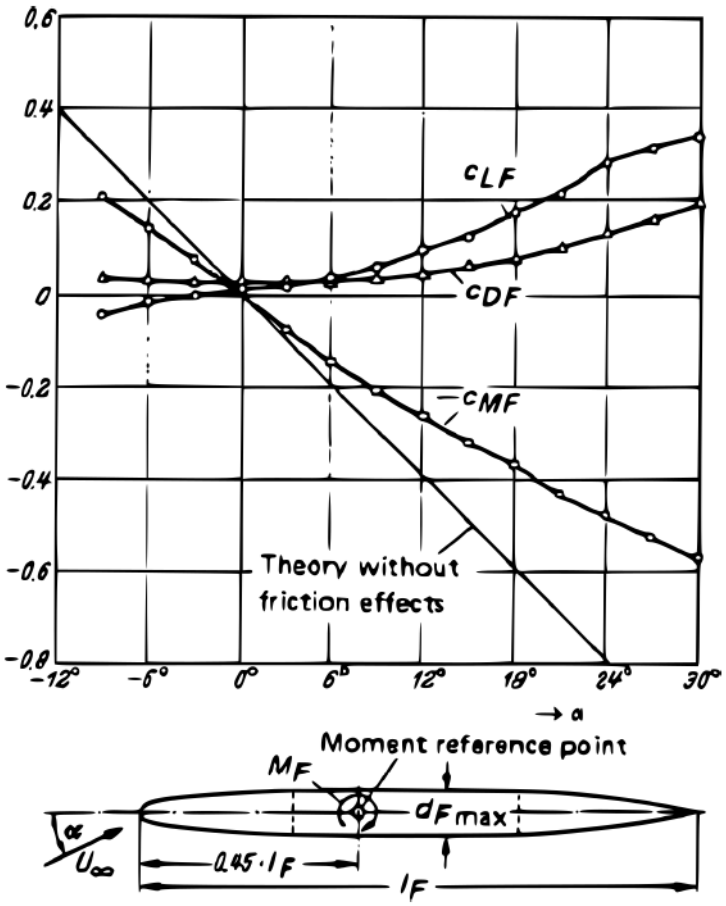

FIGURE 2.26: Experimental results on axisymmetric fuselage. Reproduced from Ref. [45].

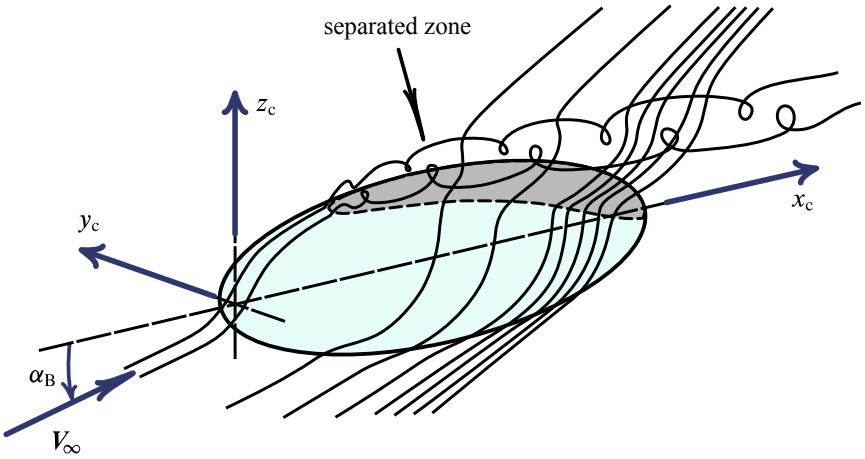

(A) Perspective on fore-body.

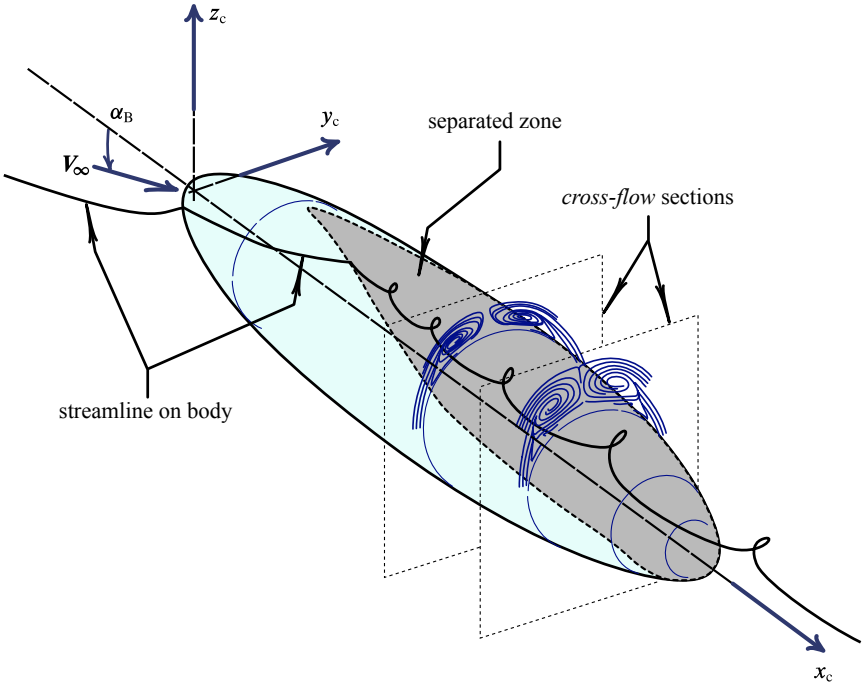

(B) Perspective on after-body.

FIGURE 2.27: Separated flow on fuselage at high angles of attack. Image courtesy of Agostino De Marco.

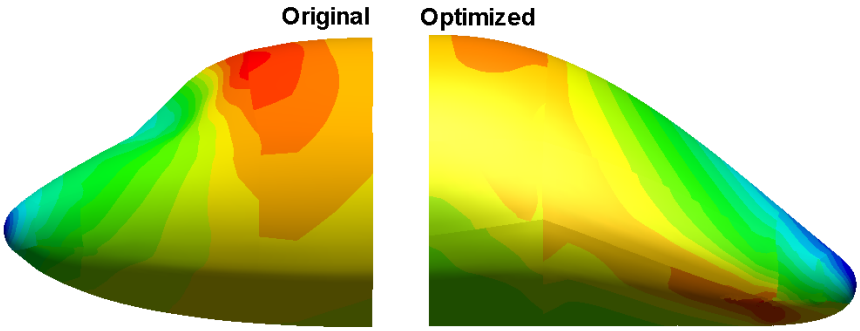

FIGURE 2.28: Optimization of the ATR-72 fuselage nose. The optimized shape has 3 drag counts (based on wing planform area) less than the original shape. Image courtesy of Della Vecchia [9].

Effect of the upsweep

Similarly, the fuselage tail has typically a lenght/diameter ratio from 2.5 to 3.0, often of conic shape for ease of production. The cross-section is usually circular or elliptical. The transition between the cylindrical cabin and the after-body should be smooth to avoid flow separation, see Figure 2.29. To obtain the required rotation at takeoff, the tail-cone is cambered with an *upsweep angle* [14, §3.5], typically around 12° for passenger aircraft, bigger for cargo with rear door. Its influence on drag and pitching moment is evaluated in the following chapters. According to Kroo and Alonso [15], the fuselage upsweep influences the flow field over the entire wing-fuselage system, reducing the total lift at a given angle of attack, but not supporting the tail download for equilibrium. Thus, it increases the drag-due-to-lift, because a higher wing C_L is needed, but increases the trim drag too. For a large transport aircraft, the drag due to the upsweep angle is less than 10 drag counts based on wing area. Because of the nose and tail-cone shapes, a fuselage may provide its minimum drag at a small angle of attack.

Effect of a blunt stern

If the stern of a body of revolution is cut, the corresponding blunt edges generates additional drag. This contribution is called *base drag*, because it is a phenomenon that involves the base of projectiles. The flow pattern behind a projectile base is similar to a jet pump that tries to pump away the

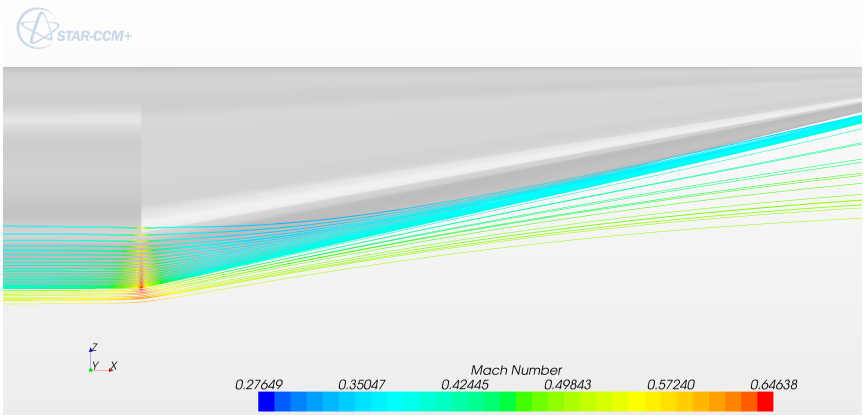

(A) Sharp cabin-tail junction.

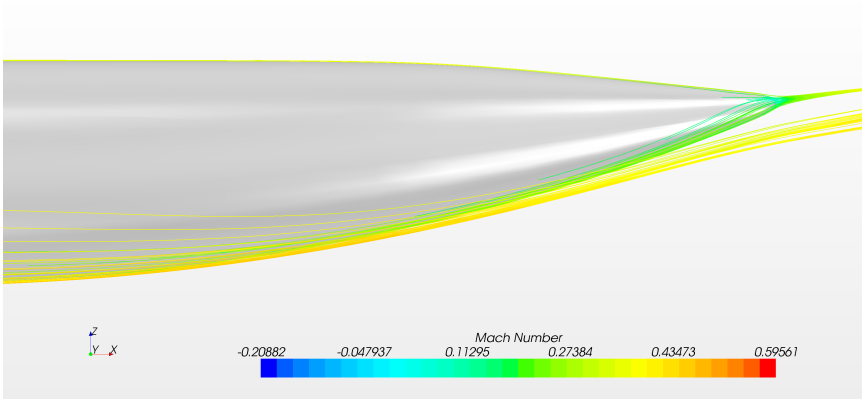

(B) Smooth cabin-tail junction.

FIGURE 2.29: Effect of upsweep angle and cabin-tail junction.

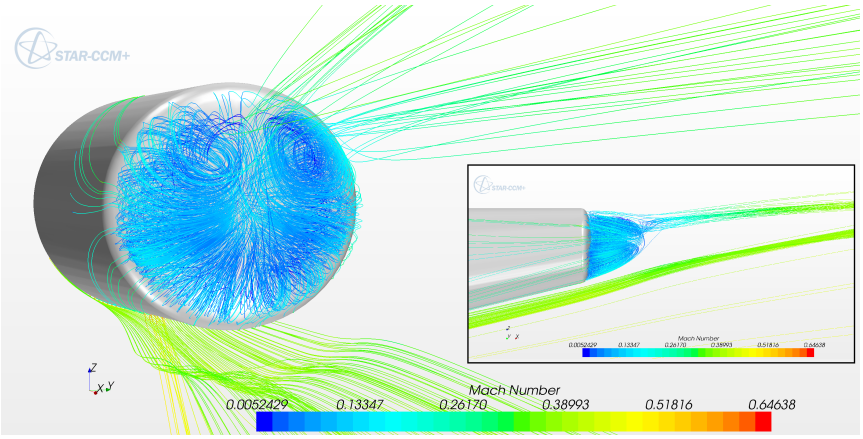

FIGURE 2.30: Base drag. A rounded shape enveloping the volume densely occupied by the streamlines should eliminate the base drag.

dead air behind the base. As a consequence, the static pressure decreases. Because of the boundary layer incoming from the fore-body, this effect is somewhat reduced. Thus, the base drag coefficient is function of the wetted area to base area ratio, base diameter to fore-body ratio, and skin friction coefficient. According to Hoerner [46, §3.8], for a diameter ratio of 0.5, there is a typical increase by 6 % of the fuselage drag. The phenomenon is shown in Figure 2.30, where it is reasonable to argue that a rounded shape enveloping the volume densely occupied by the blue streamlines would eliminate the base drag.

The wing-fuselage system

The wing-fuselage junction should be filleted for high-winged and low-winged aircraft configurations. The drag due to interference may be significantly reduced by careful fillet design. Della Vecchia [9, §3.5] performed the optimization of the ATR-72 wing-fuselage junction, named *karman*, obtaining 7 drag counts (based on wing planform area) reduction in cruise conditions. The optimized geometry creates a better geometrical ramp for the airflow and the recovery of the flow behind the wing trailing edge is better than the original one. The aerodynamic optimization has also highlighted a better behavior in terms of pressure and friction distributions. The pressure gradients

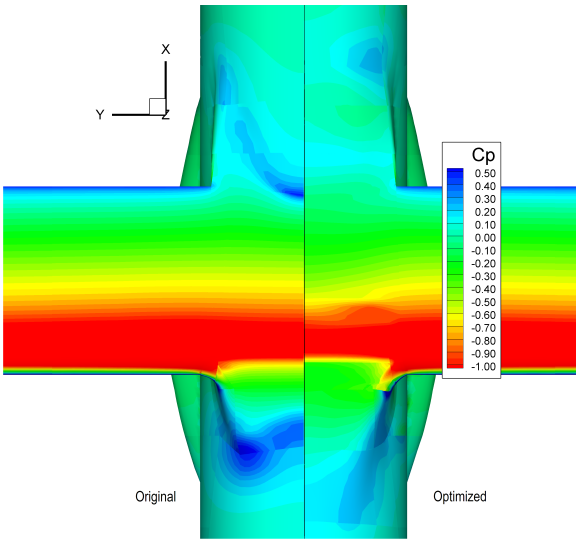

FIGURE 2.31: Comparison of karman pressure distribution. Image courtesy of Della Vecchia [9].

are reduced along the entire component and the separation in the rear part of the karman is avoided, see Figure 2.31.

As shown by investigations performed by NACA and discussed in the next section, the fuselage, by its own nature, it is an unstable body in side flow and its contribution to the lift is very small. The wing-fuselage system has an aerodynamic center shifted forward with respect to the isolated wing and its pitching instability is significantly affected by the strong upwash generated by the wing. The variation of aerodynamic coefficients with angles of attack is discussed in the Section 2.2.2 and 4.3.1, since it depends on wing shape, fuselage cross-section, airfoil geometry, Reynolds number, wing position and incidence on fuselage, fillets, etc.

The effect of the wing on the fuselage in sideslip is negligible, but their combined effect on the vertical tailplane is not, as discussed in Section 2.1.1. The effect of fuselage on rolling moment due to yaw is shown in Figure 2.32, where the aerodynamics of the wing-fuselage system in sideslip is illustrated. Because of their relative positions, for the high wing configuration the upwind side has an increased angle of attack and pressure, while the downwind side has a reduced angle of attack and pressure. This antisymmetric distribution

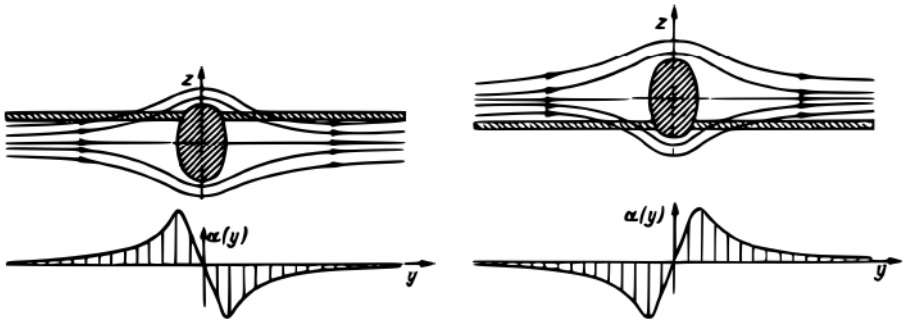

(A) High wing. (B) Low wing.

FIGURE 2.32: Antisymmetric flow over the wing-fuselage system.

[45, §6.2.1] leads to a rolling moment towards the downwind side. The opposite happens for the low wing configuration.

2.2.2 A historical review

The fuselage alone – Results of potential flow theory

The aerodynamics of the fuselage has been deeply investigated by Munk [47] and Multhopp [48]. The first presented the general theory of the aerodynamic forces acting on airship hulls of the rigid type, by request of the US Navy, in 1924. He found that the unstable moment of an airship hull can be predicted quite accurately with potential flow theory, giving

$$M = (\text{Volume})(k_2 - k_1)\frac{1}{2}\rho V^2 \sin 2\phi \tag{2.5}$$

where $(k_2 - k_1)$ is a shape factor that accounts for the elongation of the hull, considered as a body of revolution (ellipsoid), ϕ is the angle of incidence of the body. The factor $(k_2 - k_1)$ relates to the apparent additional (transverse and longitudinal, respectively) masses of air displaced by the airship during its motion, slow enough to consider a steady flow condition. Lamb [49] provided exact calculation of these additional masses. For bodies with a shape reasonably similar to ellipsoids it can be approximately assumed that $(k_2 - k_1)$ has the same value as for an ellipsoid of the same length and volume, that is the same value of the ratio Volume/L^3 [47].

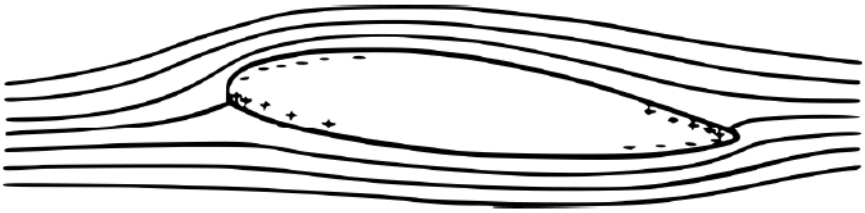

FIGURE 2.33: Fuselage in ideal flow. + positive pressure − negative pressure. Reproduced from Ref. [48].

Multhopp [48] dealt with the aerodynamics of the fuselage alone and the interactions with the wing and the tailplane. The flow around the fuselage is considered perfect, that is frictionless, providing only free moments, no lift or drag are produced. The pure moment is generated at a given angle of incidence by pressure distributions, as shown in Figure 2.33. The expression of this moment has been given by Munk in Equation 2.5, whereas Multhopp is more concerned with the effect of this moment on the longitudinal stability (small angles of attack)

$$\frac{dM}{d\alpha} = 2(\text{Volume})(k_2 - k_1)\frac{1}{2}\rho V^2 \quad (\text{rad}^{-1}) \tag{2.6}$$

but for non axisymmetric bodies the distribution of the width and of the height in the volume must be taken into account in pitch and yaw, respectively[5]

$$\frac{dM}{d\alpha} = \frac{\pi}{2}(K_2 - K_1)\frac{1}{2}\rho V^2 \int_0^L w^2 dx \tag{2.7}$$

$$\frac{dN}{d\beta} = \frac{\pi}{2}(K_2 - K_1)\frac{1}{2}\rho V^2 \int_0^L h^2 dx \tag{2.8}$$

assuming that rotations are about the fuselage center of gravity. The signs from the original report may be different, according to the reference system used. In this thesis, the usual notation of positive moments for unstable contributions has been applied. The shape factor $K_2 - K_1$ is reported in Figure 2.34.

[5]The original notation [48] reports $K = k \times$ Volume.

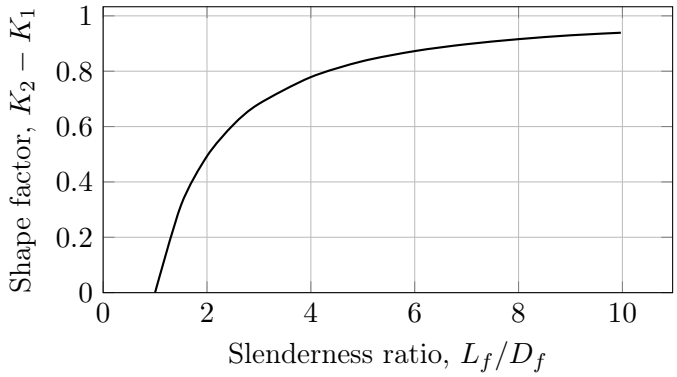

FIGURE 2.34: Fuselage shape factor provided by Munk [47].

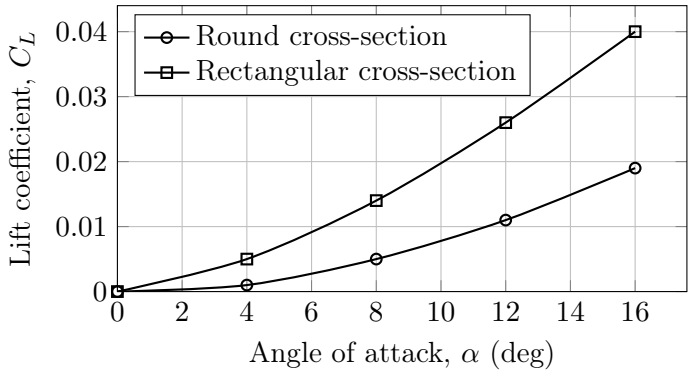

FIGURE 2.35: Fuselage lift coefficient variation with angle of attack [33].

The potential theory cannot give more information. There is some frictional lift that has been somewhat predicted by treating the fuselage as a wing of short aspect ratio and introducing a form factor, related to lift applied point, by experiments [48]. This point is far aft the fuselage, since the frictional lift and its variation with angle of attack are very small. Jacobs and Ward [33] provided some data about the fuselage alone, reported in Figure 2.35, where the lift coefficient C_L has been referred to the wing planform area, thus a direct comparison with the typical values produced by a wing is immediate. Currently, the fuselage of a conventional aircraft is still considered a non-lifting body for obvious reason.

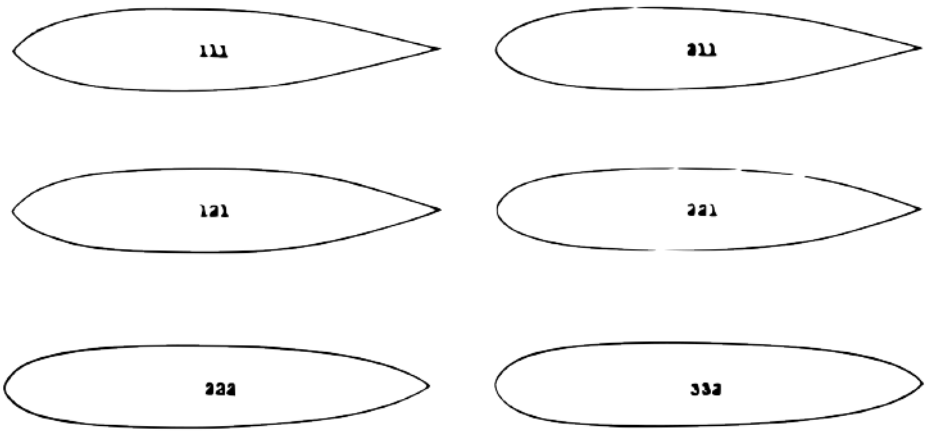

FIGURE 2.36: Geometries tested in the NACA TN-614. Reproduced from Ref. [50].

The fuselage alone – Results of experiments

In 1935 the NACA was investigating bodies at large Reynolds numbers and it was opinion that the slenderness ratio of 5 would give the lowest drag streamlined form. This basic form could be modified in a practical shape for particular type of aircraft, whose dimensions are usually dictated by the cross-sectional area required by the seating arrangement.

In 1937 Abbott [50] presented results of drag tests for six bodies of revolution with a slenderness ratio $L_f/D_f = 5$, but with different shapes derived by source-sink distributions, shown in Figure 2.36. Tests were made in the NACA variable density wind tunnel, with a Reynolds number varying from 1 500 000 to 25 000 000. Results indicated that the bodies with sharper nose and tail have the lowest drag coefficient, either if this is measured with respect to the two-thirds power of the volume or the maximum frontal area. For all the configurations, the drag coefficient decreases with increasing Reynolds number, as shown in Figure 2.37.

Hoerner [46, §6.C] collected numerous results about the drag of streamlined bodies, indicating that at several slenderness ratios, for a Reynolds number based on the fuselage length $Re_\ell < 10^6$ the flow is laminar, whereas for $Re_\ell > 10^7$ the flow is fully turbulent. In both cases the drag coefficient is a linear function of the Reynolds number as correlations made by the author have been shown. Results at $10^6 < Re_\ell < 10^7$ are difficult to predict

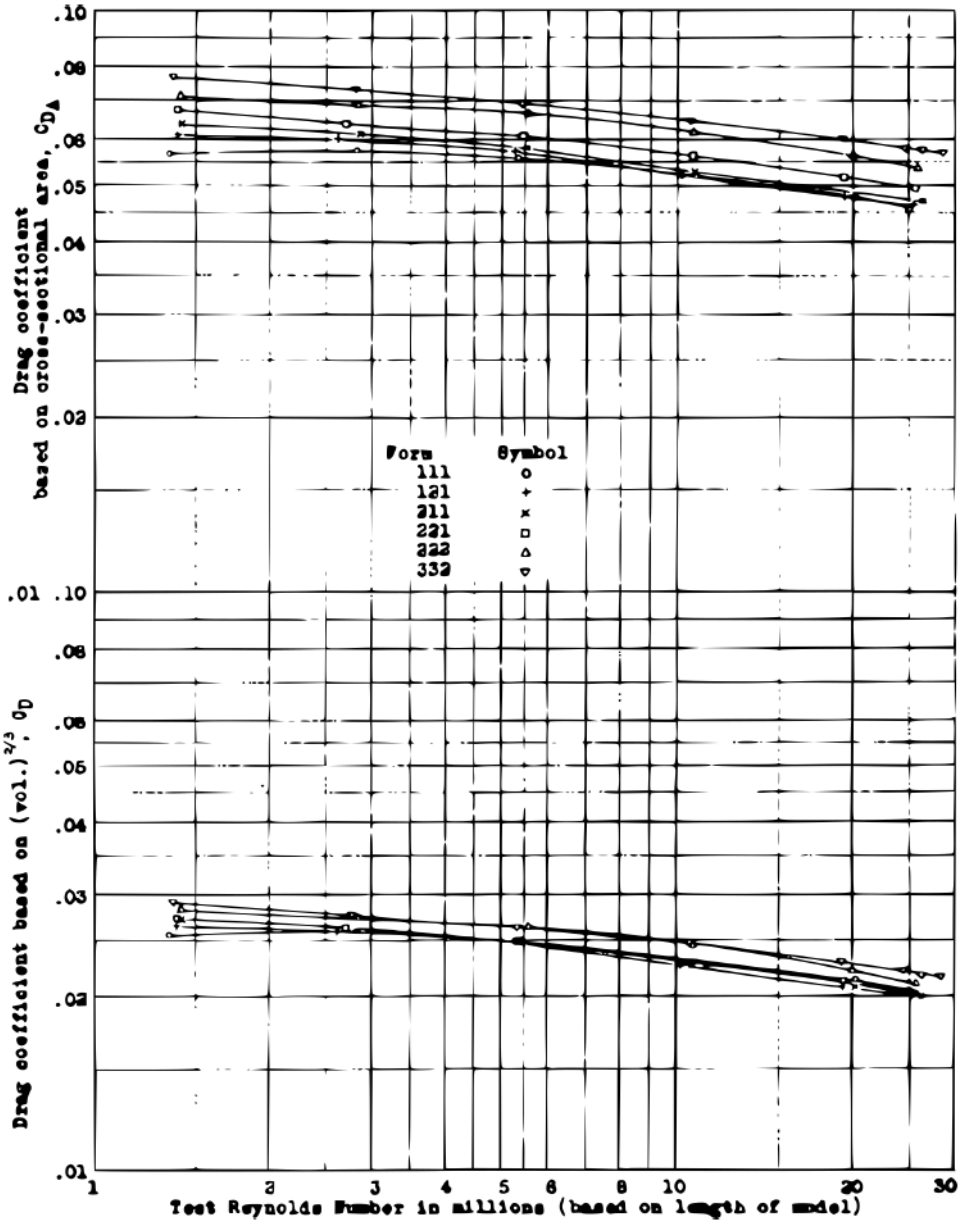

FIGURE 2.37: Results of the NACA TN-614. Reproduced from Ref. [50].

because the boundary layer transition from laminar to turbulent depends on Reynolds number, free stream turbulence, body shape, and surface roughness. In addition, the support of the model for wind tunnel testing creates an interference drag that cannot be avoided.

The wing-fuselage system – Results of the potential flow theory

The effect of the wing on the fuselage is to alter significantly the moment distribution, because of a strong *upwash* $\overline{d\beta}/d\alpha$ ahead the wing and a *downwash* $d\beta/d\alpha = 1 - d\epsilon/d\alpha$ reducing the cross-flow around the fuselage behind the wing. The change of this cross-flow on the wing is zero, since the flow is practically aligned with the wing chord. Because of the strong wing circulation, the fuselage frictional lift is absent and the shape factor $K_2 - K_1 \approx 1$, hence the stability contribution has formulation similar to that of Equation 2.7

$$\frac{dM}{d\alpha} = \frac{\pi}{4}\rho V^2 \int_0^L w^2 \frac{d\beta}{d\alpha} dx \quad (\text{rad}^{-1}) \tag{2.9}$$

while the effect of the wing on the fuselage in pure sideslip conditions is negligible and Equation 2.8 is applied [48]. The function $d\beta/d\alpha$ is reported in Figure 2.38.

The effect of wing-mounted engine nacelle is somewhat different, because of their location. It is un unstable contribution that depends on the slope of the flow at wing leading edge, center, and trailing edge. By integrating these values over the entire wing, excluding the nacelle region, Multhopp [48] proposed the following formula to calculate the order of magnitude of the nacelle contribution to the wing moment

$$\frac{dM}{d\alpha} = \frac{\pi}{32}\rho V^2 c^2 \left[w_{\text{LE}} + 2w_{\text{mid}} - 3w_{\text{TE}}\right] \quad (\text{rad}^{-1}) \tag{2.10}$$

where w_{LE}, w_{mid}, and w_{TE} are the width of the nacelle at the wing leading edge, mid chord, and trailing edge, respectively.

For longitudinal stability studies it is recommended to account for the fuselage and nacelle contributions as displacements of neutral stability points [48]

$$\frac{\Delta x_n}{c} = -\frac{C_{M_{\alpha_f}}}{C_{L_{\alpha_w}}} \tag{2.11}$$

where $C_{M_{\alpha_f}}$ is $dM/d\alpha$ normalized with the dynamic pressure $\frac{1}{2}\rho V^2$, the wing area S, and the wing (mean aerodynamic) chord c, whereas $C_{L_{\alpha_w}}$ is the wing lift curve slope.

The stability contributions of fuselage and nacelle may be summed up and expressed as function of the lift coefficient C_L, which is the independent variable in longitudinal stability

$$\frac{dC_M}{dC_L} = \frac{dM/d\alpha}{0.5\rho V^2 S c\, C_{L_{\alpha_w}}} \,. \tag{2.12}$$

These results have been resumed in the book of Perkins and Hage [16, §5.4], who also reported a simpler, but less accurate method to calculate the longitudinal stability contribution of fuselage and nacelle, based on data provided by Jacobs and Ward [33] and Gilruth and White [51]

$$\frac{dC_M}{dC_L} = \frac{K_f w_f^2 L_f}{S c\, C_{L_{\alpha_w}}} \tag{2.13}$$

where K_f accounts for wing-fuselage or wing-nacelle relative position and it is defined in Figure 2.39, w_f and L_f are the maximum width and the length of the fuselage (or nacelle), respectively.

The change in wing loading through the wing-fuselage junction is smooth. Multhopp [48] described how to compute it by potential theory, assuming the airflow as a combination of a flow parallel to the fuselage axis and a flow normal to it. The induced velocities on the wing-fuselage system are such that an upwash close to the wing-fuselage junction is generated, as it has been shown experimentally [45, §6.2]. A synthesis of the effects of the wing-fuselage interference on the aerodynamic loads is shown in Figure 2.40.

The wing-fuselage system – Results of experiments

The aerodynamic interference of 209 wing-fuselage combinations has been deeply investigated by Jacobs and Ward [33] in the NACA variable density wind tunnel (Figure 2.41a) in 1935. Here, only the results involving fuselage of circular cross-section, without engine, at $Re = 3\,100\,000$ are discussed. The fuselage is the same ellipsoid of Figure 2.12, whereas the wing is a rectangular planform with NACA 0012 section. The most important parameter for aerodynamic drag interference is the vertical location of the wing in fuselage.

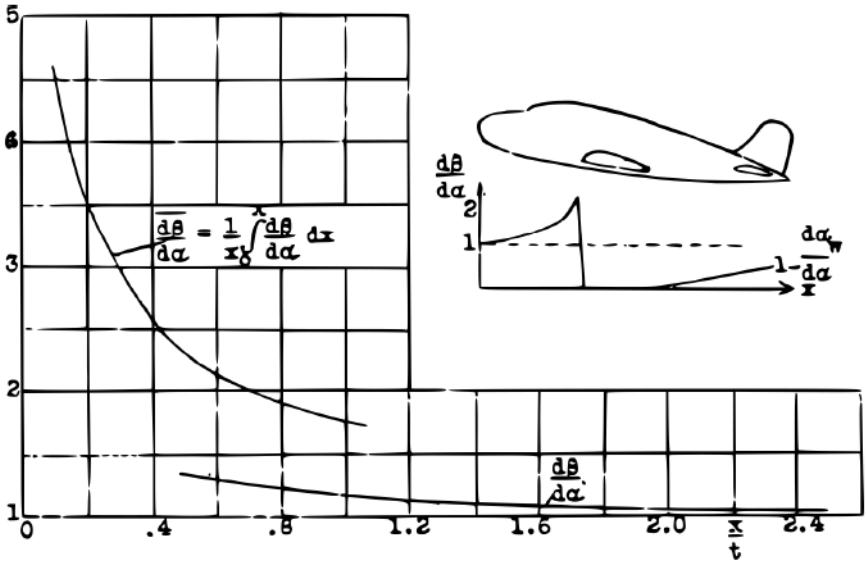

FIGURE 2.38: Effect of the wing circulation on the fuselage. Reproduced from Ref. [48].

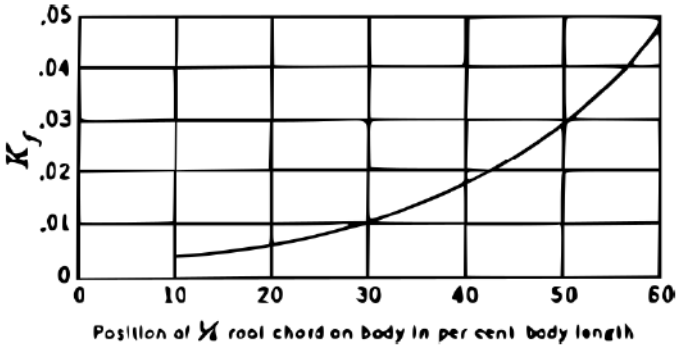

FIGURE 2.39: Fuselage stability coefficient of Equation 2.13. Reproduced from Ref. [16].

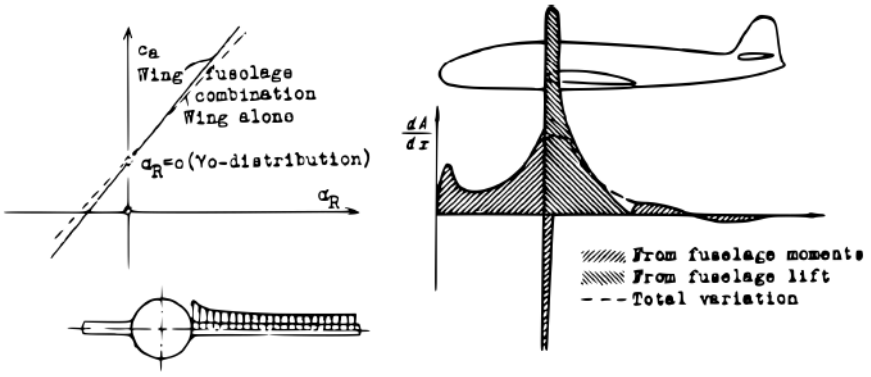

FIGURE 2.40: Wing-fuselage interference on aerodynamic loads. Reproduced from Ref. [48].

Ref. [33] provides results in terms of *effective profile-drag coefficient*, that is a drag coefficient depurated from the induced drag of an elliptical wing with the same aspect ratio

$$C_{De} = C_D - \frac{C_L^2}{\pi \mathcal{R}} \tag{2.14}$$

hence accounting only for parasite drag. In this way, the contributions of aerodynamic interference to lift and drag are separated. For instance, if two wing-fuselage combinations at the same angle of attack have different lift coefficients, they will have different drag-due-to-lift coefficients. It might result that the combination with higher lift provides bigger drag, even if the interference effect is more favorable than the other combination. The effective drag coefficient permits the use of the angle of attack as independent variable.

The NACA report presents results as the difference Δ between the total force (and moment) measured in the wind tunnel of the wing-fuselage combination and the wing alone. In this way, the aerodynamic interference is included in the Δ and can be calculated by opportune considerations. For example, the mid wing combination no. 7, whose results are reported in Figure 2.41b, has a ΔC_{De} (fuselage drag + interference) of 35 drag counts at $\alpha = 0°$. The fuselage alone has 41 drag counts in the same conditions, indicating a favorable interference effect of 6 drag counts. The authors calculated that the portion of the wing enclosed within the fuselage provides 9 drag counts instead of 6, hence, if the interference effect would be only due

to the exposed area, a difference of 9 drag counts between wing-fuselage and wing alone should be expected. The additional, unfavorable 3 drag counts arise from the intersection of boundary layers around the wing-fuselage junction.

As the angle of attack is increased up to 12°, the above mentioned mid wing combination provides lift and induced drag coefficients slightly bigger than the sum of that of wing and fuselage alone. Also, the lift curve slope C_{L_α} is increased, as the entire wing surface were exposed to the airflow together with the fuselage.

Further increments of angle of attack generates a phenomenon that the authors called *interference burble*. The drag abruptly arises, while the lift increases with a lower slope, because of an initial flow breakdown due to that particular wing-fuselage combination. This interference burble depends on wing horizontal location, wing section, and fuselage shape. The fuselage contribution in pitch is highlighted by the positive derivative dC_M/dC_L, measured at the wing quarter chord point, indicating that the aerodynamic center of the wing-fuselage combination is shifted significantly forward (i.e. towards the fuselage nose) with respect to the wing alone.

The reports continues describing that the high wing combination has an adverse drag interference effect ($\Delta C_{De} = 50$ counts), a maximum lift coefficient similar to that of the wing alone, and no interference burble at positive angles of attack, at least for those combinations whose wing-fuselage juncture has an unfavorable shape. Low wing combinations are usually unsatisfactory for the same reason — the wing-body junction. The aerodynamic drag interference is minimum for combinations with disconnected wing, but the realization of such configurations is obviously impractical and it has to be realized with a strut attachment, which increases the interference drag. Thus, the mid wing-fuselage combination is the most favorable in terms of aerodynamic drag, because wing and fuselage structural members are at right angles, minimizing the interference due to connection.

According to the data provided by Ref. [33], the wing fore-and-aft position has a little effect on the interference burble onset for the mid wing combinations, where the drag tends to increase slightly as the wing is moved backward. A similar effect is due to the wing setting, which changes the relative angle between the wing and the fuselage. This may be critical for high and low wing combination, because of their junction. The effect of the *fillets* is beneficial for high and low wing combinations, because they

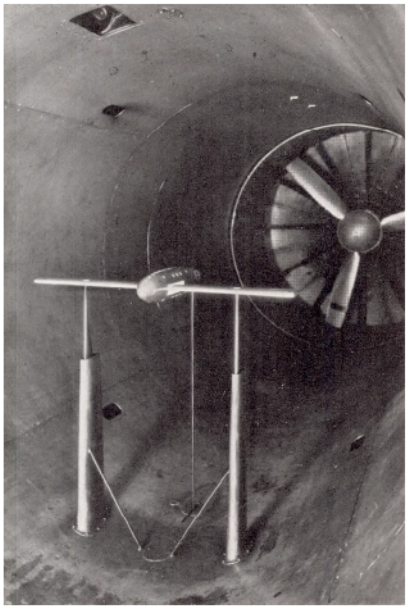

(A) The model in the NACA variable density wind tunnel.

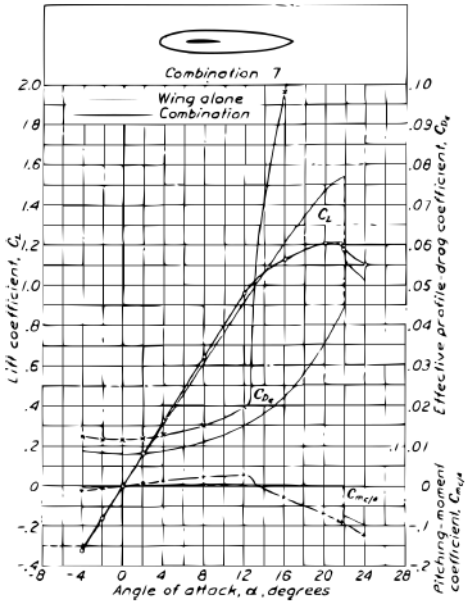

(B) Results for the mid wing combination.

FIGURE 2.41: Results of the NACA TR-540 for the mid wing combination. Reproduced from Ref. [33].

act reducing the geometric divergence and the combined adverse pressure gradients of the two bodies at the juncture. In some cases, they may also reduce the wetted area at the juncture. Their effect is evident by expanding the rear portion of the wing-fuselage filleting until the interference burble is eliminated. However, they have little or no effect on the aerodynamic drag of mid wing combinations. Finally, they affect the lift and pitching moment, since they change the chord length and wing shape at root.

Regarding the pitching moment C_M, this may be obtained as the sum of wing alone plus fuselage alone contributions, because the aerodynamic interference does not affect it before the onset of the interference burble. The aerodynamic center position depends on the wing fore-and-aft location. As previously stated, the longitudinal pitch instability dC_M/dC_L depends on the position of the aerodynamic centers, whereas the moment coefficient at zero lift C_{M0}, which is important for trim drag, is mainly affected by wing incidence angle on the fuselage, because of a change in the wing-fuselage camber. Large pitching moment variations are expected beyond the burble, especially for high wing combinations [33].

The effects on maximum lift are important as the aerodynamic drag, but usually unrelated to the interference burble. The most important parameter is, of course, the Reynolds number, which governs the viscosity effects, followed by wing shape (airfoil, planform), wing position (high wing has the same maximum lift of the wing alone), fuselage shape, and fillets, which may increase the wing exposed area, the chord length, and the camber at wing root [33].

Chapter 3

Conceptual and preliminary design methods and applications

Synopsis

✈ This chapter is divided in two parts: conceptual and preliminary design

✈ Each part deals with vertical tail and fuselage

✈ A major focus is given to the vertical stabilizer

✈ The fuselage contribution is usually that of the isolated component

✈ Applications of the methods to regional turboprop airplanes are shown

3.1 Conceptual design

This chapter describes in details the semi-empirical methods available in public domain or in textbooks concerning aircraft directional stability. The first step is a rough sizing of their characteristic dimensions, i.e. planform area for the vertical tail and slenderness ratio or frontal area for the fuselage. This is usually done in the conceptual design phase.

3.1.1 Volumetric ratio for empennage sizing

The approach is based on statistics and it can estimate only volume coefficients [12, 17]. Tail volume coefficients are non-dimensional numbers defined

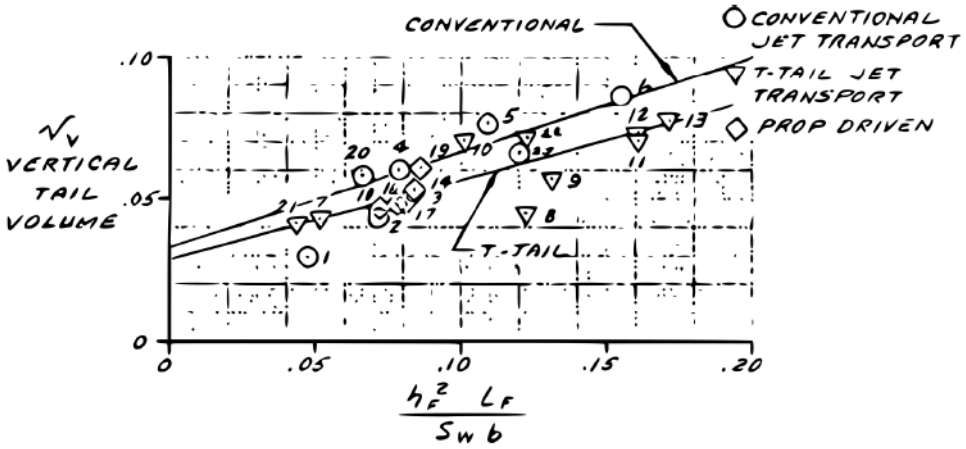

FIGURE 3.1: Correlation of aircraft vertical tail volume as a function of fuselage maximum height and length. Reproduced from [15].

as follows

$$\overline{V_h} = \frac{l_h S_h}{c_{\text{mac}} S} \tag{3.1}$$

$$\overline{V_v} = \frac{l_v S_v}{b S} . \tag{3.2}$$

Aircraft having the same volume coefficients tend to have similar static stability characteristics [52]. Usually these coefficients are assigned by simply examining a table or a chart for aircraft with similar configurations. Observations can be made by looking at historical or other general trends, as reported in Figure 3.1. An example of these coefficients for large turboprop airplanes is shown in Table 3.1 and 3.2. A plot of these data against the wing surface is in Figure 3.2. General aviation airplanes have smaller coefficients, half or less than the values shown, as reported by Hall [52].

In this section an application on the ATR-42 is shown, following the guidelines reported in Table 3.1, Table 3.2, and Figure 3.2. The aircraft is shown in Figure 3.3 without empennage, which has to be sized. Although in this case the true values are known, this example shows that, by plotting the available data and drawing regression lines, one can establish a law that correlates a given geometric parameter (in this case, the wing planform area) with tail volume coefficients.

TABLE 3.1: Volume coefficients and several dimensions for several turboprop aircrafts [53]. Lengths are in ft and areas are in ft^2.

Aircraft	b	c_{mac}	$l_{h,v}$	S	S_h	S_v	$\overline{V_h}$	$\overline{V_v}$
ATR-42	80	7.50	37	586.6	126.26	134.33	1.06	0.09
ATR-72	88	7.56	45	656.6	126.26	134.33	1.13	0.10
Q400	93	7.30	54	679.2	180.00	152.00	1.77	0.13
EMB-120	65	6.56	31	424.4	65.66	61.78	0.72	0.07

TABLE 3.2: Geometric properties of the horizontal and vertical tails of some large turboprop aircraft, partly taken from Ref. [13].

		Taper ratios			Tail volumes	
Aircraft	$\mathcal{AR}$	λ_w	λ_h	λ_v	$\overline{V_h}$	$\overline{V_v}$
Antonov An-24	11.20	0.27	0.44	0.35	1.10	0.09
ATR-72	11.96	0.59	0.60	0.61	1.13	0.10
Bombardier Q400	12.81	0.42	0.77	0.74	1.77	0.13
dHC Dash 7	10.06	0.43	0.73	0.47	1.10	0.09
Ilyushin Il-114	10.99	0.38	0.42	0.40	1.14	0.08

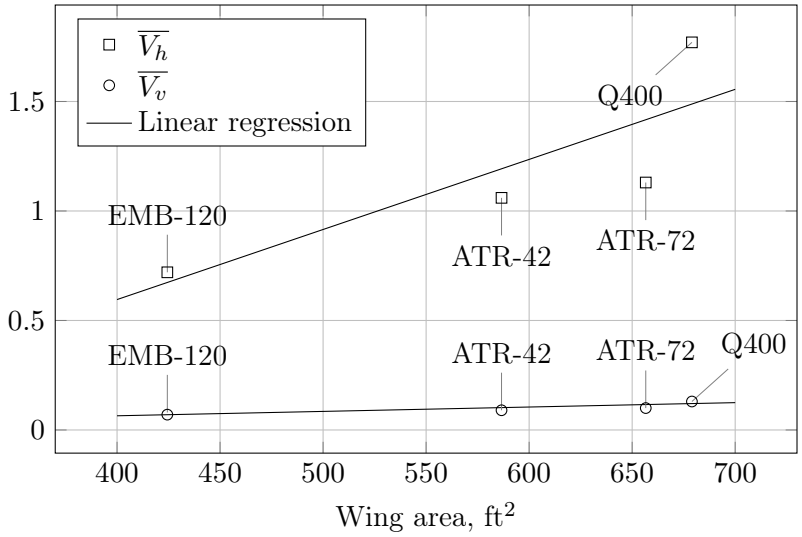

FIGURE 3.2: Plot for volume coefficients reported in Table 3.1.

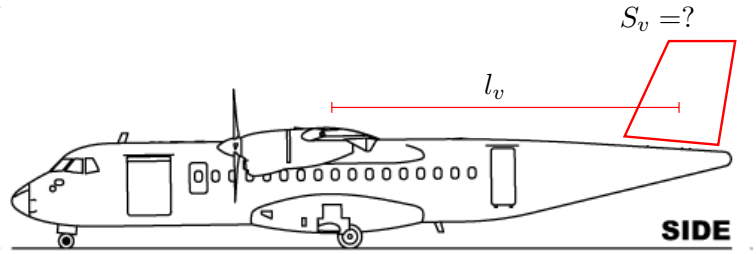

FIGURE 3.3: ATR-42 without empennage.

In Figure 3.2 there is some scatter in the horizontal tail data and the regression line may not fit very well. However, the obtained values are reasonable. This chart may be used to perform trade studies, e.g. how much increase the tail volume coefficients for every square foot added to the wing area. From the volumetric ratios shown in Equation 3.1 and 3.2 the planform areas S_h and S_v can be calculated, once *assigned* the tails position l_h and l_v. Notice that in Table 3.1 the ATR-42 and the ATR-72 have the same horizontal and vertical tail area, but different volumetric ratios. This is no error, since the ATR-72 has a stretched fuselage with respect to the ATR-42, hence the volume tail coefficient has been increased by moving aft the empennage, thus increasing the distance between wing and tails.

It is here remarked that this approach does not provide other important planform parameters, which are the aspect ratio $\mathcal{R}$, the sweep angle Λ, and the taper ratio λ. It is duty of the designer to choose them wisely, by considering aerodynamic, structural, control, and aesthetic issues. Some indications come from Raymer [12, §4.5], here reported in a general fashion in Table 3.3 and as function of the wing parameters in Table 3.4.

It is typical to oversize the empennage in this phase. This guarantees stability and control at the expense of the performance, which will be matched later in a more detailed design. A tail undersizing will not provide safety in flight and the desired performance will not be achieved anyway.

TABLE 3.3: Tail aspect ratio and taper ratio guidelines [12].

	Horizontal tail		Vertical tail	
	A_h	λ_h	A_v	λ_v
Fighter	3 to 4	0.2 to 0.4	0.6 to 1.4	0.2 to 0.4
Sail plane	6 to 10	0.3 to 0.5	1.5 to 2.0	0.4 to 0.6
Others	3 to 5	0.3 to 0.6	1.3 to 2.0	0.3 to 0.6
T-tail	—	—	0.7 to 1.2	0.6 to 1.0

TABLE 3.4: Sizing of the vertical stabilizer in function of the wing parameters [12].

Wing	Vertical tail	Comment
Λ_{LE}	35° to 55°	Tail stalls later than wing and has a higher critical Mach number.
$\mathcal{AR}$	1.3 to 2	Must be lighter than wing.
λ	0.3 to 0.6	Close to an elliptical load and easy to manufacture.
t/c	9 % to 12 %	Usually similar to wing section's relative thickness.
$\bar{c}_c/c_v$	25 % to 50 %	Typical plain flaps with same taper ratio of tailplane.

3.1.2 Fuselage slenderness ratio and its influence

The simplest approach to evaluate fuselage aerodynamics is based on the slenderness ratio L_f/D_f, that is the ratio between the fuselage length and its maximum diameter. Assuming the fuselage as a body of revolution, its contribution to longitudinal and directional aircraft stability, as well as aerodynamic drag, is quickly calculated. For the initial sizing, the designer should always look at layouts of similar airplanes. The methods here illustrated only account for aerodynamic effects, whereas other considerations, especially about structural issues and the overall aircraft layout, must be made, as discussed in Section 2.2.

The directional stability contribution $dN/d\beta$ can be calculated by Equation 2.6 [48], here expressed for the yawing moment

$$\frac{dN}{d\beta} = (\text{Volume})(K_2 - K_1)\frac{1}{2}\rho V^2 \tag{3.3}$$

where $K_2 - K_1$ has been illustrated in Figure 2.34, which is shown again below.

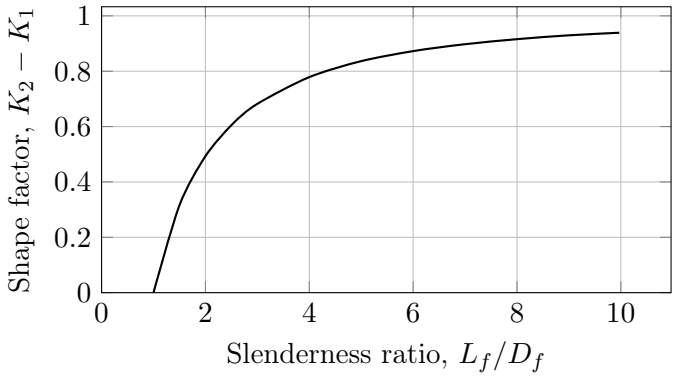

The fuselage volume for regional turboprop aircraft may be approximated as

$$(\text{Volume}) = 0.8\,\pi\frac{D_f^2}{4}L_f$$

which is the volume of a cylinder scaled by 0.8 to account for the non-cylindrical nose and tail-cone.

To calculate the yawing moment coefficient due to sideslip $C_{N_{\beta f}}$, the reference area S_{ref} and length L_{ref} must be defined. If the wing planform has already been sized, the wing area S and the wing span b should be chosen, otherwise the fuselage frontal area S_{front} and length L_f are a possible alternative. Thus,

$$C_{N_{\beta f}} = \frac{(\text{Volume})(K_2 - K_1)}{S_{\text{ref}} L_{\text{ref}}} . \tag{3.4}$$

The pitching instability may be calculated, for an axisymmetric isolated fuselage, with the same approach

$$C_{M_{\alpha f}} = \frac{(\text{Volume})(K_2 - K_1)}{S_{\text{ref}} L_{\text{ref}}} \tag{3.5}$$

where L_{ref} should be the wing mean aerodynamic chord c. A simple expression to account for the effects of the wing has been given in Equation 2.13 [16, §5.4] and Figure 2.39, here repeated

$$\frac{dC_M}{dC_L} = \frac{K_f w_f^2 L_f}{Sc\, C_{L_\alpha}}$$

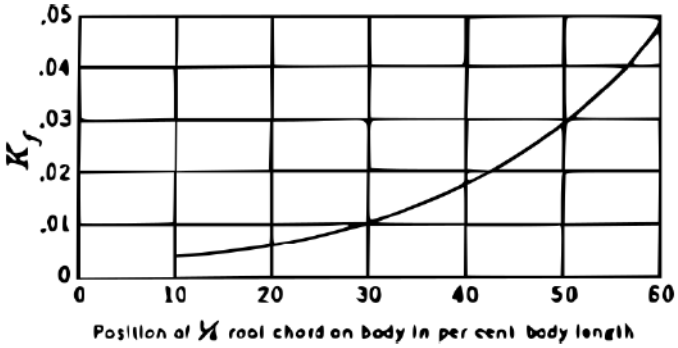

where K_f accounts for wing-fuselage or wing-nacelle relative position, w_f and L_f are the maximum width and the length of the fuselage (or nacelle), respectively. *For non-axisymmetric bodies, the methods described in Section 3.3 should be used.* The fuselage contribution in pitch and yaw is always unstable. Signs of the equations may change according to the reference system used.

Finally, the effects of fuselage slenderness ratio on aerodynamic drag can be calculated by looking at Figure 3.4, provided by Torenbeek [14, §3.1.2], which illustrates the variations of drag coefficient C_D for a streamlined body

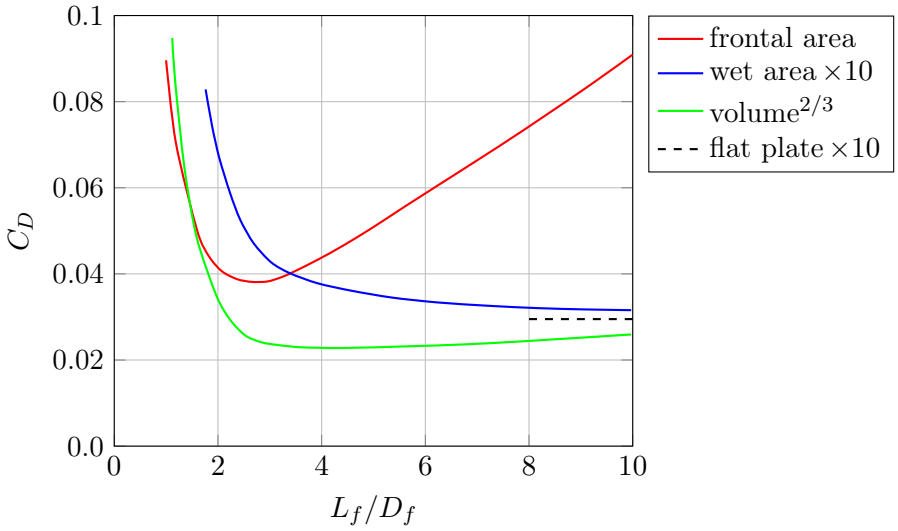

FIGURE 3.4: Empirical drag estimation for smooth streamlined bodies of revolution. $Re = 10^7$. Fully turbulent flow. Reproduced from Ref. [14].

aligned with the airflow. The slenderness ratio equal to 1 represents a sphere, whereas very streamlined bodies are indicated by high values of the abscissa. Three reference areas are considered: the body wetted surface, the body frontal area, and the area representative of the body volume. The drag coefficient strongly depends from the reference area. The curve that refers to the frontal area (which is constant with slenderness ratio) presents a minimum at L_f/D_f values between 2 and 3. On the contrary, the curve that refers to the wetted area (which increases with the slenderness ratio) presents an asymptote equal to the drag coefficient of the flat plate for high values of the slenderness ratio. Finally, the curve that refers to the volume presents a minimum for $L_f/D_f = 5$. By looking at these last two curves, it is apparent the convenience of high values of the slenderness ratio, because of the low value of the drag coefficient and the availability of space for payload, i.e. a bigger volume for a given frontal area.

A typical regional turboprop transport airplane has a slenderness ratio $L_f/D_f \approx 10$. For the ATR-42, assuming

$L_f = 22.7\,\text{m}$ fuselage length

$D_f = 2.6\,\mathrm{m}$ fuselage diameter

$b = 24.5\,\mathrm{m}$ wing span

$c = 2.0\,\mathrm{m}$ mean aerodynamic chord

$S = 50\,\mathrm{m}^2$ wing area

and applying the simplified approach, the following results are obtained

$K_2 - K_1 = 0.92$ (Figure 2.34)

$(\mathrm{Volume}) = 0.8\,\pi \frac{D_f^2}{4} L_f = 96.4\,\mathrm{m}^3$

$C_{N_{\beta_f}} = \frac{(\mathrm{Volume})(K_2 - K_1)}{Sb} = 0.0724\,\mathrm{rad}^{-1} = 0.001\,26\,\mathrm{deg}^{-1}$

$C_{M_{\alpha_f}} = \frac{(\mathrm{Volume})(K_2 - K_1)}{Sc} = 0.869\,\mathrm{rad}^{-1} = 0.0152\,\mathrm{deg}^{-1}$

$C_{D_0}\,(S_{\mathrm{wet}}) = 0.0032$

$C_{D_0}\,(S) = C_{D_0}\,(S_{\mathrm{wet}}) \frac{S_{\mathrm{wet}}}{S} = 0.0105$ (assuming $S_{\mathrm{wet}} = 164\,\mathrm{m}^2$)

which are realistic values to verify with the more accurate methods of Section 3.3.

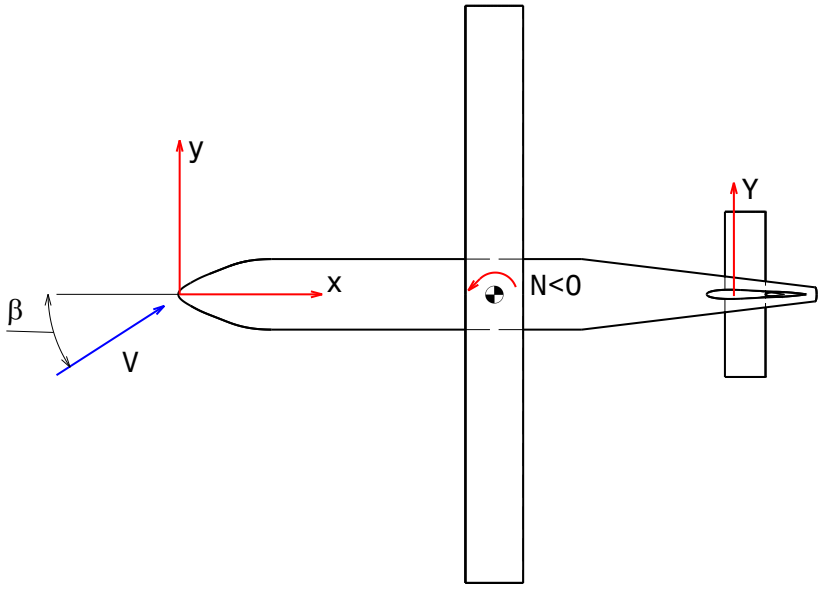

FIGURE 3.5: Aircraft directional stability reference system.

3.2 Preliminary design. Vertical tail and directional stability

This section deals with the analysis of the (single) vertical tail of a conventional airplane like a regional turboprop. The methods here reported are valid for low speed (subsonic), cruise configuration (low angle of attack, low angle of sideslip), and do not account for flaps or engine effects.

As clearly described in Chapter 2, the vertical tail is the key component of aircraft directional stability. The aerodynamic force exerted by the vertical tail in sideslip must be predicted in order to calculate the aircraft restoring yawing moment. An aircraft is said to be (statically) stable in sideslip if it yaws in the direction of the wind, by no action of the control system. Figure 3.5 shows the relative velocity coming from the left and a sideforce generated on the vertical tail such that the aircraft rotates counterclockwise about its center of gravity. Thus, the perturbation tends to be reduced and eventually removed.

The methods here discussed, reported in Refs. [24, Part VI, §10.2.4]

and [43], have a common feature: the sideforce derivative of the isolated vertical tail is corrected by the effects of wing, fuselage, and horizontal tail. However the interference factors are computed in different ways.

The basic equation is the definition of the lift curve slope for tapered wings

$$C_{L_\alpha} = \frac{2\pi\, \mathcal{AR}}{2 + \sqrt{\dfrac{B^2 \mathcal{AR}^2}{\kappa^2}\left(1 + \dfrac{\tan^2 \Lambda_{c/2}}{B^2}\right) + 4}} \tag{3.6}$$

which is the Helmbold-Diederich formula [54, 55] (see again Figure 2.19) where

$\mathcal{AR}$ is the wing (or tail) aspect ratio, see again Figure 2.3

B is the compressibility parameter, $\sqrt{(1 - M^2)}$

κ is the ratio of *section* lift-curve slope to theoretical thin-section value$c_{l_\alpha}/(2\pi\, B)$, and for thin airfoils ($c_{l_\alpha} \approx 2\pi$) it is equal to $1/B$

$\Lambda_{c/2}$ is the sweep angle at half chord.

Lateral directional derivatives are defined as follows

$$C_{N_{\beta_v}} = -C_{Y_{\beta_v}}(l_v \cos\alpha + z_v \sin\alpha)/b \tag{3.7}$$

$$C_{\mathcal{L}_{\beta_v}} = -C_{Y_{\beta_v}}(z_v \cos\alpha - l_v \sin\alpha)/b \tag{3.8}$$

where l_v and z_v are respectively the vertical tail longitudinal and vertical distance from aircraft center of gravity in the wind axes reference system.

3.2.1 USAF DATCOM

Here it is described the method initially proposed by Finck [26] and later adopted by Roskam [24, Part VI, §10.2.4] in his famous Airplane Design books.

The lift curve slope of the isolated vertical tail is calculated with Equation 3.6. By coupling the vertical tail with wing, fuselage, and horizontal tail, the *effective* aspect ratio $A_{v_{\text{eff}}}$ is defined. This accounts for fuselage height in the region of the vertical tail, horizontal stabilizer position, and empennage

planform area ratio S_h/S_v, according to the formula

$$A_{v_{\text{eff}}} = \frac{A_{v(f)}}{A_v} A_v \left[1 + k_h \left(\frac{A_{v(hf)}}{A_{v(f)}} - 1 \right)\right] \tag{3.9}$$

where the geometric parameters to calculate the effective aspect ratio are reported in Figure 3.6 and each term of the previous equation is described below:

A_v is the vertical tail geometric aspect ratio, b_v^2/S_v;

$A_{v(f)}/A_v$ is the ratio of the vertical tail aspect ratio in the presence of the fuselage to that of an isolated vertical tail, defined in Figure 3.7;

$A_{v(hf)}/A_{v(f)}$ is the ratio of the vertical tail aspect ratio in the presence of the horizontal tail and the fuselage to that of the fuselage alone, defined in Figure 3.8;

k_h is a factor which accounts for the relative size of the horizontal and the vertical tail, defined in Figure 3.9.

Here are some remarks:

- the vertical tail span b_v is referred to the isolated vertical tail planform;
- when computing the correction factors (and only in that case) in Equation 3.9 the vertical tail is extended to the fuselage centerline, and so its span (here named b_{v1}) and taper ratio;
- the *region of the vertical tail* cited in Figure 3.7 is the projection of the quarter point of vertical tail mean aerodynamic chord (m.a.c.) on the fuselage centerline;
- the vertical tailplane m.a.c. is that of the isolated tailplane. In fact, it is impossible to define the m.a.c. of the extended tailplane *a priori*, since it is necessary to know the extended tail span, which in turn depends on the projection of the quarter point of the m.a.c. on the fuselage centerline.

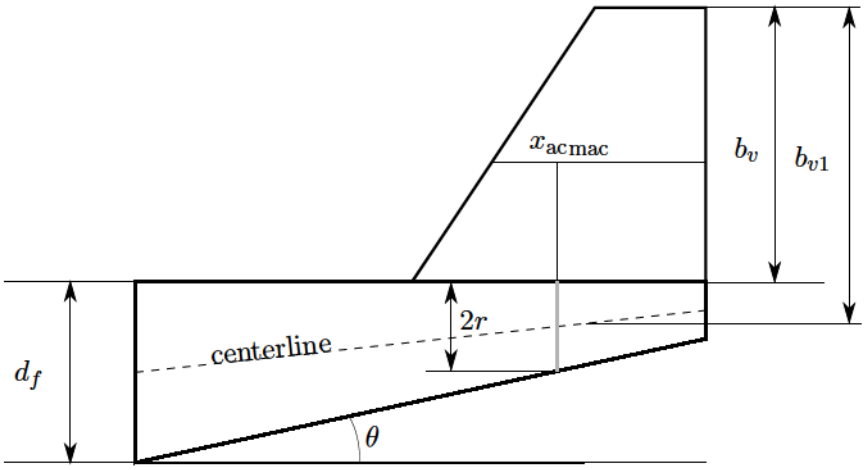

FIGURE 3.6: Definition of fuselage depth in the region of vertical panels.

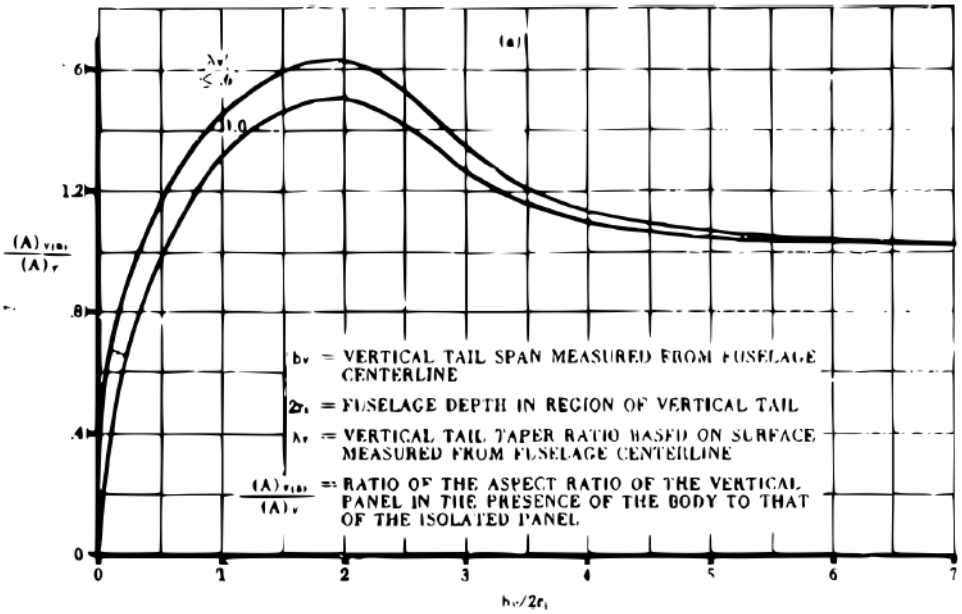

FIGURE 3.7: Fuselage-vertical tail interference factor [26].

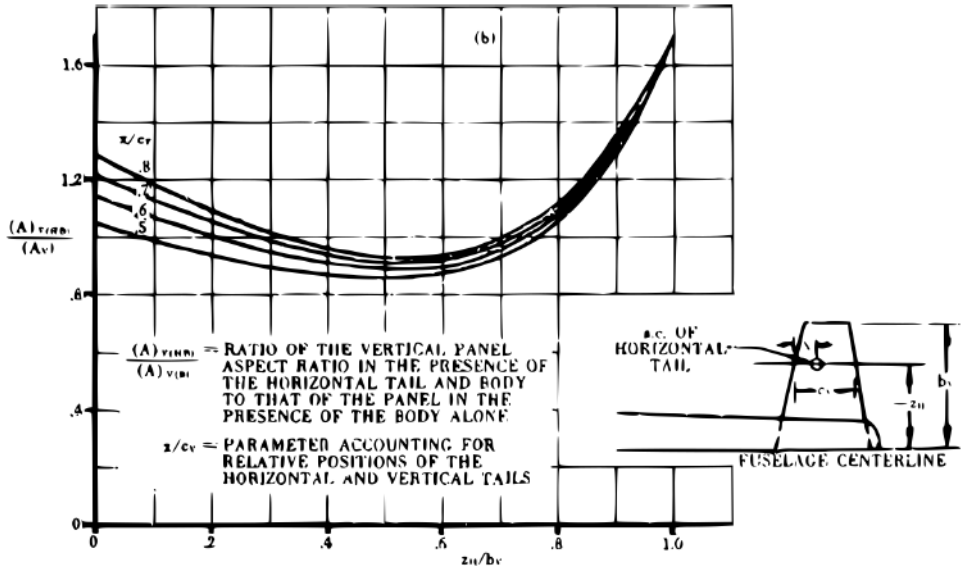

FIGURE 3.8: Fuselage-horizontal tail-vertical tail interference factor [26]. Notice that now the span b_v extends to the fuselage centerline.

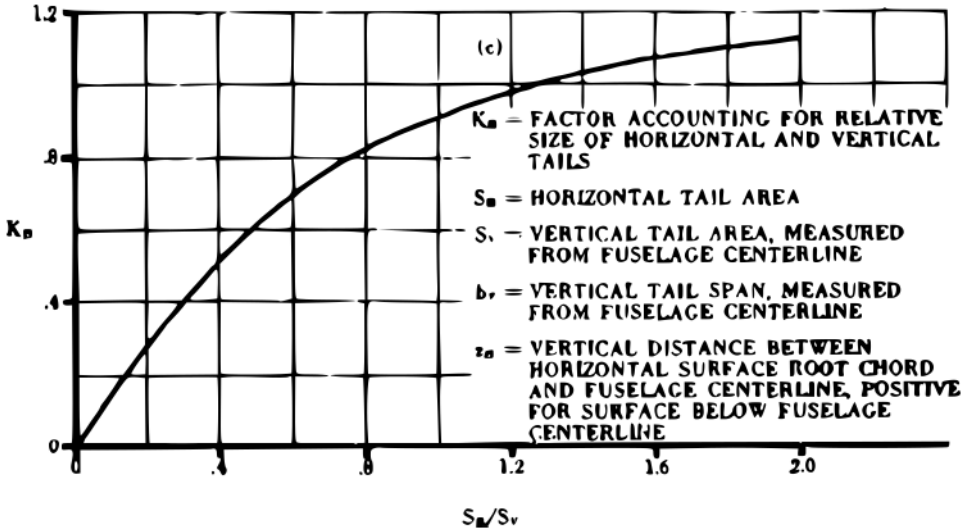

FIGURE 3.9: Factor that accounts for relative size of the horizontal and vertical tails [26].

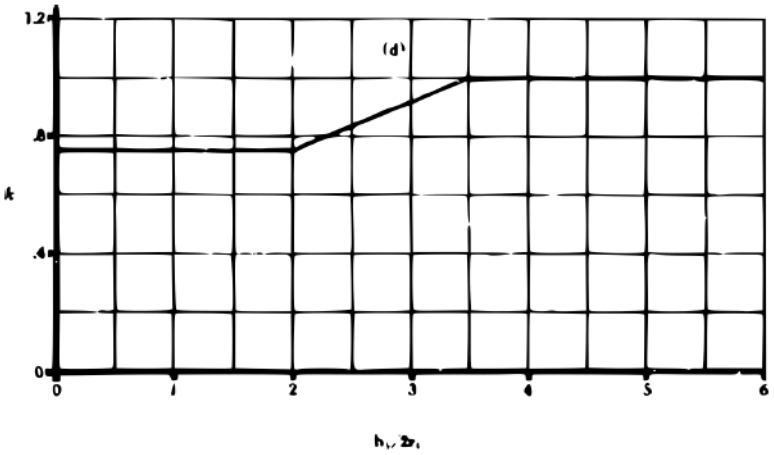

FIGURE 3.10: Empirical factor for estimating sideforce-due-to-sideslip of a single vertical tail [26].

Thus, the vertical tail contribution to the sideforce derivative is

$$C_{Y_{\beta_v}} = -k_v \, C_{L_{\alpha_v}} \left(1 + \frac{d\sigma}{d\beta}\right) \eta_v \, \frac{S_v}{S} \tag{3.10}$$

where

β is the *sideslip* angle;

k_v is given in Figure 3.10;

$C_{L_{\alpha_v}}$ is the lift curve slope corrected by $A_{v_{\text{eff}}}$ defined in Equation 3.9;

$(1 + d\sigma/d\beta)\,\eta_v$ is the *sidewash* effect;

S_v/S is the ratio of the vertical tail area to the wing area.

Thus, the corrected $C_{L_{\alpha_v}}$ is corrected again by another factor that accounts for fuselage height in the region of vertical tail, by the sidewash effect, and it is scaled by the surface ratio. The sidewash effect can be amplifying or reductive[1], the wing position being the key parameter and the aspect ratio

[1] At subsonic speeds the empirical Equation 3.10 gives the total sidewash effect directly, i.e. the combined sidewash angle and dynamic-pressure loss.

of secondary importance

$$\left(1 + \frac{d\sigma}{d\beta}\right)\eta_v = 0.724 + 3.06\,\frac{S_v/S}{1+\cos\Lambda_{c/4}} + 0.4\,\frac{z_w}{z_f} + 0.009\text{Æ} \tag{3.11}$$

where

$\Lambda_{c/4}$ is the wing quarter chord sweep angle

z_w/z_f is the ratio of the wing position, computed from centerline and negative for a high wing, to the fuselage height in the wing region, that is -0.5 for a high wing, $+0.5$ for a low wing, 0 for middle wing

Æ is the wing aspect ratio.

Sidewash parameters are additive, whereas effective aspect ratio parameters are multiplicative.

There are some additional effects that are not accounted for by the method. For instance, dorsal fins may cause a considerable error in the values obtained, although the effect of dorsal fins is more pronounced at the higher angles of sideslip. Dihedral in the horizontal surfaces is known to change the pressure loading on the vertical panel and hence its effectiveness. For rapidly converging bodies, flow separation frequently exists at the juncture of the vertical panel with the body. This effect generally decreases the effectiveness of the vertical tail and is not accounted for by the methods included herein. Similar effects can result when the maximum thickness of two orthogonal panels are made to coincide [26, §5.3.1.1].

The report by Finck [26] also compares the proposed method with test data. In Figure 3.11 the percentage error of the method for each configuration is shown. Method 1 has been described here. Method 3, not presented here, is only valid for body-mounted horizontal tail configurations. The reader can see that the configurations investigated look like supersonic jet-powered aircraft and that the DATCOM methods are not always in good agreement with test data.

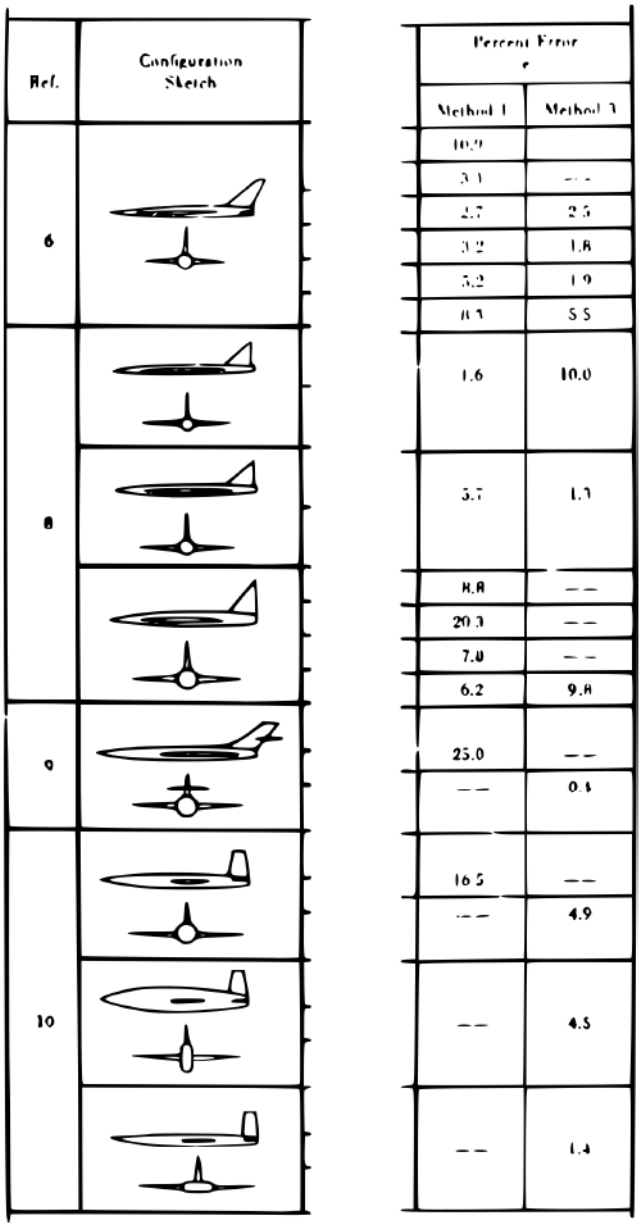

FIGURE 3.11: Subsonic contribution of vertical panels to C_{Y_β}. Data summary and substantiation. Table 5.3.1.1-B from Ref. [26].

3.2.2 ESDU

The method reported by Gilbey [43] is quite simple. The lift curve slope of the isolated vertical tailplane (see Equation 3.6) is corrected by three factors, J_B, J_T, J_W, respectively body-fin, tailplane, and wing correction factor, and it is scaled by the surface ratio S_F/S

$$Y_{v_F} = -J_B J_T J_W \, C_{L_{\alpha_F}} \, \frac{S_F}{S} \tag{3.12}$$

where $C_{L_{\alpha_F}}$ is the $C_{L_{\alpha_v}}$ defined in Equation 3.6 when the fin aspect ratio

$$A_F = 2 \, \frac{b_F^2}{S_F} \tag{3.13}$$

is substituted to A_v, so that this procedure is initially quite different from the DATCOM method, but as will be shown in Section 3.2.3, results conform for conventional geometries.

This method contemplates conventional geometries, an almost circular fuselage, and a constant sidewash. It is a synthesis of experimental analyses done from NACA, British Aerospace, SAAB, and others, from the '40s to the '70s, linked together with potential flow theory [44] where the data were highly scattered.

The vertical tail (fin) is considered a trapezoidal panel, any extension like dorsal fairing or a curved fin tip is ignored and the leading edge is extended linearly in the body. The fin panel tip chord is the chordwise distance between the leading and trailing edges of the fin at the maximum height. The fin panel root chord is the chordwise distance between the (extrapolated) leading and trailing edges of the fin at the height where the fin quarter-chord sweep line intersects the top of the body [43] (Figure 3.12). Note that the vertical tail span and planform area may be different from those calculated with DATCOM, according to the fuselage shape (for a straight upper surface like that in Figure 3.6 they are equal).

Values of J_T for body-mounted tailplanes are referred to near body centerline position, otherwise some caution is necessary for tailplanes mounted high on the body, close to the fin-body junction.

The method is applicable to conventional airplanes in cruise (clean) configuration at small angles of attack and sideslip, where there is an essentially linear variation of the sideforce, yawing moment, and rolling moment with the

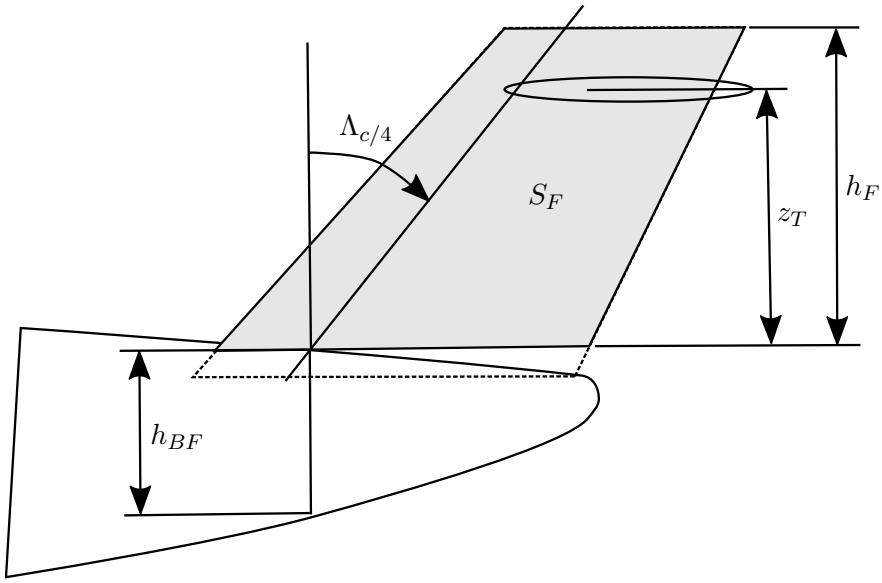

FIGURE 3.12: ESDU definition of vertical tail (fin). Reproduced from Ref. [43].

angle of sideslip. In practice, because of departures from a linear variation, static lateral stability derivatives are defined from experimental data over a small range of sideslip angles, typically between $\pm 2°$ and $\pm 5°$. Almost all of the data studied come from wind-tunnel tests carried out at low speeds and the method introduces compressibility effects only through the basic fin lift-curve slope estimated from Ref. [55].

For copyright reasons, it is not possible to show the charts of the method proposed by ESDU. The range of the parameters investigated is shown in Table 3.5.

TABLE 3.5: Range of geometries for the ESDU method [43].

Body		Wing	
$\frac{h_{BF}}{h_{BF}+h_F}$	0.1 to 0.5	A_W	2 to 11
$\frac{h_{BF}}{d_{BF}}$	1 to 1.15	$\Lambda_{1/4_W}$	0° to 60°
		$\frac{z_W}{h_{BW}}$	+0.5 to − 0.5
Vertical tail		Horizontal tail	
A_F	1.0 to 5.0	A_T	0.5 to 5.5
$\Lambda_{1/4_F}$	0° to 60°	$\Lambda_{1/4_T}$	0° to 60°
λ_F	0 to 1	λ_T	0 to 1
$\frac{S_F}{S}$	0.05 to 0.27	$\frac{b_T}{h_F}$	0.5 to 4

3.2.3 An application in MATLAB

It is interesting to compare the results of the DATCOM and ESDU methods previously described. This has been accomplished by writing a MATLAB script to account for all the aerodynamic interference effects among airplane components. It is possible to study a complete or a partial aircraft configuration as well as to perform parametric studies, to evaluate the effect of a single parameter on the whole airplane or on a partial configuration. Actually it is possible to investigate the following parameters:

1. vertical tail aspect ratio;
2. wing-fuselage relative position;
3. wing aspect ratio;
4. wing span;
5. horizontal tailplane relative position;
6. horizontal tailplane size;
7. vertical tail span vs fuselage height;
8. fuselage upsweep angle.

The input script calls user-defined MATLAB functions that are the digitized versions of the charts of the methods described in Section 3.2.1 and 3.2.2. Once defined the airplane main dimensions in the input file, the main script can be called in the MATLAB Command Window. It is possible to define different airplanes in separate files and call the one desired, without rewriting all the input data.

The script can run in two different ways. In the *single shot* mode the output is shown formatted in the Command Window and optionally written it an output file. If the *parametric* mode is selected, the stability derivatives are plotted against the chosen parameter. It calculates the sideforce, yawing moment, and rolling moment derivatives, showing also the percentage difference between the methods.

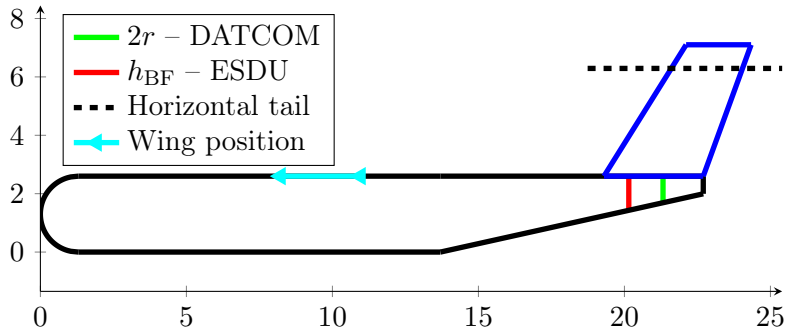

FIGURE 3.13: The ATR-42 configuration, generated by the MATLAB script. Dimensions are in m.

Analysis for a regional turboprop airplane

The sideforce coefficient derivatives of an ATR-42, shown in Figure 1.15, have been evaluated with the methods described in the previous sections. The MATLAB script also plots a schematic side-view of the configuration, here reported in Figure 3.13. Input data are presented in Table 3.6.

Results are reported from Table 3.7 to 3.10. For this particular case, differences are negligible. A side-by-side comparison cannot be made, since the methods apply different approaches. Here it is remarked that even a common starting point is difficult to achieve, since DATCOM [26] defines the vertical tailplane aspect ratio as

$$A_v = \frac{b_v^2}{S_v}$$

whereas ESDU [43] defines it as

$$A_F = 2\,\frac{b_F^2}{S_F}$$

where v stands for *vertical tail* and F stands for *fin* (with the same meaning), hence even for the same planform, the aspect ratios and lift curve slopes are different.

Table 3.6: ATR-42 main dimensions

Parameter	Symbol	Value
Aircraft mass	W	16 700 Kg
Wing surface	S	54.5 m^2
Wing aspect ratio	A	12
Wing taper ratio	λ	0.54
Wing span	b	24.6 m
Wing chord	c	2.2 m
Fuselage length	l_f	22.7 m
Fuselage width	d_f	2.6 m
Upsweep angle	θ	12.0°
Horizontal tail surface	S_h	11.5 m^2
Tailplanes relative position	z_h/b_v	0.86
Vertical tail root chord	$c_{v_{\text{root}}}$	3.5 m
Vertical tail span	b_v	4.5 m
Vertical tail surface	S_v	12.5 m^2
Vertical tail aspect ratio	A_v	1.6
Vertical tail l.e. sweep angle	$\Lambda_{v_{\text{LE}}}$	30°
Vertical tail t.e. sweep angle	$\Lambda_{v_{\text{TE}}}$	20°

Table 3.7: Correction factors provided by DATCOM method.

Effect	Lookup	Input	Output
Aft fuselage height	Figure 3.7	3.962	1.1269
Position of the horizontal tail	Figure 3.8	0.860	1.223
Relative size of the tailplanes	Figure 3.9	0.920	0.880
Empirical factor k_v	Figure 3.10	3.962	1.000
Sidewash effect	Equation 3.11	—	1.042

Table 3.8: Effect of the correction factors (DATCOM method).

Parameter	Isolated tail	Coupled bodies	Ratio
A_v	1.6	2.14	1.34
$C_{L_{\alpha_v}}$ (rad^{-1})	2.249	2.809	1.25

Table 3.9: Correction factors provided by ESDU method.

Effect	Lookup	Input	Output
Lift curve slope (rad^{-1})	Equation 3.6	—	3.611
Body-fin correction factor	ESDU 82010	0.254	0.969
Tailplane correction factor	ESDU 82010	0.860	1.110
Wing correction factor	ESDU 82010	−0.500	0.728
Corrected lift slope (rad^{-1})	*Product of previous output*		2.827

Table 3.10: Result comparison (rad^{-1}) and deviation from DATCOM.

Derivative	Symbol	DATCOM	ESDU	Δ %
Corrected lift slope	$C_{L_{\alpha_v}}$	2.809	2.827	0.64
Sideforce	$C_{Y_{\beta_v}}$	−0.647	−0.649	0.31
Yawing moment	$C_{N_{\beta_v}}$	0.276	0.273	−1.09
Rolling moment	$C_{\mathcal{L}_{\beta_v}}$	−0.087	−0.088	1.15

Parametric investigation

Once defined the airplane and its stability derivatives in Section 3.2.3, a parametric investigation has been performed. Each parameter (e.g. the aspect ratio of the vertical tail *or* the position of the horizontal tailplane *or* something else) is varied in a user-defined range, while the others are kept constant, and it is observed how stability derivatives vary with that parameter. The complete airplane has been investigated, no partial configurations have been considered. This is a test for the MATLAB script, based on a real and actual airplane.

Normalization of the coefficients is realized with the input data, that is with the ATR-42 wing planform area S. All units are per radians. The effects of the following parameters have been studied:

1. vertical tailplane aspect ratio;
2. wing-fuselage relative position;
3. wing aspect ratio;
4. horizontal tailplane position;

5. tailplanes surface ratio;

6. fuselage height in the region of vertical tail.

Vertical tail aspect ratio It is apparent the linearity of the methods involved. Differences are negligible for aspect ratios around 1.5. Figure 3.14.

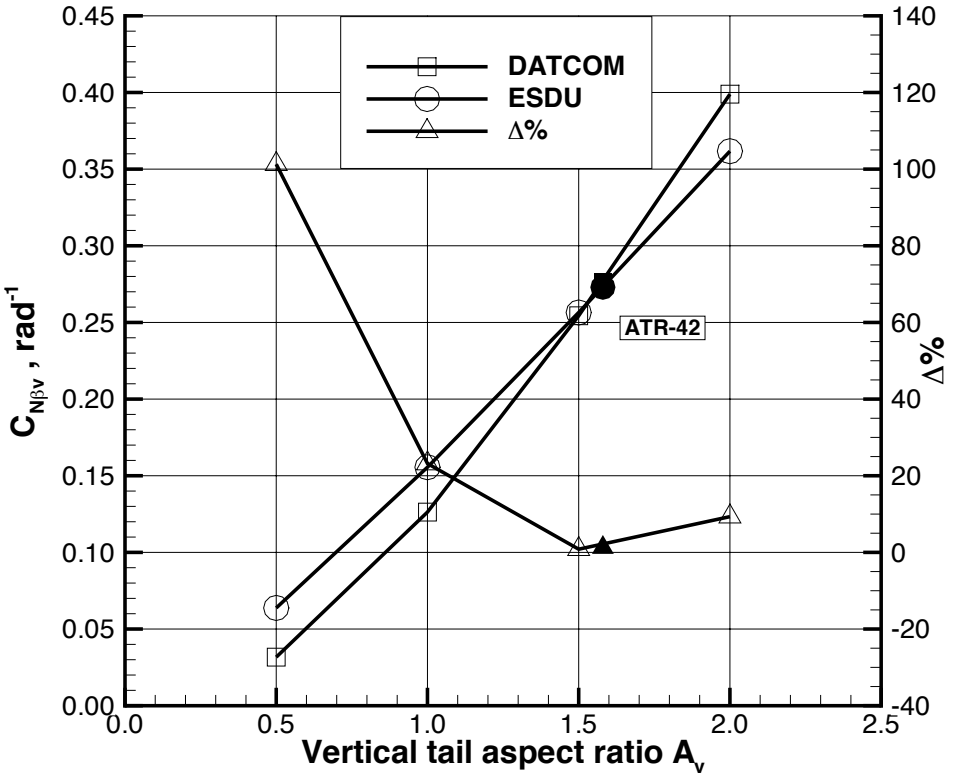

FIGURE 3.14: Yawing moment due to sideslip coefficient as function of vertical tail aspect ratio.

Wing-fuselage relative position Low wing has the maximum effect and this effect is bigger with the ESDU method. The maximum difference is about 26 %. Figure 3.15.

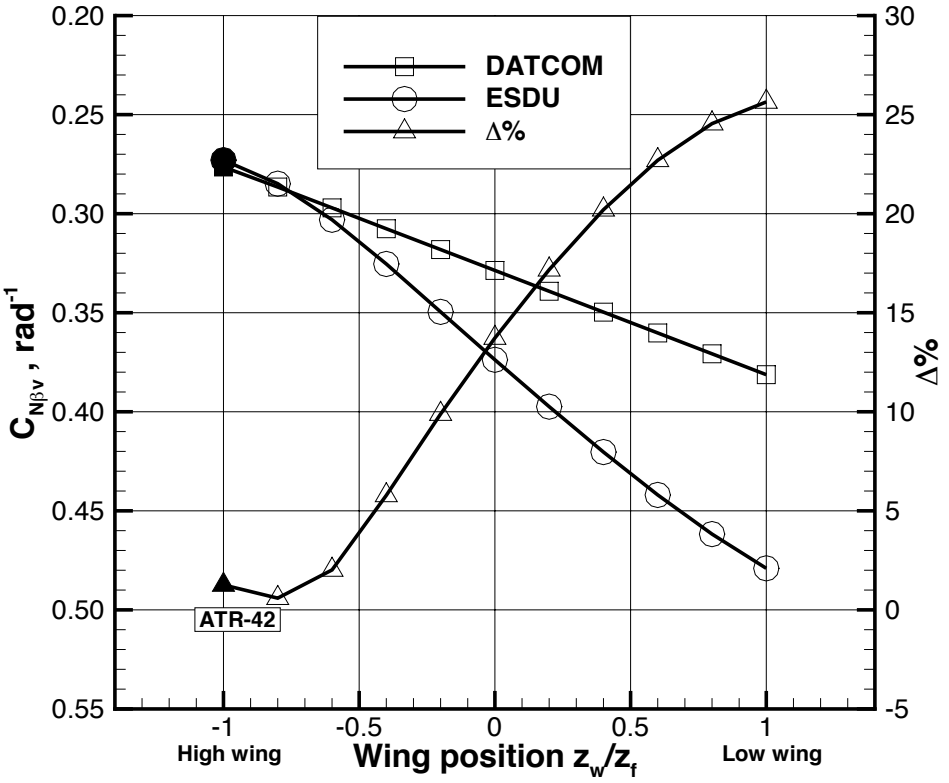

FIGURE 3.15: Yawing moment due to sideslip coefficient as function of wing position.

Wing aspect ratio Here the wing chord c is kept constant, while wing span b and the wing area S increase according to the formulas (for straight wings)

$$\text{Æ}R = b/c$$
$$S = bc$$

and it is apparent that the ESDU method considers a constant sidewash. However, differences are small, with a maximum of about 5 % for the range considered. Figure 3.16.

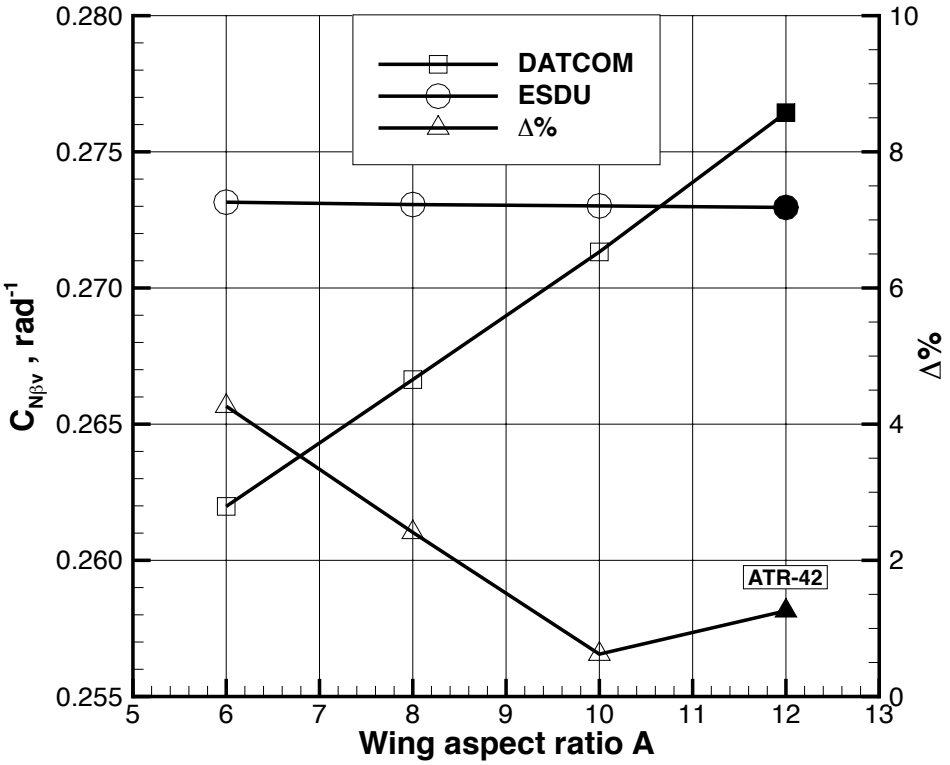

FIGURE 3.16: Yawing moment due to sideslip coefficient as function of wing aspect ratio.

Horizontal tailplane position The end-plate effect is apparent. Body-mounted tailplanes are out of axis range and plotted in Figure 3.17 only for comparison. The smoother transition from the tail-mounted to the body-mounted configuration on the DATCOM curve is due to the continuity of the curves of Figure 3.7 and 3.8, whereas the ESDU input parameters are different for body-mounted and fin-mounted horizontal tailplanes [43]. Maximum error is 25 % for body-mounted tailplane and 8 % for cruciform and T-tail configurations.

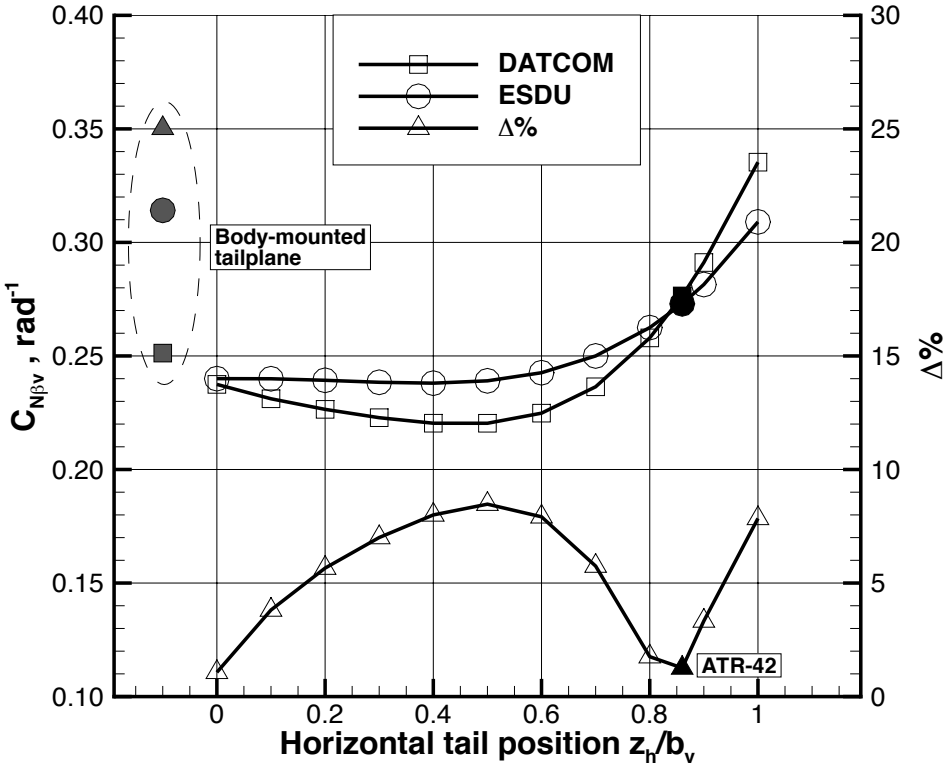

FIGURE 3.17: Yawing moment due to sideslip coefficient as function of horizontal tailplane position.

Tailplanes surface ratio The horizontal plane has a constant aspect ratio $A_h = 4.1$, hence its planform area and span increase at the same time. The two methods give close values. Figure 3.18.

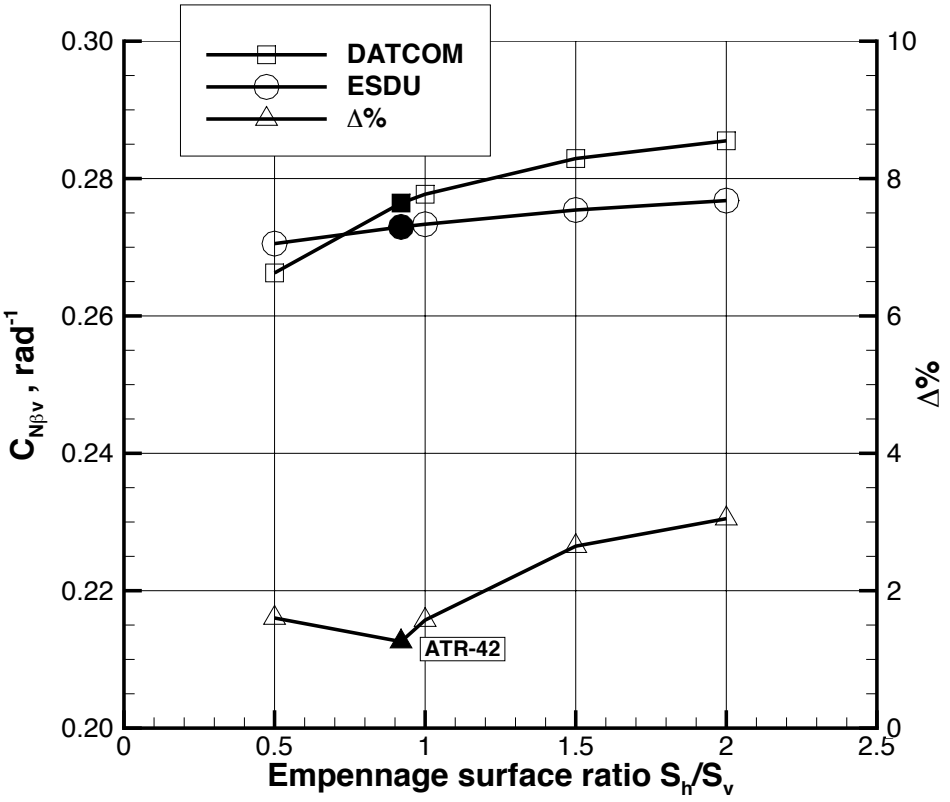

FIGURE 3.18: Yawing moment due to sideslip coefficient as function of tailplanes relative size.

Vertical tail span vs fuselage height The curves have been obtained by varying $b_v/2r$, that is the ratio of the vertical tail span on the fuselage thickness about the location of vertical tail aerodynamic center. It is expected an increase of the derivative with the fuselage height in the region of vertical tail, that is for small $b_v/2r$ values. Both methods provide this effect, but the curve provided by DATCOM [26] is not monotonic (see again Figure 2.15 and 3.7). The reference areas S and S_v have been held constant. Typical values of $b_v/2r$ for regional turboprop aircraft are between 4 and 6. Figure 3.19.

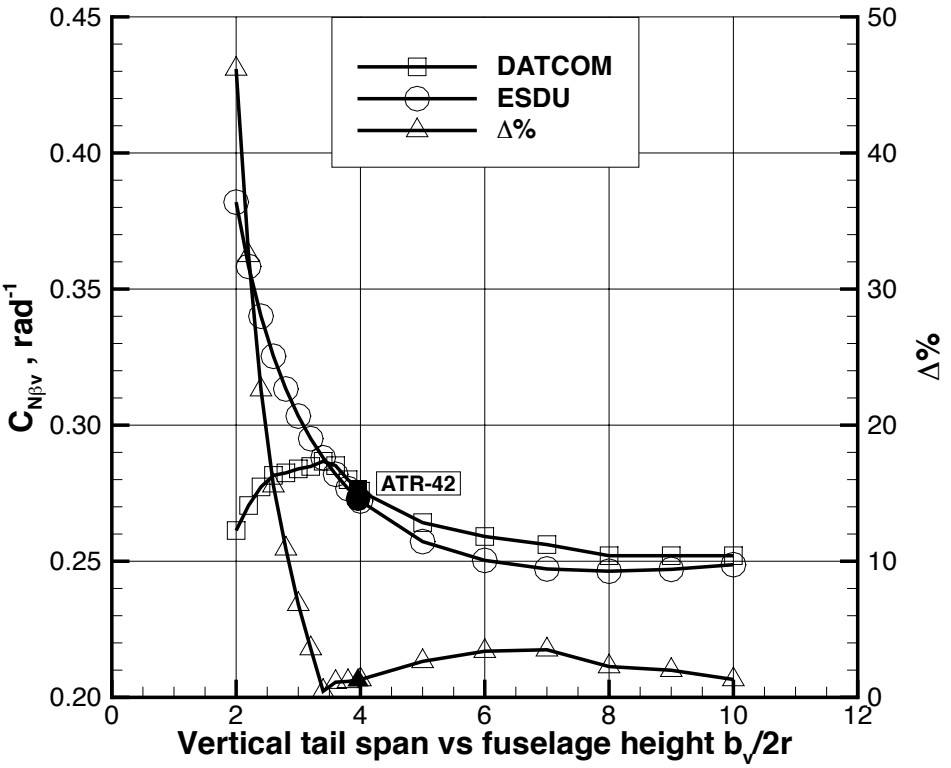

FIGURE 3.19: Yawing moment due to sideslip coefficient as function of tail-body size.

Conclusive remarks

Both methods give similar results for a regional turboprop airplane like the ATR-42 (see Table 3.10) and same trends in parametric analyses, except for wing span, where ESDU consider a constant sidewash, and fuselage thickness, where ESDU provides a decreasing curve with the ratio $b_v/2r$, whereas the curve generated by DATCOM method has a behavior like that of Figure 3.7, that is the methods present significant difference for thick bodies and small tailplanes. Finally, the methods main differences reside in:

- defining the aspect ratio of the vertical tail;
- considering the sidewash effect;
- calculating the body effect.

Both refer to the same NACA reports [34–37], yet ESDU [43] used also some unpublished data from the aviation industry. It can be stated that there is no right method, since both are based on empirical data obtained in the past.

Neither have considered the typical regional turboprop aircraft geometry (a slender body with a straight wing) and this, along the fact that for certain configurations, e.g. the body-mounted horizontal stabilizer, the methods give significant different results, was the factor that stimulated this research work: there is no method specifically developed for that kind of aircraft, although it occupies a relevant position in the regional air transport market.

3.3 Preliminary design. Fuselage aerodynamics

3.3.1 Directional stability

The fuselage contribution to aircraft directional stability can be calculated in several ways. Perkins and Hage [16, §8.2] presented an empirical formula developed by the aerodynamics group of the North American Aviation Company during World War II

$$C_{N_{\beta f}} = \frac{0.96 K_\beta}{57.3} \frac{S_s}{S} \frac{L_f}{b} \left(\frac{h_1}{h_2}\right)^{\frac{1}{2}} \left(\frac{w_1}{w_2}\right)^{\frac{1}{3}} \quad (/\text{deg}) \tag{3.14}$$

where

S_S is the projected side area;

L_f is the over-all fuselage length;

h_1, h_2, w_1, w_2 are dimensions illustrated in Figure 3.20;

L_f/h is the the slenderness ratio referred to the fuselage maximum height;

d/L_f is the non-dimensional distance of the center of gravity from the nose;

K_β is found from Figure 3.20.

Notice that this approach involves the knowledge of the wing planform area S and span b.

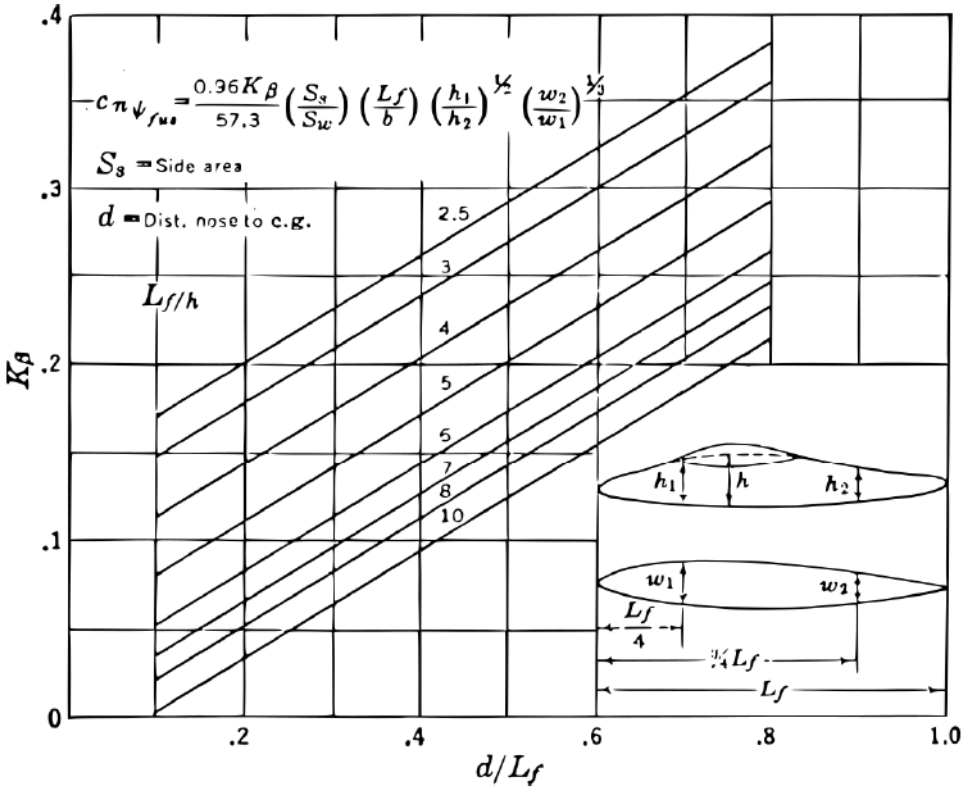

FIGURE 3.20: Fuselage directional stability coefficient. Reproduced from Ref. [16].

The USAF DATCOM [26, §5.2.3.1] proposed a similar expression for the wing-fuselage yawing moment due to sideslip $C_{N_{\beta_{wf}}}$. It accounts for the fuselage contribution plus the wing-body interference, since the wing alone contribution is important only at large angles of incidence. The proposed formulation is valid for all speed regimes, since the interference due to the wing is essentially independent from sweep, taper ratio, wing vertical position on the fuselage, and Mach number [26]. Thus, for an arbitrary moment center

$$C_{N_{\beta_{wf}}} = K_N \, K_{Re_\ell} \, \frac{S_{B_s}}{S} \frac{\ell_B}{b} \quad (/\text{deg}) \tag{3.15}$$

where

K_N is an empirical factor reported in Figure 3.21;

K_{Re_ℓ} is an empirical factor function of the fuselage Reynolds number;

S_{B_s} is the projected side body area;

ℓ_B is the length of the body.

Nomenclature has been kept the same of Ref. [26], to allow an easy examination of Figure 3.21. The factor dependent on the fuselage Reynolds number has been taken from Ref. [26, Fig. 5.2.3.1-9]

$$K_{Re_\ell} = 0.4717 \, \log\left(\frac{Re_\ell}{7584.319}\right) \tag{3.16}$$

and that is all. *According to the classical semi-empirical methods*, no further steps are necessary, since *there are no mutual aerodynamic interference effects*, with the exception of the wing, which is included in Equation 3.15.

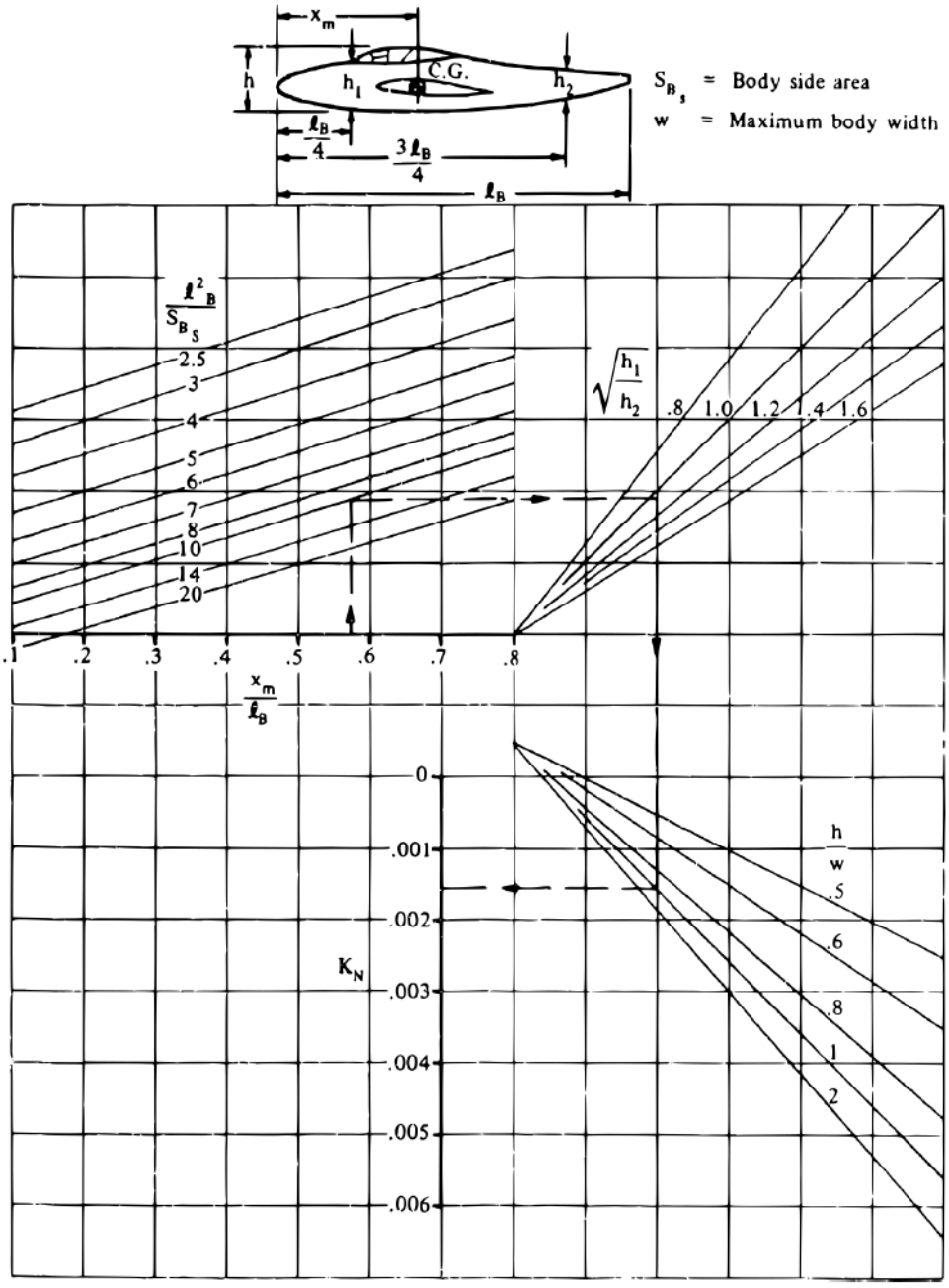

FIGURE 3.21: Empirical factor K_N related to wing-fuselage sideslip derivative. Reproduced from Ref. [26, Fig. 5.2.3.1-8].

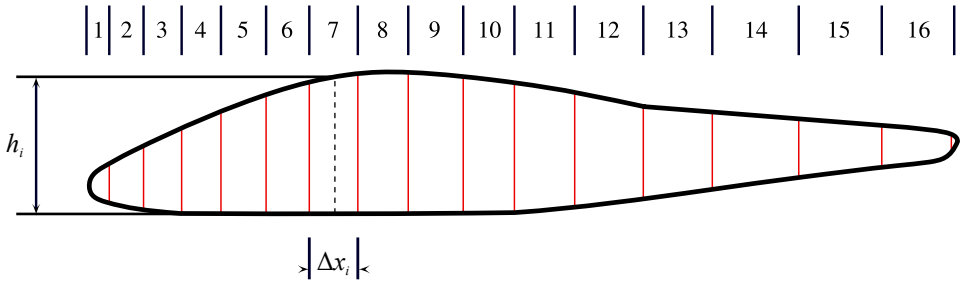

FIGURE 3.22: Fuselage side divided in strips. Graphic elaboration courtesy of Agostino De Marco.

An alternative is the application of the *strip method*, which is the classic approach in the evaluation of the fuselage pitching moment derivative (see next section). The integral of Equation 2.8 is approximated by a sum

$$C_{N_{\beta f}} = \frac{(K_2 - K_1)}{36.5\, S b} \sum_{i=0}^{n} h_i^2 \Delta x_i \quad (/\text{deg}) \tag{3.17}$$

where $(K_2 - K_1)$ has been defined in Figure 2.34, h_i and Δx_i are defined in Figure 3.22.

Here follows an application on the fuselage of the ATR-42. The geometric parameters to apply Equation 3.14 are assumed as follows

$S_s = 49\,\text{m}^2$	$h = h_1$
$S = 50\,\text{m}^2$	$L_f/h = 8.6$
$L_f = 22.7\,\text{m}$	$w_1 = 2.8\,\text{m}$
$b = 24.5\,\text{m}$	$w_2 = 2.3\,\text{m}$
$h_1 = 2.6\,\text{m}$	$d/L_f = 0.41$
$h_2 = 2.0\,\text{m}$	

and by looking at Figure 3.20 it results $K_\beta = 0.11$

$$C_{N_{\beta f}} = \frac{0.96 \times 0.11}{57.3} \frac{49}{50} \frac{22.7}{24.5} \left(\frac{2.6}{2.0}\right)^{\frac{1}{2}} \left(\frac{2.8}{2.3}\right)^{\frac{1}{3}} = 0.002\,05\,\text{deg}^{-1}$$

while to apply Equation 3.15, the factor K_N must be evaluated from Figure 3.21 with the following parameters

$$\ell_B^2/S_{B_S} = 22.7^2/49 = 10.5$$

TABLE 3.11: ATR-42 fuselage directional stability derivatives. Comparison among results of different semi-empirical methods.

Equation	Multhopp (3.4)	Perkins (3.14)	DATCOM (3.15)	Strip method (3.17)
C_{N_β} (/deg)	0.001 26	0.002 05	0.001 89	0.002 03

$$\sqrt{h_1/h_2} = \sqrt{2.6/2.0} = 1.14$$

$$h/w = 2.6/2.8 = 0.93$$

yielding to $K_N = 0.001$. The factor K_{Re_ℓ} for a 200 000 000 Reynolds number is given from Equation 3.16

$$K_{Re_\ell} = 0.4717 \log\left(\frac{200 \times 10^6}{7584.319}\right) = 2.085$$

resulting in

$$C_{N_{\beta wf}} = 0.001 \times 2.085 \frac{49}{50}\frac{22.7}{24.5} = 0.001\,89\,\text{deg}^{-1}$$

very close to the previous value.

A comparison of the results from different semi-empirical methods is reported in Table 3.11, where the Multhopp method refers to Section 3.1.2, whereas results of the strip method have been computed by a preliminary design software.

3.3.2 Outlines on longitudinal stability and aerodynamic drag

A complete treatise on semi-empirical methods about fuselage contribution in aircraft longitudinal stability and aerodynamic drag is out of the scope of this work. The physics involved has been discussed in Section 2.2.1. In this section, only outlines and references are given.

In the longitudinal plane, the effect of the wing cannot be ignored, because of the aerodynamic loading distribution on the wing-fuselage system. The

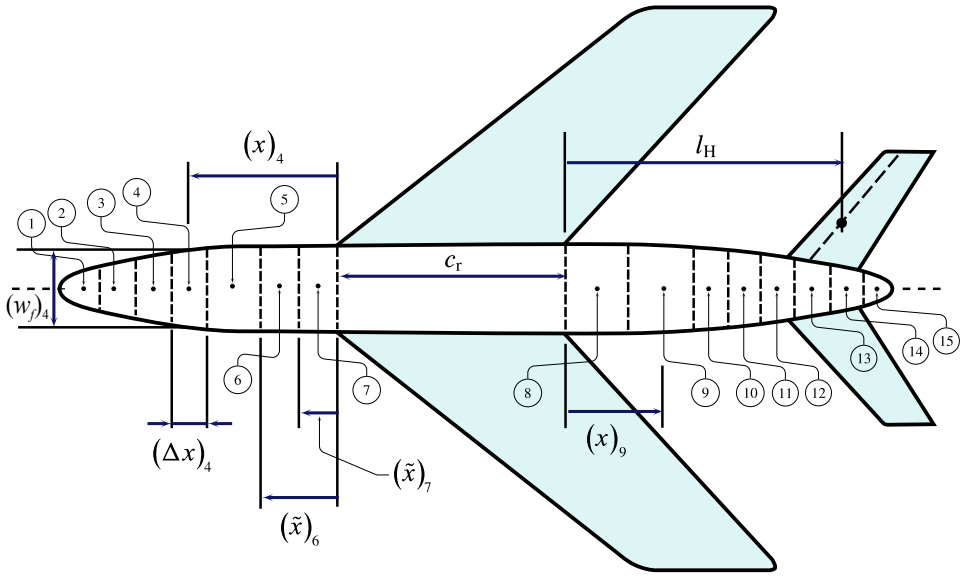

FIGURE 3.23: Fuselage planform divided in strips. Reproduced from Ref. [26, §4.2.2.1]. Graphic elaboration courtesy of Agostino De Marco.

engineering approximation [24, §8.2.5.3] of Equation 2.9 should be used

$$C_{M_{\alpha_f}} = \frac{1}{36.5\,Sc}\frac{C_{L_\alpha}}{0.08}\sum_{i=1}^{n} w_{f_i}^2 \left(\frac{d\bar{\epsilon}}{d\alpha}\right)_i \Delta x_i \tag{3.18}$$

where

w_{f_i} and Δx_i are defined in Figure 3.23

C_{L_α} is the wing lift curve slope in 1/deg

$$\left(\frac{d\bar{\epsilon}}{d\alpha}\right)_i = \begin{cases} \text{for } i = 1 \text{ to } 6, & \text{use curve 1 in Figure 3.24} \\ \text{for } i = 7, & \text{use curve 2 in Figure 3.24} \\ \text{for } i = 8 \text{ to } 15, & \text{use } \frac{x_i}{l_h}\left(1 - \frac{d\epsilon}{d\alpha}\right) \end{cases}$$

where, $d\epsilon/d\alpha$ is the wing downwash. This is called *strip method*, because the fuselage is divided in strips, which contribute with their dimension and position to the fuselage pitching moment derivative.

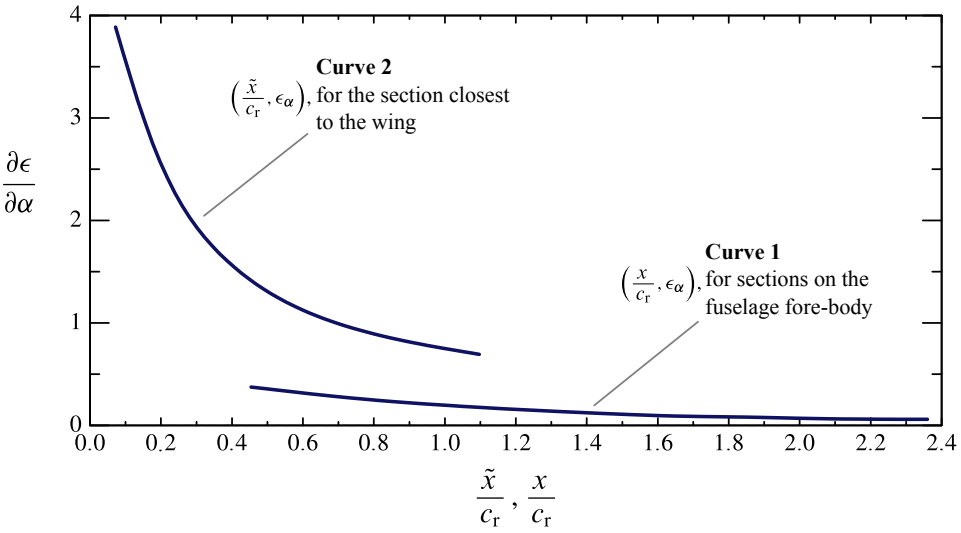

FIGURE 3.24: Longitudinal upwash variation. Graphic elaboration courtesy of Agostino De Marco.

The fuselage aerodynamic drag coefficient C_{D_0} for subsonic flow regime may be calculated as

$$C_{D_0} = C_f \left[1 + \frac{60}{(L_f/D_f)^3} + 0.0025\frac{L_f}{D_f}\right] \frac{S_{\text{wet}}}{S_{\text{front}}} + C_{D_b} \tag{3.19}$$

which has been provided in the USAF DATCOM [26, §4.2.3.1], where

C_f is the turbulent flat plate skin-friction coefficient evaluated at the fuselage Reynolds number;

L_f/D_f is the above-mentioned slenderness ratio;

S_{wet} is the fuselage wetted area (minus the base area);

S_{front} is the fuselage maximum frontal area;

C_{D_b} is the base drag coefficient [46, §3.8].

Details are reported in Refs. [24, 26, 56]. Also, it is possible to account for windshield shape and upsweep angle as interference drag, summing up these contributions to Equation 3.19.

Chapter 4

A new approach with Computational Fluid Dynamics

Synopsis

- ✈ The use of CFD in aircraft design is discussed
- ✈ Advantages and drawbacks of several methods are presented
- ✈ The approach is compared to wind tunnel testing technique
- ✈ The employed CFD software and hardware are described
- ✈ Several test cases are presented to validate the approach

The classic conceptual and semi-empirical methods used in aircraft design, with their capabilities and limits, have been deeply assessed in the previous chapters. Here, a new approach by computational fluid dynamics (CFD) is discussed. The numerical tools employed by the author are described. Test cases have been performed and here presented.

4.1 Applications of CFD in aircraft design

The use of computational fluid dynamics for industrial aircraft design started in the '60s and, since then, it has grown from a tool used to support wind tunnel or flight experiments to an identifiable new technology standing on its own, making important contributions to all stages of the design of a flight vehicle [57].

At that time only wind tunnel tests could provide useful info about directional stability [58], especially for the high subsonic and supersonic

flow regimes, because of vorticity and shock waves [59]. The wind tunnel is traditionally the primary tool to provide aerodynamic inputs for simulation databases. However, some issues in wind tunnel testing methods can lead to serious errors in the predicted stability and control characteristics [60]. For instance, the operation at a lower than free flight Reynolds number causes large discrepancies on boundary layer separation in certain configurations. Moreover wind tunnel tests require both the construction of a model and an adequate test facility. Additionally, the lag time between the paper design and the wind tunnel results can be considerable. Finally, any configuration change requires a change of the test model. This greatly increases the cost of the product and its time to market.

In the '70s first computer programs began to appear on the scene, with the application of linear, potential, subsonic flow theory: *panel methods*. These are numerical schemes for solving the Prandtl-Glauert equation for linear, inviscid, irrotational flow about aircraft flying at subsonic or supersonic speeds. There are fundamental analytic solutions to the Prandtl-Glauert equation known as source, doublet, and vorticity singularities. Panel methods are based on the principle of superimposing surface distributions of these singularities over small quadrilateral portions, called panels, of the (approximate) aircraft surface. The resulting distribution of superimposed singularities automatically satisfies the Prandtl-Glauert equation. To make the solution correspond to the desired geometry, boundary conditions are imposed at discrete points (named control points) of the panels [61]. The unknowns of the equations are located only on the panels, that is only on the aircraft surface, hence reducing the order of the problem by one and permitting the handling of complex geometries with a relative small number of unknowns [62].

In their simplest form, panel codes do not account for *viscosity*. Viscosity is responsible of momentum loss in boundary layer because of skin-friction and pressure drag, increasing boundary layer thickness, decreasing lift gradient, and flow separation [63]. Neglecting viscosity gives a good approximation only in attached flow regimes. Panel codes can be coupled with boundary layer codes to estimate the *friction drag*: a displacement thickness, due to the loss of momentum in the boundary layer, is calculated on the body walls by the viscous code; this displacement thickness is added to the previous geometry, providing the new input surface of the panel code; the process is repeated until convergence is reached [61].

However, a fundamental limitation remains: panel methods solve only linear differential equations [61], i.e. they can simulate only attached flows. As the panel methods do not compute the pressure in the separated flow regime, prediction of *pressure drag* is not possible [64]. Finally, by their own nature, panel codes can hardly provide wake-body interference, since the shape of the vortex sheet is unknown *a priori* [62]. It is possible to determine the pressure acting on bodies in the region of wing-body interference in subsonic flow by a hybrid panel method [65], but viscosity is still neglected.

A quasi-vortex-lattice method has been applied and modified to account for wing-body effect in sideslip [66]. Sophisticated panel methods provided rapid accurate estimates of the aerodynamic characteristics of aircraft and missile configurations at supersonic speeds [59]. Examples of panel codes used to evaluate airplane directional stability and control can also be found in Park et al. [67]. The complexity and costs of wind tunnel tests and the increasing viscosity effects at high angles of incidence led to more and more complex numerical tools, as panel methods that account for friction drag and Navier-Stokes solvers [60, 63, 68]. Navier-Stokes codes represent, in principle, the true simulation of the physics of the viscous flow [64]. Compared to the panel codes, they require a much longer solving time, also due to the generation of an adequate computational grid (*mesh*), and the problem of *turbulence modeling* is still open. However, adequate turbulence models do exist for aeronautical applications and the possibility to simulate and visualize a viscous flow pay back these disadvantages, as will be shown next.

Thus, the limits of wind-tunnel investigation and panel codes can be overcome by modern CFD. The powerful Navier-Stokes tools nowadays available offer significant benefits as companions to the experimental methods to predict aerodynamic parameters. Since 1985 the bigger computational power and the development of new solution techniques and turbulence modeling have permitted an extensive application of CFD in aircraft aerodynamic analysis and design [57, 69, 70]. In the last 30 years, CFD methods made use of finite differences [71], finite elements [72], and finite volume methods [69]. CFD helps designers to investigate the aerodynamics of the aircraft in the early phase of its design, in opportune conditions (viscous, compressible, transonic flow). The progress of numerical analysis techniques involved also the low subsonic flow field [67, 72]. An example of application about fuselage aerodynamics is found in the report by Embraer [73]. Moreover, CFD may provide a great aid in accounting *non-linear effects* in aircraft design, as will

be shown in Chapter 7.

In the last 15 years, the American Institute of Aeronautics and Astronautics (AIAA) has promoted the Drag Prediction Workshop (DPW) and the High Lift Prediction Workshop (HiLiftPW) Series to assess the state of the art of modern computational fluid dynamics methods using geometries and conditions relevant to commercial aircraft. In the last workshops, the experimental investigations focused on the NASA Common Research Model (CRM) wing-body configuration [74, 75]. The idea is to setup a public domain database of geometries, numerical, and experimental results to evaluate the effectiveness of current Navier-Stokes solvers and modeling techniques, to promote open discussion on areas needing additional research and development, to share knowledge and reduce the variability of CFD results [76, 77].

It is difficult to predict the aerodynamic drag: it depends on grid type, mesh refinement, and turbulence model; also, side-of-body separation, laminar bubbles, and aeroelastic effects are usually not considered in numerical simulations and of difficult prediction over complex geometries. After five DPWs, the following conclusions [77] have been drawn:

- data scatter among results has been reduced with each DPW;
- the median solution differs by about 4 counts from wind tunnel data;
- force/moment are better predicted at low angles of attack.

However, since the wind tunnel test and the CFD simulation setup are conceptually different, there is some question as to how well they *should* agree [77]. Table 4.1 shows that wind tunnel results should be used as reference only. Finally, although the encouraging results on complex geometries, there are some simple problems still remains of difficult solution, because of their physics. A few examples are: the flow around a thin airfoil in stall conditions, where a laminar bubble forms at the leading edge, the reattached flow is turbulent, and the stall may happen by explosion of the bubble; the flow at high angles of attack around a delta and double-delta wing, because of the vortex lift generated by leading-edge separation vortices. Lift and moment may be well predicted, but the flow field could be not well captured, and it is unknown if this behavior is casual or not [70]. For these situations, other techniques should be investigated, going from Reynolds Averaged Navier-Stokes (RANS)

Table 4.1: Wind tunnel vs CFD [77].

WIND TUNNEL TEST	**CFD**
Walls	Free air
Support system (sting)	Free air
Laminar/Turbulent (tripped)	"Fully" turbulent (usually)
Aeroelastic deformation	Rigid 1g shape
Measurement uncertainty	Numerical uncertainty & Error
Corrections for known effects	No Corrections

simulations to Large Eddy Simulations (LES) or Detached Eddy Simulations (DES) or hybrid LES/RANS approach.

High lift prediction is both difficult and fascinating. The numerical aerodynamic analysis of high lift configuration of commercial aircraft is a crucial item to reduce the number of wind tunnel tests and give a well-suited instrument for the industrial design of the high lift systems. The numerical simulation of these configurations is very complex, due to difficulties to simulate separations phenomena, unsteadiness, confluent boundary layers, transition, and so on. The summary of the first HiLiftPW by Rumsey et al. [76] states that the Spalart-Allmaras (SA) turbulence model [78] gives results in closer agreement with experiments than other – and more complex – models. This situation is even better with refined grids. The author performed a test case of the second HiLiftPW, applying the SA model on user-defined unstructured grids with different refinement levels, obtaining encouraging results: the stall and post-stall behavior have been predicted quite accurately, the angle of stall has been correctly evaluated, and the maximum lift coefficient has been underestimated by less than 5 % [79].

In the design process [12, 13, 57] CFD occupies the aerodynamics group with an increasing importance as computer speed, grid generation, and solving techniques progress with time. A CFD package ideally provides in an integrated environment:

1. *pre-processing* (geometry modeling, CAD repair);
2. grid generation;
3. solving;

4. *post-processing* (visualization and analysis of the results).

The solver provides physical and numerical modeling, the implementation of these models in the computer, and the execution of the code. This process involves both hardware and software [57]. Typical CFD design applications are the following:

- design and analysis of aircraft and component shape;
- performance, i.e. force and moment data to determine lift, drag, and moments;
- integration of components, e.g. wing-fuselage intersection or wing-pylon-nacelle group;
- evaluation of stability and control, by aerodynamic coefficients, force, and moment data;
- loads, for structural design;
- aeroservoelasticity.

The author and his research group have experience in numerical and experimental design and analysis, performance, high lift, loads, stability, and control evaluation of general aviation and regional turboprop aircraft [27, 79–88].

4.2 Software and hardware

The CFD has been used to investigate the mutual aerodynamic interference among components of many possible regional turboprop aircraft configurations. The software STAR-CCM+® by CD-adapco™ has been employed for this task. It allows to work in an integrated environment, where it is possible to import (or generate, if the model is very simple) the CAD geometry, automatically generate a mesh, easily setup the physics, run the analysis, and visualize the results as logs, plots, and scenes. The general workflow is shown in Figure 4.1.

The solver of this CFD package has been widely used on the grid computing infrastructure provided by the University of Naples "Federico II" to simulate lots of configurations in a short amount of time. *Sistema Cooperativo*

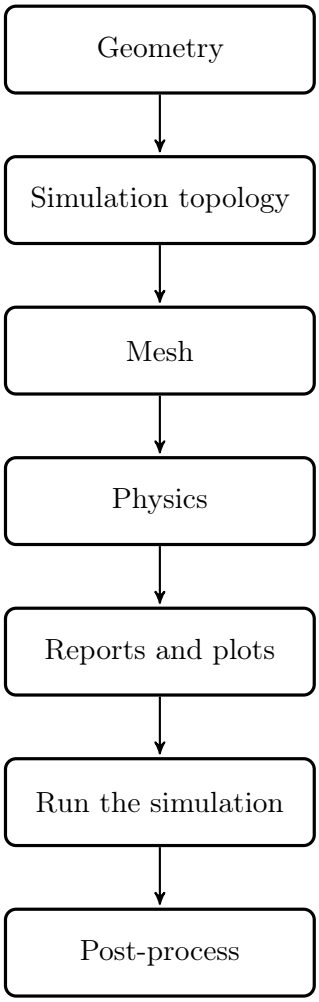

FIGURE 4.1: General sequence of operations in a STAR-CCM+ analysis.

(A) Three rack servers.

(B) Storage devices.

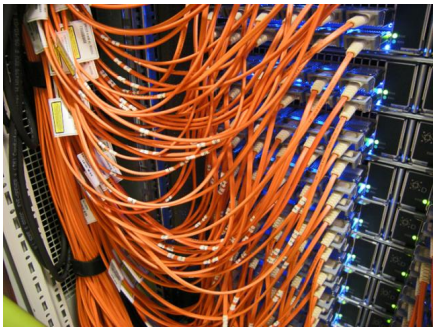

(C) Fiber optic connections.

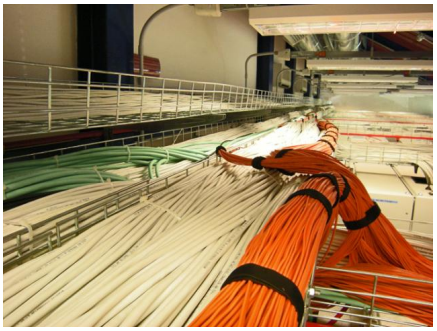

(D) Cables above the racks.

FIGURE 4.2: Some images of the SCoPE data center [89].

per Elaborazioni Scientifiche Multidisciplinari (SCoPE) is a scientific data center, based on a grid computing infrastructure (Figure 4.2), and it is a collaborative system for scientific applications in many areas of research. It is a project started in 2006 by the University of Naples "Federico II", in continuous evolution [89].

A number of 160 licenses (one per CPU) were available for these investigations. The software manual [90] recommends to employ a CPU every 250 000 cells, hence several simulations have been performed in parallel at the same time, e.g. 4 runs with 32 CPUs each. The computational time is a non-linear decreasing function with CPUs number, on a linear plot. On a logarithmic plot it is a linear function instead. Figure 4.3 represents the time necessary to get a converged solution versus CPUs number, in the two

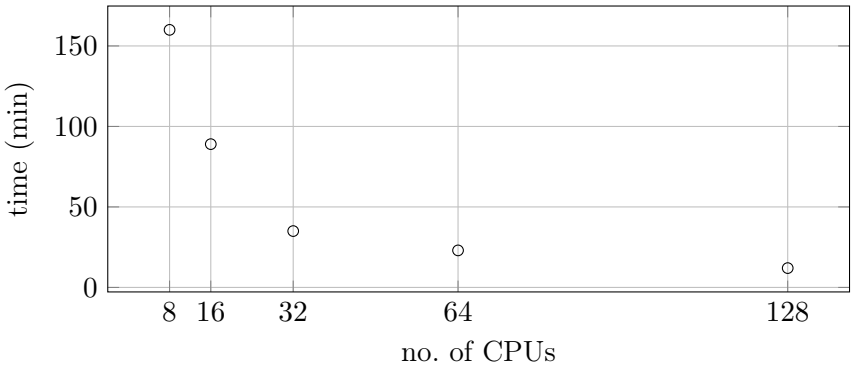

(A) Linear plot.

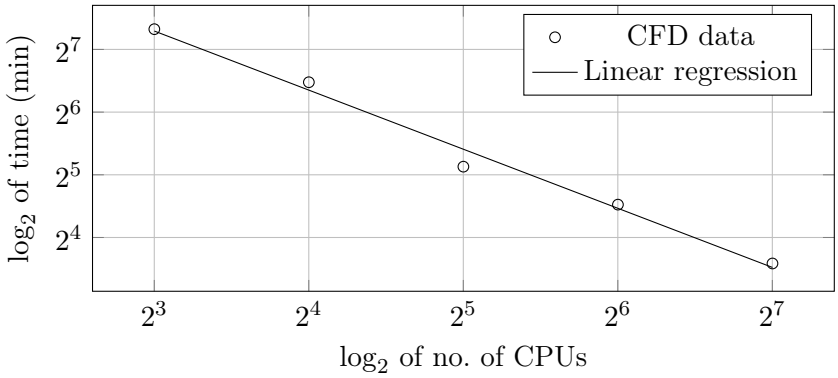

(B) Logarithmic plot.

FIGURE 4.3: CPU time for 2000 steps on 1 800 000 polyhedral cells.

different scales, with data obtained by running a body-vertical configuration with 1 800 000 cells for 2000 iterations on SCoPE.

The Spalart-Allmaras turbulent model has been chosen, since it is fast (it solves a single transport equation that determines the turbulent viscosity) and reliable for external aerodynamics, even at high angles of attack and high lift configurations for certain geometries [76, 79, 91], provided that the mesh is fine enough.

4.3 Test cases

In order to check the compliance of the CFD results with available test data, several test cases have been performed.

4.3.1 NACA TR-540

In the work of Jacobs and Ward [33] 209 wing-fuselage combinations were tested in the NACA variable-density wind tunnel, to provide information about the effects of aerodynamic interference between wings and fuselage at a large value of the Reynolds number (3 100 000). The wing section is a NACA 0012 airfoil. Three of these combinations (respectively mid, high and low wing, marked no. 7, 22, and 67 in Ref. [33]) plus a wing-alone configuration have been chosen for the test case. In short, for each combination, a round fuselage with a rectangular wing has been analyzed at various angles of attack, with no sideslip angle.

The CAD model is shown in Figure 4.4. Configurations are shown in Figure 4.5. The reference system for wing translation in fuselage is shown in Figure 4.6. Mesh data is available in Table 4.2 and a scene is shown in Figure 4.7. Results in terms of the aerodynamic lift, *effective profile drag* and moment coefficient C_L, $C_{D\mathrm{e}}$, and C_M are shown from Figure 4.8 to 4.11. Effective profile drag coefficient has been defined in Equation 2.14 as the difference between the total drag coefficient C_D and the minimum induced drag coefficient C_{Di}, that is

$$C_{D\mathrm{e}} = C_D - \frac{C_L^2}{\pi \mathcal{AR}}$$

and this to account only for parasite drag due to the interference of the wing-body combination.

This was the very first test case performed by the author on his personal computer in 2011. The numerical simulations agreed well with wind tunnel results in the linear range of the angle of attack, but, because of insufficient computational power (at that time), the mesh was not refined enough to capture the stall behavior.

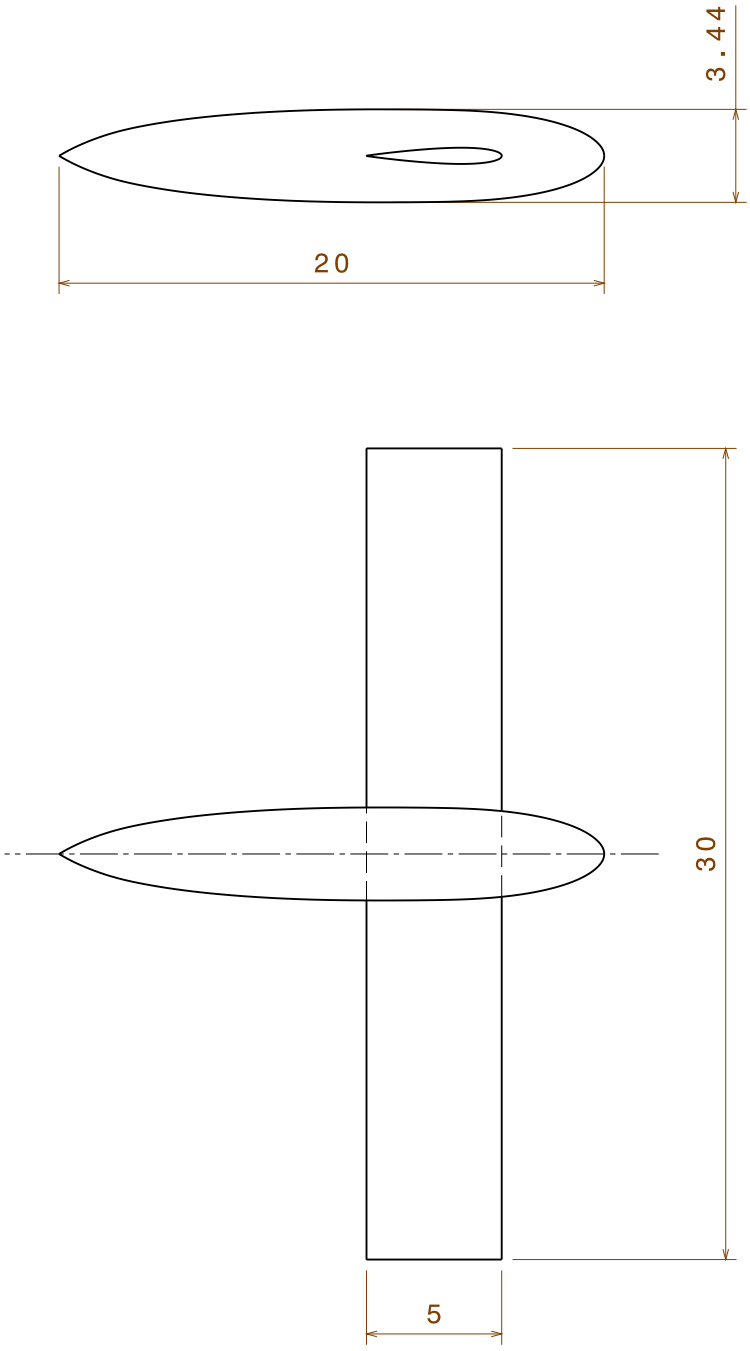

FIGURE 4.4: CAD drafting – NACA TR-540. Dimensions are in inches.

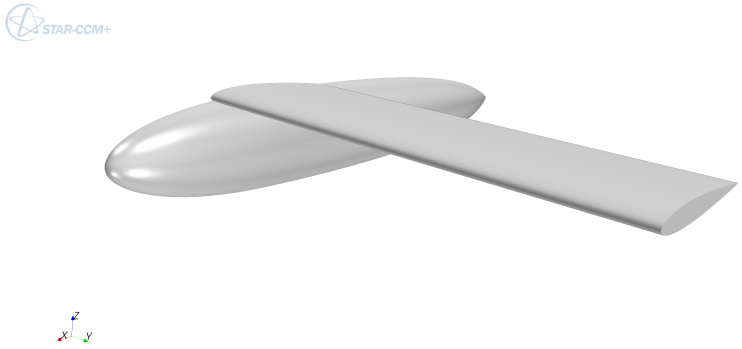

(A) High wing combination.

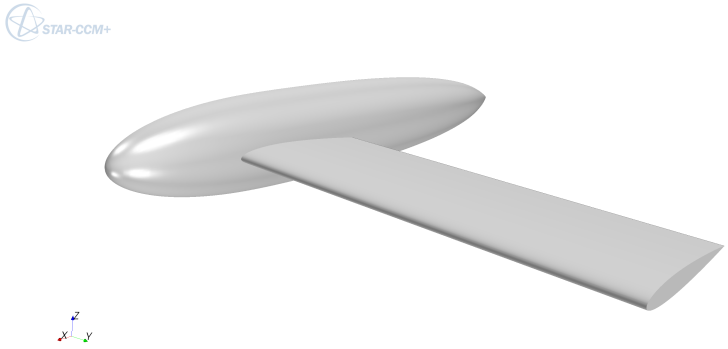

(B) Mid wing combination.

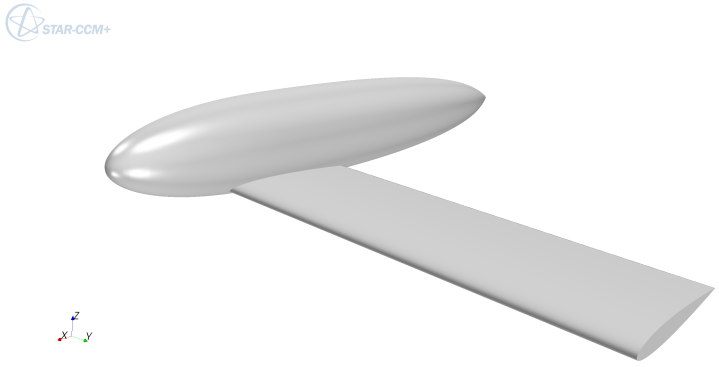

(C) Low wing combination.

FIGURE 4.5: Wing-fuselage CAD models of NACA TR-540.

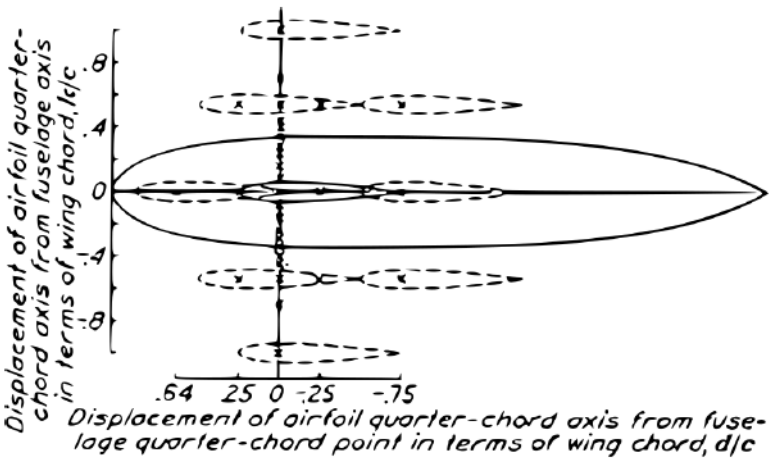

FIGURE 4.6: Model reference system – NACA TR-540. For mid wing combination the quarter chord points of fuselage and wing coincide. Reproduced from Ref. [33].

TABLE 4.2: Mesh and physics data of NACA TR-540 test case.

Mesh type	polyhedral cells		
Base size	50.0 m		
Number of prism layers	20		
Prism layer stretching	1.3		
Numbers of cells	≈ 1 000 000 (wing-body config.)		
Mesh size (in percentage of the base size)			
	Minimum	Target	Prism layer
Wing	0.02	0.2	0.03
Fuselage	0.02	0.2	0.03
Angle of attack α	$-4°$ to $16°$		
Reynolds number Re	3 100 000 (based on wing chord)		
Mach number M	0		
Flow regime	fully turbulent (SA model)		

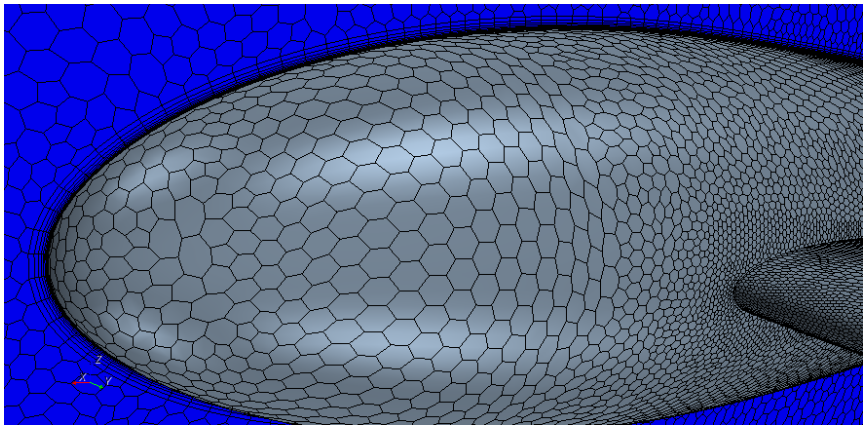

(A) Polyhedral mesh on the semi-model.

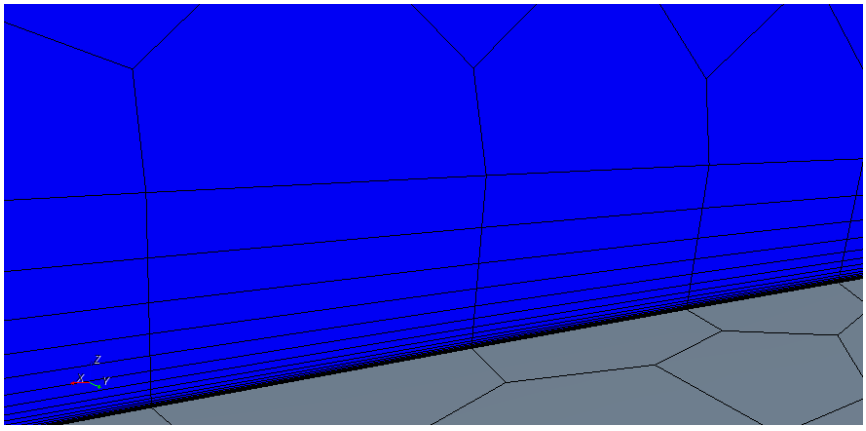

(B) Detail of the prism layer.

FIGURE 4.7: Mesh of the NACA 540 test case.

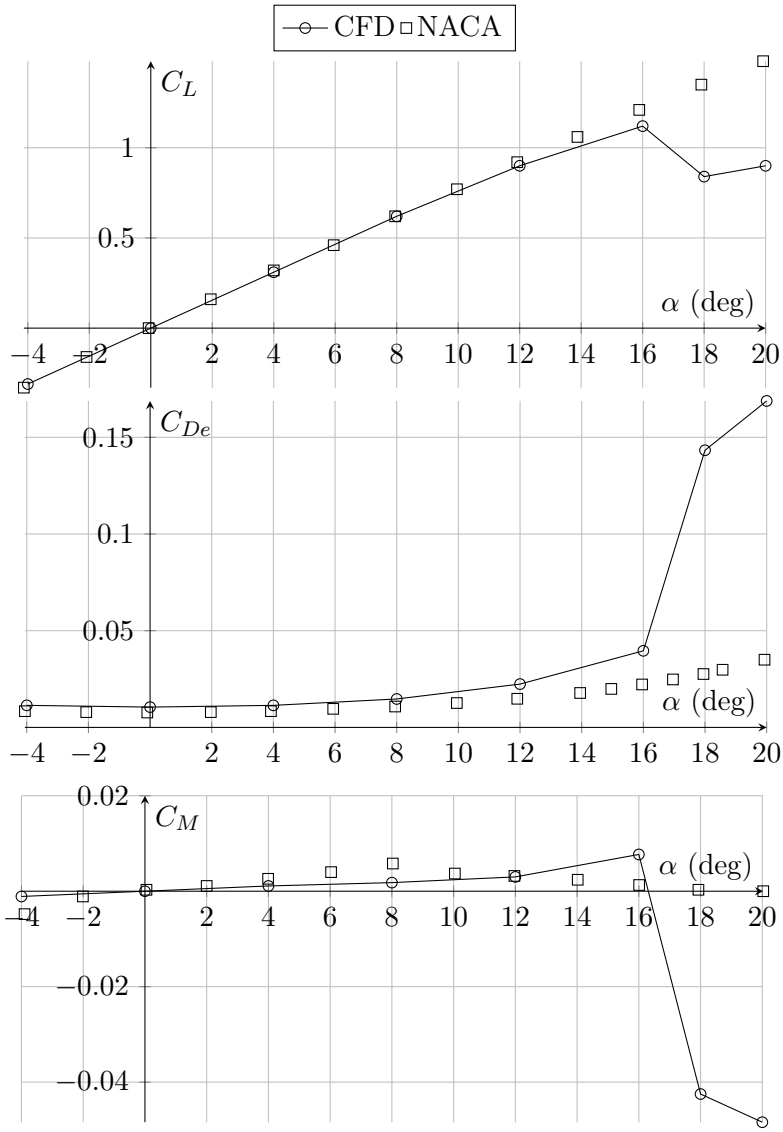

FIGURE 4.8: Results comparison for the wing alone – NACA TR-540.

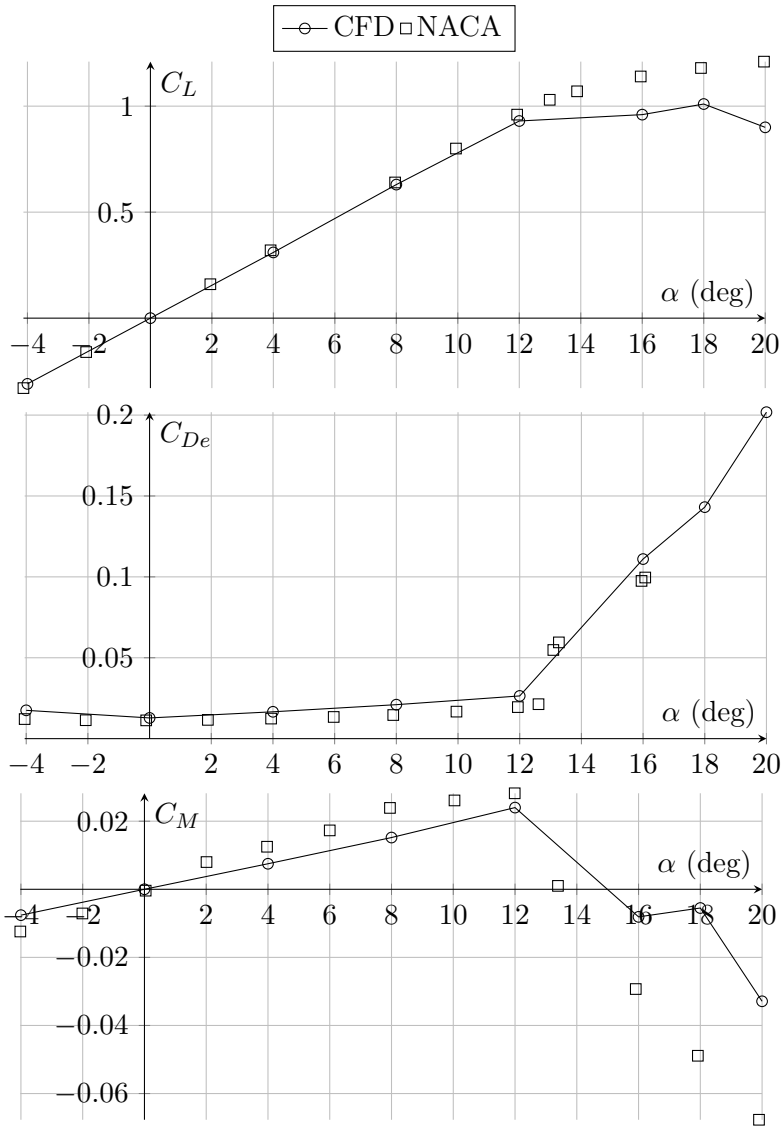

FIGURE 4.9: Results comparison for the mid wing combination – NACA TR-540.

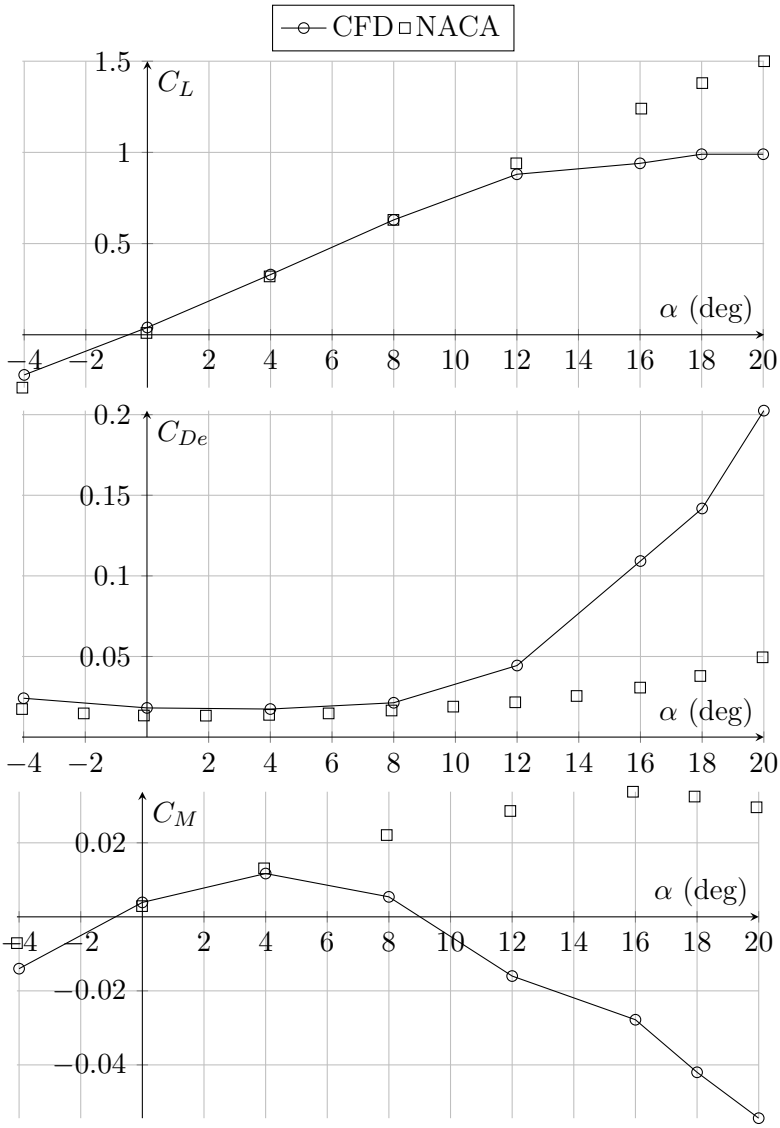

FIGURE 4.10: Results comparison for the high wing combination – NACA TR-540.

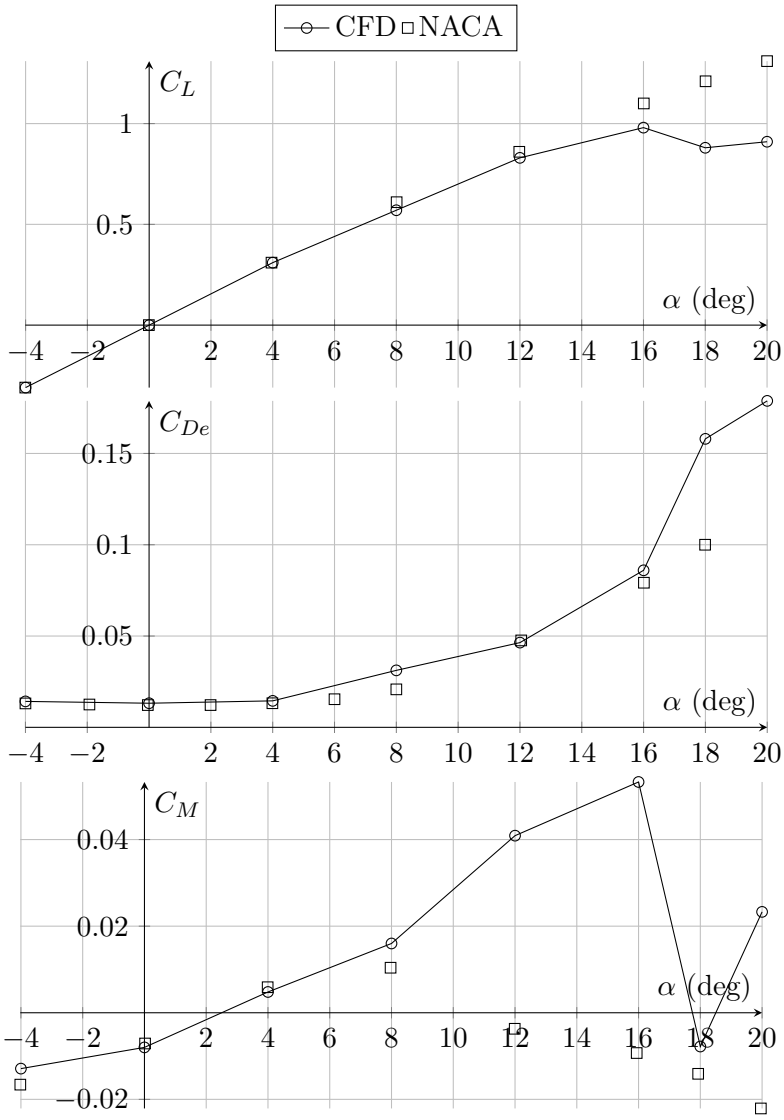

FIGURE 4.11: Results comparison for the low wing combination – NACA TR-540.

4.3.2 NACA TR-730

This is the aforementioned report of Bamber and House [35]. A NACA 23012 rectangular wing with rounded tips has been assembled with an ellipsoid of circular cross-section, representing the fuselage, at several angles of sideslip, in high, mid, and low wing combination (see Figure 4.12 for draft and Figure 4.13 for 3D views). No dihedral angle and no flap device are present on the wing. Each wing-fuselage combination has been simulated with and without vertical tail, which has a NACA 0009 section and a planform area $S_v = 45\,\text{in}$. Reynolds number is 609 000 based on wing chord. Results are evaluated in terms of the rolling moment, yawing moment, and sideforce due to sideslip coefficients, respectively $C_{\mathcal{L}_\beta}$, C_{N_β}, and C_{Y_β}. All derivatives are evaluated per deg and it is assumed linearity between 0° and 5°. Mesh data are reported in Table 4.3, with a scene shown in Figure 4.14.

Results and comparison with test data are reported in Figure 4.15 and 4.16. In Figure 4.15 it is apparent that the effect of the cross flow for the wing-body configurations without vertical tail has the same effect on the C_{Y_β} for the high and low wing combinations and a minimum for that coefficient at mid wing position, because of the double symmetry of the model. The wing-fuselage combination without vertical tail is directionally unstable ($C_{N_\beta} > 0$). Stability is introduced by the vertical tail, see results of Figure 4.16. Directional stability, measured by C_{N_β}, is maximum for the low wing combination, as stated in Section 3.2.3. A comparison between the numerical results with and without vertical tail configurations is shown in Figure 4.17.

For each configuration analyzed, by moving the wing vertically on the fuselage, the rolling moment derivative $C_{\mathcal{L}_\beta}$ changes sign because of the cross flow over the wing-fuselage system, resulting in an antisymmetric distribution of the normal velocities along the span that is equivalent to an antisymmetric angle of attack distribution [45], see Figure 2.32 again.

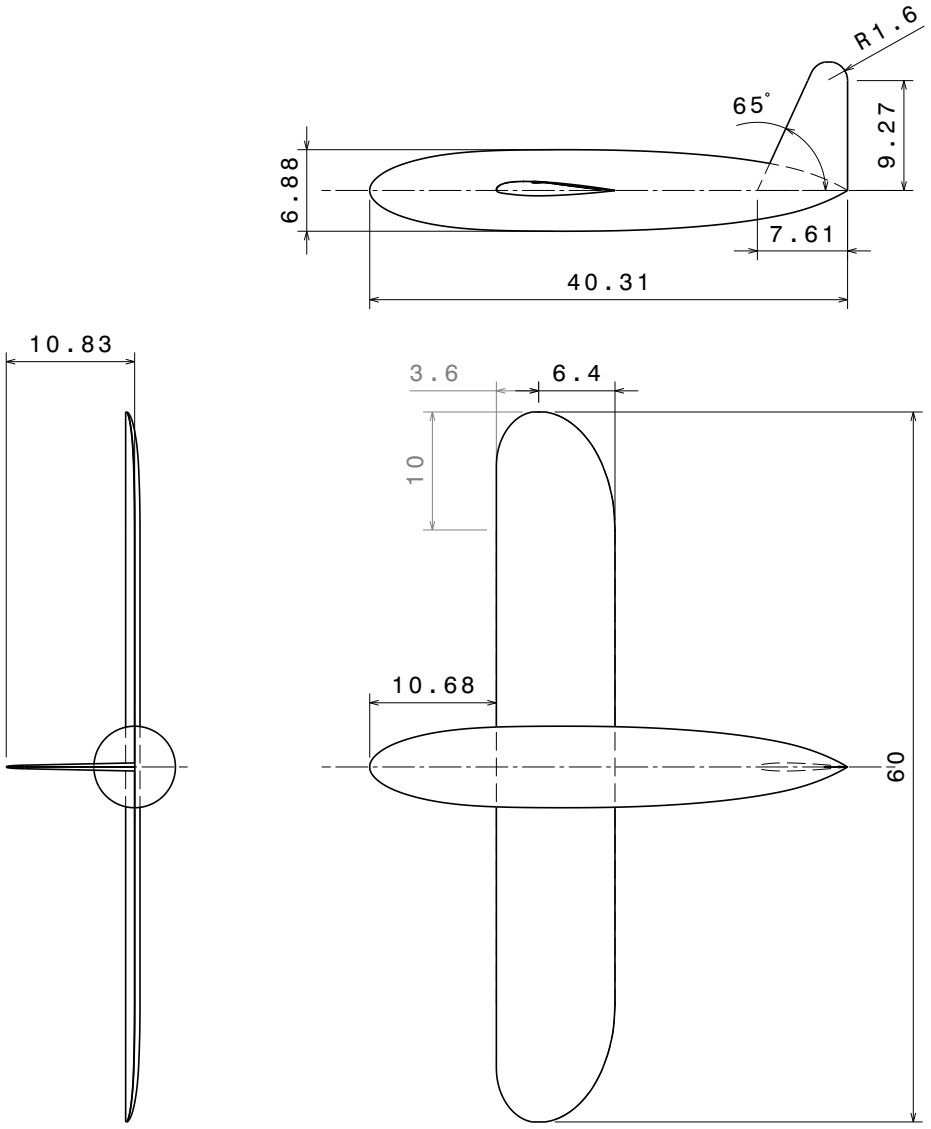

FIGURE 4.12: Draft of the CAD model of NACA TR-730. High wing is translated up by 2.66 in and low wing down by 2.98 in with respect to the mid wing position. Dimensions are in inches. See Figure 2.12 for the original sketch.

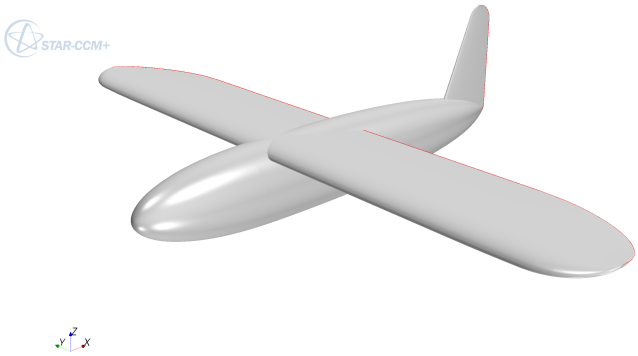

(A) High wing configuration

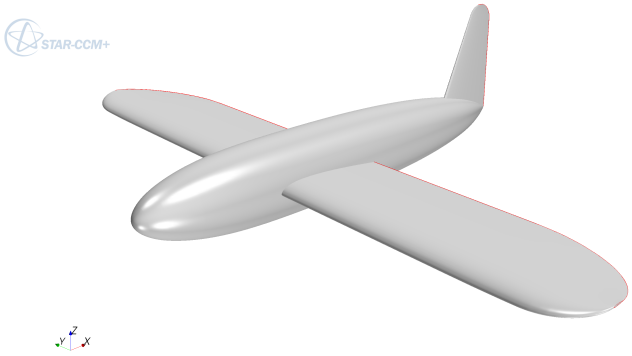

(B) Mid wing configuration

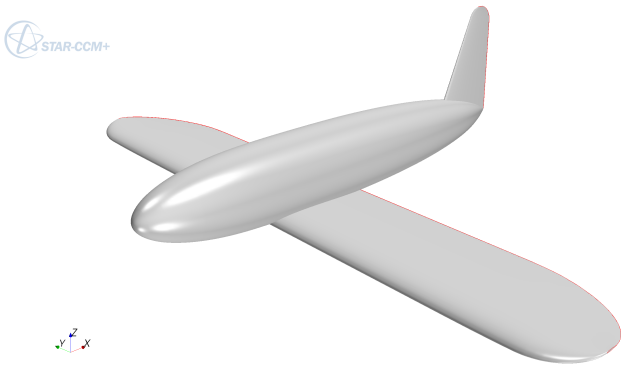

(C) Low wing configuration

FIGURE 4.13: Wing-fuselage-fin CAD models of NACA TR-730.

TABLE 4.3: Mesh and physics data of NACA TR-730 test case.

Mesh type	polyhedral cells		
Base size	1.0 m		
Number of prism layers	20		
Prism layer stretching	1.2		
Numbers of cells	≈ 5 000 000 (wing-body-fin config.)		
Mesh size (in percentage of the base size)			
	Minimum	Target	Prism layer
Wing	0.08	2.0	0.2
Fuselage	0.1	10.0	0.2
Vertical	0.05	0.5	0.1
Angle of attack α	0°		
Angle of sideslip β	5°		
Reynolds number Re	609 000 (based on wing chord)		
Mach number M	0		
Flow regime	fully turbulent (SA model)		

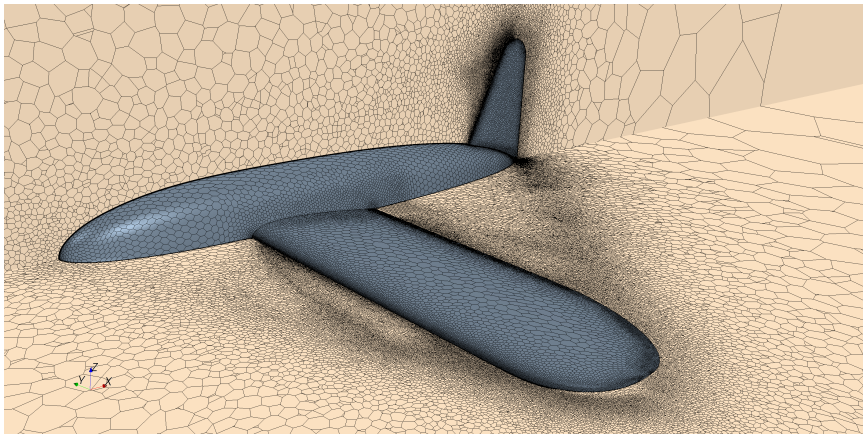

FIGURE 4.14: Mesh of NACA TR-730 test case.

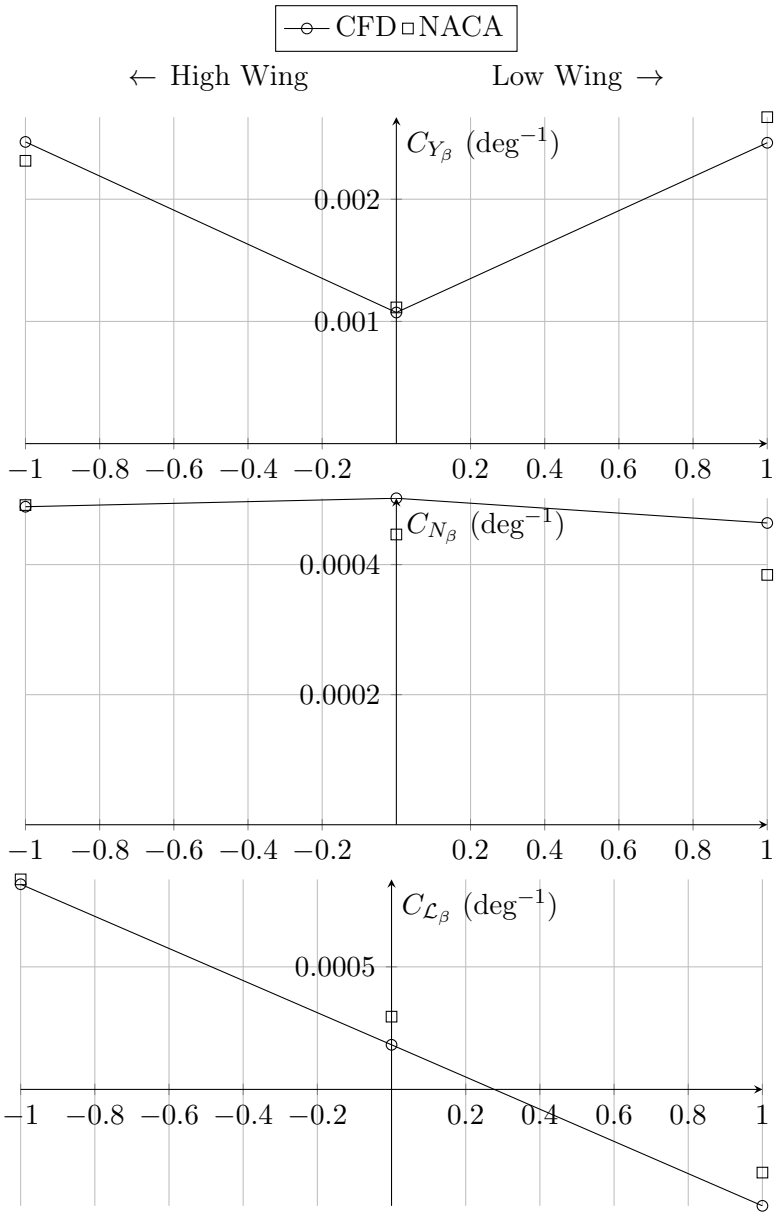

FIGURE 4.15: Results comparison for the wing-body combination, fin-off – NACA TR-730.

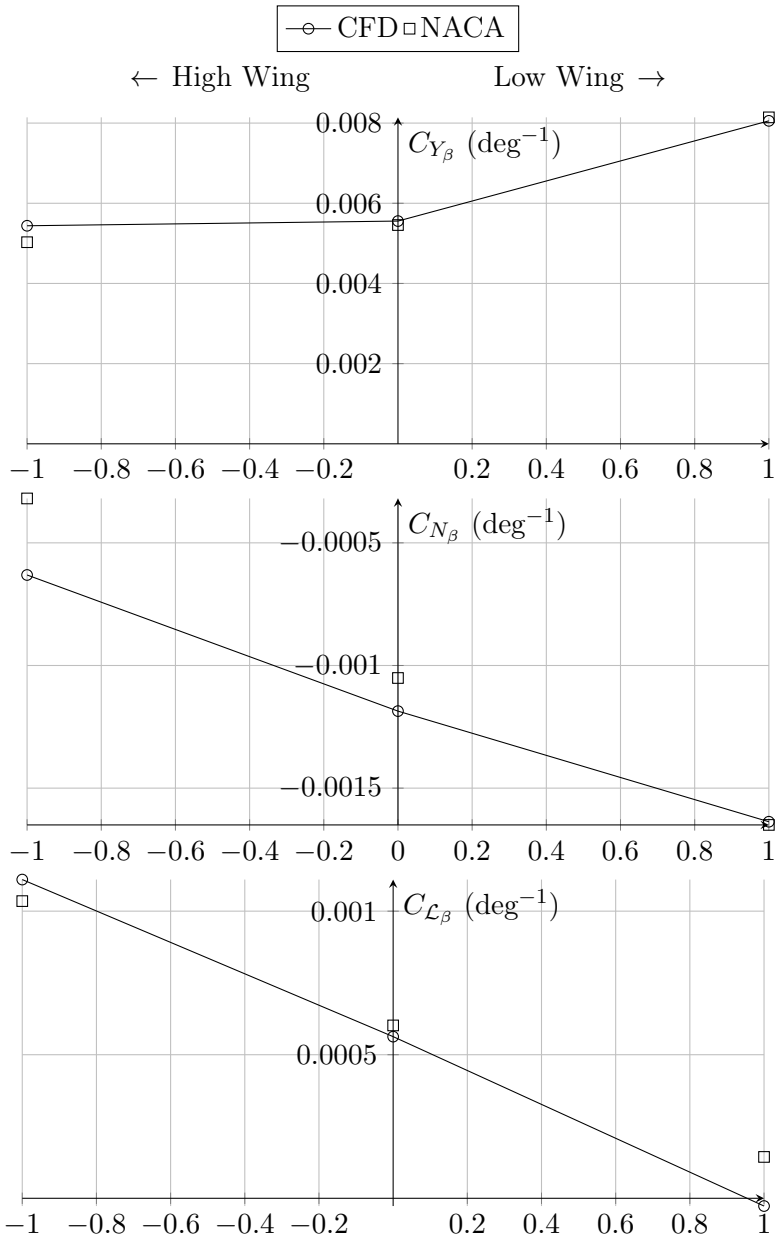

FIGURE 4.16: Results comparison for the wing-body-fin combination, fin-on – NACA TR-730.

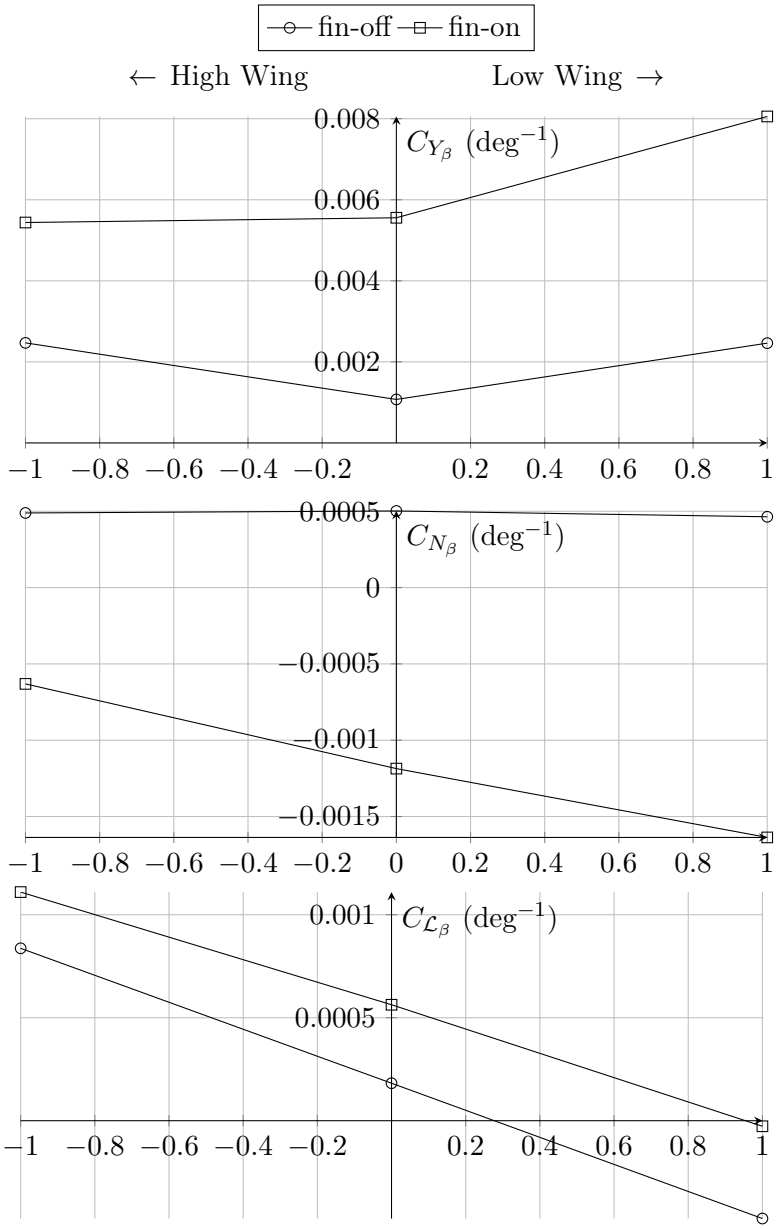

FIGURE 4.17: CFD results comparison between the fin-off and fin-on configurations – NACA TR-730.

TABLE 4.4: Mesh and physics data of NACA TR-1049 test case.

Mesh type	polyhedral		
Base size	10.0 m		
Number of prism layers	20		
Prism layer stretching	1.3		
Numbers of cells	$\approx 4\,000\,000$ (wing-body-fin config.)		
Mesh size (in percentage of the base size)			
	Minimum	Target	Prism layer
Wing	0.05	1.0	0.11
Fuselage	0.01	0.1	0.11
Vertical	0.005	0.1	0.11
Angle of attack α	0°		
Angle of sideslip β	-10° to 10°		
Reynolds number Re	710 000 (based on wing chord)		
Mach number M	0		
Flow regime	fully turbulent (SA model)		

4.3.3 NACA TR-1049

The aim of the work of Queijo and Wolhart [36] was to investigate the effects of vertical tail size and span and of fuselage shape and length on the static lateral stability characteristics of a model with 45° swept back (quarter chord line) wing and vertical tail, NACA 65A008 airfoil. As stated in Section 2.1.2, this report found an interesting relation between the effective aspect ratio of the vertical tail and the fuselage thickness where the tail is located (see again Figure 2.15). This was resumed by the USAF DATCOM method, as seen in Section 3.2.1 in Figure 3.7. The original draft has been shown in Figure 2.16. See Figure 4.18 for details on the CAD model. The mesh data are reported in Table 4.4, with a scene shown in Figure 4.19. Wall y^+ distribution is illustrated in Figure 4.20. Results are shown from Figure 4.21 to 4.23 in terms of sideforce, yawing moment, and rolling moment coefficients.

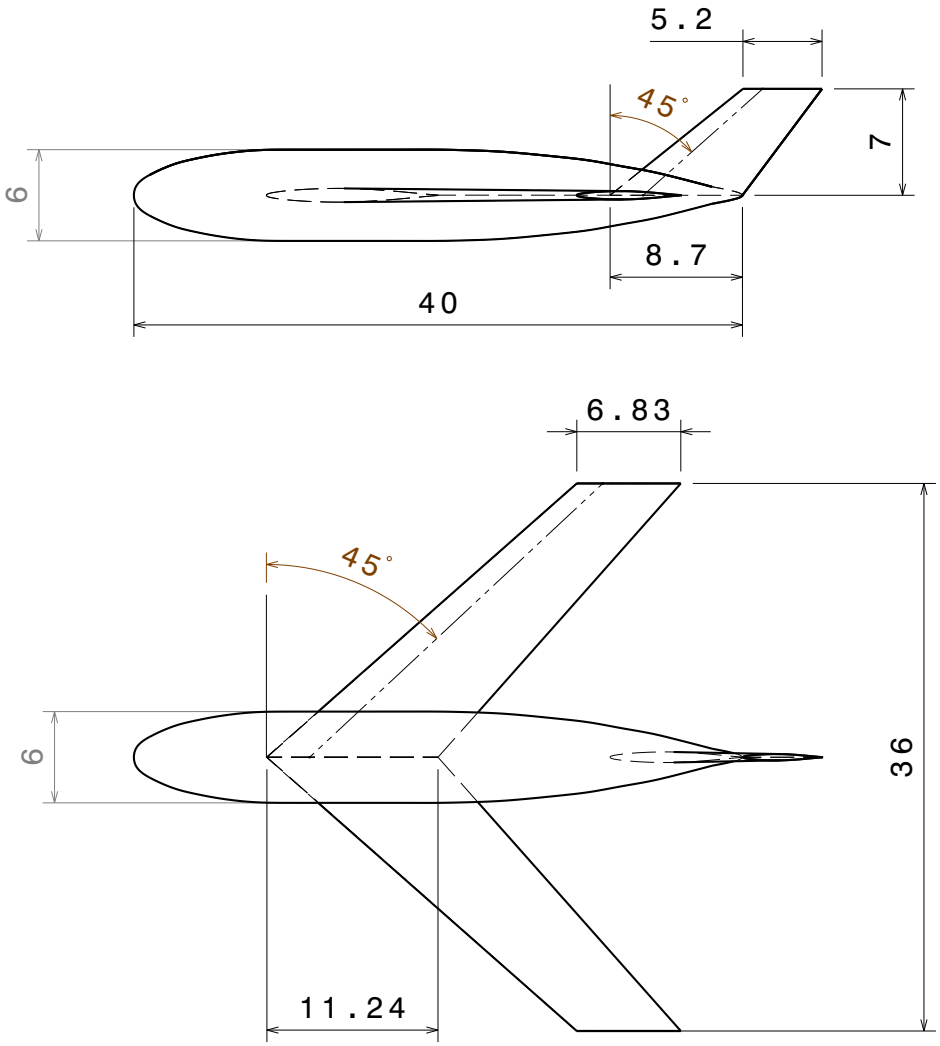

FIGURE 4.18: Draft of the CAD model of NACA TR-1049. Dimensions are in inches. See Figure 2.16 for the original sketch.

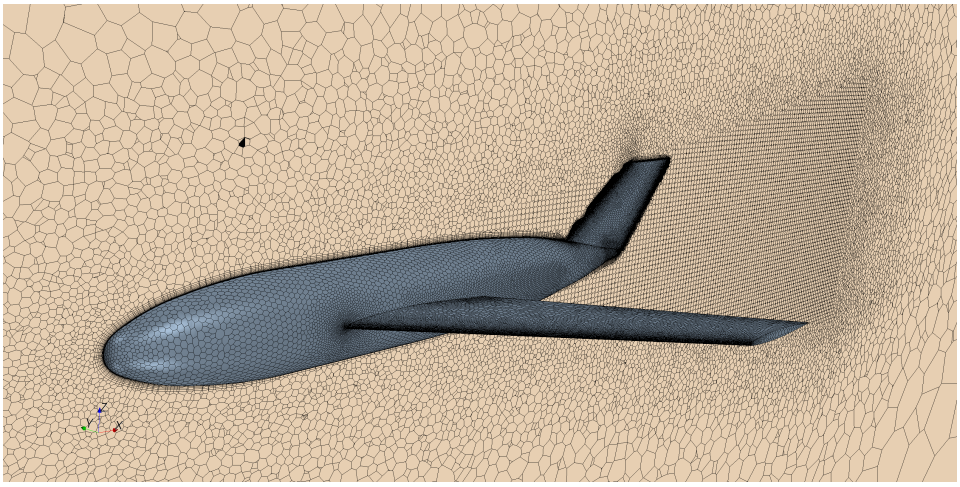

FIGURE 4.19: Mesh of NACA TR-1049 test case.

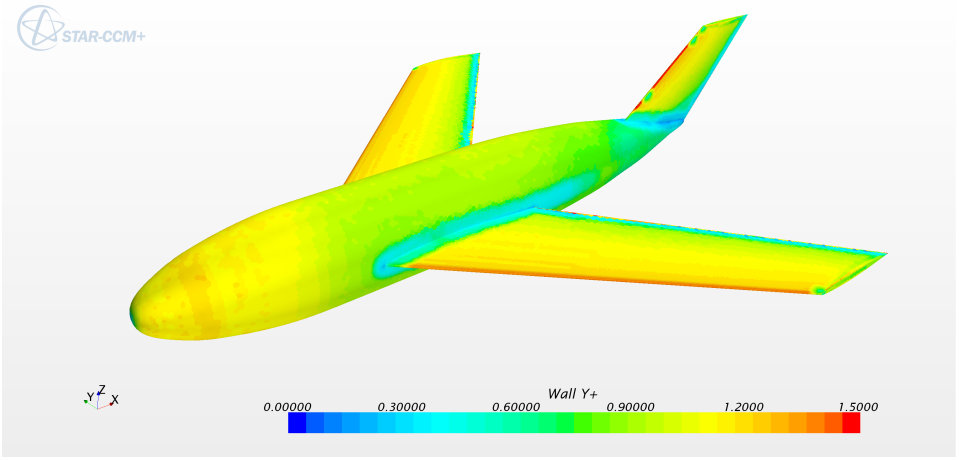

FIGURE 4.20: Wall y^+ contour of NACA TR-1049 test case.

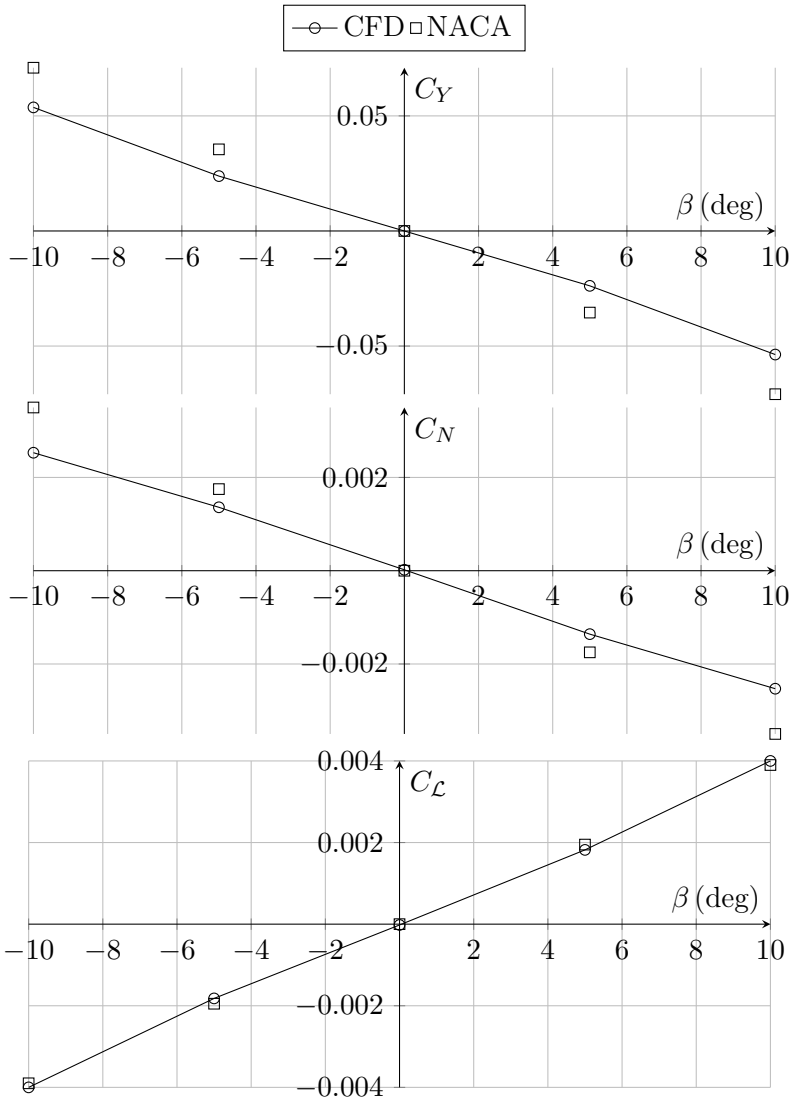

FIGURE 4.21: Results comparison for the fuselage-vertical combination – NACA TR-1049.

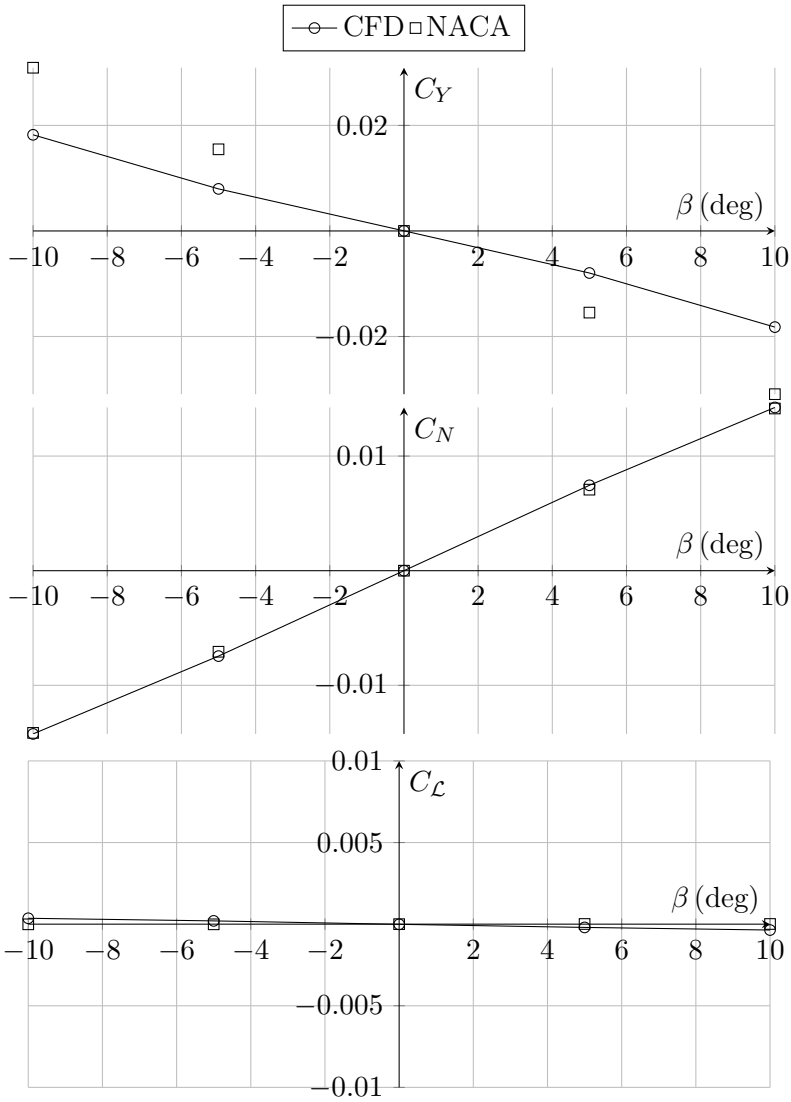

FIGURE 4.22: Results comparison for the fuselage-wing combination – NACA TR-1049.

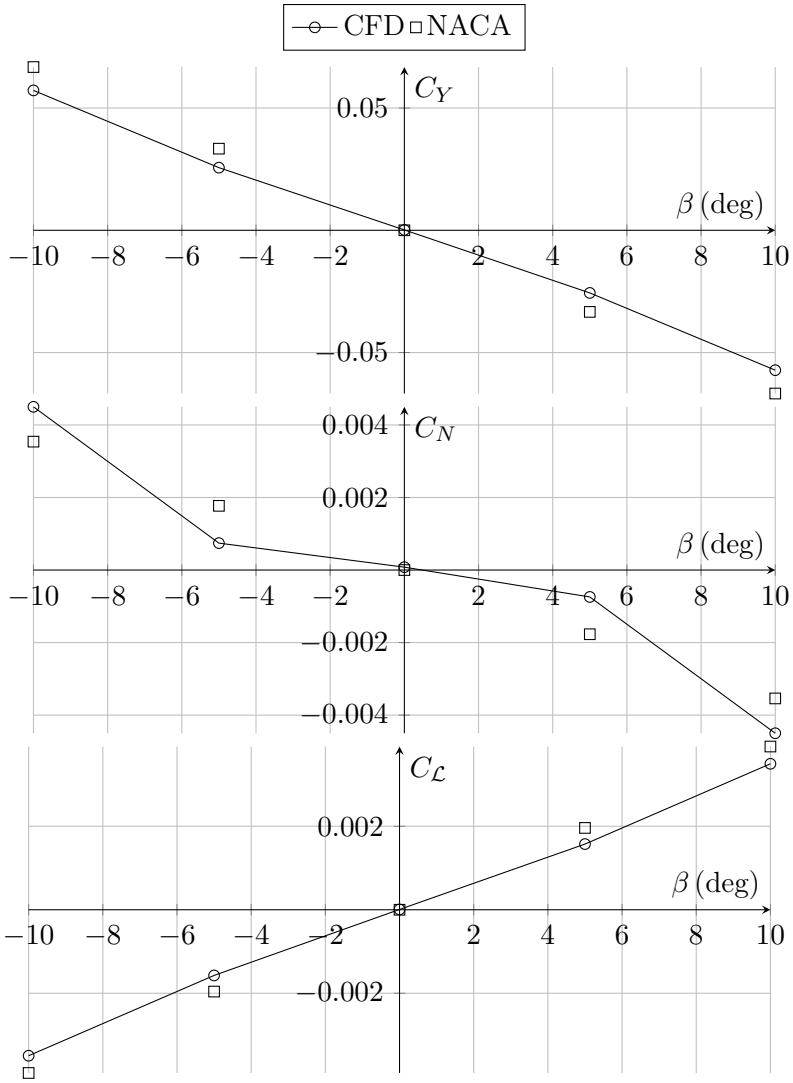

FIGURE 4.23: Results comparison for the fuselage-wing-vertical combination – NACA TR-1049.

Table 4.5: Main dimensions of the DLR-F11 model [75].

Parameter	Symbol	Value
Half span	$b/2$	1.4 m
Wing reference area	$S/2$	0.419 m^2
Reference chord	c_{ref}	0.347 m
Aspect ratio	$\mathit{Æ}$	9.353
Taper ratio	$\lambda_{1/4}$	0.3
chord sweep	$\Lambda_{1/4}$	30°
Fuselage length	L_f	3.077 m
Mass reference centre	C.G.	{1428.90, 0.00, –41.61}

4.3.4 DLR-F11 high lift configuration

This is the model used in the second HiLiftPW test case [79]. It is representative of a wide-body air transport jet. It consists of a $\Lambda = 30°$ sweepback wing with high lift devices (single flap and slat). The wing aspect ratio $\mathit{Æ}$ is 9.4 with a taper ratio λ of 0.3. A typical transport jet aircraft fuselage body with a pod fairing has been mounted. The main dimensions of the model are summarized in Table 4.5. The high lift system consists of a leading edge slat and a trailing edge fowler flap. The slat is continuously extending up to the wing tip. The fowler flap consists of three parts. The first one extends up to the wing kink, and the second one up to 71 % half span. The third element extends up to the wing tip. In this work the high lift system has been set in landing condition, with the slat deflected by 26.5° and the flap deflected by 32°.

The experimental data have been gathered in the low speed wind tunnel of Airbus-Deutschland (B-LSWT) in Bremen, Germany, by Rudnik, Huber, and Melber-Wilkending [75], as well as in the European Transonic Wind tunnel (ETW) in Cologne, Germany, as part of the EUROLIFT project [92]. In this work, only the EUROLIFT experimental data that are representative of the real flight conditions (high Reynolds number) have been considered. The wind tunnel and airflow characteristics are summarized in Table 4.6.

Details on the numerical simulations are discussed in Ref. [79]. Some pictures of the mesh are shown from Figure 4.24 to 4.27. Results are reported in Figure 4.28 and 4.29. The experimental data have been compared with CFD results of three different conditions: eulerian incompressible, viscous

TABLE 4.6: ETW flow conditions for the test with the DLR-F11 model in landing configuration [75].

Parameter	Symbol	Value
ETW run no.	—	238
Mach number (avg.)	M	0.176
Reynolds number (avg.)	Re	15 100 000
Total pressure (avg.)	P_{tot}	295 000 Pa
Total temperature (avg.)	T_{tot}	114.0 K
Angle of attack range	α	$-3.20°$ to $24.24°$

incompressible, and viscous compressible, with an increasing mesh complexity. As it can be seen in the figures, the inviscid analysis does not predict well the aerodynamic coefficients, in particular it overestimates the lift and pitching moment coefficients. Viscous incompressible and refined viscous compressible analyses well predict the lift and pitching moment coefficients, whereas they overestimate the drag coefficient as the angle of attack increases. The lift curve slope is well estimated from all the numerical simulations. Maximum lift coefficient and stall behavior are better predicted from the viscous analyses. The inviscid analysis reaches a mild stall at about $\alpha = 24°$. Both viscous analyses well identify the stall angle of attack at about $\alpha = 21°$. The maximum lift coefficient is slightly underestimated by about 5 %, thus it could be argued that a refined mesh on the leading and trailing edges and boundary layer thickness could improve the numerical solution.

Stall path and post stall lift coefficients can be explained by looking at Figure 4.30. At angles of attack up to 18° the flow results attached on the lifting surfaces. When maximum lift coefficient is reached ($\alpha = 21°$), two incipient flow separation zones can be seen on the wing root and at the tip (skin friction coefficient goes to zero). These zones grow in the post stall with an abrupt separation around $\alpha = 23°$. It is clear how CFD may help a designer to predict the stall of a realistic aircraft configuration and take care of it before the wind tunnel tests.

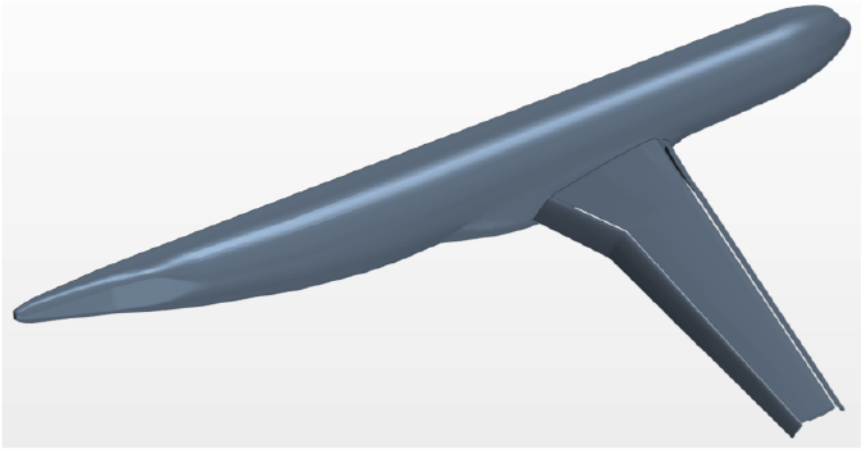

FIGURE 4.24: DLR-F11 CAD model for numerical simulation, wing, body, flap and slat. No brackets.

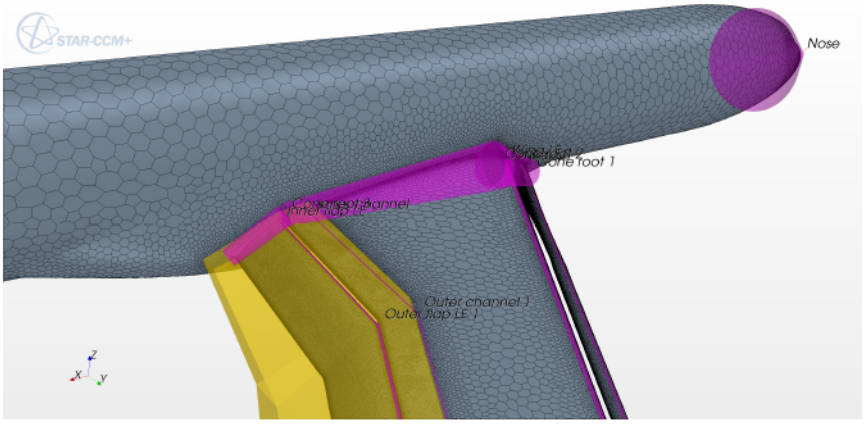

FIGURE 4.25: Mesh on the DLR-F11 model, with details of zone refinements.

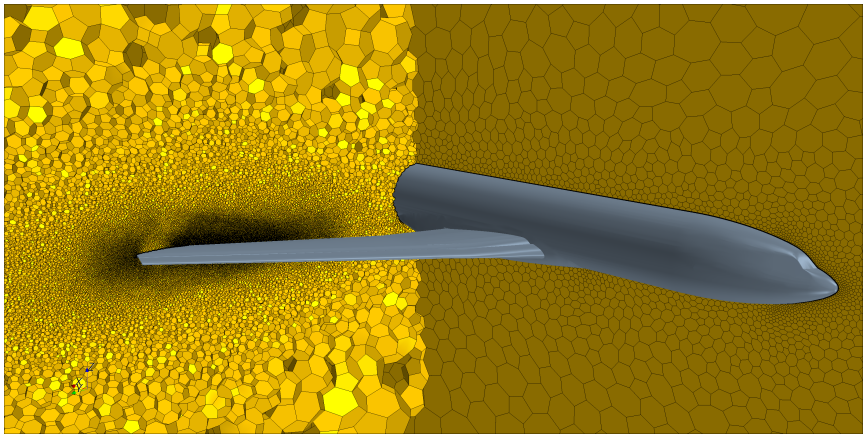

FIGURE 4.26: Volume mesh around the DLR-F11 model.

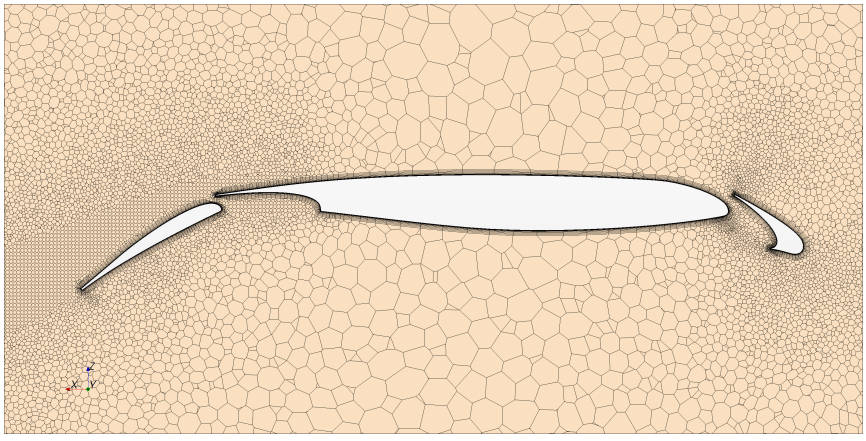

FIGURE 4.27: Volume mesh around a wing section of the DLR-F11 model.

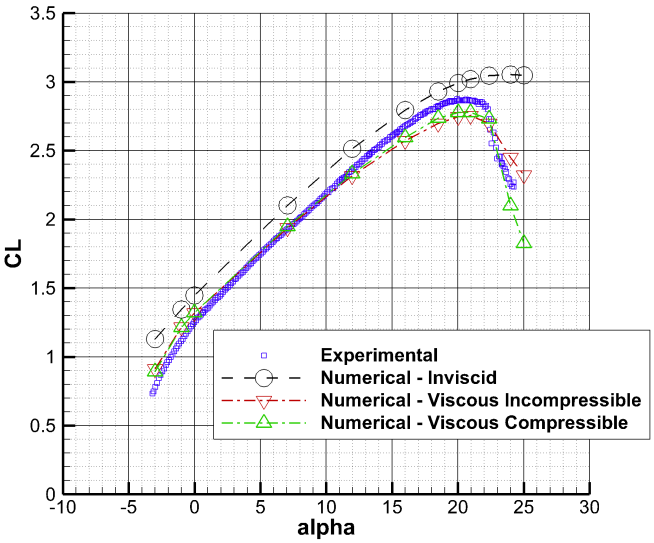

(A) Lift curves at $Re = 15.1 \times 10^6$ and $M = 0.176$.

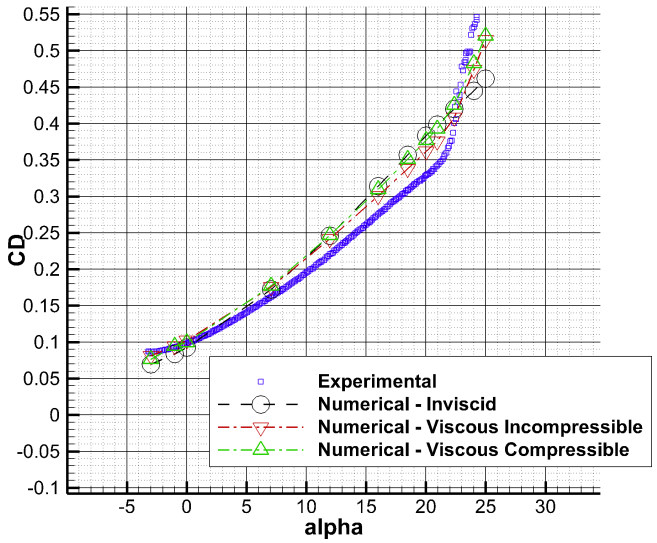

(B) Drag curves at $Re = 15.1 \times 10^6$ and $M = 0.176$.

FIGURE 4.28: DLR-F11 CFD lift and drag curves [79].

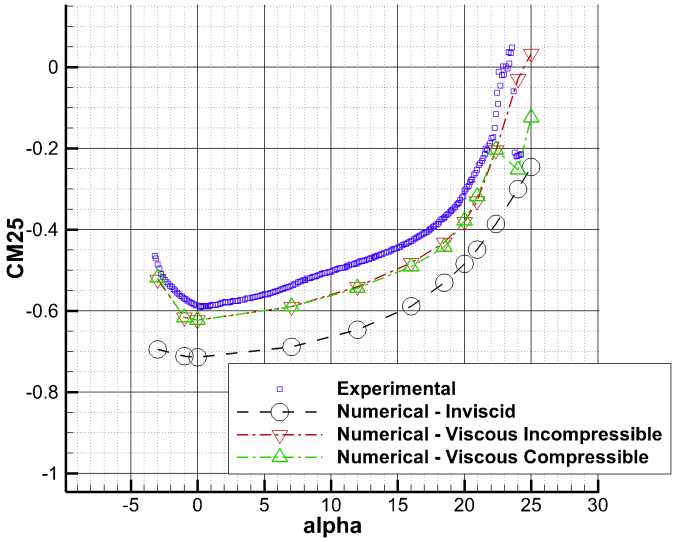

(A) Moment curves at $Re = 15.1 \times 10^6$ and $M = 0.176$.

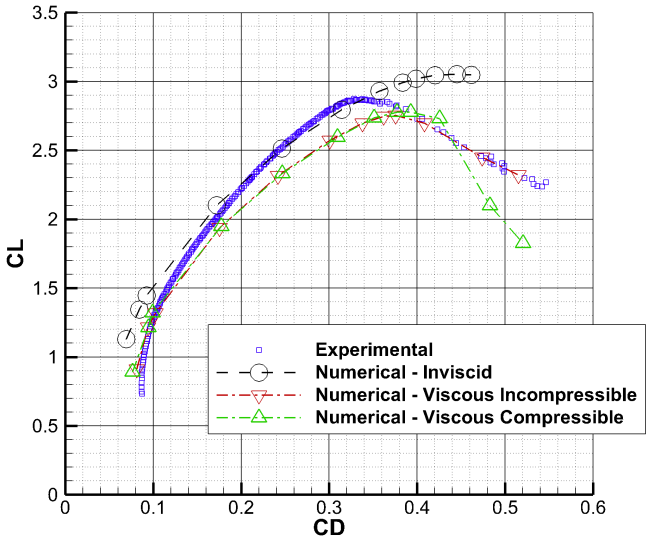

(B) Drag polar curves at $Re = 15.1 \times 10^6$ and $M = 0.176$.

FIGURE 4.29: DLR-F11 CFD pitching moment and drag polar curves [79].

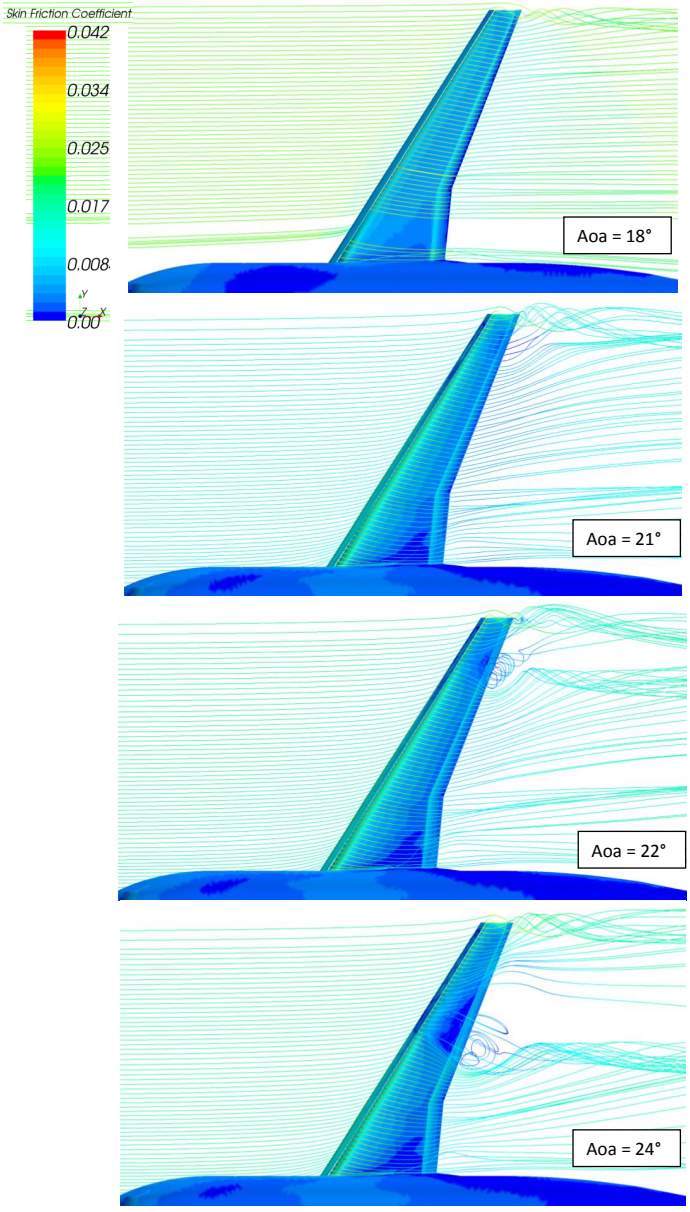

FIGURE 4.30: DLR-F11 CFD stall path [79].

4.3.5 Tecnam P2012 Traveller

The Tecnam P2012 Traveller is a new high-winged, twin piston-engined multi-role aircraft currently being developed by Costruzioni Aeronautiche Tecnam[1], which is based in Capua, Italy (near Naples). The CAD model of the aircraft is shown in Figure 4.31. Its design, numerical and experimental investigations have been deeply described by Corcione [93]. Comparisons between CFD and wind tunnel results at $Re = 600\,000$ are reported from Figure 4.32 to 4.35.

The matching between numerical and experimental data in terms of lift coefficient C_L (Figure 4.32) is very remarkable. The shift in ΔC_{L_0} of the curves at several flap deflection is due to uncertainty in the flap deflection angles measured in the wind tunnel.

It is clear that the CFD approach underestimated the aircraft drag coefficient C_D (Figure 4.33). It is here noted that experimental scale model has several gaps, i.e. control surfaces and high lift devices, flaps braces, and many excrescences that are not present in the numerical model. Moreover, the experimental tests have been conducted by applying transitional strips on all aircraft components in order to avoid laminar separation bubbles (see Chapter 6 for details on wind tunnel testing).

Differences in longitudinal stability can be appreciated in terms of a shift in the pitching moment C_M curves (Figure 4.34) due to discrepancies between the CAD geometry and the tested scale model. However, the slopes of the curves are rather close.

Directional stability and control results are compared in Figure 4.35. The C_N curves agree very well with wind tunnel data, even at very high angles of sideslip.

[1] `http://www.tecnam.com`

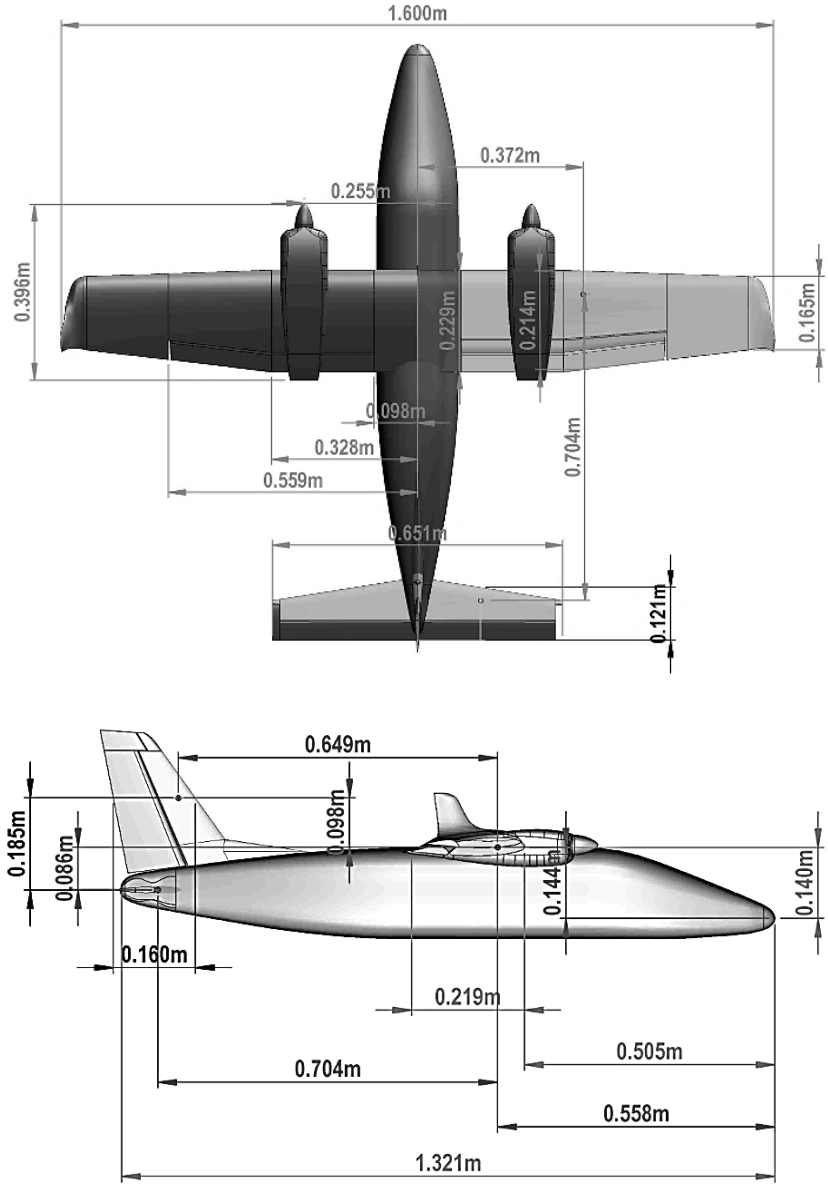

FIGURE 4.31: Tecnam P2012 CAD model. Image courtesy of Corcione [93].

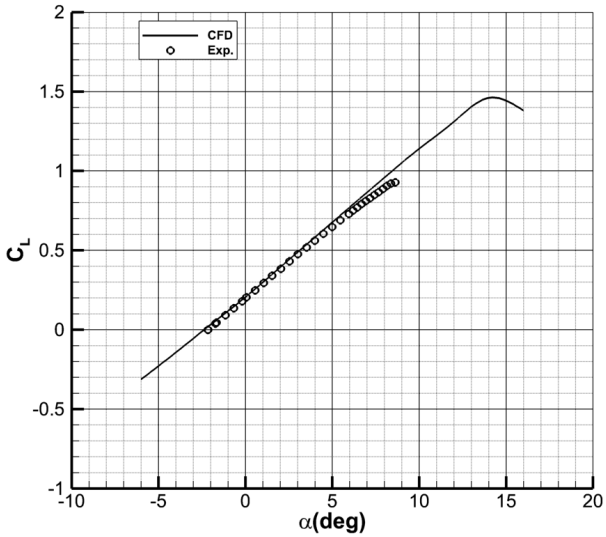

FIGURE 4.32: Tecnam P2012 lift coefficient curve at $Re = 600\,000$. Image courtesy of Corcione [93].

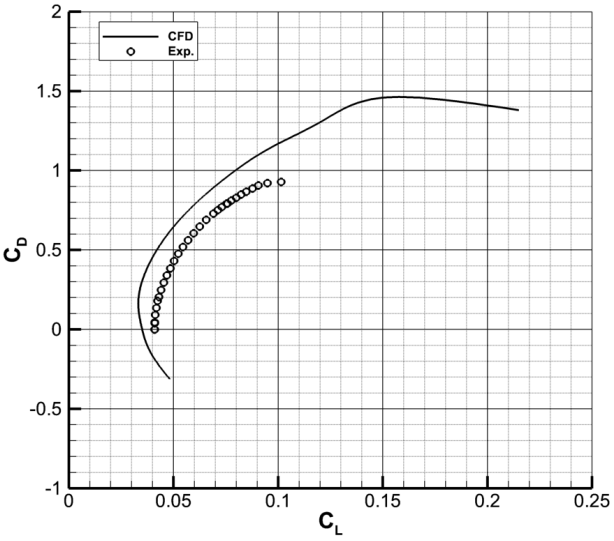

FIGURE 4.33: Tecnam P2012 drag polar curve at $Re = 600\,000$. Image courtesy of Corcione [93].

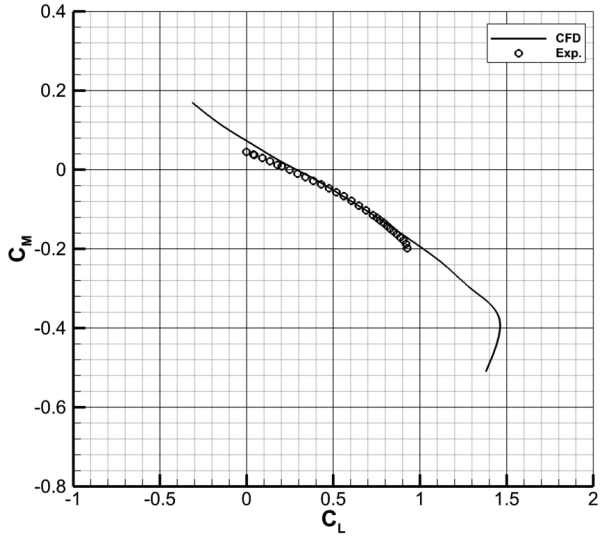

FIGURE 4.34: Tecnam P2012 pitching moment coefficient curve at $Re = 600\,000$. Image courtesy of Corcione [93].

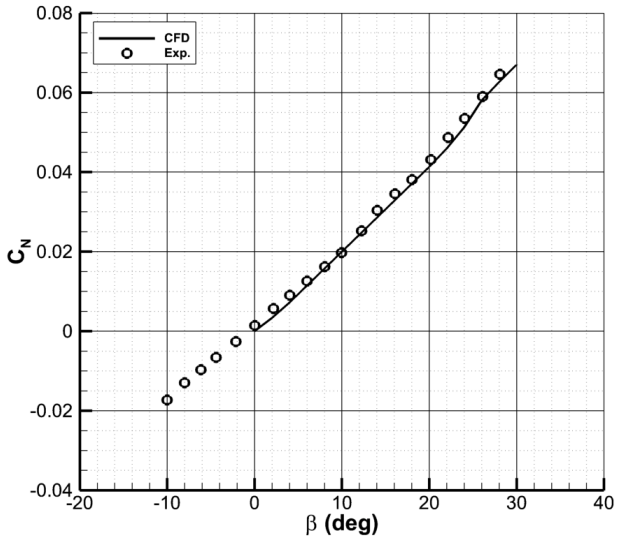

FIGURE 4.35: Tecnam P2012 yawing moment coefficient curve at $Re = 600\,000$. Image courtesy of Corcione [93].

4.3.6 Lessons learned

After several test cases, it is apparent that prediction of drag and high lift is still challenging. Drag is difficult to predict because of inevitable geometric and physic differences between what is tested in the wind tunnel and what is simulated at the computer. It has been stated that a numerical model does not provide, at least in a feasible way at time of writing, all the excrescences, roughness, and gaps of the experimental model. Moreover, the physic modeling of the flow is deeply involved. Even at the same Reynolds number, prediction of the drag coefficient at low angles of attack may be difficult. The situation worsens at high angles of attack, where flow separation and unsteadiness is not negligible.

The flow field around a wing with deployed high lift devices at high incidences is characterized by the co-existence of flow phenomena such as large pressure induced separation, compressibility effects, and strong wake/boundary layer interaction. In addition, for a realistic configuration, there are some critical areas with respect to the flow topology like the wing/fuselage junction or the engine/pylon/wing intersection, which have a strong influence on the overall aerodynamic performance [94].

As a matter of fact, it is not always sufficient to increase the number of cells to improve the accuracy of the numerical solution. Several simulations have shown that critical areas of the computational domain are the leading edges and the prism layer distribution used to capture the boundary layer. Although this is quite obvious, it is not trivial to achieve an accurate discretization of the geometry while maintaining a tolerable number of cells. Most of the difficulties may be due to the complexity of the CAD model. The mesh generation from the surface triangles could result in poor geometry representation on bodies with narrow curvatures, as flaps and wing-tips.

A blunt leading edge can lead to an underestimation of the lift coefficient because of early flow separation. Anomalies on the cells on the walls can prevent the extrusion of the prism layer, leading to an incorrect evaluation of the viscous effects, which can increase the residuals up to the divergence. The prism layer, used to get the boundary layer, is responsible of both accuracy and convergence of the simulation. A coarse distribution (few, thick cells) of this prismatic grid usually guarantees the success of the simulation at the expense of the accuracy. Conversely, numerous, thin cells, whose thickness should be related to the Reynolds number, can provide a more accurate solution, but only if the ratio between adjacent cells, the aspect ratio between

the thickness and the width of cells, and, eventually, the aspect ratio between the thickness of the whole prism layer and the width of the first core cell are reasonable (order of magnitude one). The bigger are these ratios, the bigger is the possibility of divergence in the very first iterations.

The intersection between the lifting surfaces and the fuselage is critical too. Surface triangles with very different edges length could be another issue for boundary layer capturing and solution quality. This situation usually can be avoided by increasing the number of cells in the intersection zones between bodies. The same can be stated for trailing edges and wingtips: these must be well refined, if aerodynamic drag and flow separation have to be investigated.

This concludes the test case section. The limitations of comparing CFD and wind tunnel results resumed in Table 4.1 are apparent. Confidence in the CFD as a tool for aircraft design has strongly established.

Chapter 5

The VEDSC method

Synopsis

✈ The new approach is presented

✈ The numerical model setup is described

✈ The contribution of each airplane part is evaluated

✈ A guided procedure to apply the new method is illustrated

✈ Results of the application are encouraging

In this chapter, the development of the numerical database about regional turboprop aircraft directional stability characteristics is discussed. From the gathered data, a new preliminary design method has been developed. This is named *Vertical tail Design, Stability, and Control* (VEDSC).

5.1 Geometry, mesh, and physics description

The model geometry has the typical regional turboprop layout. Several wing positions, wing aspect ratios, vertical tailplane planforms, horizontal tailplane positions, and three fuselages have been arranged in many different combinations (Figure 5.1) to allow for a parametric investigation.

The wing is straight and untapered with an aspect ratio $\mathcal{AR}$ varying from 6 to 14. The fuselage is a narrow body with a circular section and with three different after-bodies (tail-cones). The horizontal stabilizer is straight and untapered, with a fixed aspect ratio ($A_h = 4.5$). Three different vertical tailplane planforms have been considered in the first analyses to highlight possible variations in aerodynamic interference due to planform. Vertical

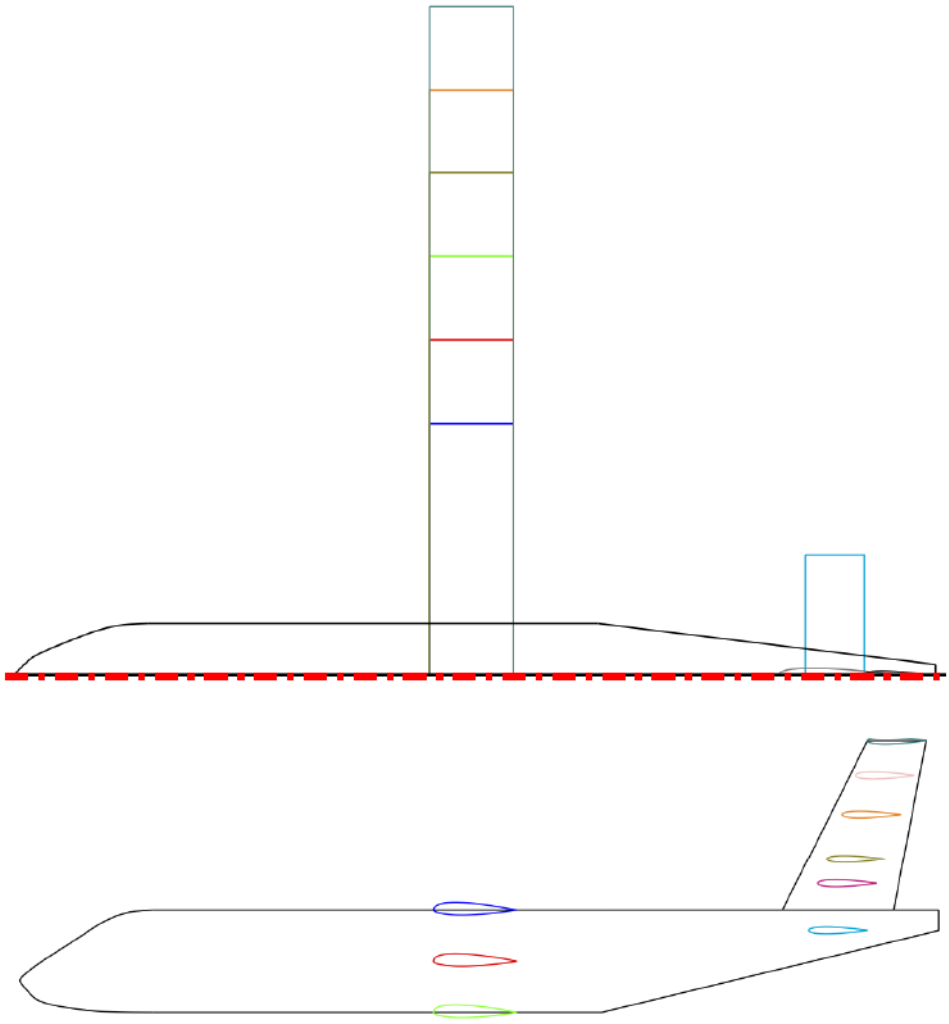

FIGURE 5.1: The layout of the model used for numerical analyses.

TABLE 5.1: Geometric data of the numerical model.

Parameter	Symbol	Values
Vertical tail aspect ratio	A_v	0.25 to 2.5
Vertical tail taper ratio	λ_v	0.3 to 1.0
Vertical tail sweep angle	Λ_v	0° to 60°
Wing aspect ratio	$\mathcal{AR}$	6 to 16
Wing position	z_w/r_f	−1 to 1
Horizontal tail position	z_h/b_{v1}	0 to 1
Fuselage tail-cone ratio	z_{ftc}/r_f	0 to 1
Fuselage slenderness ratio	L_f/D_f	7 to 12
Fuselage nose slenderness ratio	L_n/D_f	1.1 to 1.7
Fuselage tail-cone slenderness ratio	L_n/D_f	2.3 to 3.0

TABLE 5.2: Number of configurations in the numerical analyses.

Conf.	No. of sims	Changing parameters
F	3	z_{ftc}/r_f
V	18	A_v ; λ_v ; Λ_v
FV	30	A_v ; λ_v ; Λ_v ; z_{ftc}/r_f
WFV	45	A_v ; λ_v ; z_{ftc}/r_f ; $\mathcal{AR}$; z_w/r_f
WFVH	115	A_v ; λ_v ; z_{ftc}/r_f ; z_w/r_f ; z_h/b_{v1} ; S_h/S_v

tailplane aspect ratio A_v is varied from 0.4 to 4, sweep angle Λ_v from 0° to 60°, and taper ratio λ_v from 0.3 to 1. These parameters are summarized in Table 5.1. The number of the simulations for each configuration is reported in Table 5.2. More than 200 simulations have been performed to realize a database about regional turboprop directional stability.

The geometries have been kept simple to automate the mesh generation process and to realize a modular model to test in the wind tunnel. A bigger emphasis has been given to the vertical tailplane and the fuselage, since these are the most important components in aircraft directional stability. The analyses [27, 84, 85] have shown that wing and horizontal stabilizer do not directly affect directional stability, but rather influence the vertical tailplane and fuselage contributions in sideslip.

The computational domain is made up of polyhedral cells, which number

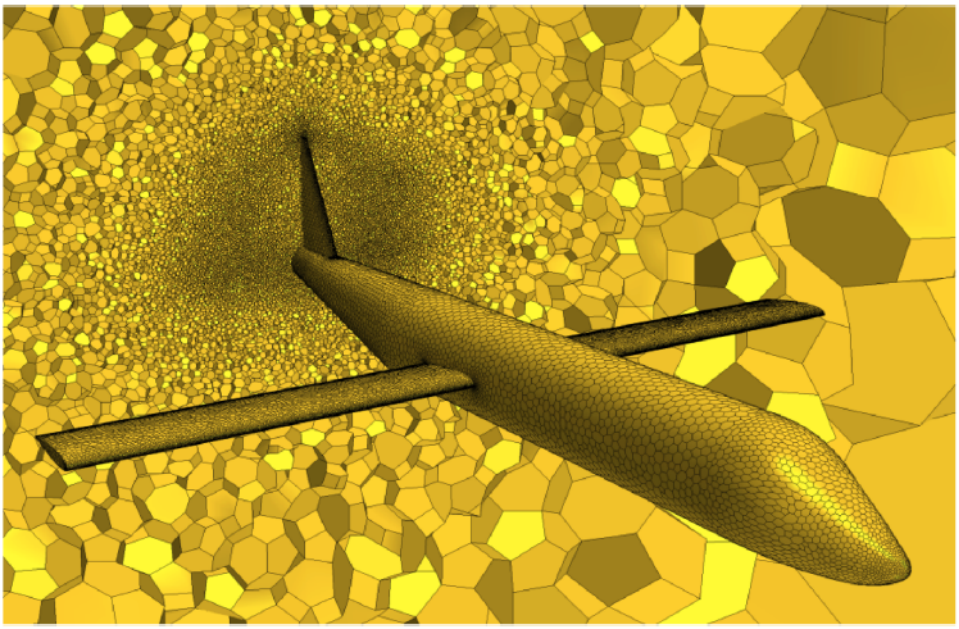

FIGURE 5.2: Volume mesh around the VEDSC model.

changes according to the configuration analyzed and increases up to 10 million for a complete aircraft configuration. By enabling an expansion rate of the volume cells, it is possible to save up memory and computational time, reducing the total cells number to 3 million for a complete aircraft configuration, keeping the same surface mesh and results. A mesh scene is shown in Figure 5.2. To account for boundary layer effect, a prismatic mesh of 20 layers has been extruded from the aircraft walls. The flow is stationary, viscous, incompressible, and fully-turbulent (SA model). All the analyses have been performed at angle of attack $\alpha = 0°$ and angle of sideslip $\beta = 5°$.

The aerodynamic interference among airplane components is evaluated by the ratio of aerodynamic coefficients between two configurations, which differ for only one component. For instance, the effect of the fuselage on the vertical tail contribution to directional stability is given by the ratio $C_{N_{\beta_v}}(\text{FV})/C_{N_{\beta_v}}(\text{V})$, where F stands for fuselage and V stands for vertical tailplane. The effect of the wing (W) on the previous body-tail combination is given by the ratio $C_{N_{\beta_v}}(\text{WFV})/C_{N_{\beta_v}}(\text{FV})$. Similarly, for the horizontal tailplane $C_{N_{\beta_v}}(\text{WFVH})/C_{N_{\beta_v}}(\text{WFV})$. In this way, the global

effect of the aerodynamic interference can be obtained by multiplying these factors. The superposition of the effects has been verified by performing further investigations, some of which are not included in the list of Table 5.2, like the fuselage - horizontal tail - vertical tail (FHV) configuration or the isolated empennage (VH) configuration, since they do not concur to the definition of the VeDSC method (see next section), but provide confidence in the approach taken. Each effect is described in the following sections by a factor K, which is the result of the C_{N_β} ratios for different aircraft configurations. They are defined such that

$$K \begin{cases} < 1, & \text{the aerodynamic interference } \textit{decreases } C_{N_\beta}, \\ = 1, & \text{the aerodynamic interference } \textit{does not affect } C_{N_\beta}, \\ > 1, & \text{the aerodynamic interference } \textit{increases } C_{N_\beta}. \end{cases}$$

5.2 Methodology description

The aircraft yawing moment coefficient derivative due to sideslip can be calculated as follows

$$C_{N_\beta} = C_{N_{\beta_v}} + C_{N_{\beta_f}} + C_{N_{\beta_w}} + C_{N_{\beta_h}} \tag{5.1}$$

assuming that the aerodynamic interference effects are included in each term, otherwise they must be added to the previous equation, as shown by Perkins and Hage [16, §8.2]. For a regional turboprop airplane, with a straight tapered wing, the vertical tailplane and the fuselage are the main contributions, defined as follows

$$C_{N_{\beta_v}} = K_{F_v} K_{W_v} K_{H_v} C_{L_{\alpha_v}} \frac{l_v}{b} \frac{S_v}{S} \tag{5.2}$$

$$C_{N_{\beta_f}} = K_{V_f} K_{W_f} K_{H_f} C_{N_{\beta_f}}^{\text{isolated}} \tag{5.3}$$

where the mutual aerodynamic interference effects are included in both derivatives, hence the sum of the effects is valid. The vertical tail contribution is stable (and usually reported with positive sign), whereas the fuselage contribution is unstable. The lift curve slope of the isolated vertical tailplane $C_{L_{\alpha_v}}$ and the yawing moment coefficient due to sideslip of the isolated fuselage $C_{N_{\beta_f}}$ are corrected by the interference factors K, which are so defined:

K_{F_v} interference factor of the fuselage on the vertical tail (Sec. 5.4)
K_{V_f} interference factor of the vertical tail on the fuselage (Sec. 5.4)
K_{W_v} interference factor of the wing on the vertical tail (Sec. 5.5)
K_{W_f} interference factor of the wing on the fuselage (Sec. 5.5)
K_{H_v} interference factor of the horizontal tail on the vertical tail (Sec. 5.6)
K_{H_f} interference factor of the horizontal tail on the fuselage (Sec. 5.6)

5.3 Isolated components contributions

The lift curve slope $C_{L_{\alpha_v}}$ of the isolated vertical tailplane is function of its planform, airfoil shape, and Mach number. It can be predicted by the Helmbold-Diederich [54, 55] formula (Equation 3.6), here repeated for vertical tail and illustrated in Figure 5.4

$$C_{L_{\alpha_v}} = \frac{2\pi\, A_v}{2 + \sqrt{\dfrac{B^2 A_v^2}{\kappa^2}\left(1 + \dfrac{\tan^2 \Lambda_{v,c/2}}{B^2}\right) + 4}} \tag{5.4}$$

where

A_v is the vertical tail aspect ratio, b_v^2/S_v

B is the compressibility parameter, $\sqrt{(1-M^2)}$

κ is the ratio of *section* lift-curve slope to theoretical thin-section value, $c_{l_\alpha}/(2\pi\, B)$, and for thin airfoils ($c_{l_\alpha} \approx 2\pi$) it is equal to $1/B$

$\Lambda_{v,c/2}$ is the vertical tail sweep angle at half chord.

The yawing moment coefficient $C_{N_\beta}{}_f^{\text{isolated}}$ of the isolated fuselage (a scheme is reported in Figure 5.3) may be predicted as described in Ref. [88]

$$C_{N_\beta}{}_f^{\text{isolated}} = C_{N_\beta f_{\text{slend}}} + \Delta C_{N_\beta f_{\text{nose}}} + \Delta C_{N_\beta f_{\text{tail}}} \tag{5.5}$$

where

$C_{N_\beta f_{\text{slend}}}$ is the yawing moment coefficient as function of fuselage slenderness ratio L_f/D_f (see Figure 5.5);

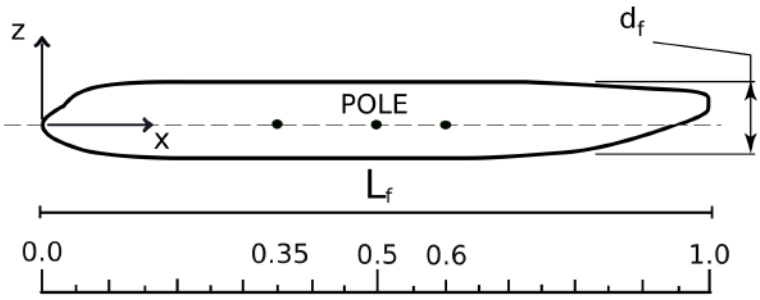

FIGURE 5.3: Fuselage reference system.

$\Delta C_{N_{\beta f_{\text{nose}}}}$ is the yawing moment nose correction factor. It depends on the nose slenderness ratio L_n/D_f (see Figure 5.6);

$\Delta C_{N_{\beta f_{\text{tail}}}}$ is the yawing moment tail correction factor. It depends on the tail-cone slenderness ratio L_t/D_f (see Figure 5.7).

The values obtained from Figure 5.5 to 5.7 – which refer to the fuselage frontal area S_{front} and cabin diameter or height d_f, see Equation 5.6 – must be corrected to take into consideration the actual non-dimensional reference area and length for yawing moment coefficient. Thus, if the method proposed in this section is used to calculate the isolated yawing moment coefficient of the fuselage, use Equation 5.7 instead of Equation 5.3 to calculate the fuselage contribution in sideslip

$$C_{N_\beta f}^{\text{isolated}} = \frac{N_f}{\frac{1}{2}\rho V^2 S_{\text{front}} d_f} \tag{5.6}$$

$$C_{N_{\beta f}} = K_{V_f} K_{W_f} K_{H_f} \frac{S_{\text{front}}}{S} \frac{d_f}{b} C_{N_\beta f}^{\text{isolated}} . \tag{5.7}$$

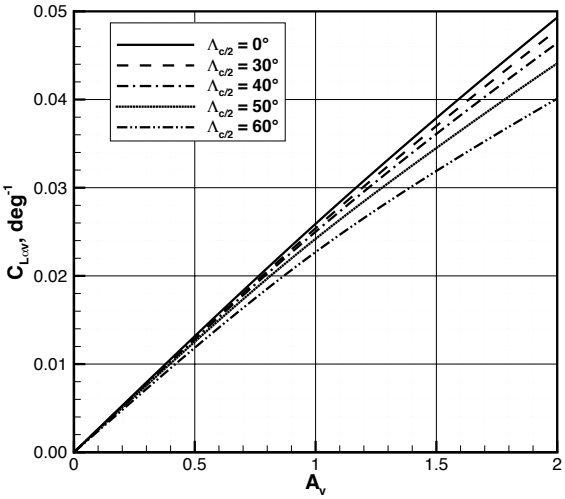

FIGURE 5.4: Isolated vertical tail lift curve slope. Non-dimensioned on vertical tail planform area S_v.

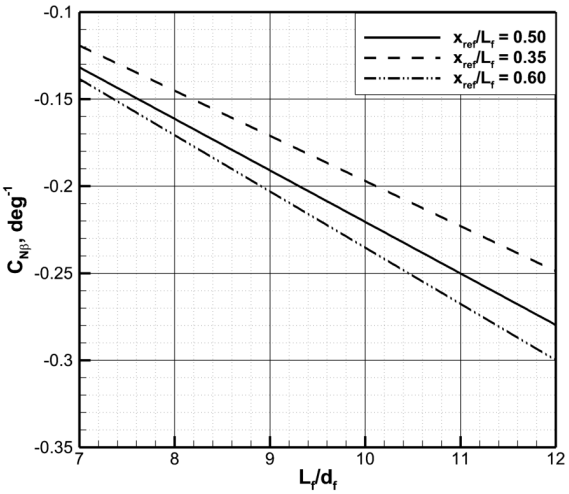

FIGURE 5.5: Effect of fuselage slenderness ratio. Non-dimensioned on fuselage diameter d_f and frontal area S_{front}.

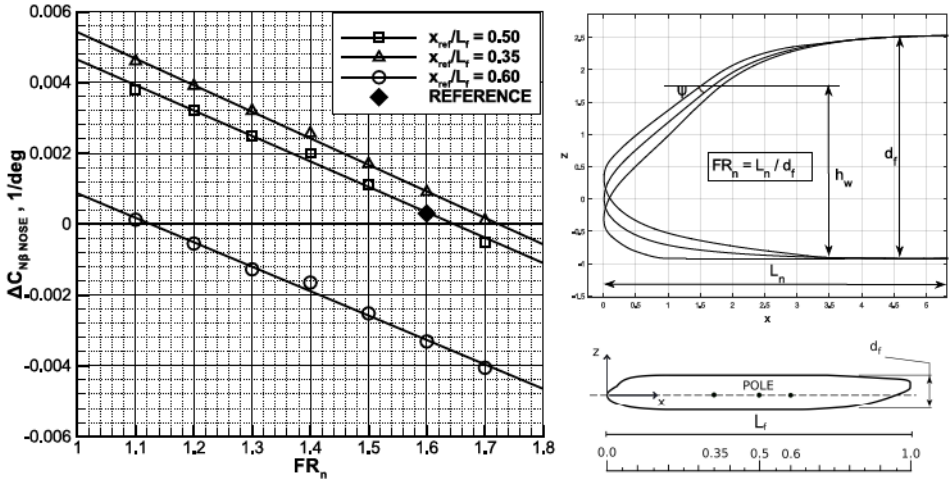

FIGURE 5.6: Effect of fuselage nose slenderness ratio. Non-dimensioned on fuselage diameter d_f and frontal area S_{front}.

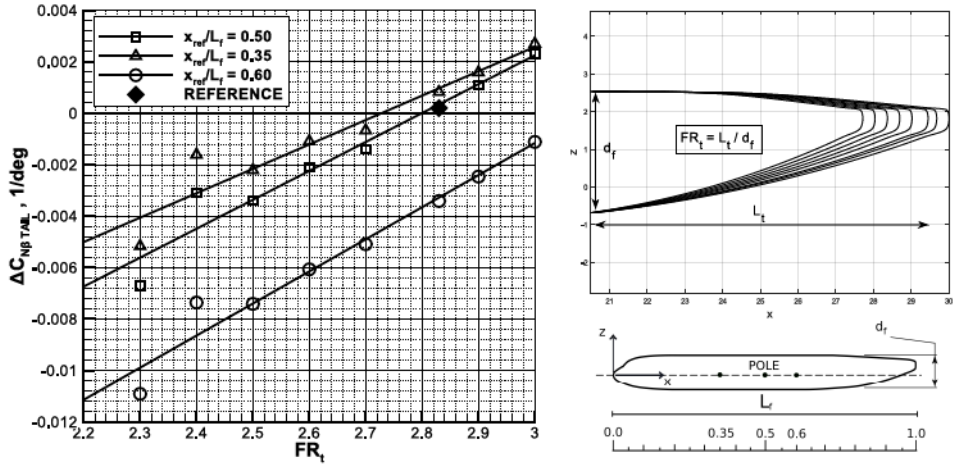

FIGURE 5.7: Effect of fuselage tail-cone slenderness ratio. Non-dimensioned on fuselage diameter d_f and frontal area S_{front}.

5.4 Fuselage - vertical tail interference factors K_{F_v} and K_{V_f}

The interference factor K_{F_v} is defined as the ratio between the yawing moment coefficient of the fuselage - vertical tail combination to the yawing moment coefficient of the isolated vertical tailplane

$$K_{F_v} = \frac{C_{N_{\beta_v}}(\mathrm{FV})}{C_{N_{\beta_v}}(\mathrm{V})} \tag{5.8}$$

where the geometric parameter governing this factor is the ratio of the vertical tail span b_v to fuselage height d_{fv}, representing the relative size between the vertical stabilizer and the fuselage section where the former is located, see Figure 5.8. The effect of the tailplane planform can be neglected, although visible as scatter data around the best fit curves [84]. The three curves have been parameterized according to fuselage tail-cone shape, defined in Figure 5.9. The effect of the fuselage on the vertical tailplane in sideslip is represented in Figure 5.10. *There is an increase of vertical tail effectiveness in sideslip* (i.e. $K_{F_v} > 1$) *in almost all the configurations analyzed*, although each fuselage exhibits a different trend.

The effect of the vertical tailplane on the fuselage in sideslip is represented in Figure 5.11. The interference factor K_{V_f} is defined as the ratio between the yawing moment coefficient of the fuselage - vertical tail combination to the yawing moment coefficient of the isolated fuselage

$$K_{V_f} = \frac{C_{N_{\beta_f}}(\mathrm{FV})}{C_{N_{\beta_f}}(\mathrm{F})} \tag{5.9}$$

that depends on the same geometric parameter b_v/d_{fv}. It is here noted that for all the combinations investigated, the interference factor $K_{V_f} < 1$ anywhere, that is, in the range investigated, *the vertical tailplane always reduces the fuselage instability in sideslip*. Typical regional turboprop values of b_v/d_{fv} vary from 3 to 5. In this range, the coupling between vertical tailplane and fuselage is always beneficial for both: the vertical tailplane increases its effectiveness in sideslip by 10 % to 20 %, whereas the fuselage directional instability has reduced by the same amount. Both contribute to the yawing moment coefficient derivative C_{N_β} of the airplane.

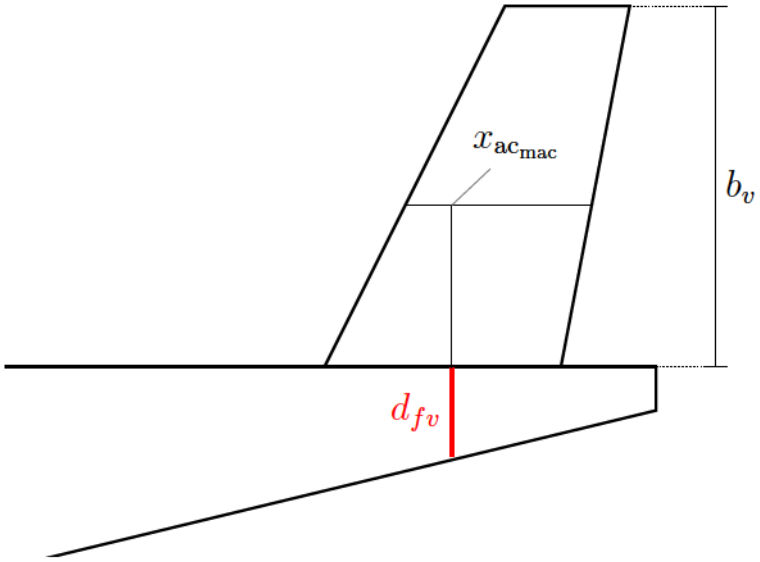

FIGURE 5.8: Fuselage-tail reference system. Definition of b_v/d_{fv}.

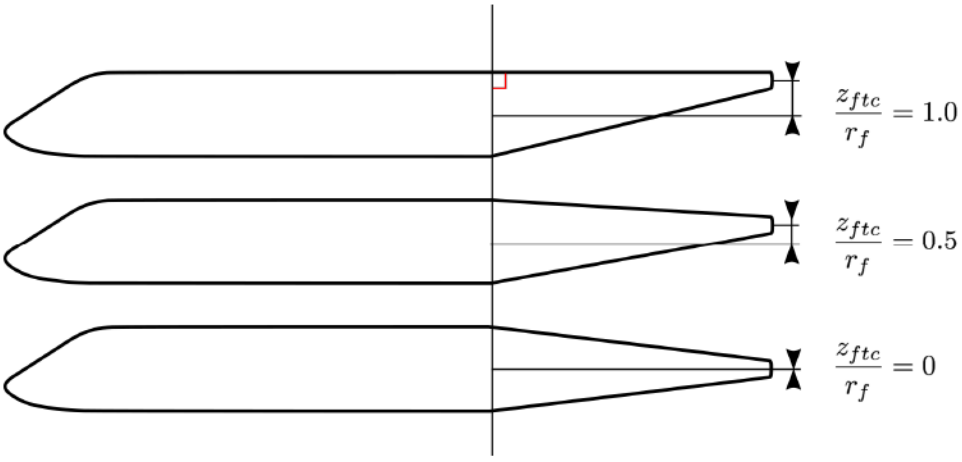

FIGURE 5.9: Tail-cone reference system. Definition of z_{ftc}/r_f.

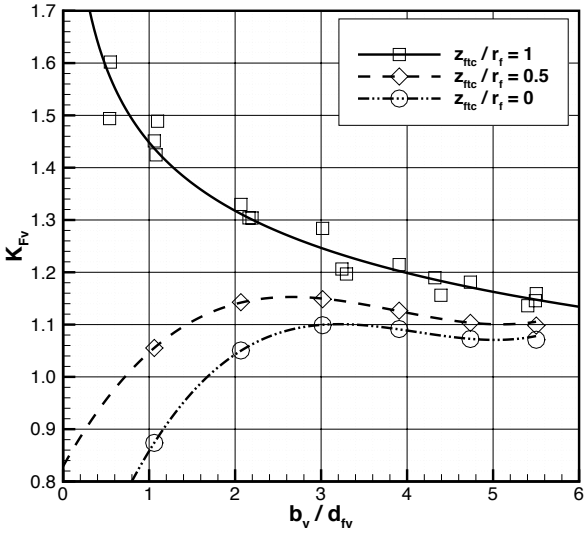

FIGURE 5.10: Aerodynamic interference factor K_{F_v}. Effect of the fuselage on the vertical tail.

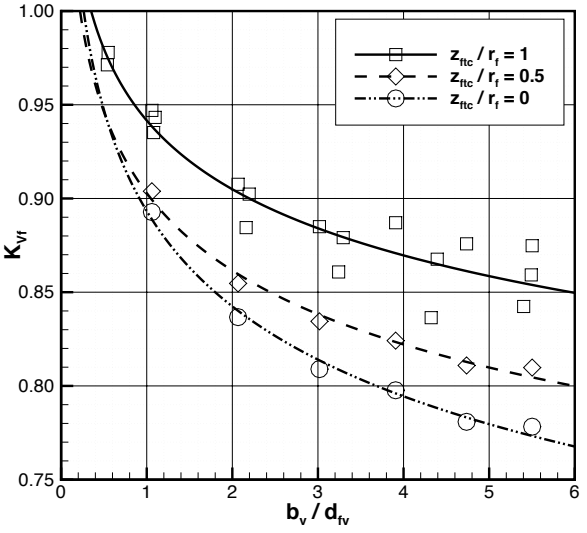

FIGURE 5.11: Aerodynamic interference factor K_{V_f}. Effect of the vertical tail on the fuselage.

5.5 Wing interference factors K_{W_v} and K_{W_f}

The wing interference factors K_{W_v} and K_{W_f} represent the effects of wing sidewash on the vertical tailplane and fuselage, respectively

$$K_{W_v} = \frac{C_{N_{\beta_v}}(\text{WFV})}{C_{N_{\beta_v}}(\text{FV})} \tag{5.10}$$

$$K_{W_f} = \frac{C_{N_{\beta_f}}(\text{WFV})}{C_{N_{\beta_f}}(\text{FV})} \tag{5.11}$$

shown in preview in Figure 5.12. These effects are functions of the vertical wing location on the fuselage z_w/r_f, fuselage tail-cone shape z_{ftc}/r_f (i.e. wing - vertical tailplane relative position), and wing aspect ratio $\mathcal{R}$. If an aircraft configuration is not directly represented, it is always possible to interpolate values between two charts. The reference system for wing position is shown in Figure 5.13, whereas that describing the fuselage tail-cone shape has been reported in Figure 5.9.

Results are reported from Figure 5.14 to 5.16 for the interference effect of the wing on the vertical tail K_{W_v}. The mid-low position is the most favorable, increasing the vertical tail contribution to directional stability up to 13%, whereas the high wing reduces this contribution from 7 % to 17 % according to wing position and fuselage tail-cone shape. In particular, the curves of Figure 5.16 are translated down by 0.05 with respect to the curves of Figure 5.14 and 5.15. The effect of the wing aspect ratio is to slightly decrease the K_{W_v} factor, especially at the high and low wing positions, $z_w/r_f = 0$ and 1 respectively.

The charts representing the interference effect of the wing on the fuselage K_{W_f} are shown from Figure 5.17 to 5.19. Their trend is the opposite of those describing the K_{W_v} factor, as resumed in Figure 5.12. Since the fuselage is an aerodynamically unstable body, an interference factor $K > 1$ indicates an increase in directional instability. Thus, a high wing that *decreases* the vertical tail stability contribution to sideslip $C_{N_{\beta_v}}$ by 7%, *increases* the fuselage instability in sideslip $C_{N_{\beta_f}}$ by 15%, as it can be observed by comparing Figure 5.14 with Figure 5.17. Further details about these numerical analyses are given in Appendix A.

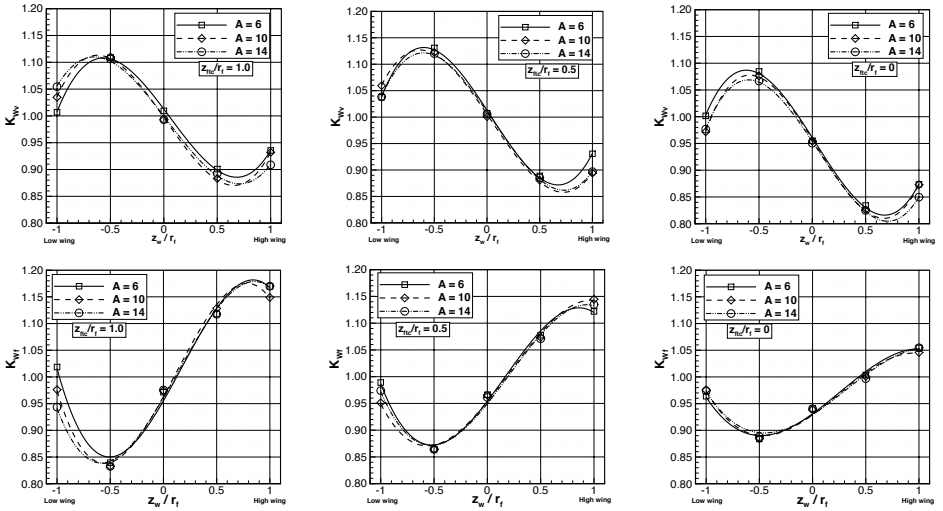

FIGURE 5.12: Preview of the charts describing the effects of the wing on the vertical tail and the fuselage in sideslip conditions.

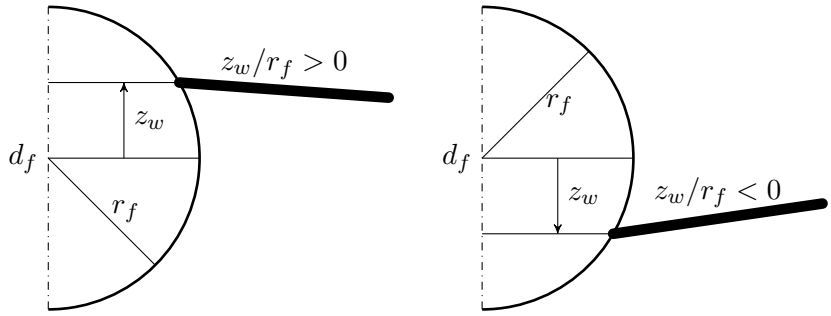

(A) High wing. (B) Low wing.

FIGURE 5.13: Wing position reference system.

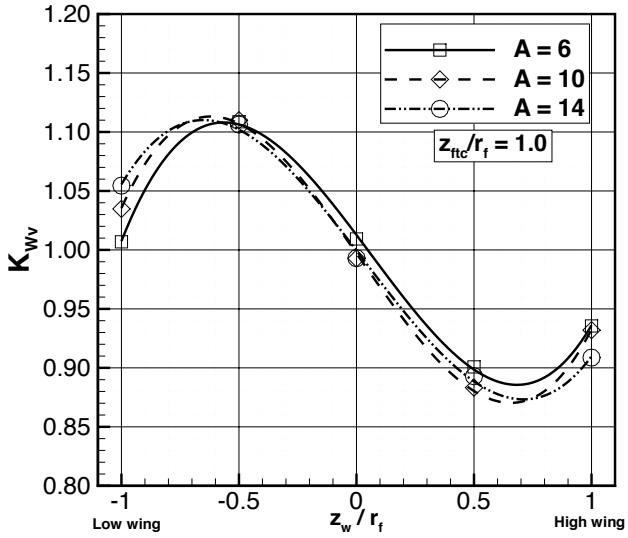

FIGURE 5.14: Aerodynamic interference factor K_{W_v}. Effect of the wing on the vertical tail, configuration with $z_{ftc}/r_f = 1$.

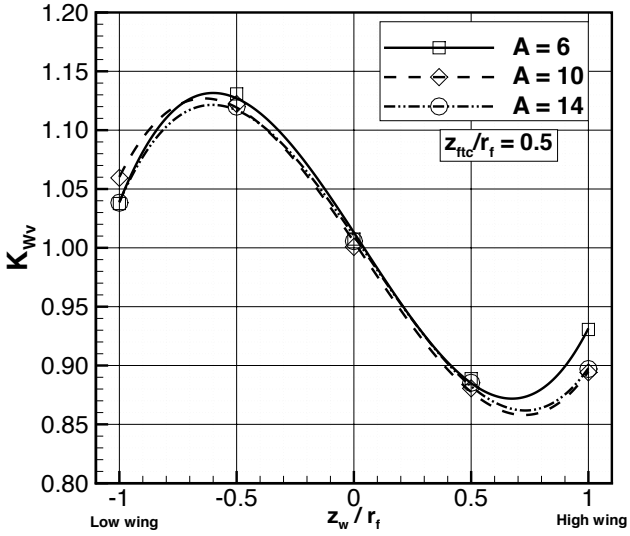

FIGURE 5.15: Aerodynamic interference factor K_{W_v}. Effect of the wing on the vertical tail, configuration with $z_{ftc}/r_f = 0.5$.

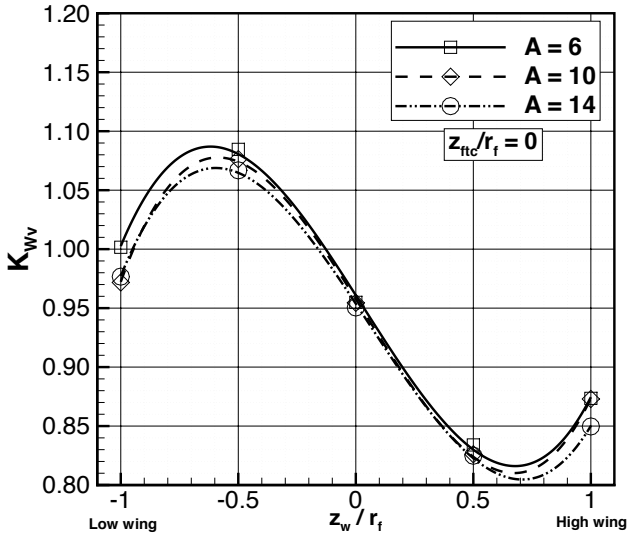

FIGURE 5.16: Aerodynamic interference factor K_{W_v}. Effect of the wing on the vertical tail, configuration with $z_{ftc}/r_f = 0$.

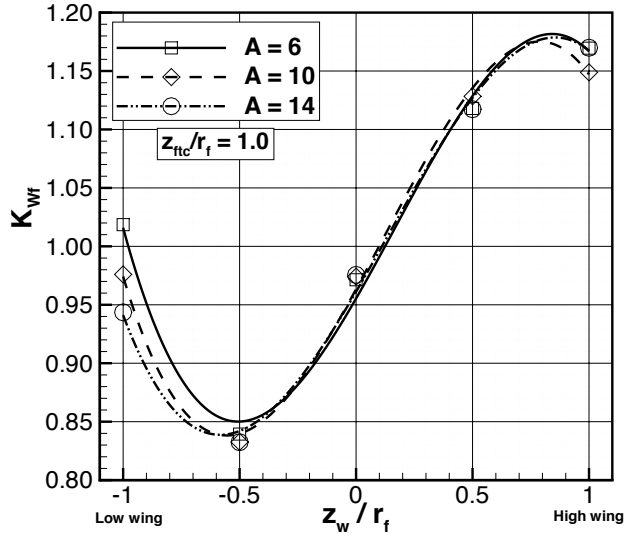

FIGURE 5.17: Aerodynamic interference factor K_{W_f}. Effect of the wing on the fuselage, configuration with $z_{ftc}/r_f = 1$.

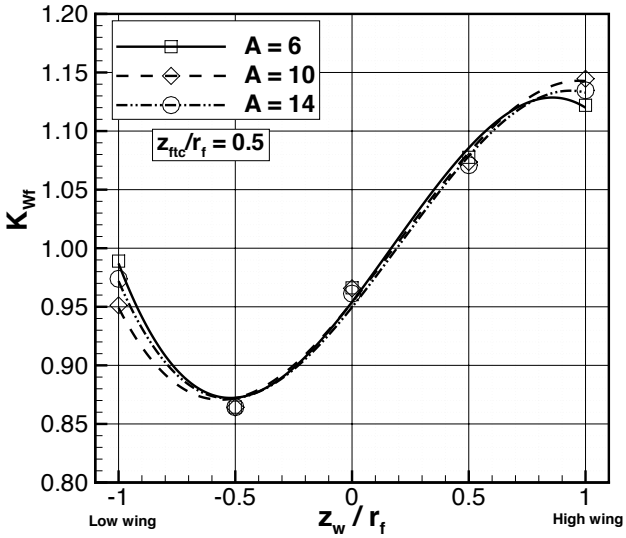

FIGURE 5.18: Aerodynamic interference factor K_{W_f}. Effect of the wing on the fuselage, configuration with $z_{ftc}/r_f = 0.5$.

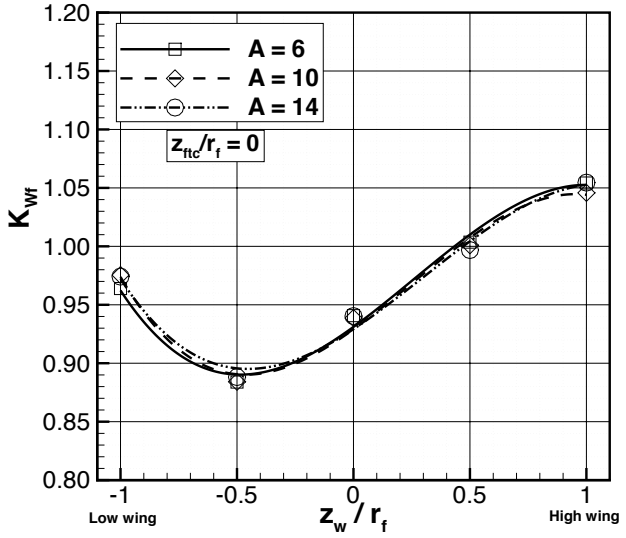

FIGURE 5.19: Aerodynamic interference factor K_{W_f}. Effect of the wing on the fuselage, configuration with $z_{ftc}/r_f = 0$.

5.6 Horizontal tail interference factors K_{H_v} and K_{H_f}

The horizontal tailplane interference factors are defined as follows, for the vertical tail and fuselage, respectively

$$K_{H_v} = \frac{C_{N_{\beta_v}}(\text{WFVH})}{C_{N_{\beta_v}}(\text{WFV})} \tag{5.12}$$

$$K_{H_f} = \frac{C_{N_{\beta_f}}(\text{WFVH})}{C_{N_{\beta_f}}(\text{WFV})}. \tag{5.13}$$

Results are shown in preview in Figure 5.20 for the influence on the vertical tail and in Figure 5.21 for the effects on the fuselage. As it can be seen, 18 charts are needed to characterize the effects of the empennage configuration by fuselage tail-cone shape z_{ftc}/r_f, wing position z_w/r_f, vertical tail aspect ratio A_v, and horizontal tail position z_h/b_{v1}. If an aircraft configuration is not directly represented, it is always possible to interpolate values between curves and charts. Also, translation of the horizontal tailplane along a chord of the vertical stabilizer and the effects of the relative size of tailplanes are one order of magnitude less than the presented values [84], hence they are here neglected.

The reference system describing the empennage configuration is shown in Figure 5.22, whereas that describing the fuselage tail-cone shape has been reported in Figure 5.9. Results of the effects on the vertical tail are reported from Figure 5.23 to 5.31. The horizontal tailplane increases the effectiveness of the vertical stabilizer in sideslip up to 45% according to the aircraft configuration, whereas a cruciform empennage configuration can decrease it by 8%. Results of the effects on the fuselage are reported from Figure 5.32 to 5.40. The fuselage directional instability is usually reduced in the body-mounted horizontal tail configuration by 4 % to 12 %. Further details about these numerical analyses are given in Appendix A, where the effect of the horizontal tail longitudinal position and its size with respect to the vertical tail size are accounted for.

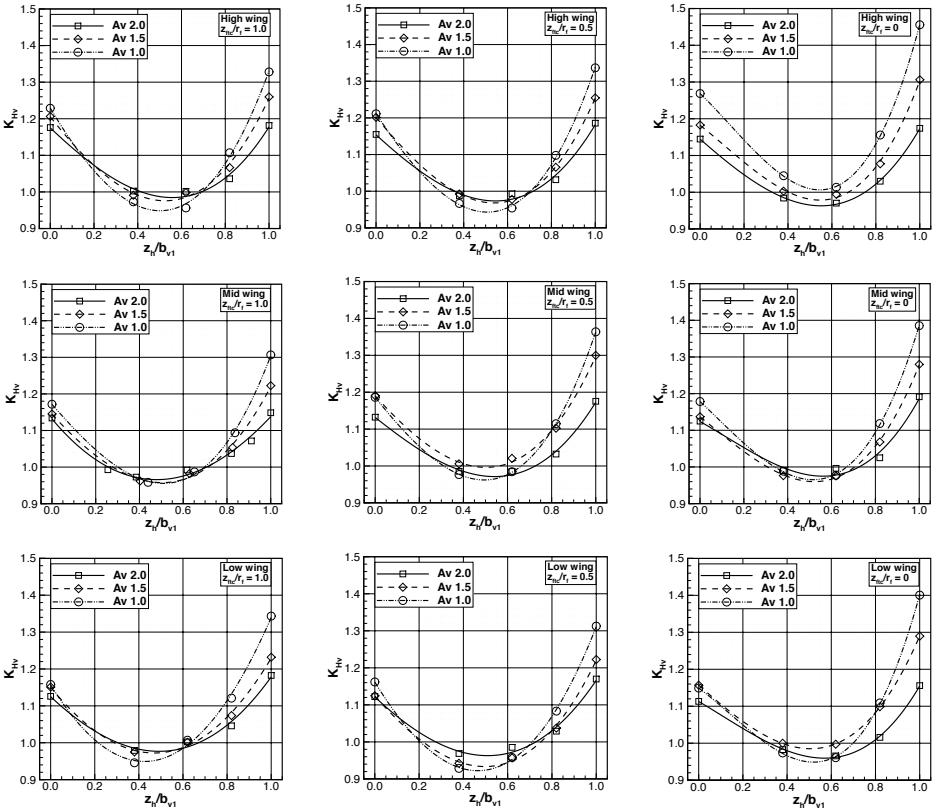

FIGURE 5.20: Preview of the charts describing the effects of the horizontal tail position on the vertical tail in sideslip conditions.

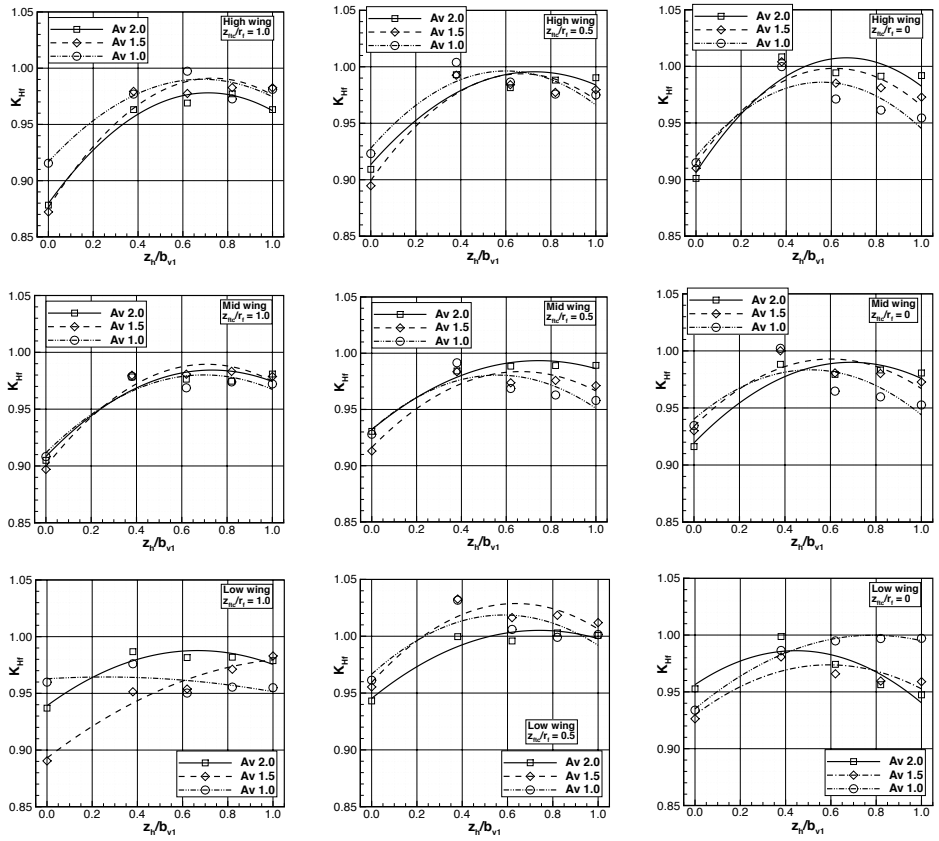

FIGURE 5.21: Preview of the charts describing the effects of the horizontal tail position on the fuselage in sideslip conditions.

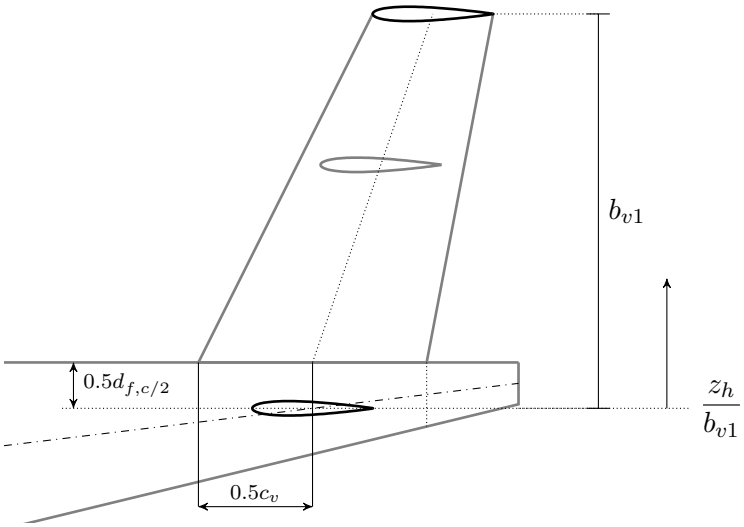

FIGURE 5.22: Empennage reference system.

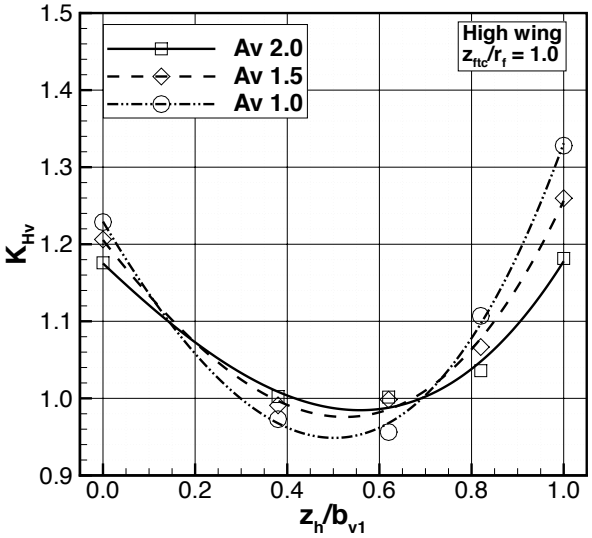

FIGURE 5.23: Aerodynamic interference factor K_{H_v}. Effect of the horizontal tail on the vertical tail, configuration with $z_{ftc}/r_f = 1$ and high wing.

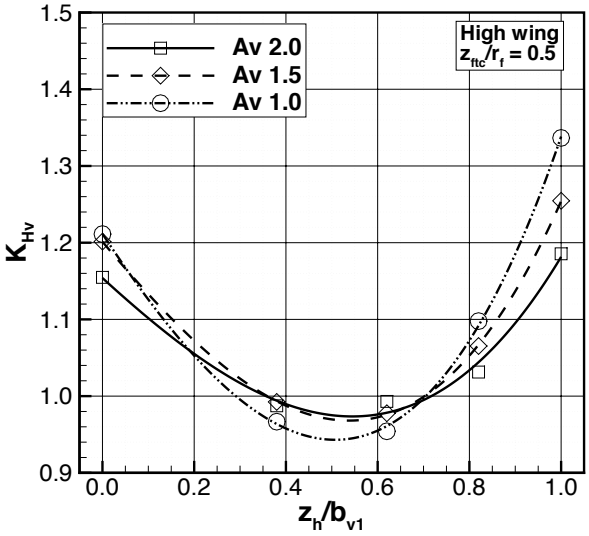

FIGURE 5.24: Aerodynamic interference factor K_{H_v}. Effect of the horizontal tail on the vertical tail, configuration with $z_{ftc}/r_f = 0.5$ and high wing.

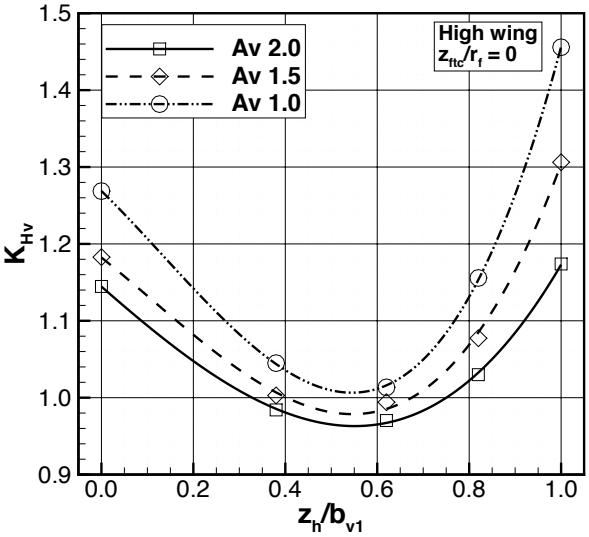

FIGURE 5.25: Aerodynamic interference factor K_{H_v}. Effect of the horizontal tail on the vertical tail, configuration with $z_{ftc}/r_f = 0$ and high wing.

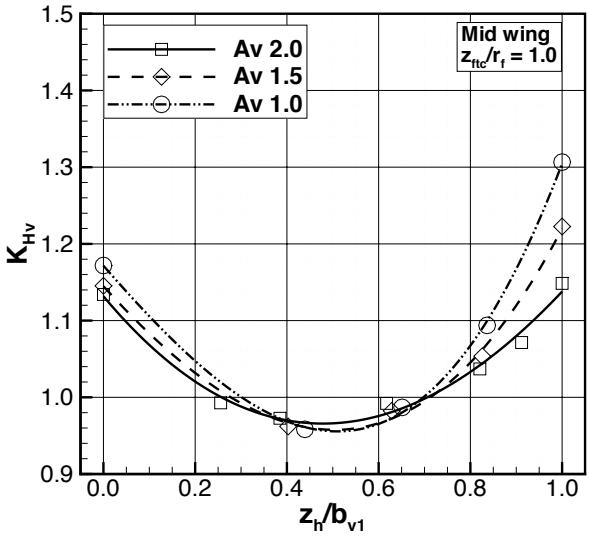

FIGURE 5.26: Aerodynamic interference factor K_{H_v}. Effect of the horizontal tail on the vertical tail, configuration with $z_{ftc}/r_f = 1$ and mid wing.

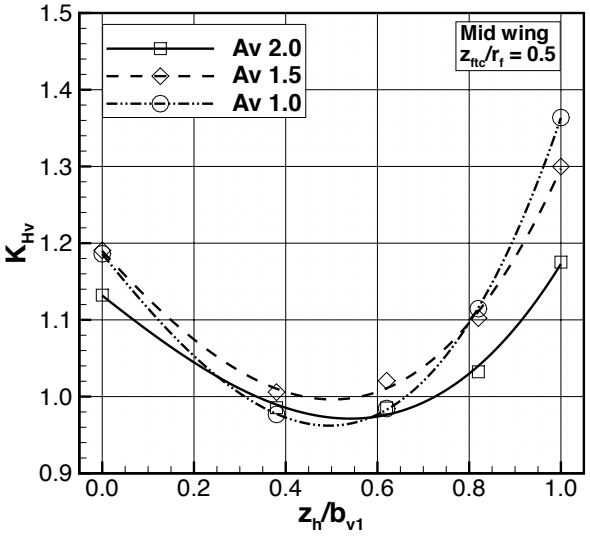

FIGURE 5.27: Aerodynamic interference factor K_{H_v}. Effect of the horizontal tail on the vertical tail, configuration with $z_{ftc}/r_f = 0.5$ and mid wing.

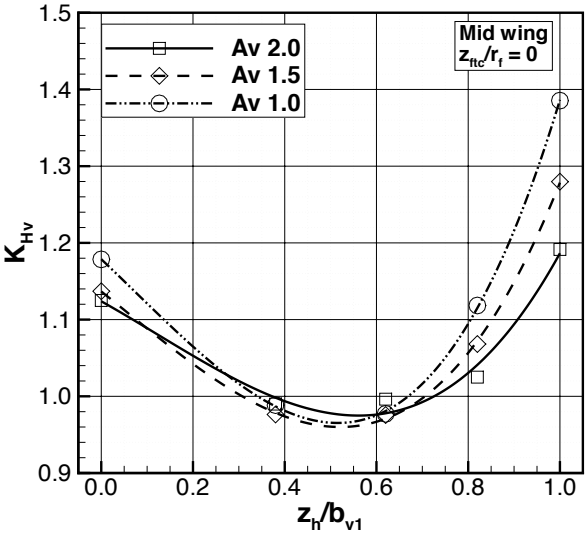

FIGURE 5.28: Aerodynamic interference factor K_{H_v}. Effect of the horizontal tail on the vertical tail, configuration with $z_{ftc}/r_f = 0$ and mid wing.

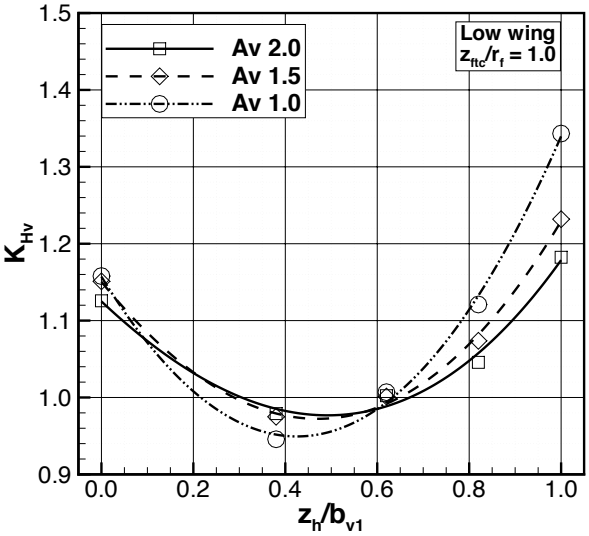

FIGURE 5.29: Aerodynamic interference factor K_{H_v}. Effect of the horizontal tail on the vertical tail, configuration with $z_{ftc}/r_f = 1$ and low wing.

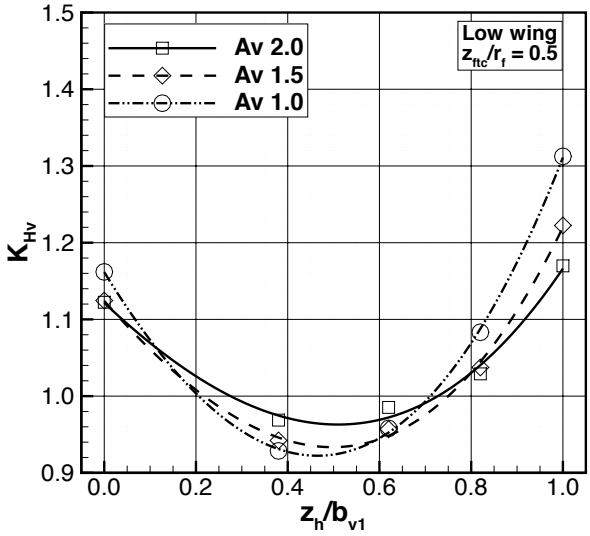

FIGURE 5.30: Aerodynamic interference factor K_{H_v}. Effect of the horizontal tail on the vertical tail, configuration with $z_{ftc}/r_f = 0.5$ and low wing.

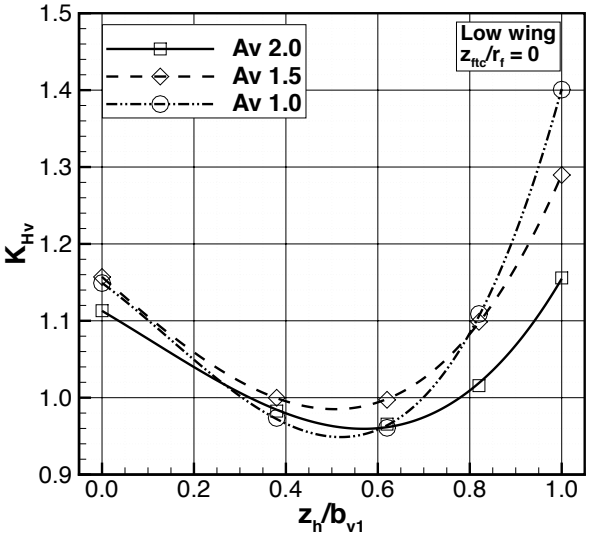

FIGURE 5.31: Aerodynamic interference factor K_{H_v}. Effect of the horizontal tail on the vertical tail, configuration with $z_{ftc}/r_f = 0$ and low wing.

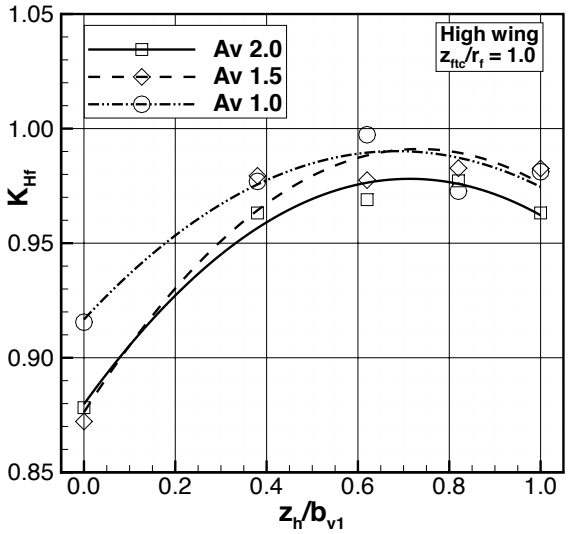

FIGURE 5.32: Aerodynamic interference factor K_{H_f}. Effect of the horizontal tail on the fuselage, configuration with $z_{ftc}/r_f = 1$ and high wing.

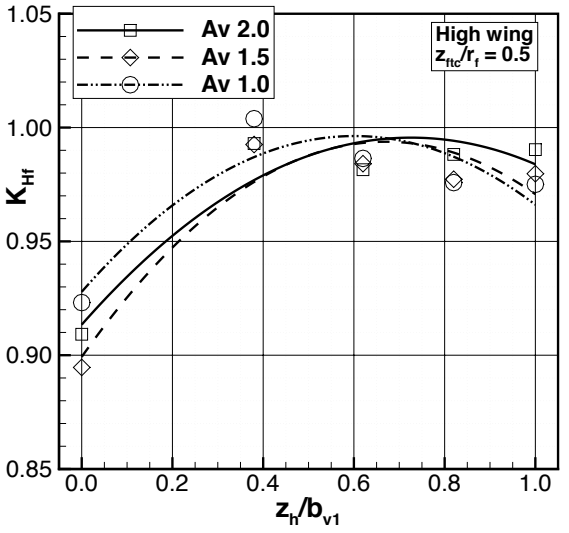

FIGURE 5.33: Aerodynamic interference factor K_{H_f}. Effect of the horizontal tail on the fuselage, configuration with $z_{ftc}/r_f = 0.5$ and high wing.

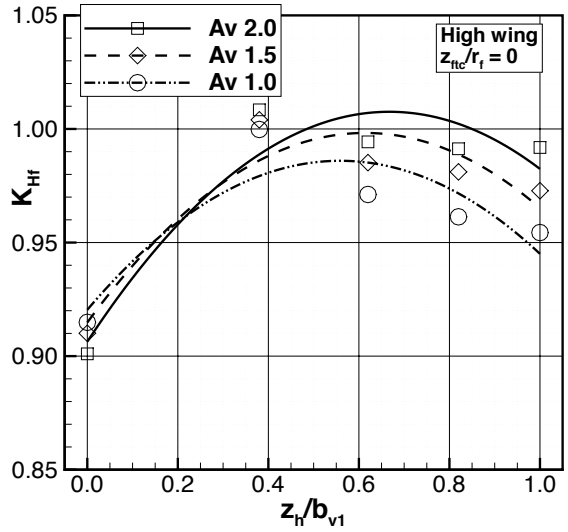

FIGURE 5.34: Aerodynamic interference factor K_{H_f}. Effect of the horizontal tail on the fuselage, configuration with $z_{ftc}/r_f = 0$ and high wing.

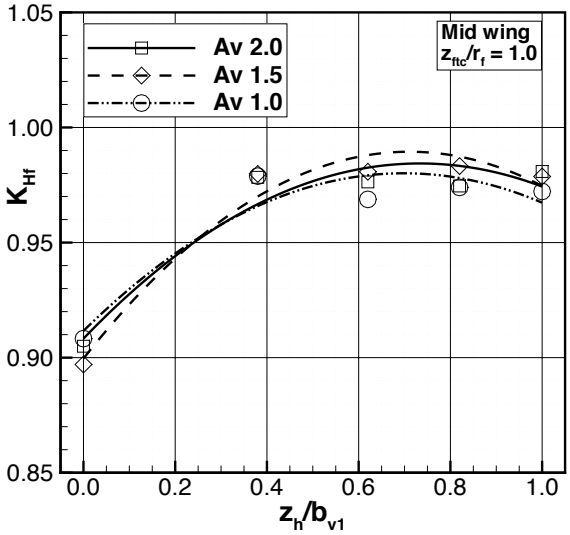

FIGURE 5.35: Aerodynamic interference factor K_{H_f}. Effect of the horizontal tail on the fuselage, configuration with $z_{ftc}/r_f = 1$ and mid wing.

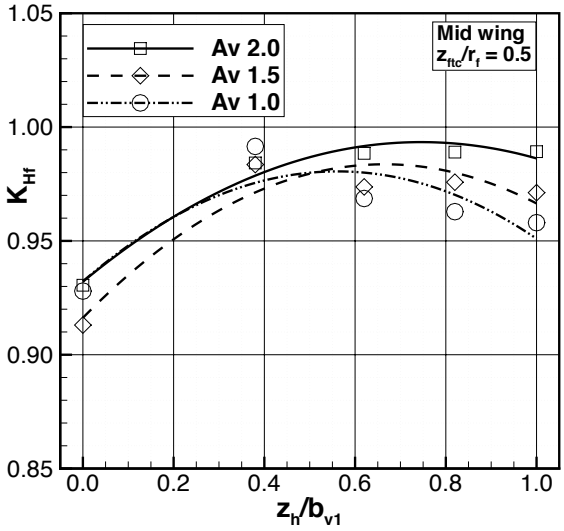

FIGURE 5.36: Aerodynamic interference factor K_{H_f}. Effect of the horizontal tail on the fuselage, configuration with $z_{ftc}/r_f = 0.5$ and mid wing.

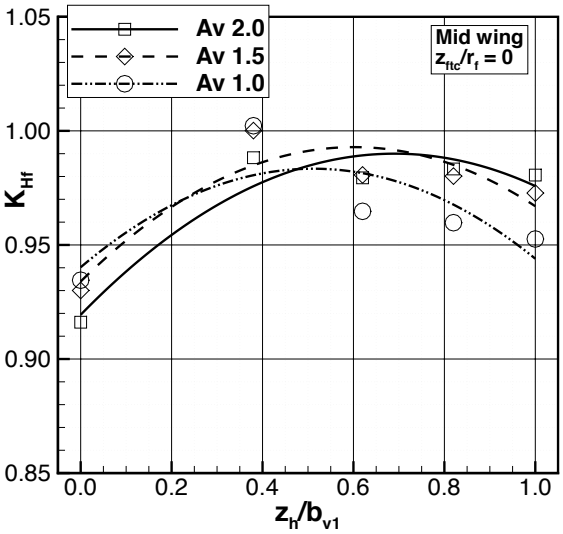

FIGURE 5.37: Aerodynamic interference factor K_{H_f}. Effect of the horizontal tail on the fuselage, configuration with $z_{ftc}/r_f = 0$ and mid wing.

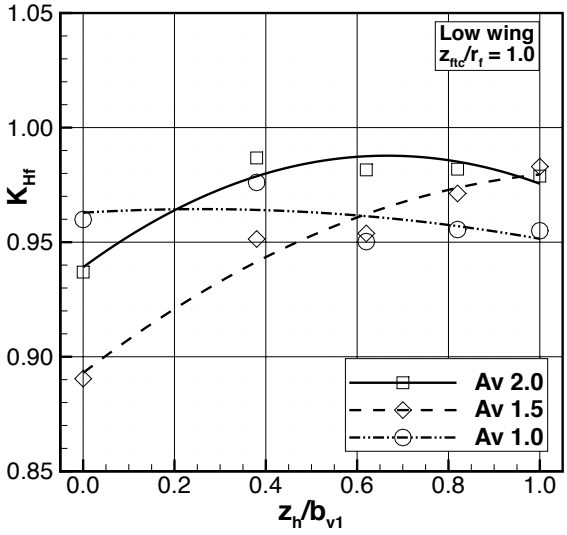

FIGURE 5.38: Aerodynamic interference factor K_{H_f}. Effect of the horizontal tail on the fuselage, configuration with $z_{ftc}/r_f = 1$ and low wing.

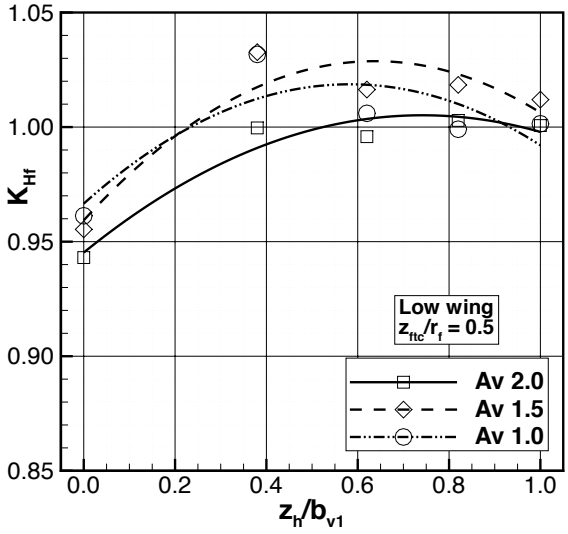

FIGURE 5.39: Aerodynamic interference factor K_{H_f}. Effect of the horizontal tail on the fuselage, configuration with $z_{ftc}/r_f = 0.5$ and low wing.

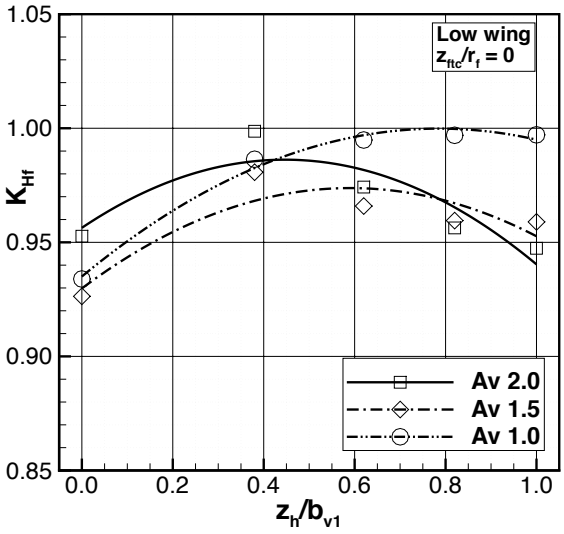

FIGURE 5.40: Aerodynamic interference factor K_{H_f}. Effect of the horizontal tail on the fuselage, configuration with $z_{ftc}/r_f = 0$ and low wing.

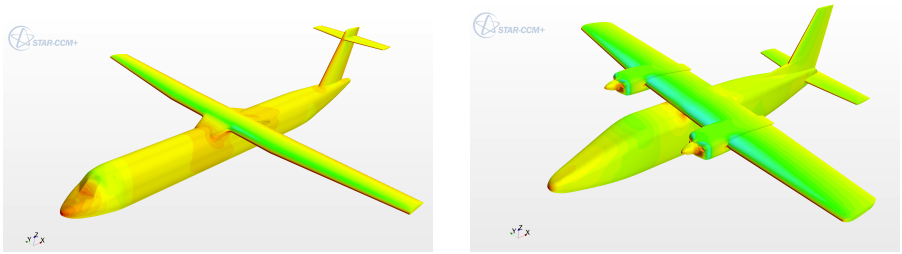

(A) Generic Regional Turboprop. (B) Tecnam P2012.

FIGURE 5.41: CFD pressure contour distribution on the reference airplanes.

5.7 Applications of the VEDSC method

An application of the VEDSC method is here given for a generic regional turboprop (GRT, Figure 5.41a) and for the Tecnam P2012 commuter (Figure 5.41b). A guided procedure is here illustrated for the first one, *which is a different aircraft from the model used to develop the method.* The aim is to calculate the aircraft directional stability expressed by Equation 5.1

$$C_{N_\beta} = C_{N_{\beta_v}} + C_{N_{\beta_f}} + \text{minor effects}$$

where the *direct* contributions of the wing and of horizontal tail have been neglected, because the former is function of the sweep angle Λ, which is very small, the latter can be considered as a wing scaled by the dynamic pressure ratio and planform area ratio $\eta_v \, S_h/S$. According to the VEDSC method, it is sufficient to calculate the following contributions (Equation 5.2 and 5.3)

$$C_{N_{\beta_v}} = K_{F_v} K_{W_v} K_{H_v} C_{L_{\alpha_v}} \frac{l_v}{b} \frac{S_v}{S}$$

$$C_{N_{\beta_f}} = K_{V_f} K_{W_f} K_{H_f} C_{N_{\beta_f}}^{\text{isolated}}$$

where each term is a function of the geometric layout of the aircraft. Input data for the GRT aircraft have been reported in Table 5.3. This guided procedure is focused on the first equation.

TABLE 5.3: Generic Regional Turboprop (GRT) data.

Parameter	Symbol	Value
Wing position	z_w/r_f	1.0
Wing area	S	$61.0\,\mathrm{m}^2$
Wing aspect ratio	$\mathcal{AR}$	12.0
Vertical tail aspect ratio	A_v	1.55
Vertical tail area	S_v	$12.5\,\mathrm{m}^2$
Vertical tail span	b_v	4.5 m
Horizontal tail position	z_h/b_{v1}	0.85
Tail to fuselage height	b_v/d_{fv}	3.8
Tail moment arm	l_v/b	0.5
Fuselage fineness ratio	L_f/d_f	10.3
Fuselage moment arm	d_f/b	0.1
Fuselage area ratio	S_{front}/S	0.1

The isolated vertical tail lift curve slope $C_{L_{\alpha_v}}$ can be calculated with Equation 5.4, assuming $M = 0$, airfoil $c_{l_\alpha} = 2\pi$, and $\Lambda_{v,c/2} = 25°$, together with $A_v = 1.55$ as reported in Table 5.3

$$C_{L_{\alpha_v}} = \frac{2\pi\, A_v}{2 + \sqrt{\dfrac{B^2 A_v^2}{\kappa^2}\left(1 + \dfrac{\tan^2 \Lambda_{v,c/2}}{B^2}\right) + 4}} = 0.0388\ (/\mathrm{deg})$$

also reported in the following figure.

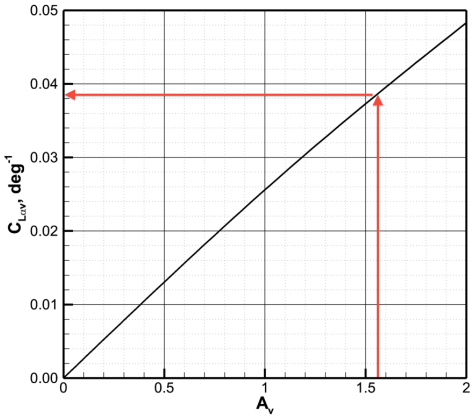

Next, the effect of the fuselage on the vertical tail K_{F_v} has to be calculated with Figure 5.10, with the geometric data provided in Table 5.3 giving $b_v/d_{fv} = 3.81$ and $z_{ftc}/r_f = 0.55$. Interpolation between two curves must be solved. It results $K_{F_v} = 1.14$, that is the fuselage increases the vertical tail contribution in sideslip by 14 %.

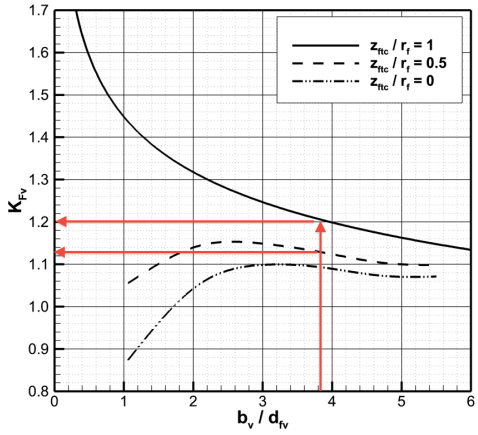

In regards of the wing effects K_{W_v}, the interpolation must be made between two charts, Figure 5.14 and 5.15, with high wing and $\mathcal{AR} = 12$ as shown. It results $K_{W_v} = 0.90$, that is the high wing reduces the vertical tail contribution in sideslip by 10 %.

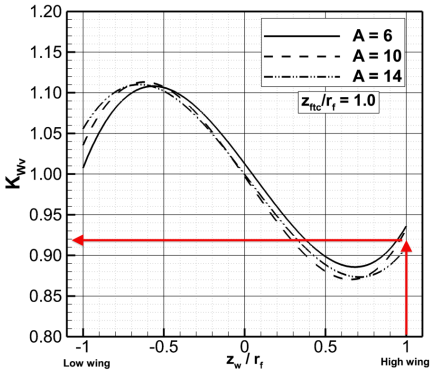

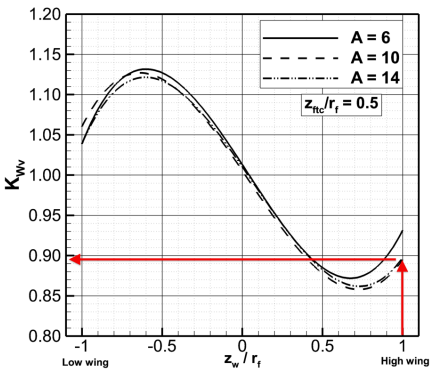

Finally, the effects of the horizontal tail K_{H_v} should be accounted by interpolating two curves (because of $A_v = 1.55$) in two charts (because of $z_{ftc}/r_f = 0.55$), Figure 5.23 and 5.24, respectively. As it can be seen from the following figures, in this case there is a negligible difference between the two charts, hence the calculation could have been simplified by taking only the values on Figure 5.24. It results $K_{H_v} = 1.08$, that is the empennage configuration increases the vertical tail contribution in sideslip by 8 %. According to the VEDSC method, much higher values can be reached if the horizontal stabilizer could be moved on the vertical tail tip (from 20 % to 25 %).

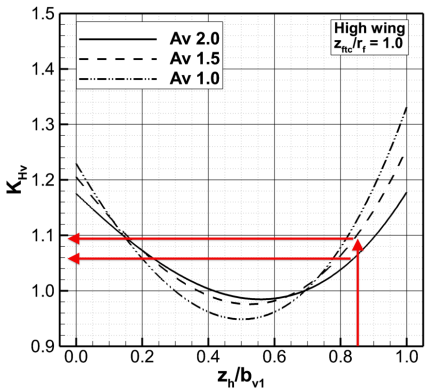

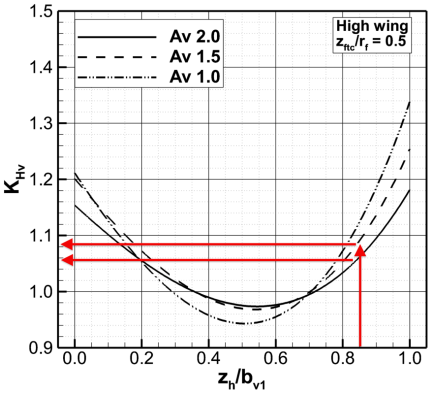

By multiplying the obtained values, the VEDSC method yields to

$$\begin{aligned} C_{N_{\beta_v}} &= K_{F_v} K_{W_v} K_{H_v} C_{L_{\alpha_v}} \frac{l_v}{b} \frac{S_v}{S} \\ &= 1.14 \times 0.90 \times 1.08 \times 0.0388 \times 0.478 \times 0.205 \\ &= 0.004\,21 \ (/\text{deg}). \end{aligned}$$

The procedure for the calculation of $C_{N_{\beta_f}}$ is the same, hence it has not been illustrated. Results are resumed from Table 5.4 to 5.6. The same procedure has been followed for the Tecnam P2012. Input data and results are reported from Table 5.7 to 5.10. The CFD results about Tecnam P2012 have been provided by Corcione [93].

The comparisons reported in Table 5.6 and 5.10 show a good agreement between CFD and the new proposed VEDSC method. CFD results have been obtained with a simulation of the complete aircraft at $\alpha = 0°$ and $\beta = 5°$ without nacelle, propellers, and winglet (for the P2012). Assuming CFD results as reference, percentages of error have been calculated for the methods. Signs of the derivatives are omitted. Maximum percentage difference is about 7 % for the P2012 aircraft. However, it is here remarked that this aircraft is not a regional turboprop and the new method is not focused on its geometric layout. For a typical turboprop aircraft, represented by the GRT model, the new method leads to accurate yawing moments prediction for both the vertical tail and fuselage contributions. DATCOM and ESDU methods provide a difference of about 10 % to 15 % in the vertical tail contribution for the GRT model. For the P2012 aircraft DATCOM misses the CFD values by 30 %, whereas the ESDU method leads to a very close result (1 % higher) about the vertical tailplane. As previously stated in Chapter 3, semi-empirical methods do not account for separate effects between fuselage and vertical tail, therefore they usually overestimate vertical tail contribution to compensate the fuselage variation (reduction of fuselage instability).

TABLE 5.4: Application to the GRT aircraft vertical tail.

Item	Reference	Value
Fuselage	K_{F_v} (Sec. 5.4)	1.14
Wing	K_{W_v} (Sec. 5.5)	0.90
Horizontal tail	K_{H_v} (Sec. 5.6)	1.08
Total aerodynamic interf.	$K_{F_v} K_{W_v} K_{H_v}$	1.108
Vertical tail lift slope (/deg)	$C_{L_{\alpha_v}}$ (Eq. 5.4)	0.0388
Area ratio S_v/S	Table 5.3	0.205
Vertical tail arm ratio l_v/b	Table 5.3	0.478
Isolated $C_{N_{\beta_v}}$ (/deg)	$C_{L_{\alpha_v}} S_v/S\, l_v/b$	0.003 80
Stability derivative (/deg)	$C_{N_{\beta_v}}$ (Eq. 5.2)	0.004 21

TABLE 5.5: Application to the GRT aircraft fuselage.

Item	Reference	Value
Vertical tail	K_{V_f} (Sec. 5.4)	0.83
Wing	K_{W_f} (Sec. 5.5)	1.14
Horizontal tail	K_{H_f} (Sec. 5.6)	0.98
Total aerodynamic interf.	$K_{F_f} K_{W_f} K_{H_f}$	0.927
Isolated $C_{N_{\beta_f}}(S_{\text{front}})$ (/deg)	Figure 5.5	0.23
Area ratio S_{front}/S	Table 5.3	0.099
Vertical tail arm ratio d_f/b	Table 5.3	0.102
Isolated $C_{N_{\beta_f}}(S)$ (/deg)	$C_{N_{\beta_f}} S_{\text{front}}/S\, d_f/b$	0.002 32
Stability derivative (/deg)	$C_{N_{\beta_f}}$ (Eq. 5.3)	0.002 15

TABLE 5.6: GRT aircraft results, assuming CFD as reference.

	Vertical tail		Fuselage	
	$C_{N_{\beta_v}}$ (/deg)	Δ%	$C_{N_{\beta_f}}$ (/deg)	Δ%
CFD	0.004 26	—	−0.002 18	—
DATCOM	0.004 75	11.5	0.002 16	−0.65
ESDU	0.004 90	15.0	—	—
VEDSC	0.004 21	−1.09	0.002 15	−1.29

Table 5.7: Tecnam P2012 data.

Parameter	Symbol	Value
Wing position	z_w/r_f	1.0
Wing area	S	$24.9\,\mathrm{m}^2$
Wing aspect ratio	$\mathcal{R}$	7.87
Vertical tail aspect ratio	A_v	1.89
Vertical tail area	S_v	$3.5\,\mathrm{m}^2$
Vertical tail span	b_v	2.57 m
Horizontal tail position	z_h/b_{v1}	0
Tail to fuselage height	b_v/d_{fv}	3.57
Tail moment arm	l_v/b	0.429
Fuselage fineness ratio	L_f/d_f	7.35
Fuselage moment arm	d_f/b	0.107
Fuselage area ratio	S_{front}/S	0.081

Table 5.8: Application to the Tecnam P2012 vertical tail.

Item	Reference	Value
Fuselage	K_{F_v} (Sec. 5.4)	1.10
Wing	K_{W_v} (Sec. 5.5)	0.87
Horizontal tail	K_{H_v} (Sec. 5.6)	1.14
Total aerodynamic interf.	$K_{F_v}K_{W_v}K_{H_v}$	1.091
Vertical tail lift slope (/deg)	$C_{L_{\alpha_v}}$ (Eq. 5.4)	0.0377
Area ratio S_v/S	Table 5.7	0.140
Vertical tail arm ratio l_v/b	Table 5.7	0.429
Isolated $C_{N_{\beta_v}}$ (/deg)	$C_{L_{\alpha_v}}\,S_v/S\,l_v/b$	0.002 26
Stability derivative (/deg)	$C_{N_{\beta_v}}$ (Eq. 5.2)	0.002 55

TABLE 5.9: Application to the Tecnam P2012 fuselage.

Item	Reference	Value
Vertical tail	K_{V_f} (Sec. 5.4)	0.80
Wing	K_{W_f} (Sec. 5.5)	1.05
Horizontal tail	K_{H_f} (Sec. 5.6)	0.90
Total aerodynamic interf.	$K_{F_f} K_{W_f} K_{H_f}$	0.758
Isolated $C_{N_{\beta f}}(S_{\text{front}})$ (/deg)	Figure 5.5	0.14
Area ratio S_{front}/S	Table 5.3	0.081
Vertical tail arm ratio d_f/b	Table 5.3	0.107
Isolated $C_{N_{\beta f}}(S)$ (/deg)	$C_{N_{\beta f}} S_{\text{front}}/S \, d_f/b$	0.001 21
Stability derivative (/deg)	$C_{N_{\beta f}}$ (Eq. 5.3)	0.000 92

TABLE 5.10: Tecnam P2012 results, assuming CFD as reference.

	Vertical tail		Fuselage	
	$C_{N_{\beta v}}$ (/deg)	Δ%	$C_{N_{\beta f}}$ (/deg)	Δ%
CFD	0.002 74	—	0.000 90	—
DATCOM	0.001 87	−31.8	0.001 20	33.0
ESDU	0.002 73	1.1	—	—
VEDSC	0.002 55	−7.31	0.000 92	2.20

Chapter 6

Wind tunnel tests

Synopsis

✈ Wind tunnel testing is introduced

✈ The CAD model and its manufacturing are deeply described

✈ The wind tunnel, with its instrumentation, is described

✈ Preliminary test and balance checks are discussed

✈ Wind tunnel tests results are presented and discussed

This chapter describes the experimental investigations performed to validate the VeDSC method of Chapter 5.

6.1 Introduction to wind tunnel testing

The wind tunnel is a device involved in experimental aerodynamic research to study the effects of airflow around solid objects. Its use is motivated by a wide interest in practical problems in aerodynamics and by the fact that theoretical and computational methods are not able to provide the full range of results needed to solve many of the above-mentioned problems [95]. The physical principle is the Galilean invariance, that is the laws of motion are the same in all inertial reference frames: to have an aircraft at rest and the air moving with respect to it produces the same results if the air is still and the aircraft is moving through it (in the same flow conditions). A short history of wind tunnel testing has been resumed by Corcione [93] and reported in the following lines.

The earliest wind tunnels were invented towards the end of the 19th century, in the early days of aeronautic research. The wind tunnel was envisioned as a means of reversing the usual paradigm: instead of the air standing still and an object moving at speed through it, the same effect would be obtained if the object stood still and the air moved at speed past it. Benjamin Robins (1707-1751), an English military engineer and mathematician, invented a whirling arm apparatus to determine drag and did some of the first experiments in aviation theory. Sir George Cayley (1773-1857) also used a whirling arm to measure the drag and lift of various airfoils. However, at the end of the 19th century, the major fault of the whirling arm was apparent. This fault was due that the wing was forced to fly in its own wake. Francis Herbert Wenham (1824-1908), a Council Member of the Aeronautical Society of Great Britain, addressed these issues by inventing, designing, and operating the first enclosed wind tunnel in 1871. Konstantin Tsiolkovsky built an open-section wind tunnel with a centrifugal blower in 1897, and determined the drag coefficients of flat plates, cylinders, and spheres. In the early 1890s, a Danish inventor, Poul la Cour, applied wind tunnels in his process of developing technology of wind turbines. Carl Rickard Nyberg used a wind tunnel when designing his Flugan from 1897 and onwards. In a classic set of experiments, the Englishman Osborne Reynolds (1842-1912), of the University of Manchester, demonstrated that the airflow pattern over a scale model would be the same for the full-scale vehicle if a certain flow parameter were the same in both cases. This factor, now known as the Reynolds number, is a basic parameter in the description of all fluid-flow situations. This comprises the central scientific justification for the use of models in wind tunnels to simulate real-life phenomena. The Wright brothers' use of a simple wind tunnel in 1901 to study the effects of airflow over various shapes while developing their Wright Flyer was in some ways revolutionary. In France, Gustave Eiffel (1832-1923) built his first open-return wind tunnel in 1909, running about 4000 tests between 1909 and 1912 and contributing to set new standards for aeronautical research. Eiffel's contribution into improvement of the open-return wind tunnel by enclosing

the test section in a chamber was followed by a number of wind tunnels later built (Eiffel was also the first to design a flared inlet with honeycomb flow straightener). Subsequent use of wind tunnels proliferated as the science of aerodynamics and discipline of aeronautical engineering were established and air travel and power were developed. The US Navy in 1916 built one of the largest wind tunnels in the world at that time at the Washington Navy Yard. Until the Second World War, the world's largest wind tunnel was built in 1932-1934 and located in a suburb of Paris, Chalais-Meudon, France. It was designed to test full size aircraft and had six large fans driven by high powered electric motors. The Chalais-Meudon wind tunnel was used by ONERA under the name S1Ch until 1976, contributing to the development of the Caravelle and Concorde airplanes. Actually, this wind tunnel is preserved as a national monument. During the Second World War large wind tunnels were built, and the development of wind tunnel science accompanied the development of the flying machines. In 1941 the US constructed one of the largest wind tunnels at that time at Wright Field in Dayton, Ohio. The wind tunnel used by German scientists at Peenemünde prior to and during WWII is an interesting example of the difficulties associated by extending the useful range of large wind tunnels. By the end of the Second World War, the US had built eight new wind tunnels, including the largest one in the world at Moffett Field near Sunnyvale, California, and a vertical wind tunnel at Wright Field. Later on, wind tunnel study came into its own: the effects of wind on man made structures or objects needed to be studied when buildings became tall enough to present large surfaces to the wind, and the resulting forces had to be resisted by the building's internal structure. Determining such forces was required before building codes could specify the required strength of such buildings and such tests continue to be used for large or unusual buildings. Still later, wind-tunnel testing was applied to automobiles, not so much to determine aerodynamic forces per se, but more to determine ways to reduce the power required to move the vehicle on roadways at a given speed.

The flow conditions in a wind tunnel are not completely the same as in

"free air". This happens because of constraints due to the tunnel walls and scale effects, which are discussed in Section 6.5 and 6.6.2.

6.2 The VEDSC model

The aircraft model for the wind tunnel has been designed to have interchangeable components. The aim is to reproduce the configurations investigated by numerical analyses. Most of the layouts described in Chapter 5 have been, in fact, reproduced. The design effort resides in the practical realization of such a *modular model*. It must be easy to manufacture and assembly. The geometric *numerical* model for the CFD analyses has been designed to comply with these requirements, but the *physical* model for the wind tunnel analyses must also be easy to setup quickly, since the objective of the experimental investigations is to provide aerodynamic data (force and moment coefficients) for many configurations. For the evaluation of the VEDSC method described in Chapter 5 it is sufficient to get data in the linear range of the incidence angles, even if the wind tunnel tests will provide results in the whole range of angles of sideslip. Therefore, the time to switch among configurations must be as short as possible. Moreover, to assess the effects of aerodynamic interference on the vertical tail, a solution allowing the *direct measure* of the aerodynamic force on the empennage has been designed.

To comply with the above stated requirements, the experimental model is made from the following main components:

1 fuselage nose;

1 fuselage cabin;

3 fuselage tail-cones;

1 wing;

2 horizontal tailplanes (2 semi-span pairs);

3 vertical tailplanes.

The model main dimensions are reported in Figure 6.1. It is 2.0 m long and 1.5 m wide. The wing span is limited by the wind tunnel test section

TABLE 6.1: Bill of materials. Surface and volume are reported only for the machined components. Items ID are shown in Figure 6.2.

ID	Description	Q.ty	Surface (cm^2)	Volume (cm^3)
1	Sheet covering wind tunnel balance	1	n.a.	n.a.
2	Fuselage nose	1	2201.66	7789.57
3	Fuselage tail-cone $z_{ftc}/r_f = 1$	1	4343.85	13 730.58
4	Fuselage cabin	1	10 142.43	29 703.78
5	Left horizontal tail (fuselage)	1	592.19	280.54
6	Right horizontal tail (fuselage)	1	591.63	280.66
7	Left horizontal tail (T empennage)	1	690.67	325.44
8	Right horizontal tail (T empennage)	1	690.01	325.60
9	Vertical tail web	3	n.a.	n.a.
10	T empennage cover	1	92.88	19.14
11	Vertical tail $A_v = 1.0$	1	1019.83	606.92
12	Vertical tail $A_v = 1.5$	1	1296.00	796.99
13	Vertical tail $A_v = 1.0$	1	1508.75	916.57
14	Vertical tail cover	3	225.51	91.37
15	Horizontal tail spar (bar)	4	n.a.	n.a.
19	Interface plate wind tunnel balance	1	n.a.	n.a.
20	Wind tunnel balance	1	n.a.	n.a.
21	Fuselage tail-cone $z_{ftc}/r_f = 0$	1	4396.79	13 528.05
22	Fuselage tail-cone $z_{ftc}/r_f = 0.5$	1	4468.52	13 316.18
24	Wing-fuselage cover (bottom)	1	357.16	142.87
25	Wing-fuselage cover (top)	1	287.28	77.55
26	Wing	1	5691.37	5105.80
27	Trimming support plate	1	n.a.	n.a.
28	Vertical tail load cell support plate	1	n.a.	n.a.
29	Vertical tail support plate	1	n.a.	n.a.
30	Stern fillet	1	59.65	25.93
31	Sheet covering fuselage tail-cone	1	n.a.	n.a.

width. The aspect ratio is held to $\mathcal{AR} = 8.3$. The model total height (with the longest vertical tail span) is about 0.6 m.

The complete list of the components is reported in Figure 6.2 and Table 6.1. The dimensions of the main components are reported in Table 6.2 and 6.3. Detailed descriptions are in the following sections. The CAD model has been realized in SOLIDWORKS®. The physical realization of the model is described in Section 6.3. The CAD drawings of the main components and metal parts are reported in Appendix B.

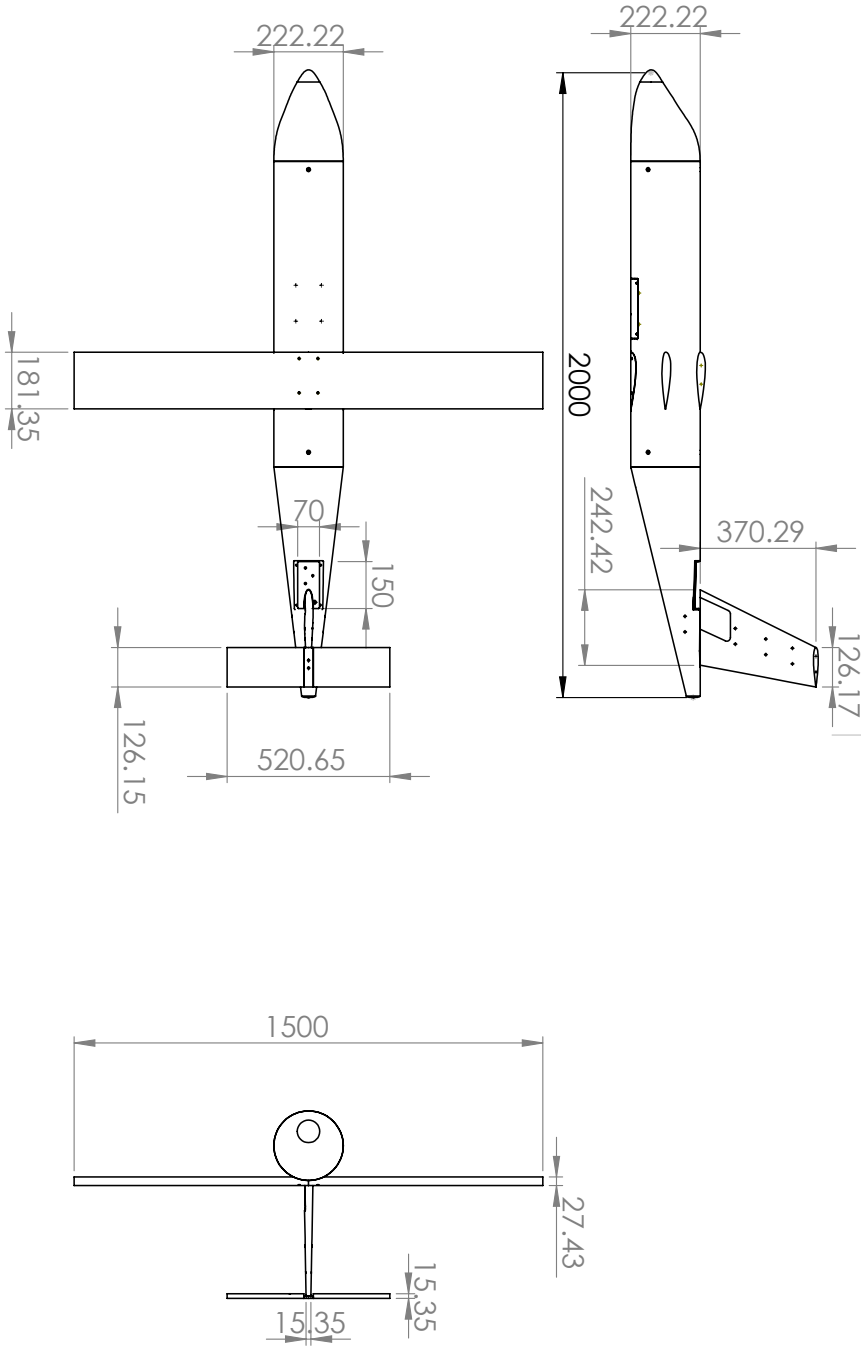

FIGURE 6.1: VEDSC model main dimensions. Units in mm.

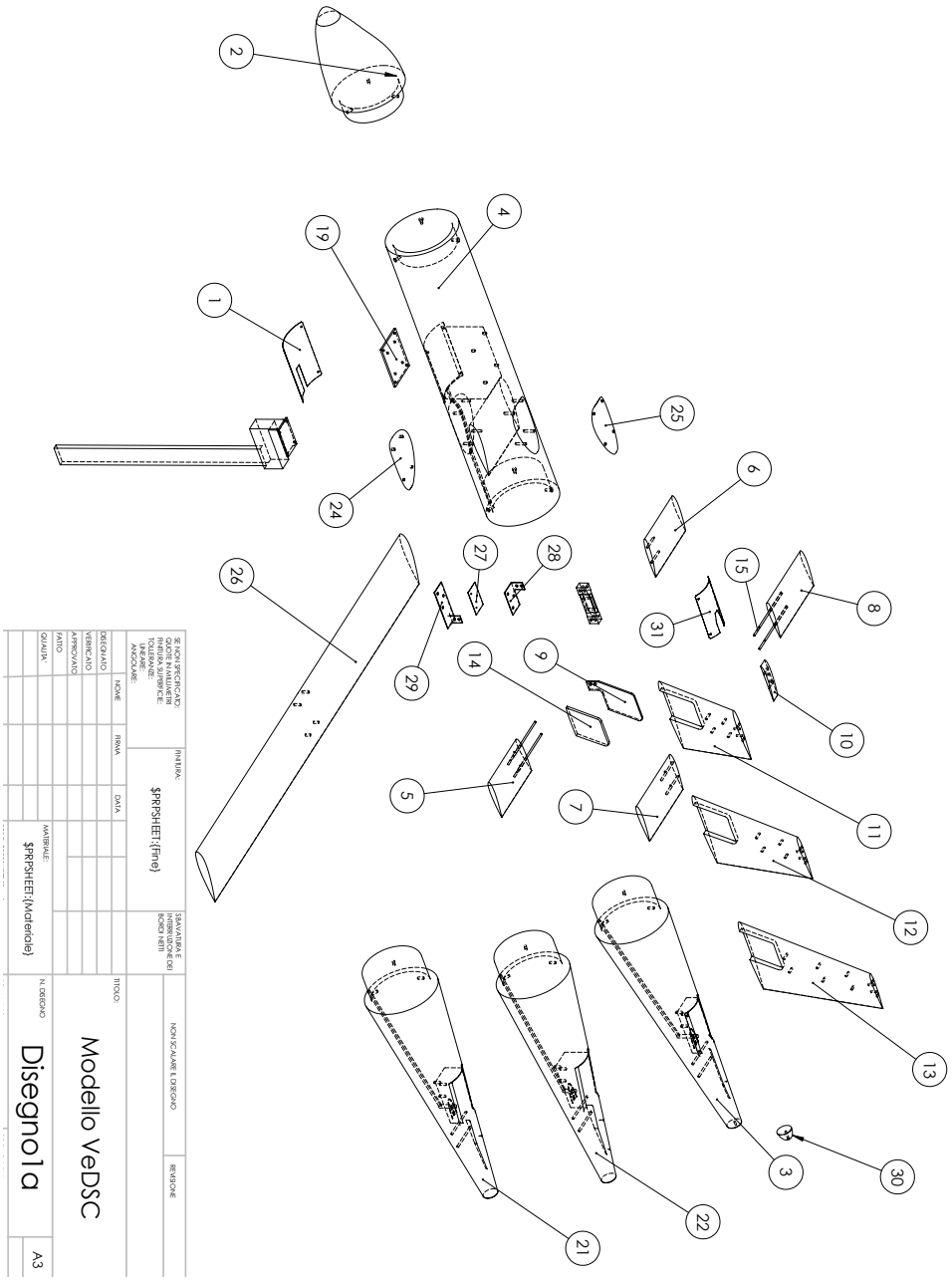

FIGURE 6.2: VeDSC model exploded view. The markings correspond to the items ID of Table 6.1.

TABLE 6.2: Dimensions of the fuselage components of the VEDSC model. Items ID are shown in Figure 6.2.

ID	Description	Length (m)	Width (m)
2	Fuselage nose	0.293	0.222
3, 21, 22	Fuselage tail-cone	0.733	0.222
4	Fuselage cabin	0.978	0.222

TABLE 6.3: Dimensions of the lifting surfaces of the VEDSC model. Items ID are shown in Figure 6.2.

ID	Description	$\mathcal{AR}$	λ	S (m^2)	c_{root} (m)	c_{tip} (m)	b (m)
26	Wing	8.3	1.0	0.273	0.182	0.182	1.5
5 to 8	Horizontal tail	4.1	1.0	0.066	0.128	0.128	0.521
11	Vertical tail	1.0	0.73	0.044	0.242	0.177	0.210
12	Vertical tail	1.5	0.62	0.058	0.242	0.151	0.295
13	Vertical tail	2.0	0.53	0.068	0.242	0.128	0.370

6.2.1 Fuselage nose

The fuselage nose is the component shown in Figure 6.3. The cylinder extruded from its rear is needed to attach the fuselage nose to the cabin and fix their relative positions by three countersunk M6 screws. To provide assembly tolerance when coupling nose and cabin, the extruded cylinder is 0.6 mm smaller in diameter than the hollow counterpart of the cabin.

6.2.2 Fuselage cabin

The fuselage cabin (Figure 6.4) is the central component to which all the other main parts are linked. It provides housing for the wind tunnel balance, obtained by hollowing the central, lower part, see Figure 6.5. It allows the wing to be placed in low, mid, and high position. The mid position is obtained by hollowing the cabin from side to side. This feature has been realized in the CAD model by placing the wing airfoil in the airplane symmetry plane, at the mid wing position, then making an offset of 0.3 mm to provide assembly tolerance, and finally extruding the airfoil shape in both normal directions to subtract material from the cabin solid. The high and low wing locations have been obtained by performing a boolean subtract operation

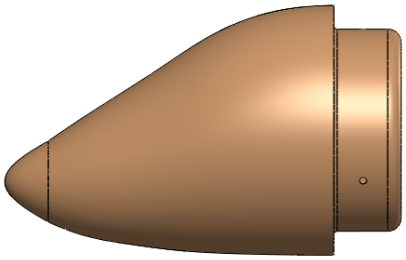

FIGURE 6.3: Fuselage nose.

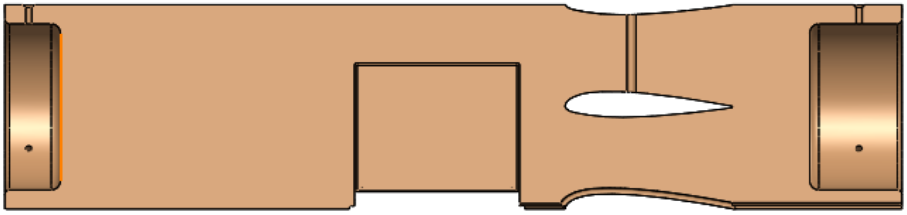

FIGURE 6.4: Fuselage cabin longitudinal section.

between the wing in those positions and the fuselage. In this way, the wing root chord is tangent to the cabin surface. Four countersunk M6 screws have been provided to keep the wing in the high and low positions.

6.2.3 Wing

The wing is shown in Figure 6.6. The airfoil section is a NACA 23015, typical for regional turbopropeller transport airplane. The wing has a straight untapered planform of 1.5 m span and 8.3 aspect ratio. The effects of the latter have not been investigated experimentally. As previously stated, the wing span, and hence the aspect ratio, is limited by the wind tunnel test section width. Four countersunk M6 screws are used to attach the wing in high and low positions in fuselage.

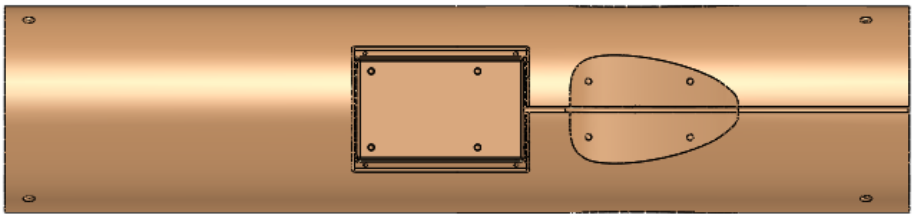

FIGURE 6.5: Fuselage cabin bottom.

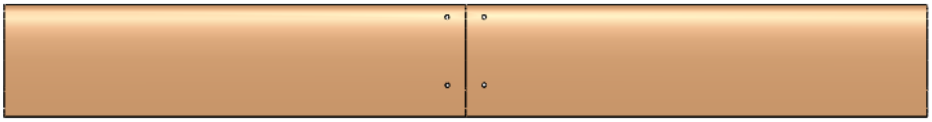

FIGURE 6.6: Wing.

6.2.4 Vertical tail

Three vertical tails, shown in Figure 6.7, are provided. The airfoil section is the NACA 0012. The root chord and the sweep angle is the same for the three planforms. The aspect ratios A_v investigated are 1.0, 1.5 and 2.0. In the CAD model, the three vertical tails have been obtained from the $A_v = 2.0$ planform by cutting the solid with a plane parallel to the root section. Each planform presents pairs of holes at several span stations. These are used to insert the horizontal tail spars to get different empennage configurations. The T-tail configuration presents an additional element, shown in Figure 6.8a and attached on the vertical tail tip (Figure 6.8b), to provide a continuos surface on the horizontal stabilizer (Figure 6.8c).

The vertical tail is linked to the fuselage by a plate, acting as a structural web and shown in Figure 6.9a, which is sunk in the former. To comply with production requirements (see Section 6.3), the internal volume that receives the vertical tail plate has been obtained by removing material from the vertical tail by extruding the plate right section with offset edges, then providing a covering part, obtained by a boolean association between the

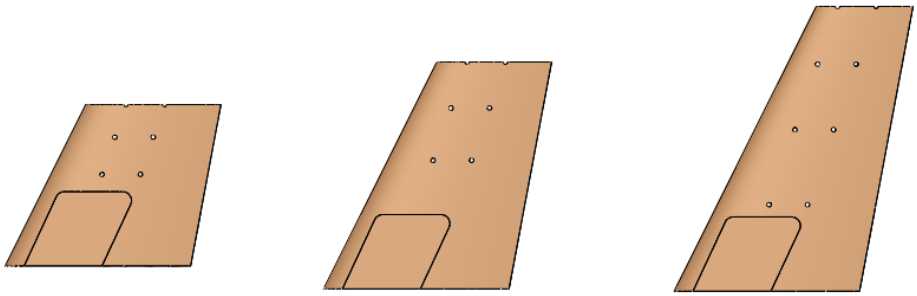

FIGURE 6.7: Vertical tails comparison.

plate extruded left section and the uncut vertical tail[1], to be glued on the plate and on the vertical stabilizer, shown in Figure 6.9b. An assembly tolerance of 1.5 mm has been given to glue the plate on the vertical tail and on its cover.

6.2.5 Fuselage tail-cone

Three fuselage tail-cones, shown in Figure 6.10, are provided to investigate the effects of the wing-body wake on the empennage. To get experimental data about the vertical tail in various aircraft configurations, the vertical stabilizer must be attached to a separate load cell, which, in turn, is attached to the fuselage. The space to allow load cell and empennage mounting is shown in Figure 6.11. It provides enough volume to protect the load cell and supporting plates from the aerodynamic flow. A duct has been designed to allow the data acquisition cable to be taken from the load cell to the wind tunnel instrumentation, through a slot on the bottom fuselage surface. The slot continues on the fuselage cabin, as shown in Figure 6.5, allowing the cable to be taken to the wind tunnel balance sting, thus avoiding aerodynamic interference. The tail-cone is a crucial component, because it must:

[1]The right and left sections of the vertical tail plate are equal, but they are obviously separated by the plate thickness. The removal volume made by the (in-plane) offset of the right section edges creates a hollowing in the vertical tail (with assembly tolerance), while the extrusion of the left section (without edges offset) creates a dummy volume to be associated to an uncut copy of the vertical tail solid and it is needed to create the vertical tail cover.

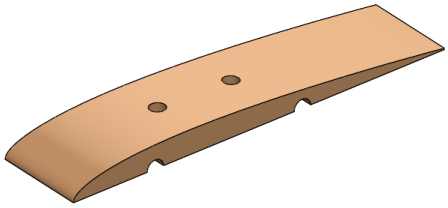

(A) Cover of the T-tail configuration.

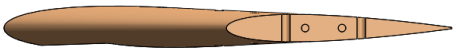

(B) Vertical tail tip with holes to attach the tip cover.

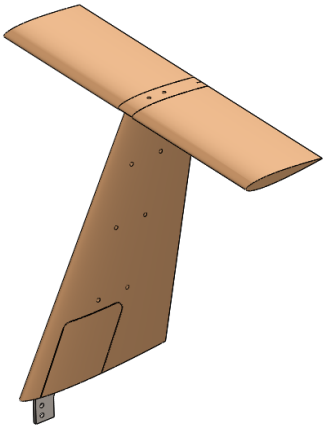

(C) T-tail configuration.

FIGURE 6.8: Arrangement for the T-tail configuration.

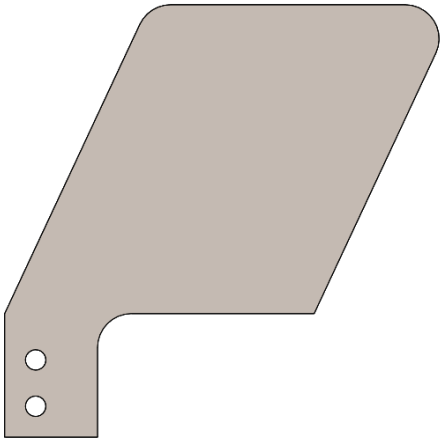

(A) Plate (web).

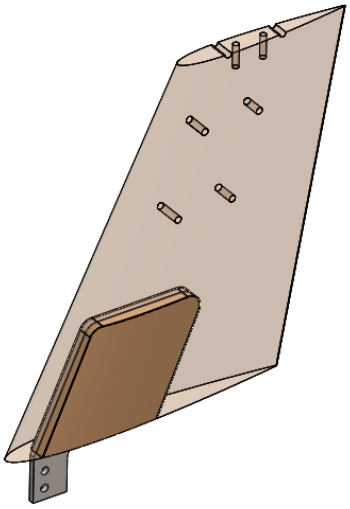

(B) Assembly.

FIGURE 6.9: Vertical tail plate and cover.

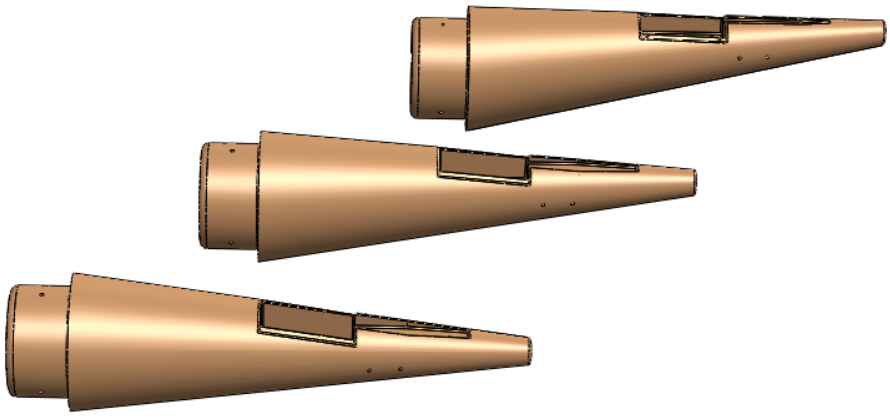

FIGURE 6.10: Fuselage tail-cones comparison.

- support the empennage;
- be stiff enough to not be deformed under aerodynamic loads;
- be easily handled during the change of configuration;
- not weigh too much on the fuselage cabin.

The only constraint between the vertical tail and the fuselage is the load cell, described in Section 6.4.1 and shown in Figure 6.12, which is linked to the fuselage on one side and to the vertical stabilizer on the other side. Thus, the latter is suspended on the load cell, since no contact can be allowed with the fuselage to avoid the *direct* transmission of the aerodynamic loads from the tail to the body, in order to measure the aerodynamic forces acting on the vertical tail in a given aircraft configuration. For this reason, an empty space few millimeters thick between the vertical tail root section and the fuselage has been provided. The empennage assembly is shown in Figure 6.13 and a description of the load path is reported in Figure 6.14. The idea is to get aerodynamic data from both the vertical tail (through the load cell) and the entire aircraft (through the wind tunnel balance) at the same time, to evaluate the aerodynamic interference following the approach of the VEDSC method of Section 5.

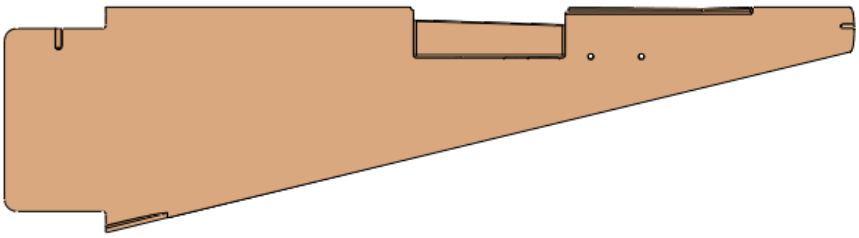

(A) Tail-cone longitudinal section.

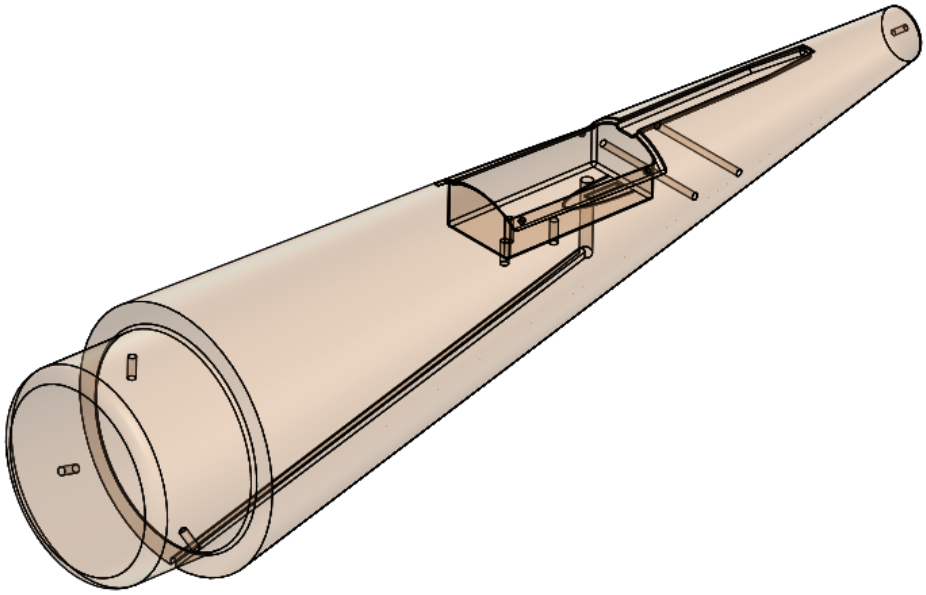

(B) Tail-cone in transparency.

FIGURE 6.11: Fuselage tail-cone details.

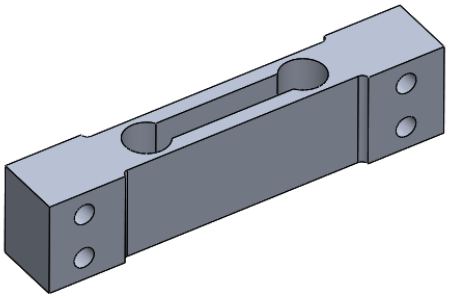

FIGURE 6.12: Vertical tail load cell.

If, for any reason, it is not possible to proceed with the direct measurement of the aerodynamic force on the vertical stabilizer, another supporting plate will provide a direct attachment between the fuselage and the vertical tail, as shown in Figure 6.15. This substitutes the assembly of Figure 6.13. The supporting plates are shown in Figure 6.16.

6.2.6 Horizontal tail

There are two pairs of horizontal tail semi-spans, shown in Figure 6.17: one for the body-mounted tail configuration (Figure 6.17a) and the other for the tail-mounted configuration (Figure 6.17b). Both have been obtained by extruding a NACA 0012 section, but the former has been cut such to be fit on the fuselage tail-cone. The tail spars are two aluminum bars that are fixed to one side and can be locked on the other side by two M2 screws.

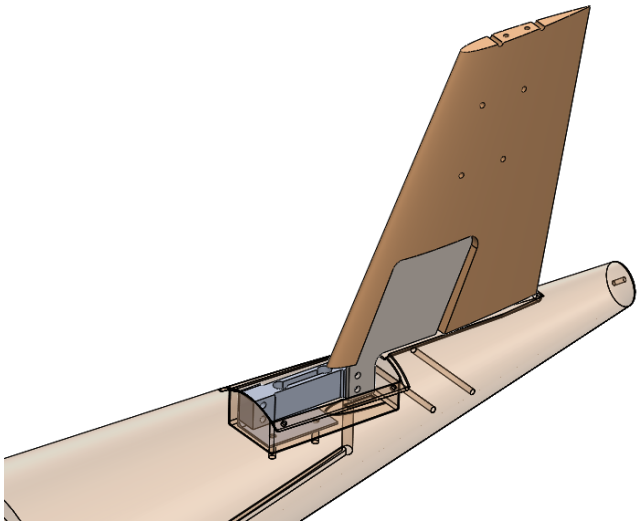

FIGURE 6.13: Vertical tail assembly with load cell.

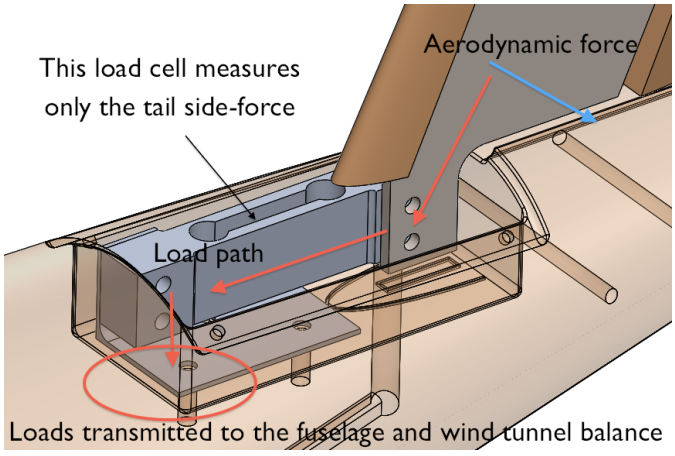

FIGURE 6.14: Loads path with the vertical tail load cell.

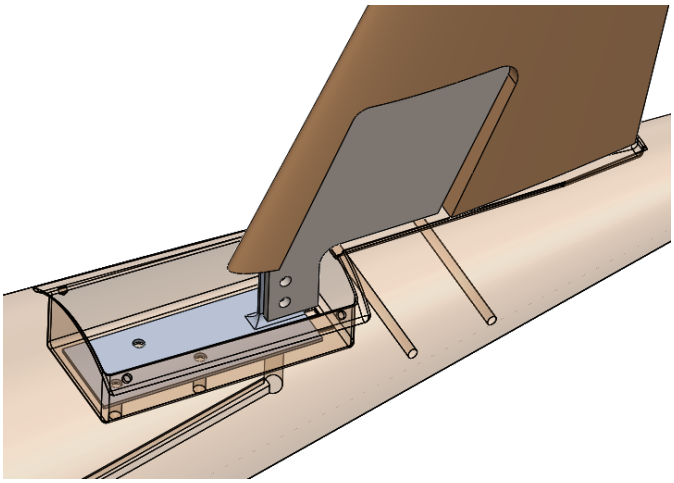

FIGURE 6.15: Vertical tail assembly without load cell.

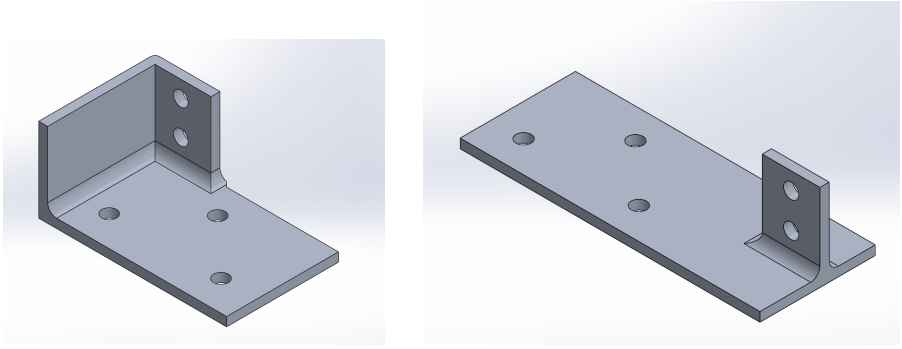

(A) Load cell supporting plate. (B) Vertical tail supporting plate.

FIGURE 6.16: Tail supporting plates. They cannot be used at the same time.

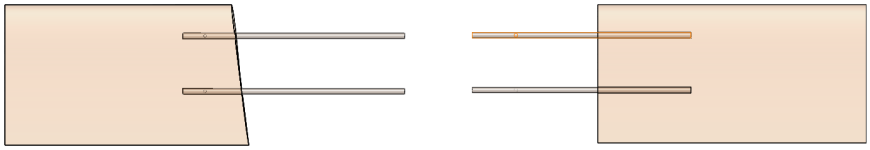

(A) Body-mounted. (B) Tail-mounted.

FIGURE 6.17: Horizontal tails.

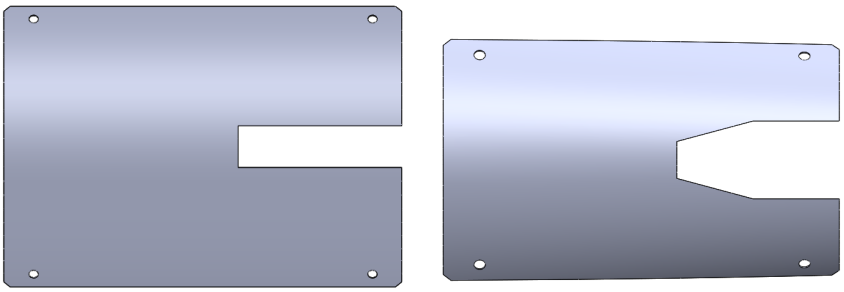

(A) Wind tunnel balance cover. (B) Tail load cell cover.

FIGURE 6.18: Covering aluminum sheets.

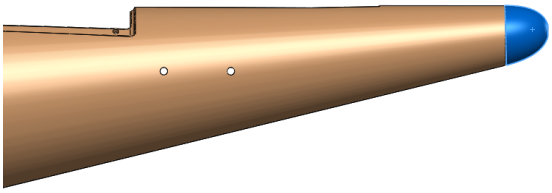

FIGURE 6.19: Tail-cone stern fillet.

6.2.7 Other small components

The other items not presented in the previous section are here described:

- the wind tunnel balance and the tail load cell are covered by folded metal sheets, shown in Figure 6.18;
- the tail-cone stern can be filleted by adding the item shown in Figure 6.19;
- the iron interface plate between the lateral-directional wind tunnel balance (Section 6.4.1) and the model is shown in Figure 6.20.

An example of the assembled model is given in Figure 6.21.

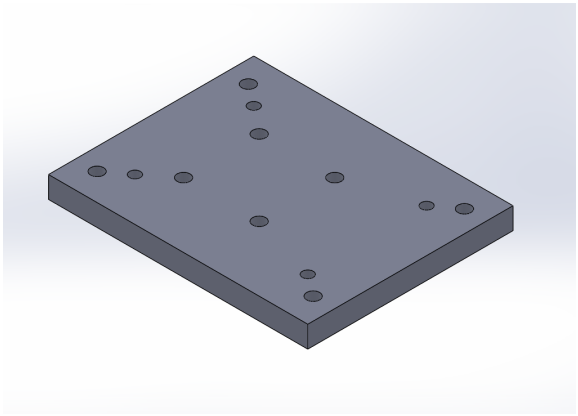

FIGURE 6.20: Wind tunnel balance interface plate.

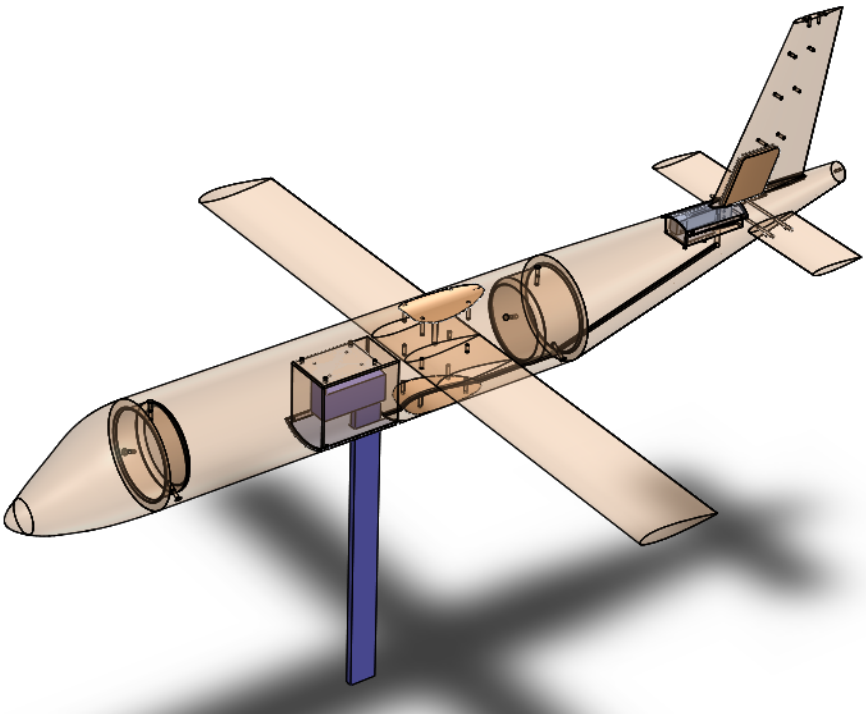

FIGURE 6.21: Example of a configuration of the assembled model.

TABLE 6.4: PROLAB 65 properties.

Property	Unit	Value
Color	n.a.	brown
Density at 23 °C	g/cm^3	0.65
Hardness	Shore D1	63
Flexural modulus	MPa	1000
Flexural strength	MPa	34
Compressive strength	MPa	28

6.3 Manufacturing the model

The CAD model has been mainly realized by computer numerical control (CNC) milling. The non-metal parts are made from a high density machinable polyurethane slab named PROLAB 65 (Table 6.4), which has the following characteristics (as reported in the specification sheet):

- non-porous material;
- excellent surface aspect (direct paint after sanding);
- very good dimensional stability;
- machining by hand or by machine with wood or aluminum cutting tools.

The complete model weighs up to 40 kgf, with a center of gravity close to the wing leading edge. The total milled surface is about 3.90 m^2. The total production cost is about 7000 € + VAT.

Some features of the CAD model have been developed in collaborations with production engineers. *Even for a simple layout, design is an iterative process.* These features are here listed:

- the length and the fillet radius (12 mm) of the nose and tail-cone attach cylinders (Figure 6.3 and 6.10);
- the 0.6 mm diameter tolerance on the connections;
- the diameters of the holes that receive the threaded bushings;

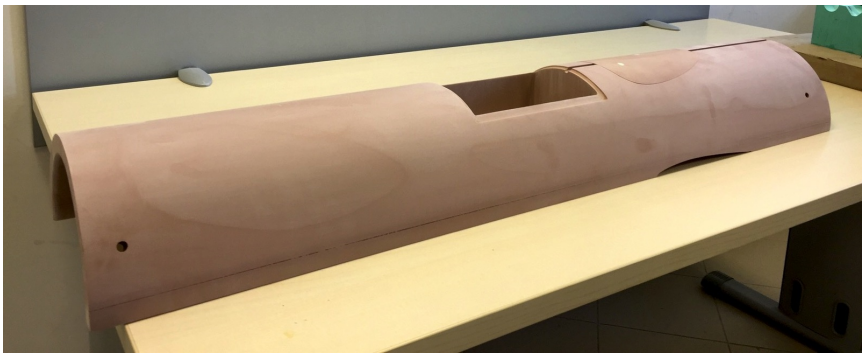

FIGURE 6.22: The machined fuselage cabin.

- the 0.8 mm thickness of the wing and tail trailing edges;
- the 1.5 mm tolerance between the vertical tail and its plate (web);
- the 3 mm radius of internal fillets.

Threaded bushings have been provided to limit the use of self-threading screws, which may become loose after numerous changes of configuration, and to ensure a safe and recurring assembly.

The fuselage cabin has been produced in two parts, separated on the horizontal plane as shown in Figure 6.22, since it was not possible to provide the mid wing location by milling 22 cm deep with a minimum thickness of 0.8 mm on the wing trailing edge.

The socket in the vertical tail receiving its (web) plate, as described in Section 6.2.4, has been designed according to production tools requirements: the left side of the vertical stabilizer is cut by the CNC mill and a cavity is created to allow the plate of Figure 6.9 to be positioned and glued. The section has large radii of curvature on the edges, but it is flat on its side, and it has 0.75 mm offset on each side to provide space for the glue between the plate and the vertical tail. The cover has the same width of the plate, allowing the same tolerance. Its shape is such that it closes the socket, providing a continuos external surface. Most of the components, finished and painted, are shown in Figure 6.23.

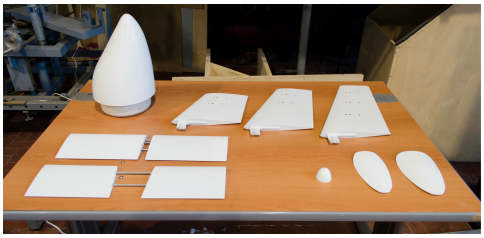

(A) Small components.

(B) Fuselage tail-cones.

(C) Sterns of the tail-cones.

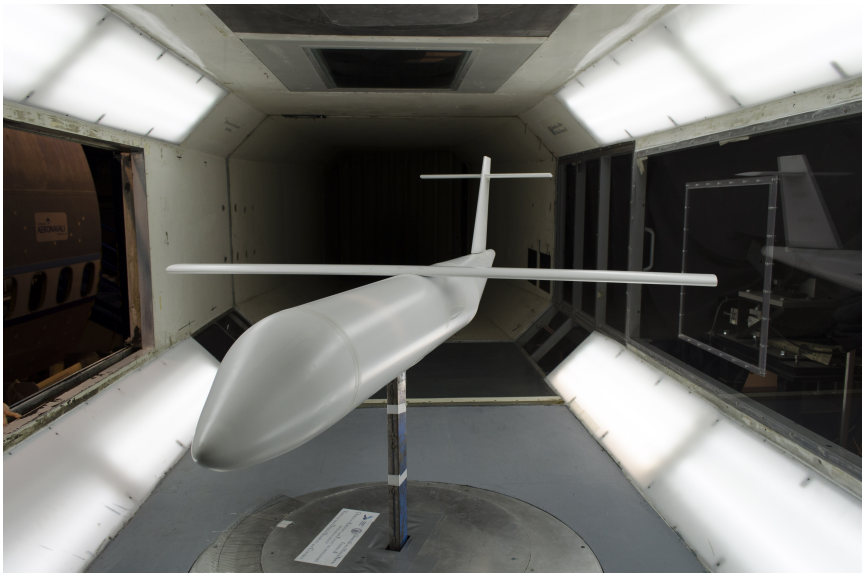

(D) The model in the test section.

FIGURE 6.23: Components of the manufactured model.

Table 6.5: Wind tunnel of the DII, main characteristics.

Test section dimensions	2.0 m × 1.4 m
Maximum available wind speed	50 m/s
Turbulence level	0.10 %
Maximum power	150 kW

6.4 The wind tunnel

The experimental tests campaign has been performed in the main subsonic wind tunnel facility of the Department of Industrial Engineering (DII). This is a subsonic, closed circuit tunnel, with a tempered rectangular cross section, as shown in Figure 6.24. The main wind-tunnel characteristics are summarized in Table 6.5. The main components of the closed circuit tunnel are described in the following. Capital letters refer to the sections of Figure 6.24b.

Test section It is 4 m long, 2 m wide, and 1.4 m high, with a rectangular, with tempered corners, cross-section of 2.68 m^2. Sections from A to B.

Diffuser There are three diffusers in order to slow down the airflow coming from the test chamber. The first diffuser (B-C) has a length of about 5 m and an expansion angle of about 3° and it links the last section of the test chamber to the first corner. The second diffuser (D-E) is placed between the first two corners and has a length of about 1.8 m. The last diffuser (G-I) is the longest one (about 12.3 m), it increases the tunnel section with an expansion angle of about 3°, and it is placed between the second and the third corner.

Screen It is placed immediately before the first corner (section C), with the aim to protect the turning vanes against any possible object or scrap that could be lost by the model in the test section. The screen has squared cells of about 13 mm per edge.

Corners The first corner (C-D) is placed behind the first diffuser and has a constant section with turning vanes with a chord of about 450 mm and a maximum thickness of 14.4 %. The second corner (E-F) is placed behind the fan and is equipped with tabs having a chord of about 490 mm and maximum thickness of 13.3 %. The second corner section

(A) Main subsonic wind tunnel facility.

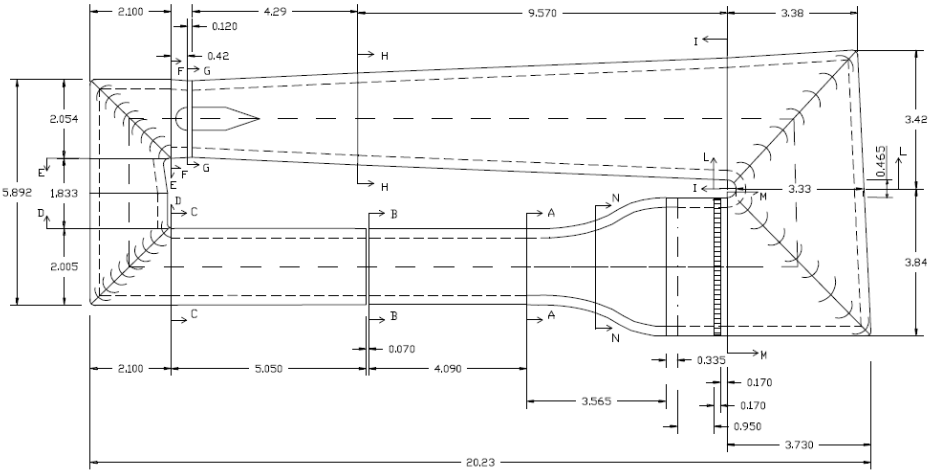

(B) Main subsonic wind tunnel diagram.

FIGURE 6.24: Main subsonic wind tunnel od the DII.

is slightly divergent, such as the third and the fourth corner. The third corner (I-L) has diverters with a chord of 925 mm and maximum thickness of 17.3 %, whereas the fourth corner (L-M) tabs have a length of 875 mm with a maximum thickness of 18.3 %.

Fan It is placed immediately ahead of the second corner (D-E). Upstream the six blades propeller, a four blade flow straightener ring is placed. The ogive of the fan has a maximum diameter of 700 mm.

Honeycomb flow straighteners They are elliptical section cells placed at the beginning of the stagnation chamber. Section M.

Mesh screen It has the function to reduce the turbulence axial component of the flow in the test section allowing a turbulence level of 0.10 %.

Stagnation chamber It has a length of 0.035 m and it is placed ahead of the nozzle. Section M.

Nozzle It has a length of 3.56 m, with an inlet section of about 12.7 m^2 and an outlet section of 2.7 m^2, with a ratio of 4.83. Sections from M to N.

6.4.1 Available instrumentation

The *measurement instrumentation* consists of an internal strain gage balance for the measurement of aerodynamic forces and moments, a Venturi system to measure the dynamic pressure, an inclinometer to measure the angle of attack, a potentiometer to measure the sideslip angle, and a temperature probe to measure the static temperature in the test section. Some details are given in the following.

Internal strain gage balance It has three channels and it is used to measure the sideforce, yawing moment, and rolling moment. It is made from an Al-2024-T3 aluminum block, shown in Figure 6.25. The calibration has been previously performed by Corcione [93], who followed the procedure described in the book of Barlow, Rae, and Pope [95, §7.6]. The calibration procedure is also essential to estimate the balance center in order to transfer forces and moments to the desired reference point, e.g. the 25 % of wing m.a.c. Table 6.6 summarizes the maximum error found for the balance readings after the calibration procedure. The maximum error in average is about 0.1 % of the full

scale maximum load of each measured force or moment. The actual balance readings have been deeply verified by applying the combination of predicted loads to be encountered during the tests. Corrections have been provided to account for the combination of weight, pitching moment, rolling moment, and yawing moment, due to the particular layout of the test model, see Section 6.6.1.

Off-center load cell It is a Picotronik AAC model, used to directly measure the sideforce generated by the vertical tail. It is made from aluminum alloy and it has 15 kgf full scale, with 2.0 mV/V ±10 % nominal sensitivity. Its dimensions are $130 \times 30 \times 22$ mm. The load cell can measure forces in the side direction, colored in white in Figure 6.26. Its location on the model has been shown in Figure 6.14, whereas its calibration and installation are discussed in Section 6.6.1.

Venturi The wind tunnel of the DII is equipped with 4 static pressure probes placed on both faces of initial and final sections of the nozzle. A pressure transducer (with 2500 Pa full scale and 3 Pa accuracy) measures the static pressure variation between these sections and, through the continuity equation, gives the dynamic pressure at the exit of the nozzle. Several tests without the model in the test section and at different air speeds have shown that the dynamic pressure at the end of the nozzle is 1.09 the measured dynamic pressure. Since it is impossible to use a Pitot probe to measure the dynamic pressure in the test section in presence of the scale model (the test section should be long enough to guarantee that the measure is not affected by the pressure field produced by the model in the test section), the only available measure of the dynamic pressure is obtained by the Venturi, thus the above-mentioned 9 % increase is assumed to be valid also with the model in the test section.

Inclinometer It is the uni-axial tilt sensor CXLA01, produced by CrossBow (San Jose, CA, USA). The sensor measures the component of the acceleration of gravity that lies in the plane of the instrument reference face. The inclinometer has been mounted on the sting of the wind tunnel balance.

Potentiometer The sideslip angle has been measured through the use of a potentiometer with an accuracy of 0.1°. Once installed, the available

Table 6.6: Strain gage balances margin of error.

Force/Moment	Max. Error	Full scale
Sideforce	0.02 kgf (0.1 %)	20 kgf
Yawing moment	0.02 kgf · m (0.1 %)	20 kgf · m
Rolling moment	0.02 kgf · m (0.1 %)	20 kgf · m

range for the sideslip angle β is from $-15°$ to $25°$. The sideslip angle has been defined positive when the airflow comes from the left wing of the model. This is the opposite of the usual convention [16, §8.1], because of the operator's point of view of the test chamber.

Temperature probe It consists of a flush wall-mounted probe for the measurement of the static temperature in order to determine the true test section speed through the use of Bernoulli's incompressible equation and to obtain the mass density through the equation of state. The temperature measurements are also needed to take under control the heating of the strain gage sensors that are affected by temperature change, which during a test ranges from 30 °C to 50 °C, according to environment temperature too.

The *control instrumentation* used in this test campaign consists of a kinematic mechanism (handled by the operator) with a crank handle fixed at the end of a horizontal shaft acting as worm-screw. This shaft transmits the rotatory motion to the vertical axis of a small diameter gear wheel. The rotatory motion is then transmitted to a larger gear wheel through a steel chain reducing the angular velocity of the model. A steel plate, which is at level with the floor, is fixed to the axis of the second gear wheel. The steel plate allows the whole assembly sting-balance-model to rotate.

The *instrumentation for acquisition and elaboration* consist of: a 16 channels SPARTAN system (produced by Imc DataWorks, LLC) for the acquisition and conversion into 16 bit of output data coming from the measurement instrumentation; a desktop PC with Windows XP, provided with an interface software for the A/D converter; a software for the elaboration and visualization of the acquired data. The software, named WT6, has been developed by researchers of the DII laboratory.

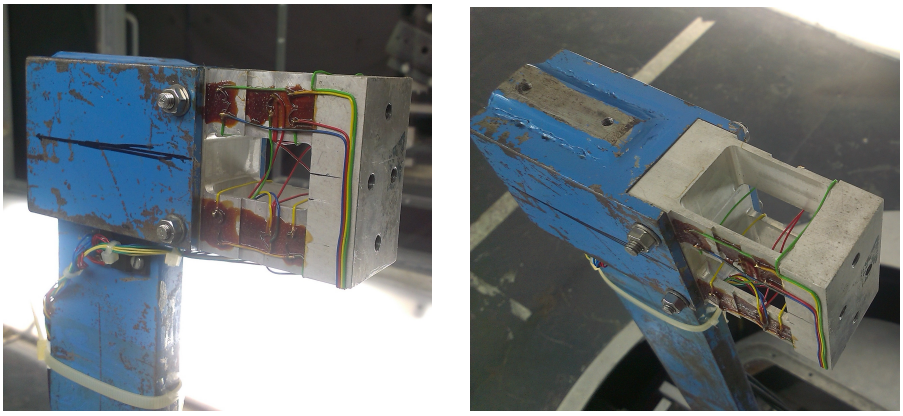

FIGURE 6.25: Lateral-directional internal strain gage balance.

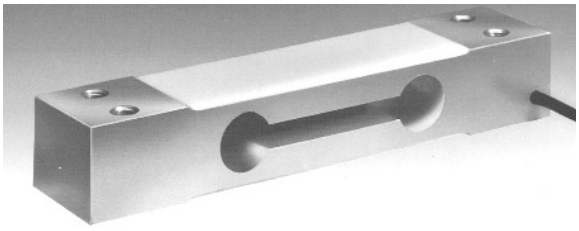

FIGURE 6.26: The off-center load cell.

6.5 Wind tunnel corrections

In wind tunnel testing there are some constraints due by the nature of the tunnel itself. While there is no difference in having the model at rest and the air moving around it, the distances of some or all of the *stream boundaries* from the article under test are usually less than the corresponding distances for actual operations. In addition, the flow properties in the test section may not be the same in space and time. To include appropriate corrections, the following effects must be considered [95, Chap. 9].

Horizontal buoyancy It refers to a variation of static pressure along the test section when no model is present. It produces a drag force analogous to the hydrostatic force on objects in a stationary fluid in a uniform gravitational field.

Solid blockage It is linked to the volume occupied by the model in the test section. This is the most influent effect, since it produces a variation in oncoming dynamic pressure. Essentially, the wind tunnel is a tube where the model in the test section "chokes" the flow. This effect produces surface stresses larger than the corresponding free-air operations. The stress distribution is assumed to be unchanged.

Wake blockage Every body immersed in a moving fluid has a wake, which size is function of the body shape and (in wind tunnel testing) of the ratio between the wake area and the tunnel area. The wake has a mean velocity lower than the free stream. According to the law of continuity, the velocity outside the wake in a closed tunnel must be higher than the free stream. By Bernoulli's principle, the higher velocity in the main stream has a lowered pressure. As the boundary layer on the model (which later becomes the wake) grows, the model is put in a pressure gradient, hence there is a velocity increment on the model.

Streamline curvature It refers to an alteration to the curvature of the streamlines of the flow about a body in a wind tunnel as compared to the corresponding curvature in an infinite stream. In a closed tunnel, the lift, pitching moment, hinge moments, and angle of attack are increased.

Normal downwash change It refers to the component of induced flow in the lift direction at the test article and it is due to the finite distances

to the boundaries. In a closed jet, the lift produced is too large and the drag too small at a given geometric angle of attack, corresponding to a smaller downwash.

Spanwise downwash distortion It refers to an alteration to the local angle of attack along the span of a lifting wing. In a closed test section the angle of attack near the wingtips of a model with large span are increased, making the tip stall start at a lower geometric angle of attack. This effect becomes negligible if the model span is less than 0.8 the tunnel width.

Tail downwash change It refers to an alteration to the normal downwash behind the wing, so that the static stability is unnaturally increased.

These effects have been assessed for the model in all configurations and inserted in the wind tunnel software to have in output both the corrected and uncorrected values. However, for the actual work focused on lateral-directional stability derivatives, differences between corrected and uncorrected results are not negligible only at high angles of sideslip, whereas the slope of the curves are unaffected by corrections. For the complete configuration (wing on, tail on) of Figure 6.27, the effects of corrections are shown in Figure 6.28 and 6.29. Solid blockage for this layout is $\epsilon_{sb} = 0.0115$. The minimum value is obtained with the isolated fuselage and it is $\epsilon_{sb} = 0.0101$.

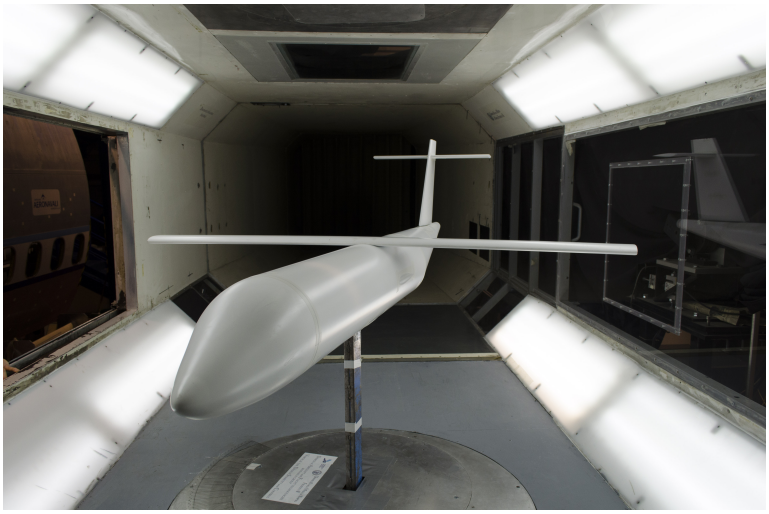

(A) Perspective view.

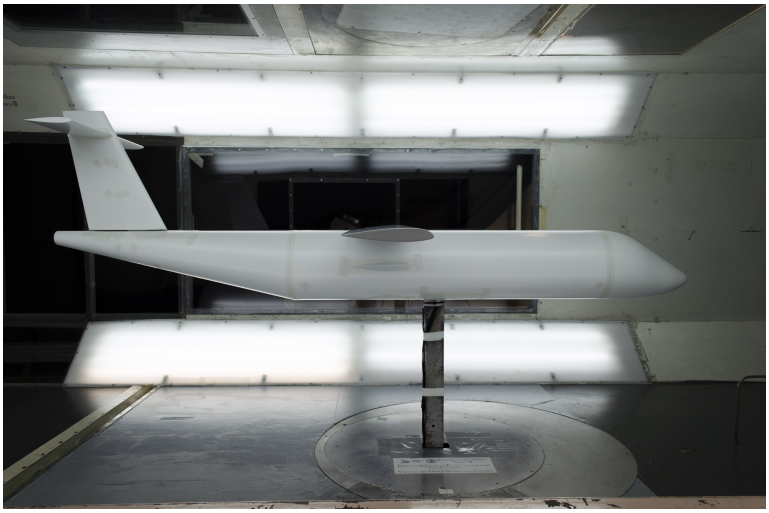

(B) Side view.

FIGURE 6.27: A typical complete model layout, with high wing, high fuselage tail-cone, vertical tail with aspect ratio $A_v = 2.0$ and high horizontal stabilizer.

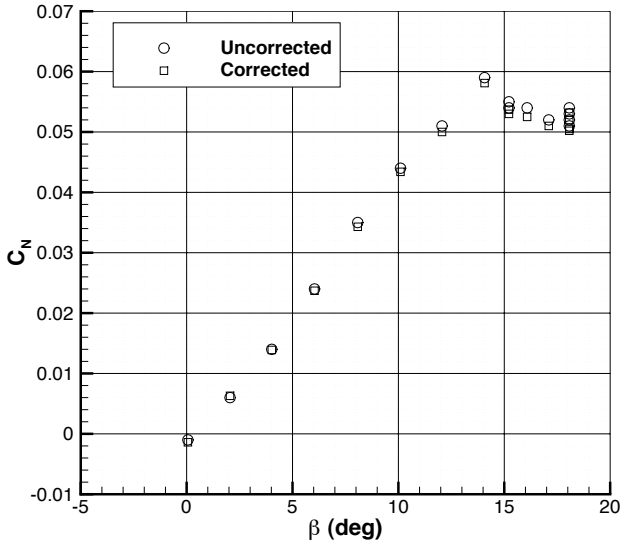

FIGURE 6.28: Effects of wind tunnel corrections on yawing moment coefficient. Solid blockage $\epsilon_{sb} = 0.0115$.

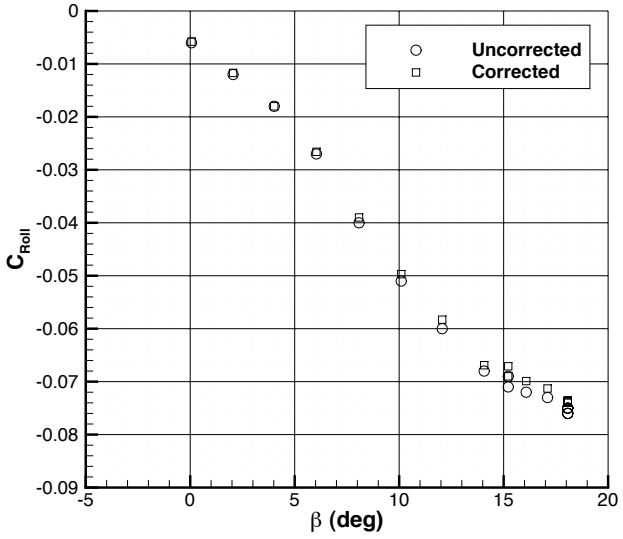

FIGURE 6.29: Effects of wind tunnel corrections on rolling moment coefficient. Solid blockage $\epsilon_{sb} = 0.0115$.

6.6 Setup of the wind tunnel

A preliminary setup of the wind tunnel instrumentation, as well as of the test model, is needed before any operation. The measurement, control, and elaboration instrumentation must be checked. In particular, the wind-tunnel balance readings must be verified (Section 6.6.1). Then, the model can be mounted in the test section and the whole assembly can be verified in place. Finally, the effects of low Reynolds number can be measured and corrected (Section 6.6.2).

6.6.1 Verification of the balance readings

The internal strain gage balance is a very delicate item. Its readings must be checked prior to every test campaign, since it is the main, if not the unique, source of measurement. The verification consists in applying known loads in several positions and acquiring the balance readings. If the acquired data are not consistent with the applied loads, corrections must be provided from the former, e.g. by plotting regression lines that are best fit curves on the charts of gathered data in all load conditions.

For the model investigated, since the balance is located in a hollowing forward of the wing, and the center of gravity is located between the wing aerodynamic center and the leading edge, a balancing mass of about 9 kg has been put in the fuselage nose, to move the center of gravity closer to the balance center and reduce the pitching moment due to weight. This brought the total weight to about 50 kgf, with a pitching moment (due to the inevitable offset between the lift and the balance center) that in the worst case, for the model aircraft in its complete configuration, at no angle of attack and at a wind speed of 40 m/s, is about 1.8 kgf $\cdot$ m. For this reason, the sting of the balance has been stiffened by soldering another iron plate of the same thickness on its side, as shown in Figure 6.30.

The balance readings have been verified in numerous cases, by varying the weight on the balance center, the pitching, yawing, and rolling moments, and the sideforce applied at several distances from the balance center, in both horizontal and vertical directions. Most of the loads have been applied for the above-mentioned weight and pitching moment conditions. Results provided that the yawing moment N is not affected by the eccentricity of the applied loads, whereas the sideforce Y and the rolling moment $\mathcal{L}$ do,

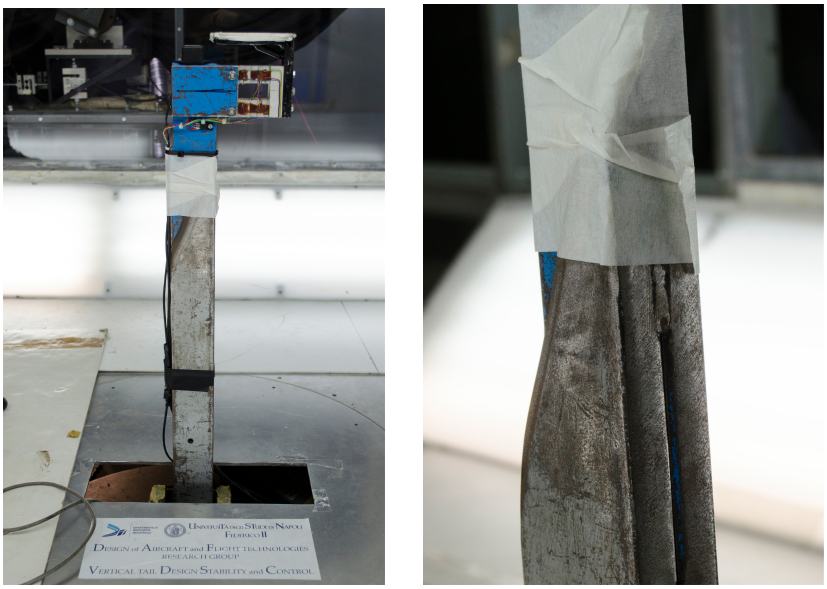

FIGURE 6.30: Strengthened sting balance.

suggesting the following corrections

$$Y_{\text{corr}} = Y_{\text{meas}} - \text{err}_Y(N) - \text{err}_Y(\mathcal{L}_{\text{corr}}) \tag{6.1}$$

$$\mathcal{L}_{\text{corr}} = 0.98\,[\mathcal{L}_{\text{meas}} - \text{err}_{\mathcal{L}}(N)] \tag{6.2}$$

where

Y_{corr} is the sideforce corrected for the effects of yawing and rolling moments

Y_{meas} is the uncorrected sideforce read by the wind tunnel software

$\text{err}_Y(N)$ is the sideforce error due to the applied yawing moment N

$\text{err}_Y(\mathcal{L}_{\text{corr}})$ is the sideforce error due to the corrected rolling moment $\mathcal{L}_{\text{corr}}$

$\mathcal{L}_{\text{meas}}$ is the measured rolling moment

$\text{err}_{\mathcal{L}}(N)$ is the rolling moment error due to the applied yawing moment N.

The error functions are defined as

$$\mathrm{err}_Y(N) = 0.0034N^3 + 0.0040N^2 - 0.0821N \tag{6.3}$$

$$\mathrm{err}_{\mathcal{L}}(N) = 0.0025N^3 + 0.0109N^2 - 0.1118N \tag{6.4}$$

$$\mathrm{err}_Y(\mathcal{L}_{\mathrm{corr}}) = 0.24\,\mathcal{L}_{\mathrm{corr}} \tag{6.5}$$

which allow the correct results in output.

Finally, the off-center load cell (Section 6.4.1) has been calibrated. The procedure is very simple, since it is a single axis load cell. Its end with the acquisition cable has been fixed to a rigid constraint, with the sensible side parallel to the ground. At the other end a known mass has been suspended. From the tension read on the PC display, the tare constant has been calculated from the simple relationship

$$\mathrm{Force} = K_{\mathrm{cell}} \cdot \mathrm{Tension} \tag{6.6}$$

where K_{cell} has the dimension of kgf/V. The tare has then been verified by mounting the cell in the fuselage tail-cone and the vertical tail on the cell and applying a known mass in several positions to check the load cell readings, see Figure 6.31.

6.6.2 Scale effects and trip strips

The term *scale effects* refers to differences that arise when the fluid dynamic dimensionless parameters, mainly the Reynolds number, are not the same in low-speed wind tunnel tests and flight operations. Reynolds number is defined as

$$Re = \frac{\rho V c}{\mu} \tag{6.7}$$

where ρ is the air density, V is the air speed, c is the wing mean aerodynamic chord (which is the reference length), and μ is the viscosity of the air. For a large turbopropeller aircraft, the characteristic wing chord c is between 2.5 and 3.0 m, while the entire aircraft can be 30 m long. It is clear that full Reynolds number are not easily achievable in a wind tunnel, also because of power requirements (see again Table 6.5), unless the air temperature is decreased to reduce its viscosity and the total pressure is increased to arise the air density, as done in high speed wind tunnels [79].

(A) Installation in fuselage tail-cone.

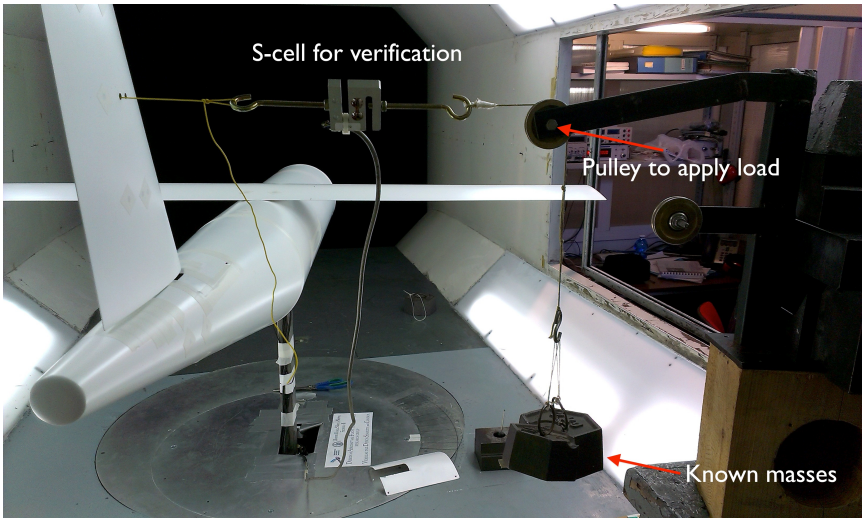

(B) Test by application of a known mass.

FIGURE 6.31: Installation and test of the off-center load cell.

Since the Reynolds number of low-speed wind tunnels cannot be the same of flight conditions, other artifices are needed to replicate the boundary layer of the full scale aircraft, otherwise laminar separations will affect the measurements. A simple and effective mean to comply with this need is the *trip strip*, which is an artificial roughness added to the model to fix the location of the transition from a laminar to turbulent boundary layer on the model [95, §8.2]. A correct installation prevents the realization of laminar bubbles and their consequences on the aerodynamic behavior of the model.

Trip strips made of adhesive tape with triangular edges have been placed on all components of the aircraft in order to promote the transition of the flow. The thickness and the right position of the trip strips has been estimated by tests of flow visualization through the use of fluorescent oil, as shown in Figure 6.32. Results led to the conclusion that two layers of tape are sufficient to get the boundary layer transition at the desired place. The location of the trip strips is at about 5 % local chord for wing and horizontal tail, even closer to the leading edge for the vertical tail, whereas they have been placed at 20 % nose length on the fuselage.

The effects of trip strips are reported from Figure 6.33 to 6.35 and they have been evaluated on the configuration shown in Figure 6.27. It is shown that the slope of the curves is affected by the trip strip, especially the vertical tail contribution, because of the laminar bubble on the un-tripped section.

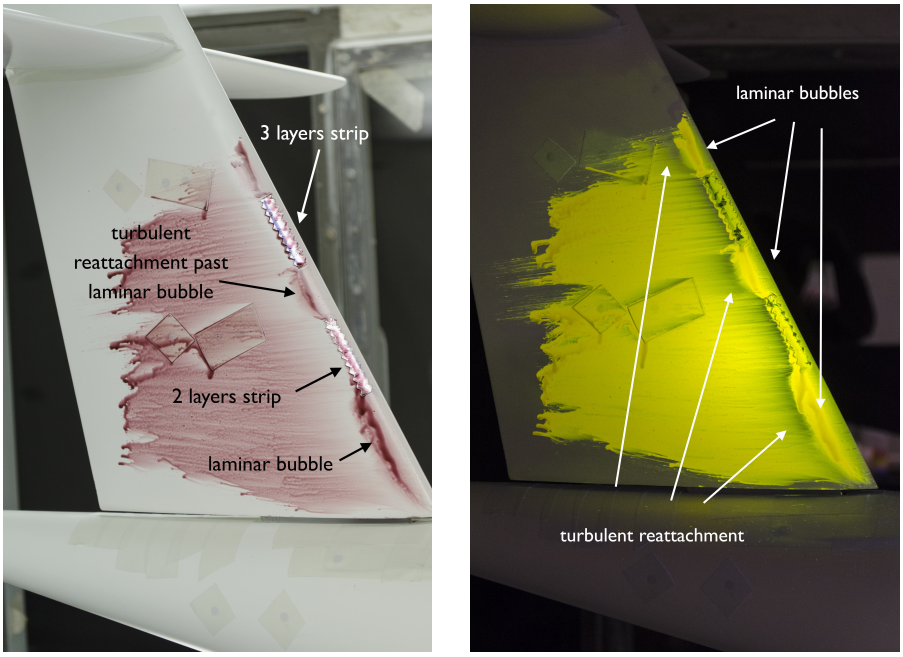

(A) Vertical tail. Airfoil section NACA 0012.

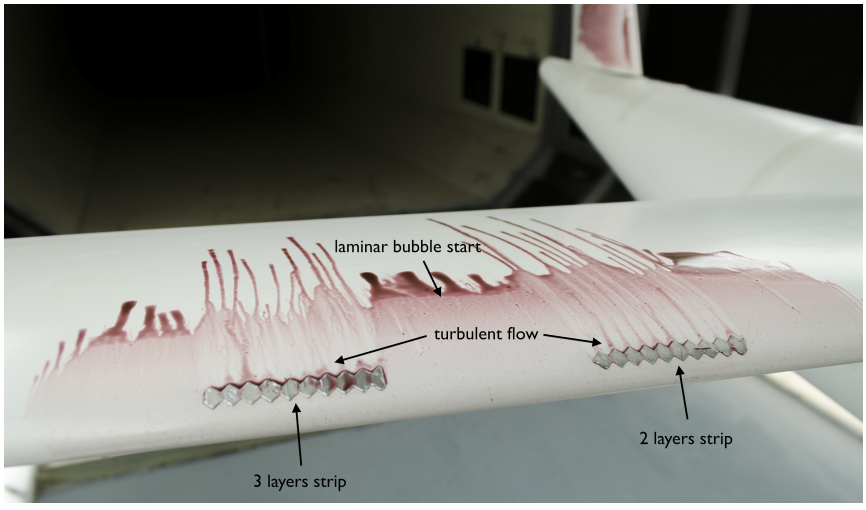

(B) Wing. Airfoil section NACA 23015.

FIGURE 6.32: Flow visualization on wing and vertical tail. Effects of the trip strips at $Re = 470\,000$, $\alpha = 0°$, $\beta = 10°$.

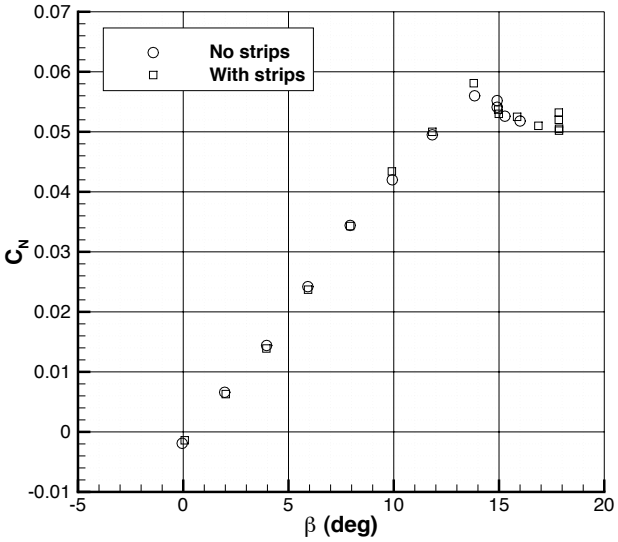

FIGURE 6.33: Effects of trip strips on yawing moment coefficient. $Re = 470\,000$, $\alpha = 0°$.

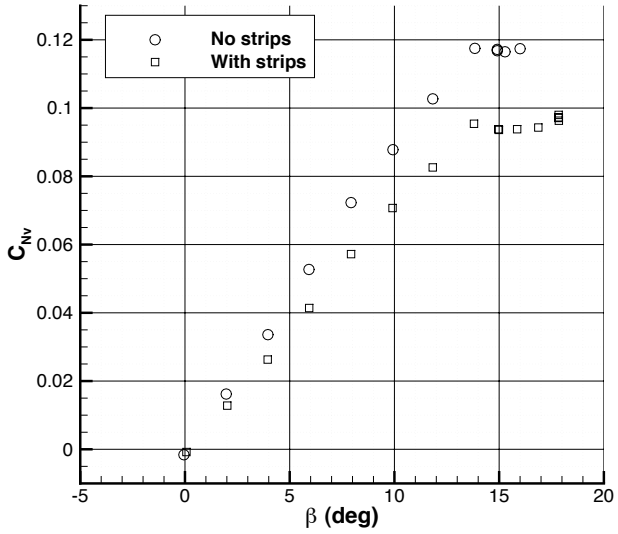

FIGURE 6.34: Effects of trip strips on vertical tail yawing moment coefficient. $Re = 470\,000$, $\alpha = 0°$.

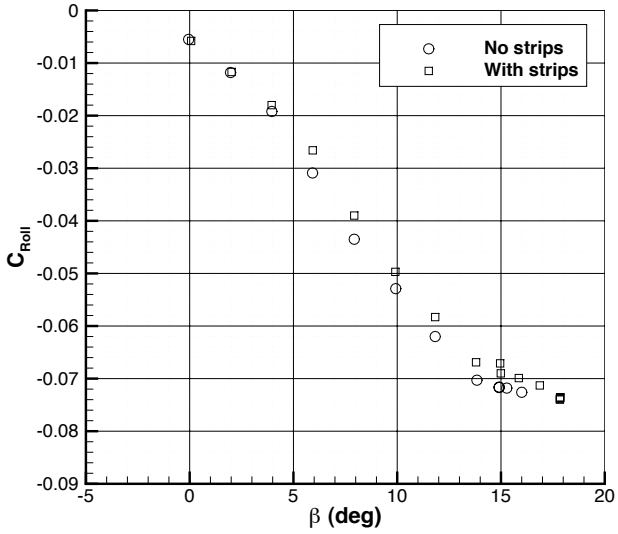

FIGURE 6.35: Effects of trip strips on rolling moment coefficient. $Re = 470\,000$, $\alpha = 0°$.

6.7 Results of the wind tunnel tests

The reference system adopted, shown in Figure 6.36, has the origin of the axes at the balance center, with the x axis parallel to the fuselage waterline and positive towards the fuselage stern, the y axis perpendicular to the symmetry plane and positive towards the right wing, and the z axis perpendicular to the other two and positive upward. The sideslip angle β is considered positive when both the wind components are positive, i.e. when the side wind is coming from the left wing. With this reference system, for a positive sideslip angle β, a yawing moment $N > 0$ means the model is directionally stable, whereas a rolling moment $\mathcal{L} < 0$ means the model is laterally stable. In other words:

$C_{N_\beta} > 0$ is required for directional stability;

$C_{\mathcal{L}_\beta} < 0$ is required for lateral stability.

Yawing, rolling moments, and their derivatives have been reduced to the mid wing aerodynamic center, which is also the reference point in the numerical analyses of Chapter 5. Its location related to the balance center is shown in Figure 6.37. The quantities of interest are the yawing moment coefficient derivative C_{N_β}, the rolling moment coefficient derivative $C_{\mathcal{L}_\beta}$, and the vertical tail yawing moment coefficient derivative $C_{N_{\beta_v}}$, approximated as the incremental ratio

$$C_{x_\beta} = \frac{C_x(\beta_1) - C_x(\beta_2)}{\beta_1 - \beta_2} \tag{6.8}$$

between $\beta = -6°$ and $6°$ (C_{x_β} represents the generic stability derivative). The Reynolds number based on wing mean aerodynamic chord for each test varies from 470 000 down to 450 000 because of the increasing flow temperature, which effects are included in the corrected results. Flow speed is held constant at 35 m/s and the angle of attack α is kept zero. Features of the configurations are shown from Figure 6.38 to 6.41.

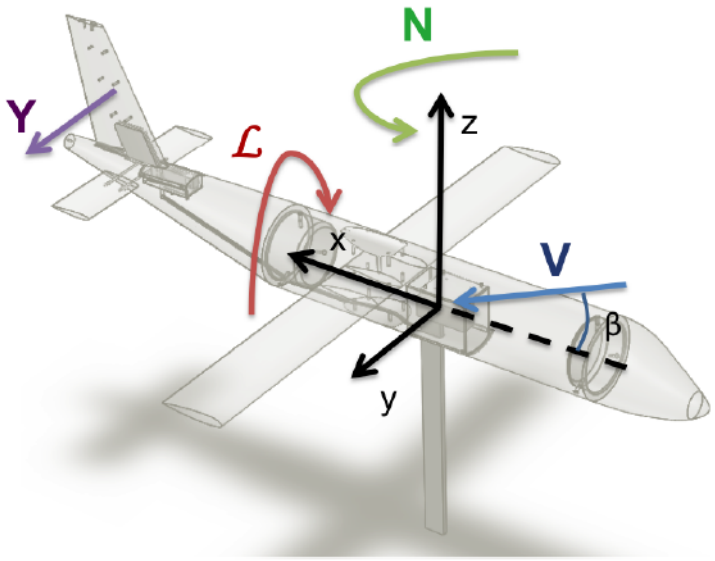

FIGURE 6.36: Reference system.

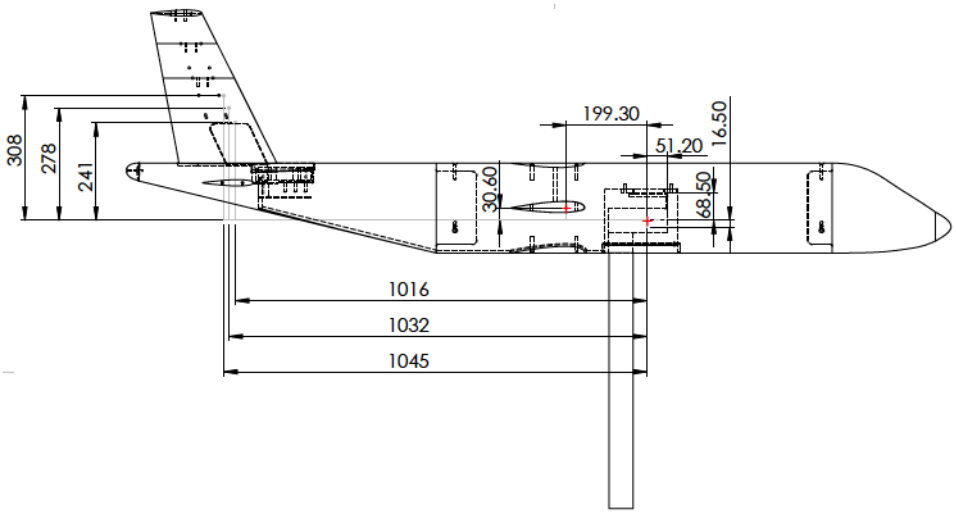

FIGURE 6.37: Relative position of moments reference points. Vertical tail aerodynamic centers are measured with respect to the balance center. Units in mm.

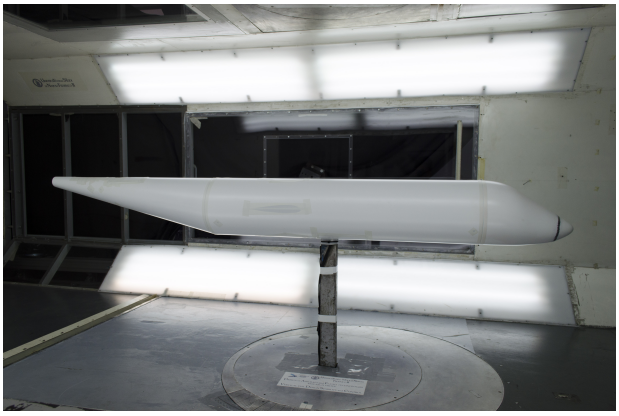

(A) High tail-cone $z_{ftc}/r_f = 1.0$ (BH).

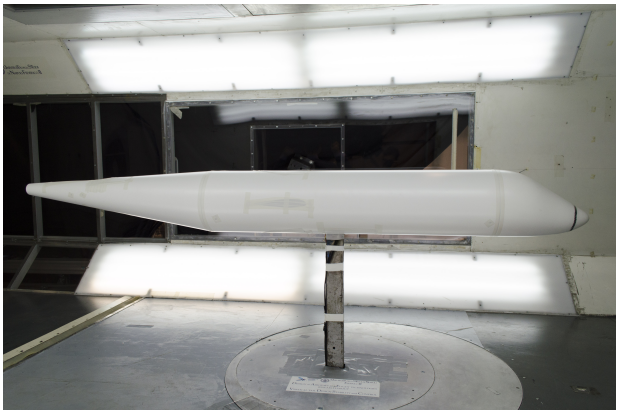

(B) Mid tail-cone $z_{ftc}/r_f = 0.5$ (BM).

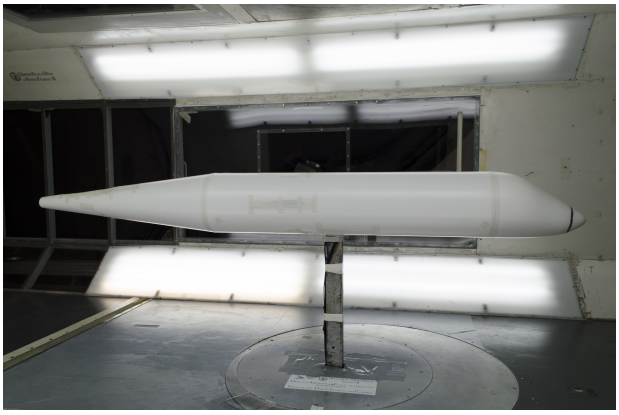

(C) Low tail-cone $z_{ftc}/r_f = 0$ (BL).

FIGURE 6.38: Fuselage tail-cones or after-bodies.

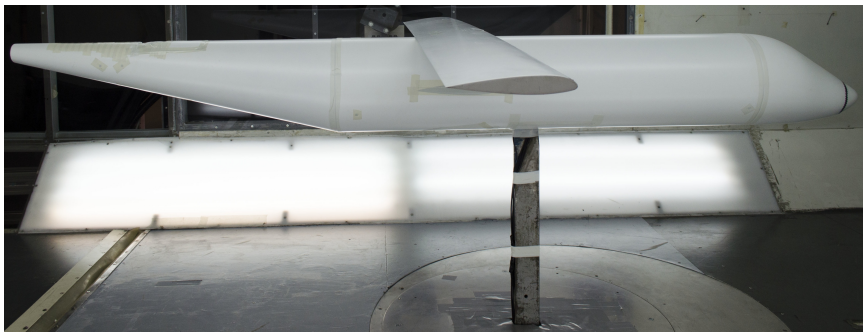

(A) High wing $z_w/r_f = 1$ (WH).

(B) Mid wing $z_w/r_f = 0$ (WM).

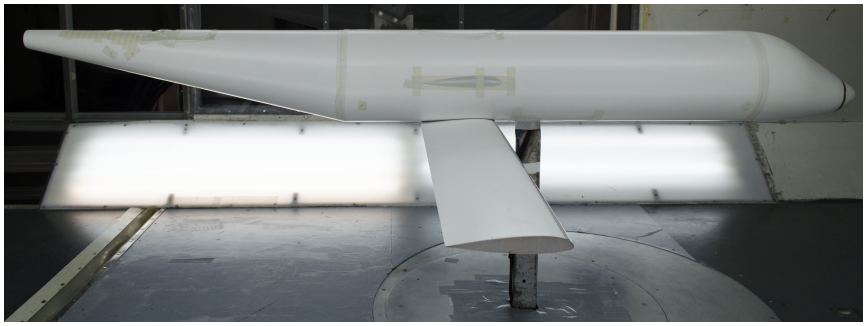

(C) Low wing $z_w/r_f = -1$ (WL).

FIGURE 6.39: Wing positions in fuselage.

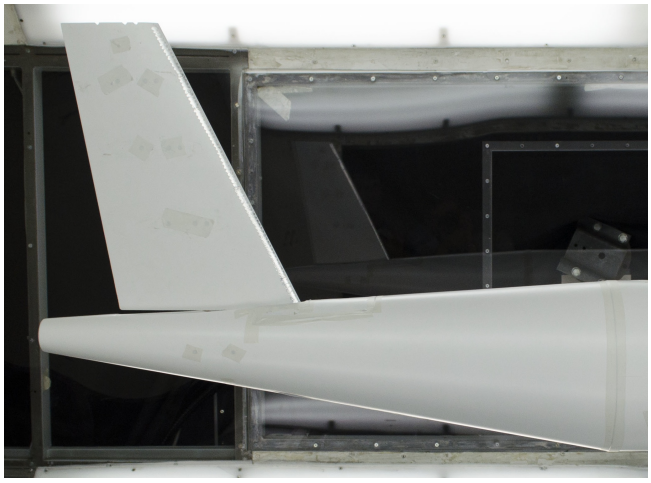

(A) Vertical tail $A_v = 2.0$ (V20).

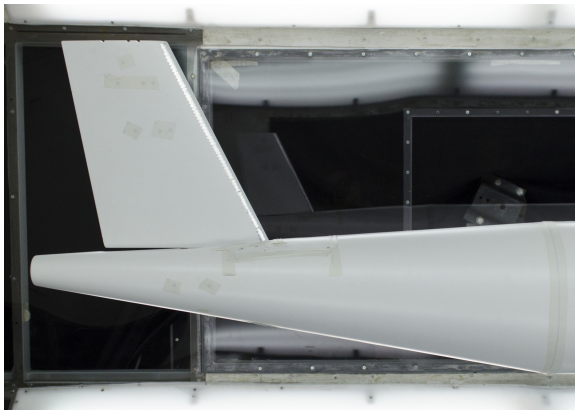

(B) Vertical tail $A_v = 1.5$ (V15).

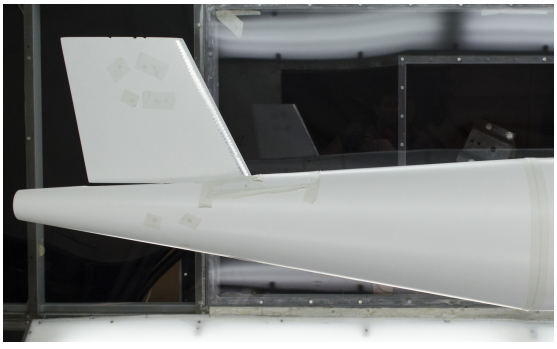

(C) Vertical tail $A_v = 1.0$ (V10).

FIGURE 6.40: Vertical tail planforms.

(A) T-tail (H5).

(B) Cruciform tail (H4).

(C) Cruciform tail (H3).

(D) Cruciform tail (H2).

(E) Body-mounted tail (H1).

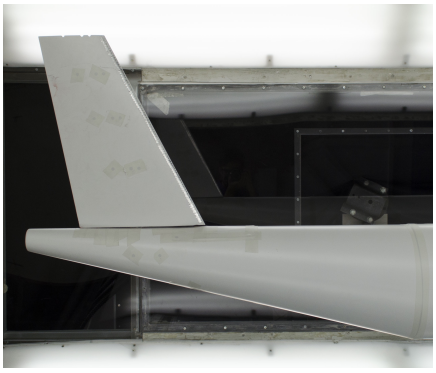

(F) No tail.

FIGURE 6.41: Horizontal tail positions.

6.7.1 Uncertainty of measurements

There are two types of uncertainties: *random* and *systematic*. Random components produce different results in repeated experiments, assumed that all the controllable parameters are held as constant as possible. The true value of a quantity may be found by an accurate average of a population of results. Systematic components in repeated experiments produce the same results, but these results are different from the true value, which remains unknown. For this reason, systematic errors are usually the most difficult to figure out [95, §12.2]. Sources of uncertainty in this work have been classified as follows.

Random errors

- Turbulence
- Environment temperature
- Instrumentation accuracy
- Assembly of the model
- Vibrations during a test

Systematic errors

- Manufacturing and assembly errors
- Other non-random errors

Turbulence, environment temperature, and instrumentation accuracy have been discussed in Section 6.4.1. The assembly of the model is related to the operator's skill, who must change the configuration of the model between tests. Effects of vibrations are minimized by averaging results over hundreds of acquired samples.

Since the model should be symmetric about its vertical plane, lateral-directional aerodynamic coefficients at no angle of sideslip should be zero. Any deviation from the null value has been considered as a systematic error due to manufacturing and assembly issues. For instance, the vertical tail in a particular configuration may be mounted at incidence, resulting in a non-zero yawing and rolling moment coefficients at zero sideslip angle. With this assumption, systematic errors are easy to figure out and, most important, they do not affect the stability derivatives of the model in any configuration.

Replication, randomization, and blocking are defined as the three basic principles in *design of experiments* [95, §12.2].

Replication refers to multiple repetitions of the basic experiments.

Randomization refers to the goal of producing replications of conditions for which the resulting experimental observations are stochastically independent.

Blocking refers to manipulations of the experimental conditions to isolate a particular effect (e.g. tail on versus tail off).

It is clear that the blocking principle is the scope of this work: to evaluate the effects of increments of the added aircraft parts. Replication and randomization are more difficult to obtain in a wind tunnel test campaign involving about 200 different configurations. To deal with uncertainty, initially three tests have been performed to measure the effects of sampling frequency. The default value of the acquisition and elaboration instrumentation is 1000 samples in 1000 ms, hence an average of the last 1000 samples recorded in the last second is obtained. Because of vibrations, the number of recorded sample has been finally changed to 200 and the acquisition frequency to 100 Hz. The configuration involved in this specific investigation is shown in Figure 6.42 and it represents a typical T-tail layout. The large aspect ratio chosen ($A_v = 2.0$) and the tip-mounted empennage are a suitable configuration to measure the uncertainty due to vibrations. Results are shown from Figure 6.43 to 6.45. As it can be observed, the last sampling frequency is sufficiently high and the recording time is long enough "to damp the oscillations" of the displayed averaged results.

Results of other repeated tests are reported from Figure 6.46 to 6.48. They refer to the same configuration (similar to the above mentioned one, but with the horizontal tail mounted in fuselage) and include the effects of assembly due to a change of configuration. With these preliminary tests the whole effects of uncertainty on the lateral-directional static stability derivatives have been estimated below 3 %.

It has been stated that systematic errors are evaluated as shift of the curves from the origin of the axes, since the sideforce, yawing, and rolling moments should be zero at zero angle of sideslip. The maximum deviation for the yawing moment coefficients C_N and C_{N_v} is about ± 0.0020, whereas for the rolling moment coefficient $C_{\mathcal{L}}$ is about -0.0060. These value may slightly

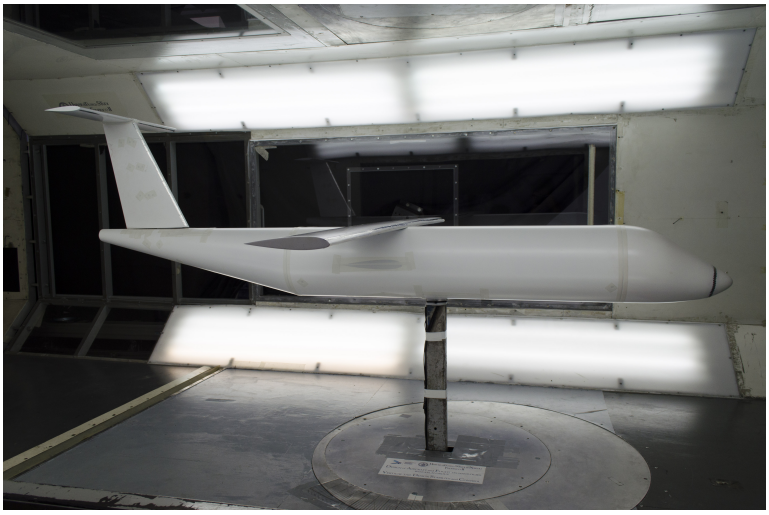

FIGURE 6.42: The configuration involved in the investigation about the effects of sampling frequency. $Re = 470\,000$, $\alpha = 0°$.

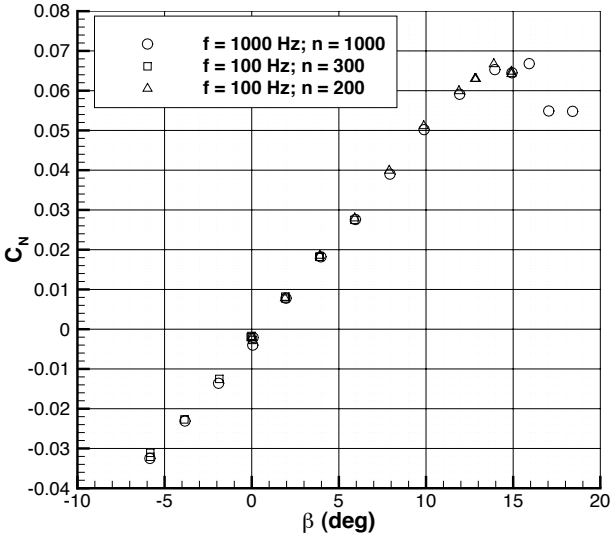

FIGURE 6.43: Effects of sampling frequency on yawing moment coefficient. $Re = 470\,000$, $\alpha = 0°$.

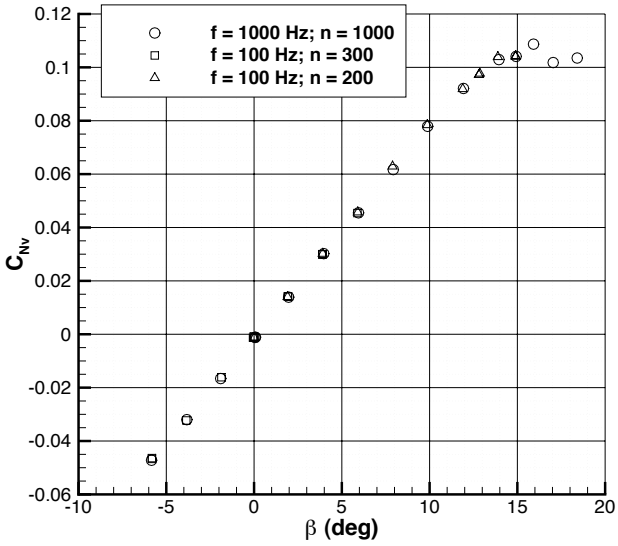

FIGURE 6.44: Effects of sampling frequency on vertical tail yawing moment coefficient. $Re = 470\,000$, $\alpha = 0°$.

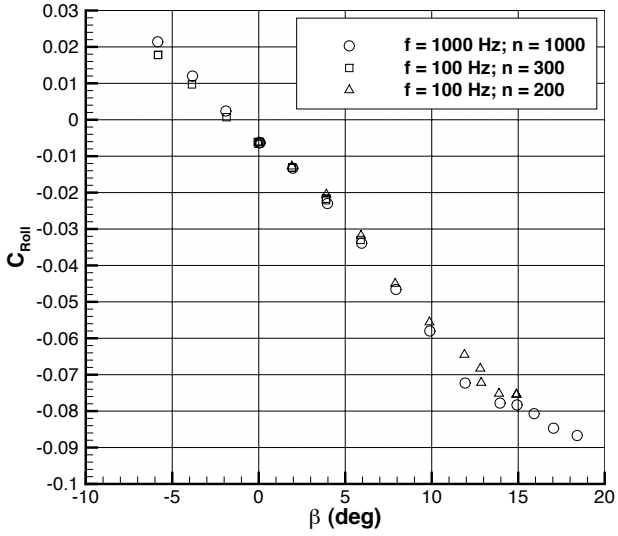

FIGURE 6.45: Effects of sampling frequency on rolling moment coefficient. $Re = 470\,000$, $\alpha = 0°$.

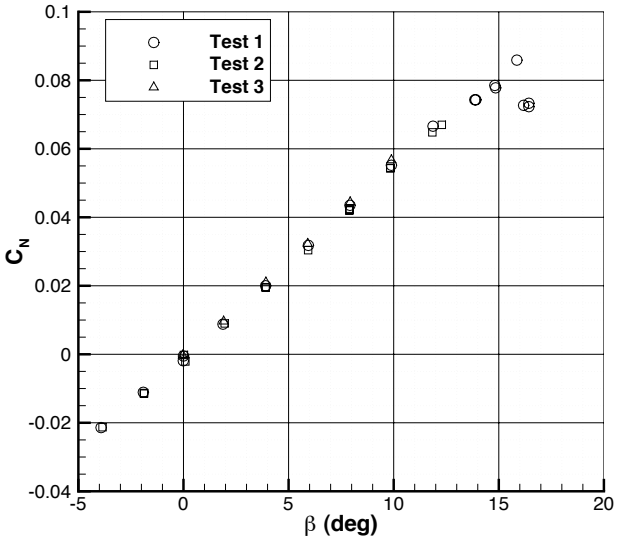

FIGURE 6.46: Effects of repeated tests on yawing moment coefficient. $Re = 470\,000$, $\alpha = 0°$.

change for other configurations due to the above mentioned manufacturing and assembly errors, but they can be easily solved by translating the curves such to intercept the origin of the axes at zero sideslip angle. However, it is again remarked that the stability derivatives of interest are not affected by this type of error.

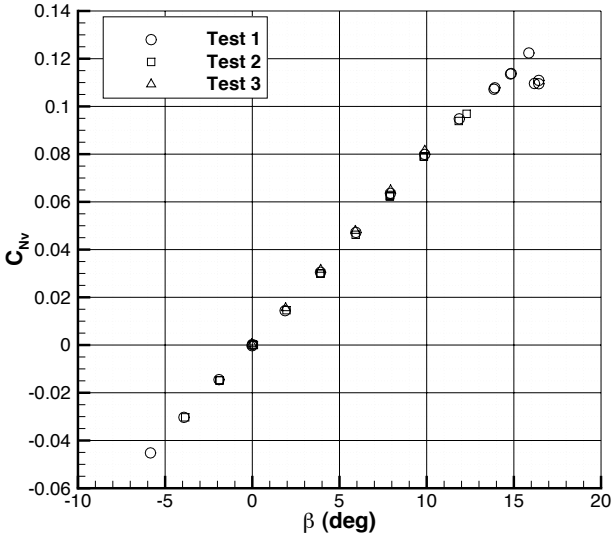

FIGURE 6.47: Effects of repeated tests on vertical tail yawing moment coefficient. $Re = 470\,000$, $\alpha = 0°$.

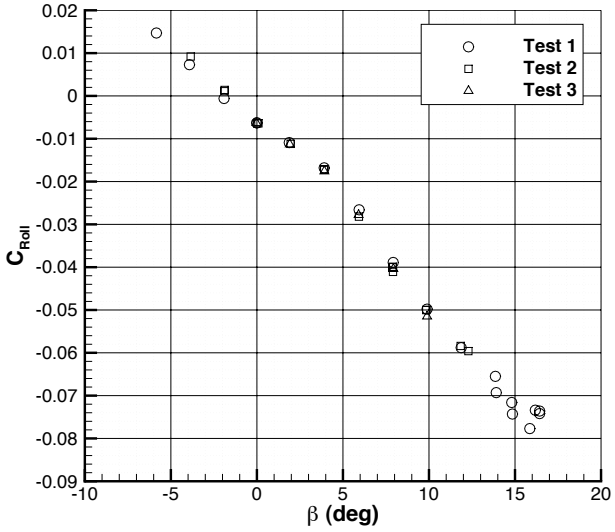

FIGURE 6.48: Effects of repeated tests on rolling moment coefficient. $Re = 470\,000$, $\alpha = 0°$.

6.7.2 Comparison with CFD simulations

Comparisons between numerical and wind tunnel tests are here presented for several configurations involving the fuselage with high tail-cone, the vertical tail planform $A_v = 1.5$, high and low wing, and T-tail horizontal stabilizer, shown in Figure 6.49.

Results for the isolated components (V and B) are reported in Figure 6.50 and 6.51, where the significant difference between numerical and experimental data at high sideslip angles is worthy of further investigations.

Figure 6.52 shows the results for the body - vertical tail combination (BV). The total and the vertical tail contributions, BV and V respectively, have been directly measured, whereas the fuselage contribution B has been measured as the difference $(C_N - C_{N_v})$. The curves of the vertical tail contribution are overlapped, hence the difference in the total yawing moment (BV) is due to the above mentioned effect of the fuselage after-body.

For the high wing - body - vertical tail combination (WBV), the effect of the wing is to increase the difference between numerical and experimental results of the total yawing moment, whereas the vertical tail contributions still agree, as reported in Figure 6.53a. A better situation is found in Figure 6.53b for the low wing - body - vertical tail combination, where the difference between the two WBV curves is decreased, because of the reduced fuselage after-body contribution. Again, the total and the vertical tail contributions, WBV and V respectively, have been directly measured, whereas the wing-body contribution WB has been measured as the difference $(C_N - C_{N_v})$.

By adding the horizontal stabilizer, the difference between numerical and experimental data is further reduced, for both the high and low wing configurations (Figure 6.54). For the T-tail configuration, the off-center load cell measures both the aerodynamic forces on the entire empennage (VH), but the horizontal tail provides only aerodynamic interference and not a direct contribution to directional stability, as also proved by the strong agreement between numerical and experimental data about the vertical tail.

The maximum deviation from wind tunnel results of the stability derivative C_{N_β} predicted by CFD is about 15 % on the isolated fuselage and between 2 % to 6 % on the $C_{N_{\beta_v}}$ of other configurations.

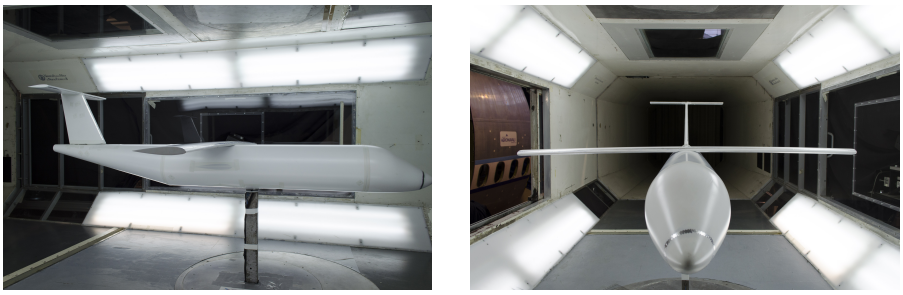

(A) High wing.

(B) Low wing.

FIGURE 6.49: Two complete aircraft configurations.

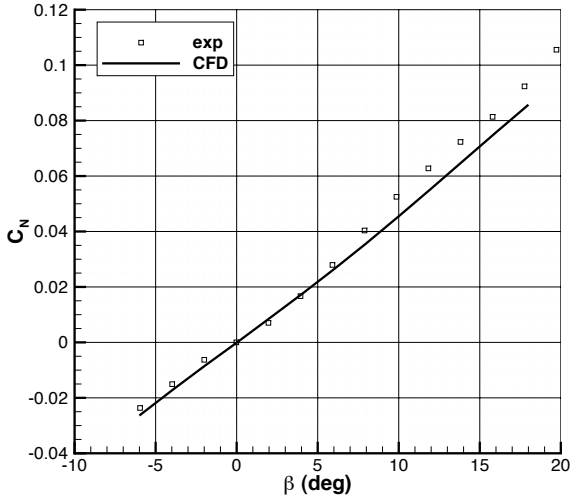

FIGURE 6.50: Comparison on the isolated vertical tail. $Re = 470\,000$, $\alpha = 0°$.

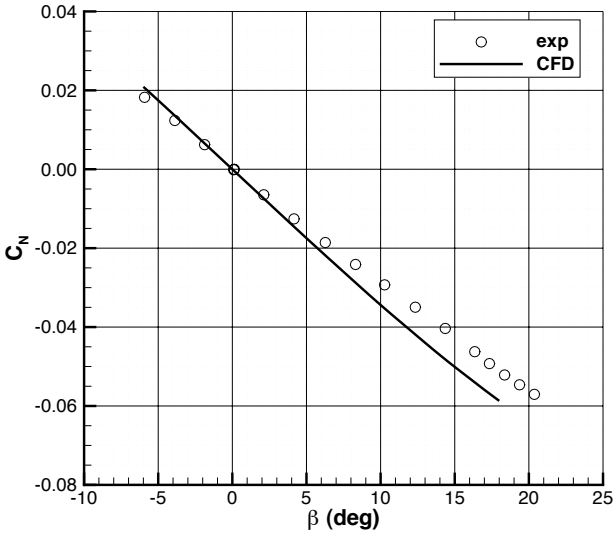

FIGURE 6.51: Comparison on the isolated fuselage. $Re = 470\,000$, $\alpha = 0°$.

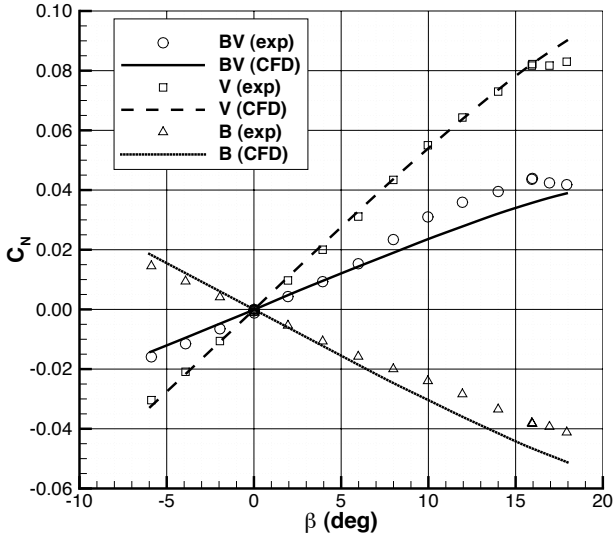

FIGURE 6.52: Comparison on the body - vertical tail combination. $Re = 470\,000$, $\alpha = 0°$.

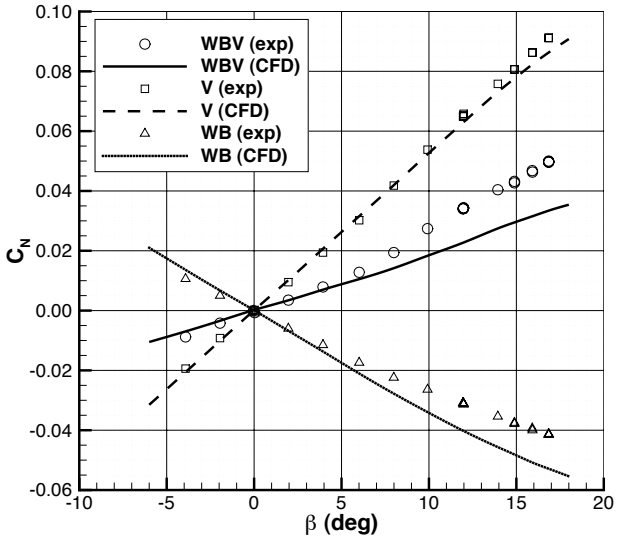

(A) High wing.

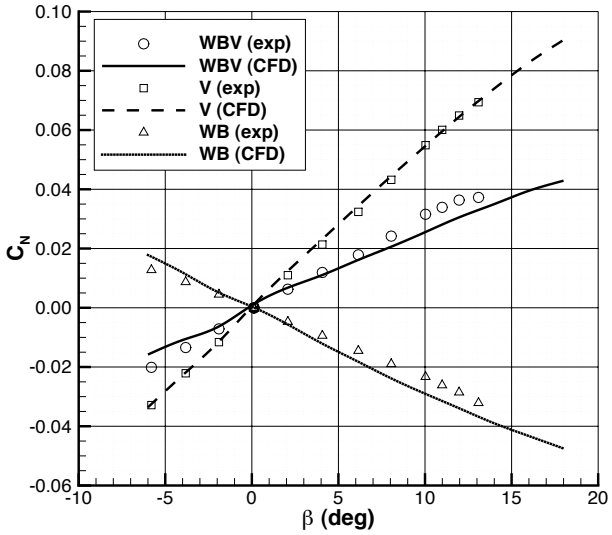

(B) Low wing.

FIGURE 6.53: Comparison on the wing - body - vertical tail combination. $Re = 470\,000$, $\alpha = 0°$.

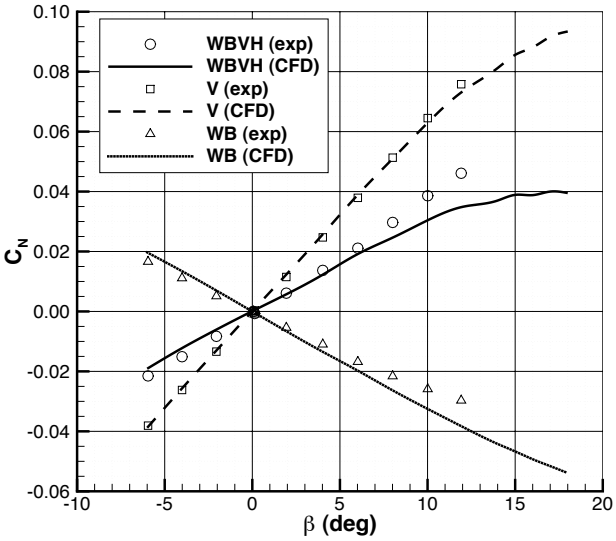

(A) High wing.

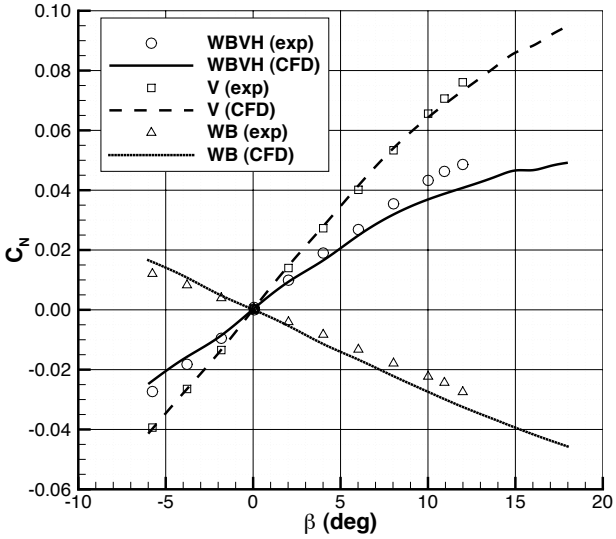

(B) Low wing.

FIGURE 6.54: Comparison on the complete configuration. $Re = 470\,000$, $\alpha = 0°$.

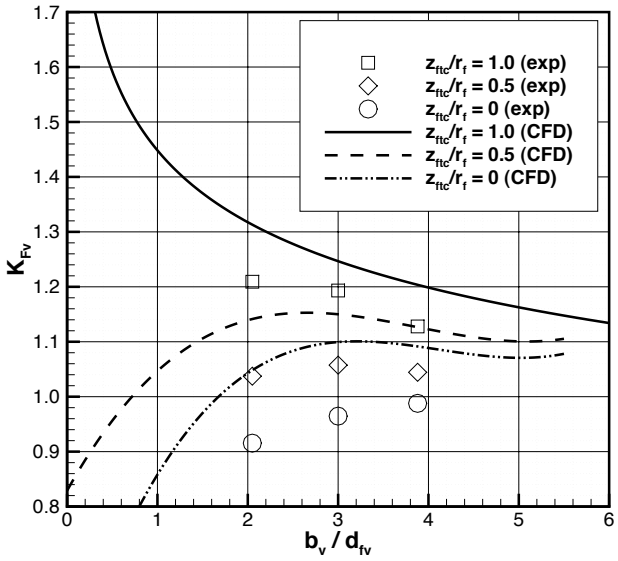

FIGURE 6.55: Effect of the fuselage on the vertical tail. Reference geometry in Figure 5.8 and 5.9.

6.7.3 Validation of the VEDSC method

At this point, once evaluated the effects of wind tunnel corrections and measurement uncertainty, and once compared the results of several configurations between numerical analyses and experimental investigations, the work proceeds with the *redde rationem*, i.e. the validation of the VEDSC method of Chapter 5. The factors K_{F_v}, K_{W_v}, and K_{H_v}, described from Section 5.4 to 5.6, have been reproduced from about 180 wind tunnel tests. Detailed results about stability derivatives are reported in Appendix C for each configuration. The effects of the added subparts is shown from Figure 6.55 to Figure 6.67. The aerodynamic interference factors reproduced experimentally usually underestimate the numerical results up to 10 % for some configurations, whereas in other cases the agreement is strong. This is worthy of further investigations.

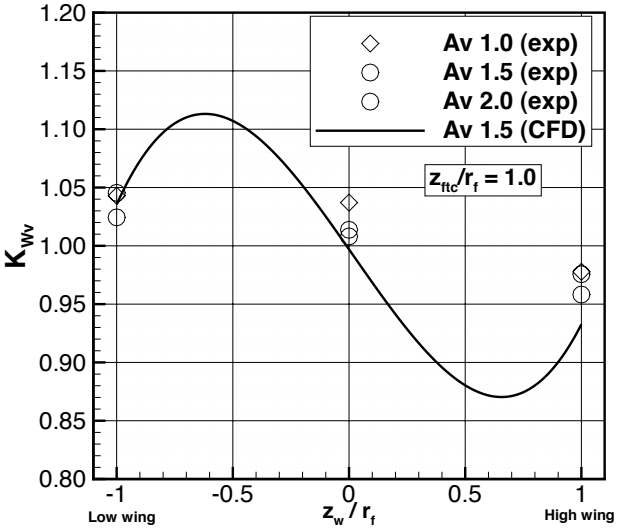

FIGURE 6.56: Effect of the wing on the vertical tail for the high tail-cone. Reference geometry in Figure 5.13.

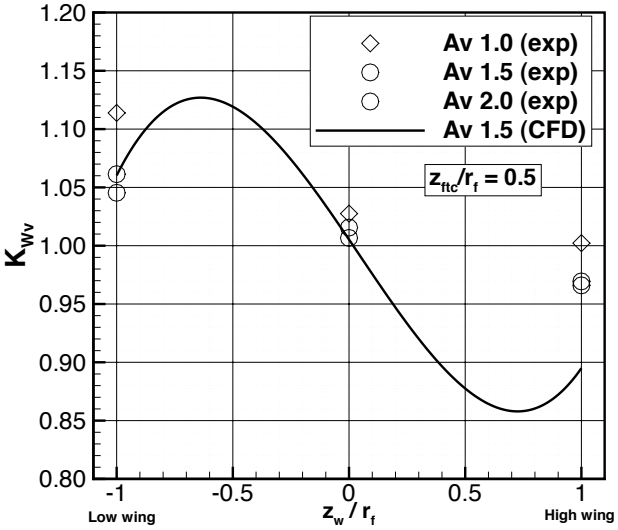

FIGURE 6.57: Effect of the wing on the vertical tail for the mid tail-cone. Reference geometry in Figure 5.13.

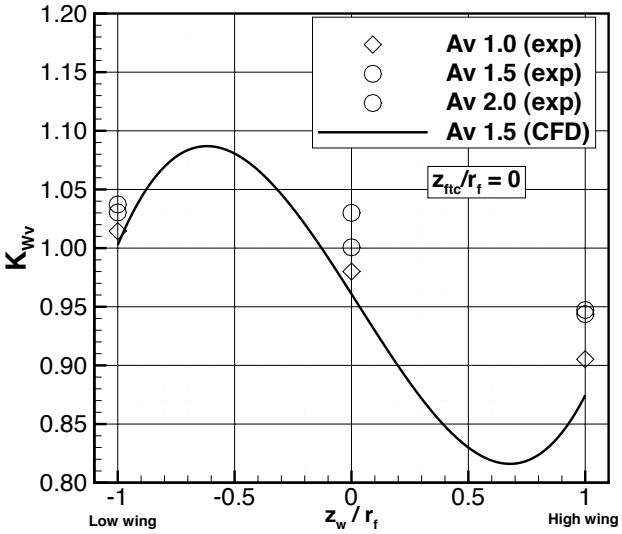

FIGURE 6.58: Effect of the wing on the vertical tail for the low tail-cone. Reference geometry in Figure 5.13.

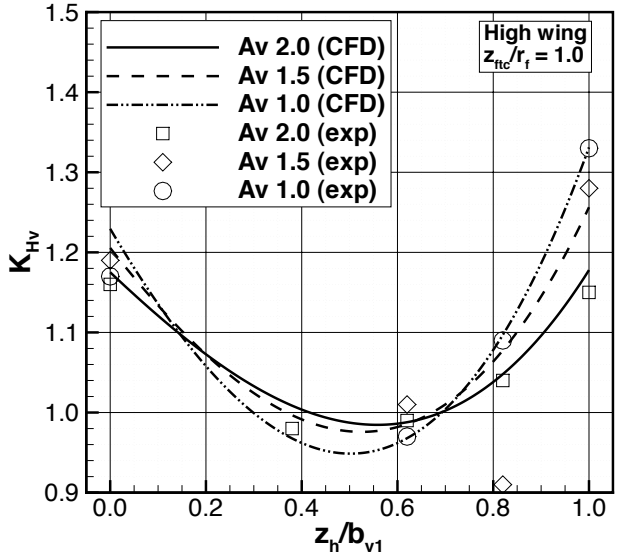

FIGURE 6.59: Effect of the horizontal tail on the vertical tail for the high tail-cone with high wing. Reference geometry in Figure 5.22.

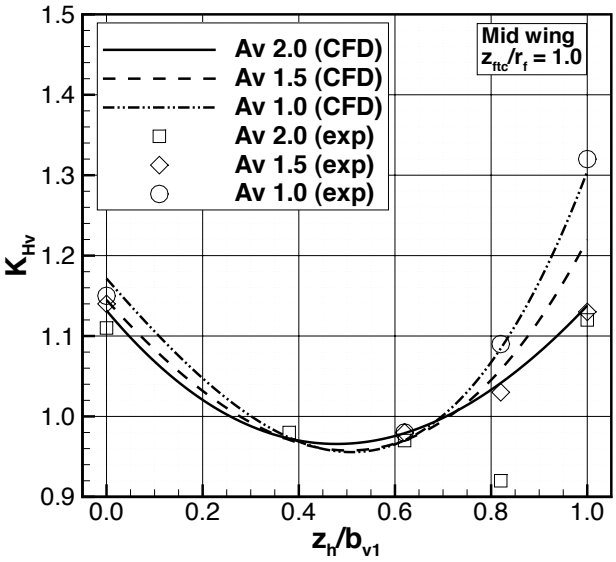

FIGURE 6.60: Effect of the horizontal tail on the vertical tail for the high tail-cone with mid wing. Reference geometry in Figure 5.22.

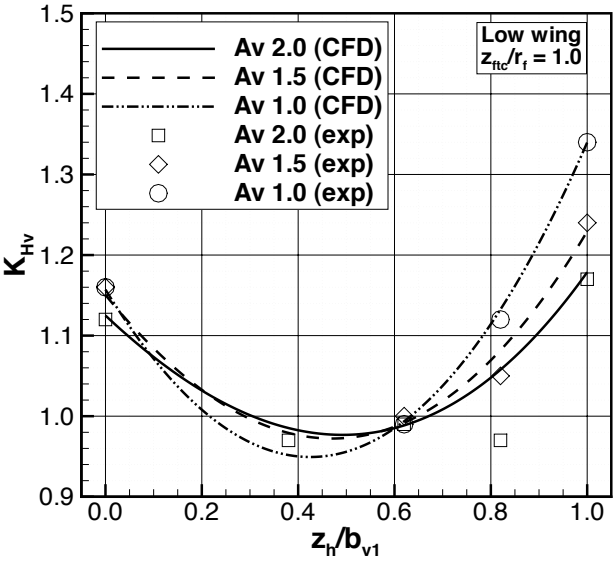

FIGURE 6.61: Effect of the horizontal tail on the vertical tail for the high tail-cone with low wing. Reference geometry in Figure 5.22.

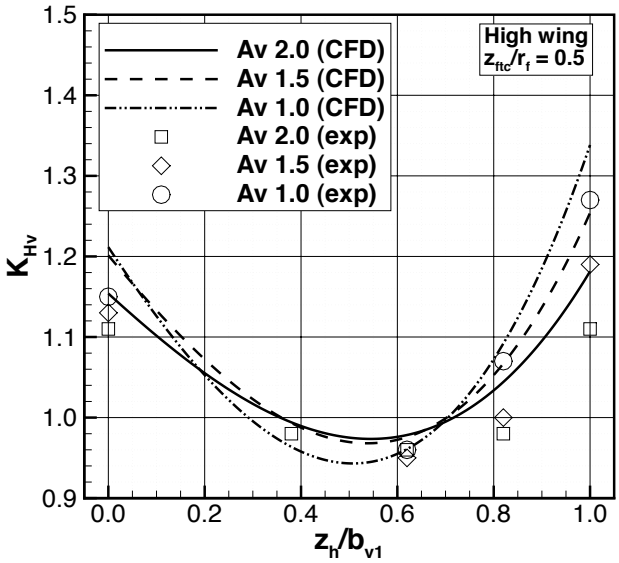

FIGURE 6.62: Effect of the horizontal tail on the vertical tail for the mid tail-cone with high wing. Reference geometry in Figure 5.22.

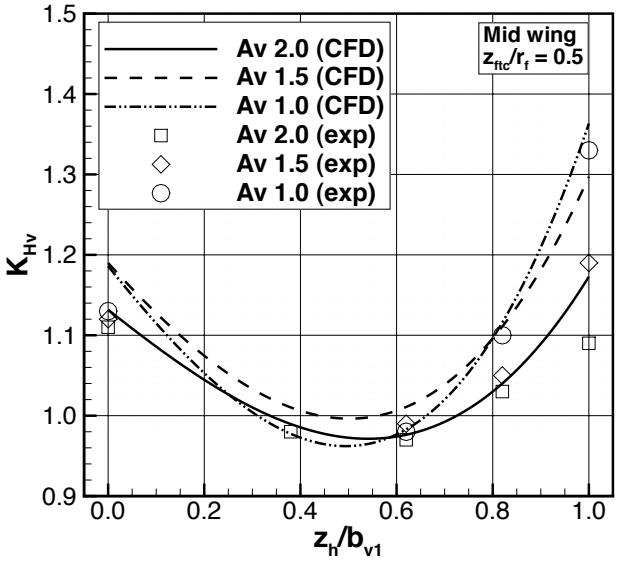

FIGURE 6.63: Effect of the horizontal tail on the vertical tail for the mid tail-cone with mid wing. Reference geometry in Figure 5.22.

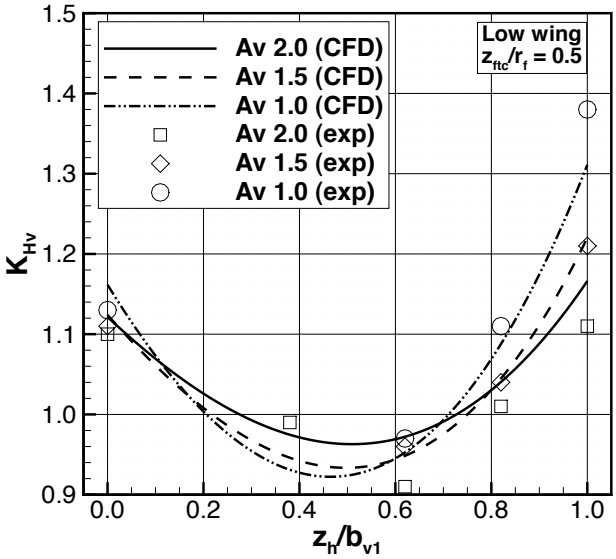

FIGURE 6.64: Effect of the horizontal tail on the vertical tail for the mid tail-cone with low wing. Reference geometry in Figure 5.22.

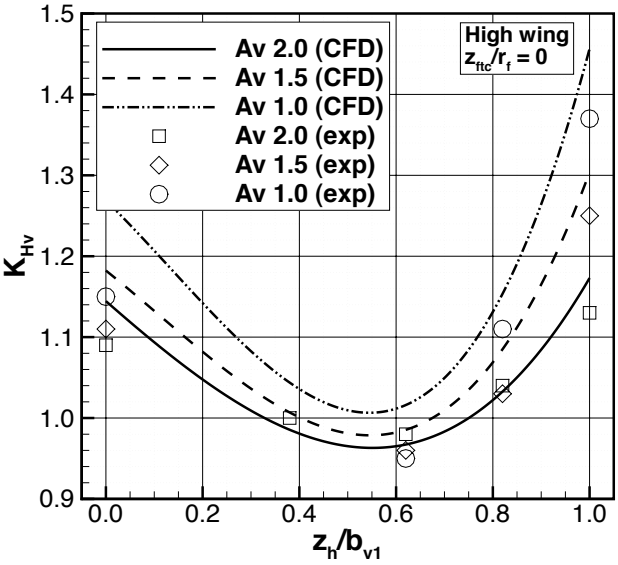

FIGURE 6.65: Effect of the horizontal tail on the vertical tail for the low tail-cone with high wing. Reference geometry in Figure 5.22.

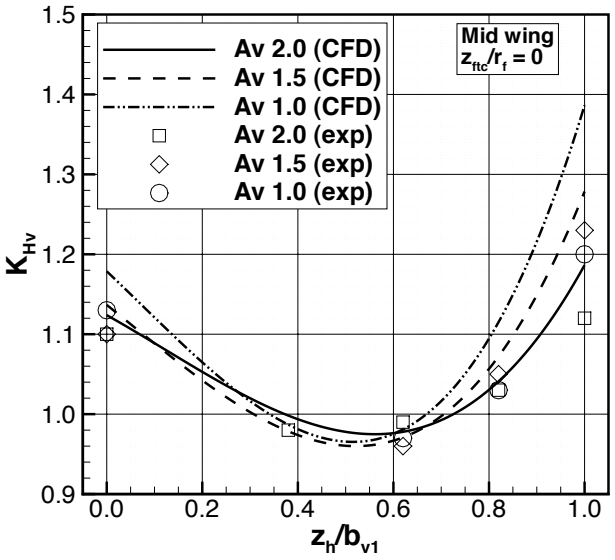

FIGURE 6.66: Effect of the horizontal tail on the vertical tail for the low tail-cone with mid wing. Reference geometry in Figure 5.22.

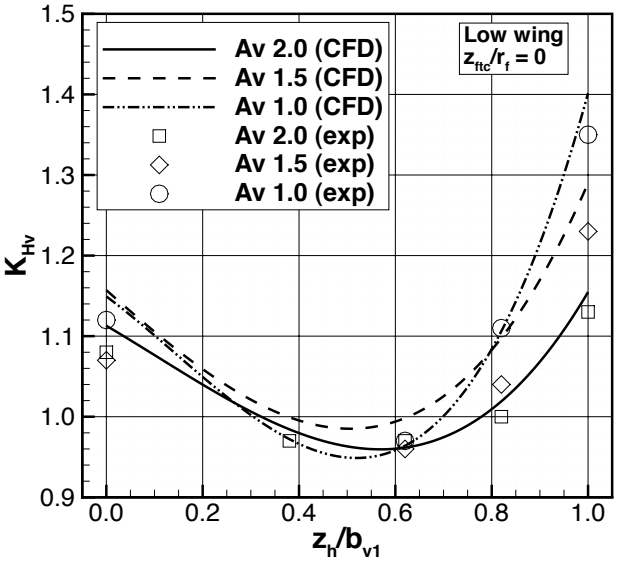

FIGURE 6.67: Effect of the horizontal tail on the vertical tail for the low tail-cone with low wing. Reference geometry in Figure 5.22.

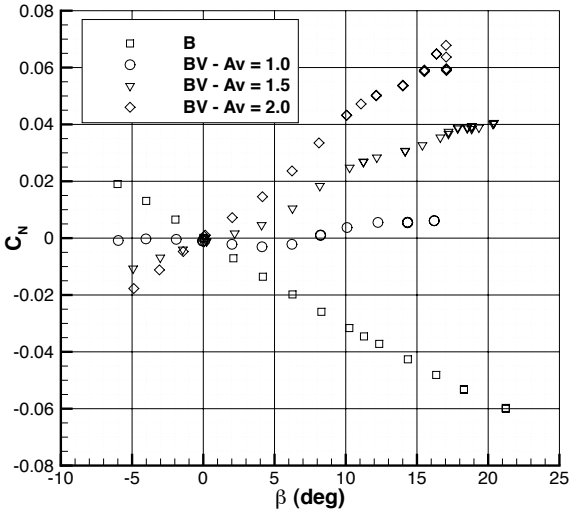

FIGURE 6.68: Non-linear effects on the yawing moment coefficient of mid after-body configuration. $Re = 470\,000$, $\alpha = 0°$.

6.7.4 Non-linear tail-body effects

For the fuselage - vertical tail configuration it is possible to evaluate the contribution of both components in sideslip. The fuselage yawing moment coefficient C_{N_f} in the presence of the vertical tail is calculated as $(C_N - C_{N_v})$, where the former is obtained through the wind tunnel balance, the latter is obtained through the off-center load cell mounted in the fuselage tail-cone. It is interesting to compare the effects of tail aspect ratio and area on the three yawing moment coefficients. For the fuselage with the mid after-body (Figure 6.38b), but analogous results have been obtained for the other bodies, the experimental results from Figure 6.68 to 6.70 show that, as the sideslip angle increases over a certain value, the total yawing moment coefficient C_N increases its slope, while the slope of the vertical tail contribution C_{N_v} remains almost constant up to the stall, and the fuselage instability, represented by the negative slope of the C_{N_f} curve, is decreased. *Wind tunnel tests have shown the true repartition of the aerodynamic forces.* The fact that all the aerodynamic interference contributions should not be added to the vertical tailplane has been numerically and experimentally demonstrated.

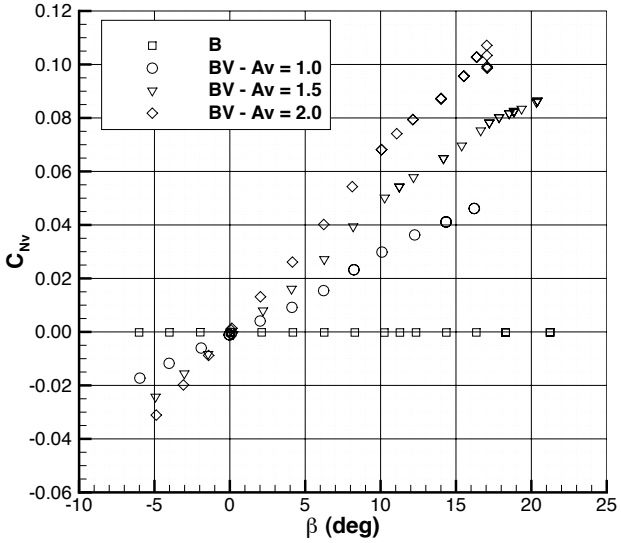

FIGURE 6.69: Non-linear effects on the vertical tail yawing moment coefficient of mid after-body configuration. $Re = 470\,000$, $\alpha = 0°$.

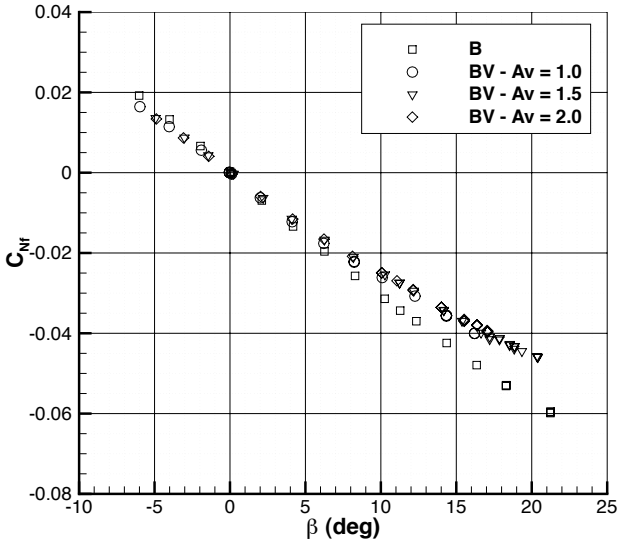

FIGURE 6.70: Non-linear effects on the fuselage yawing moment coefficient of mid after-body configuration. $Re = 470\,000$, $\alpha = 0°$.

Chapter 7

Conclusion and future works

7.1 Conclusion

This thesis presented a research work on the development of an improved design methodology for aircraft directional stability, focusing on the aerodynamic interference effects on the sizing of the vertical stabilizer of regional turbopropeller airplanes. The attention on this aircraft category is mainly due to economic reason, since the regional turboprop is competitive on short routes for the low fuel consumption and the increasing oil price makes the turboprop engine more desirable. Also, it has been stated (Section 1.1.3) that from 1400 to 3400 new turboprops, including large 90+ seaters, should be manufactured in the next 20 years, because of replacement and new deliveries, especially in the Asia and South America.

The topic of a reliable prediction of aircraft directional stability in preliminary design has been pushed by the fact that semi-empirical methods as DATCOM and ESDU:

1. are based on the results of wind tunnel tests involving models that *do not* represent actual transport airplanes;
2. *do assign* all the aerodynamic interference effects on the vertical tail;
3. *may* consequently oversize or undersize aircraft directional stability and control surfaces.

Chapter 2 presented the aerodynamics of the vertical tail and fuselage, describing the NACA technical papers that investigated the aerodynamic interference among aircraft components. The layout of the models tested in the wind tunnel at that time has been shown to be very different from actual transport airplanes and it has been highlighted that the results of

these technical reports have been collected in semi-empirical methods as DATCOM and ESDU.

Conceptual and preliminary design methods about aircraft directional stability have been discussed in Chapter 3, with a major focus on the vertical tail, since all the aerodynamic interference effects predicted by DATCOM and ESDU are assigned to it, whereas the contribution of the fuselage to aircraft directional stability is that of the isolated body. Applications of the these methods are shown by a MATLAB program written by the author for the ATR-42 airplane and a parametric investigation around its layout, highlighting significant differences in the results of the two methods for some aircraft configurations.

The approach of CFD in aircraft design, stability, and control has been presented in Chapter 4, with several examples of applications and test cases performed by the author and his research group. Advantages and drawbacks of the numerical approach have been described for different techniques and the lessons learned enabled confidence in the use of CFD as a tool for aircraft design process.

The advantages of the numerical approach have been exploited in the development of a preliminary design method for aircraft directional stability and vertical tail sizing, presented in Chapter 5. The new approach is focused on the evaluation of aerodynamic interference among airplane subparts, calculated as the ratio between static directional stability derivatives of aircraft configurations differing for one component (e.g. wing on versus wing off), for hundreds of combinations. The reliability of this method is the due to the nature of the approach taken: *CFD is not used to get absolute results, but to evaluate the effects of increments in results*, hence canceling eventual systematic errors in the analyses. The new developed method, named VEDSC (as Vertical tail Design, Stability, and Control) is simple to understand and to apply. The aerodynamic interference factors as function of aircraft geometric parameters have been reported in charts: once the aircraft side-view layout has been defined, the effects of fuselage, wing, and empennage on directional stability can be easily calculated. Examples of application have been given for a regional and a general aviation airplane, results have been compared with those provided by semi-empirical methods, and the new method proved to be satisfactory.

However, a method developed by only numerical analyses does not provide sufficient trust. A wind tunnel investigation on about 180 configurations

has been performed to validate the VeDSC methods. The test model has been CNC machined by the same CAD geometry of the numerical analyses, including some fixes to allow the modularity of the assembly and to directly measure the vertical tail aerodynamic forces in the presence of other parts. In this way, about 200 combinations between partial and complete aircraft configurations are possible with less than 30 interchangeable components. Results of wind tunnel tests have been compared with those of CFD analyses, especially the aerodynamic interference factors defined by numerical simulations, which have been reproduced from the results of the experimental investigations. The close agreement between the numerical and the experimental results fully validate the VeDSC method.

It is opinion of the author that the new method can be trustfully applied in aircraft design as a tool in addition to classical semi-empirical methods. For a regional turboprop airplane, the VeDSC method should give more reliable results, hopefully reducing the time-to-market, especially if the vertical tail has not to be resized after wind tunnel testing.

7.2 Future works

The research topic discussed in this thesis may be extended to consider the effects of aerodynamic interference issues in aircraft directional control, the non-linear effects at high angles of sideslip, the effects of a dorsal fin, and the effects of swept wings. Some indications come from preliminary analyses performed during the PhD research activities.

7.2.1 Directional control

The rudder is the aerodynamic control surface of the vertical tailplane. A preliminary numerical study [27], performed on the same model described in this work, investigates the effects of aerodynamic interference among aircraft components at several sideslip and rudder deflection angles.

Numerical analyses have shown that the deflection of the rudder generates a *local* angle of sideslip on the fuselage after-body. This effect is increased by the fuselage and the horizontal tail, in contrast with the approach of semi-empirical procedures, which evaluate the interference effects as the whole aircraft were in sideslip. The most important parameters that characterize the aerodynamics of directional control (neglecting propeller and flap effects)

in cruise conditions are: the vertical tail aspect ratio, the ratio between the vertical tail span and the fuselage diameter at vertical tail aerodynamic center, and the horizontal tailplane position. The wing has a negligible effect, because of its distance from the asymmetric flow field induced by the rudder.

An interesting result is shown in Figure 7.1, where the effects of fuselage, wing, and horizontal tail on the vertical tail are built-up on a given aircraft configuration (mid wing, T-tail), at several angles of sideslip and rudder deflection. In absence of sideslip, there is an increase in the sideforce generated by the vertical tail due to the deflection of the rudder. This is attributed to the aerodynamic interference among the aircraft components and it is conserved at angles of sideslip. The solid lines, starting from the origin of the axes, represent the complete and partial aircraft configurations in sideslip, with no rudder deflection ($\delta_r = 0°$). Adding the fuselage, wing, and horizontal tailplane increases the curve slope of the vertical tail sideforce coefficient. The dashed lines represent the same configurations with a rudder deflection of $\delta_r = 10°$. It can be observed that the addition of the aircraft components changes the slope and translates the curves, except for the wing contribution, which is negligible. Linearity is conserved up to 5° of sideslip. In the linear range, the dashed lines are parallel to the solid lines, hence the slope is conserved and the directional stability derivative C_{N_β} (which is strictly bound to the slope $dC_{Y_v}/d\beta$) is unaffected. Thus, the deflection of the rudder simply translates the solid lines, providing an increase of the aerodynamic coefficients even in zero sideslip condition. Linearity is particularly important for rudders, because strong non-linearities may cause unacceptable variations in control surfaces [63].

A preliminary formulation follows the same approach described in Chapter 5 and defines the rudder control power as

$$C_{N_{\delta_r}} = C_{L_{\alpha_v}} K_{\delta_r} \tau \frac{S_v}{S} \frac{l_v}{b} \tag{7.1}$$

where $C_{L_{\alpha_v}}$ is the isolated vertical tail lift curve slope (Section 5.3), K_{δ_r} is the interference factor due to rudder deflection (defined below), and $\tau = \partial\beta/\partial\delta_r$ is the rudder effectiveness, which has not been investigated yet and must be calculated with other methods. From unpublished numerical and experimental data of the Design of Aircraft and Flight technologies research group, it results that τ can be around 0.6 with a 0.35 chord ratio, even at 25° of rudder deflection, whereas semi-empirical methods give lower

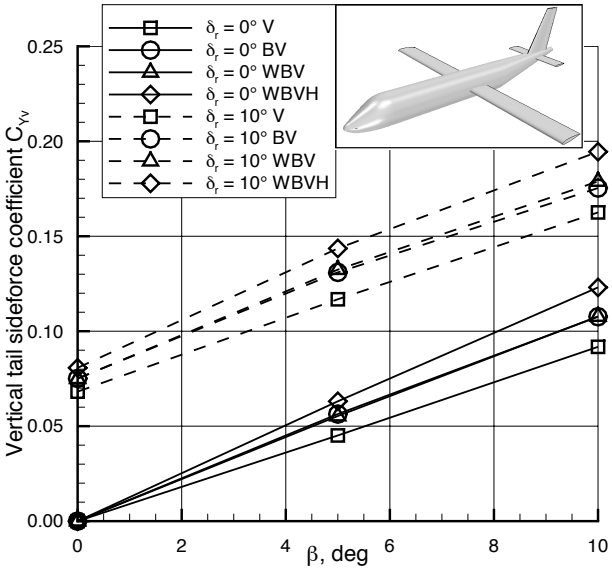

FIGURE 7.1: Effects of rudder deflections on vertical tail sideforce in several configurations at different angles of sideslip.

values. The factor K_{δ_r} has been preliminary defined as

$$K_{\delta_r} = \begin{cases} 1.07 \left(1 + \frac{K_{Fv}-1}{2.2}\right) & \text{for body-mounted tail} \\ (1.33 - 0.09A_v) \left(1 + \frac{K_{Fv}-1}{2.2}\right) & \text{for T-tail configuration} \end{cases} \tag{7.2}$$

where the factor K_{Fv} is the same of that in Section 5.4. To investigate the effects of rudder effectiveness τ, numerical and experimental investigations have been planned for tail planforms with different aspect ratios and chord ratios (Figure 7.2), which will be mounted on several configurations of the VEDSC model described in Section 6.7.

7.2.2 Non-linear effects at high angles of sideslip

Non-linear effects at high angles of sideslip are interesting. The change in the slope of the yawing moment slope indicates a change in directional stability, although stability is formally defined about an equilibrium point. The author and his department colleagues are working to develop a method to predict

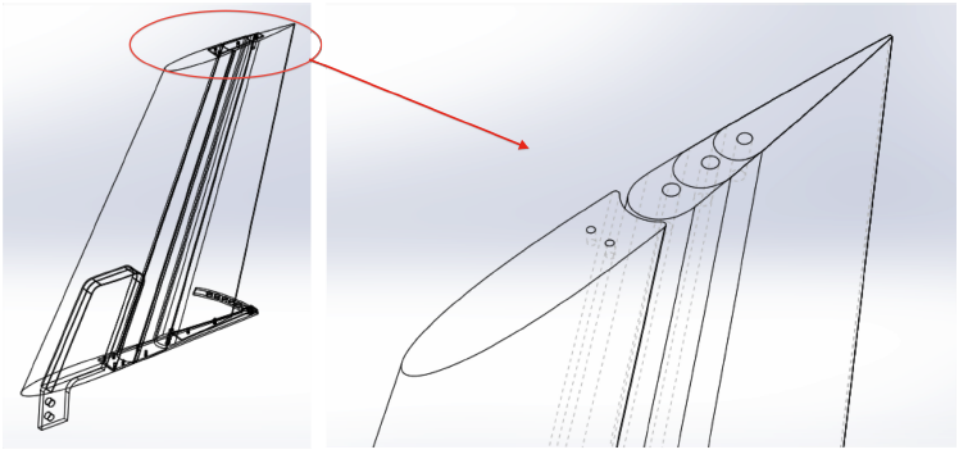

FIGURE 7.2: Rudder configurations planned for directional control analyses.

the non-linear behavior of fuselage and vertical stabilizer. Usually, tails and bodies have a reduction in their lift curve slope at high angles of incidence, although the vortex lift phenomenon can be enabled for very low aspect ratio planforms. Some results have been presented in Section 6.7.4.

The effects of a dorsal fin has been described in Section 2.1.1. Parametric studies with several dorsal fin planforms have been performed to develop a preliminary sizing method, since dorsal fin sizing is usually done in late wind tunnel tests with the aim to increase the planform area of the vertical stabilizer without providing major modification to its layout[1], or to delay the vertical tail stall and the rudder lock phenomenon [16, §8.4] to higher angles of sideslip, or to give the aircraft a novel look.

The effects of a dorsal fin are apparent, as reported in Figure 7.3, which shows several body - vertical tail combinations with dorsal fin of different heights and one configuration without dorsal fin. The model investigated is the same of the VEDSC method of Chapter 5. The vertical tail stall is delayed from 18° to 40° and higher. Also, the curve slope increases from the linear range, because of the vortices generated by the dorsal fin. The quantitative results must be taken with care, since, as stated in Chapter 4,

[1]Although the aspect ratio and hence directional stability may be reduced, the planform modification is limited to the tail root and the effects of the added surface may be predominant. Also, the directional instability of the fuselage may be reduced by a fin long in chord and short in span.

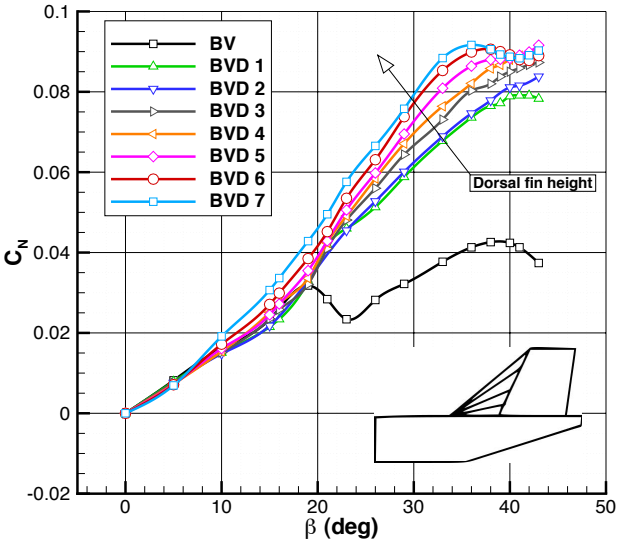

FIGURE 7.3: Effects of dorsal fin height. CFD fully turbulent simulations at $Re = 1\,000\,000$, $\alpha = 0°$.

the prediction of separated flow fields is still challenging. For this reason and for the availability of the experimental model described in Chapter 6, wind tunnel tests on several dorsal fins will be performed in the next future.

Appendix A

Further effects in VEDSC method

There are some effects that have not been discussed in Chapter 5. It is here shown that these effects are usually negligible, but nonetheless they can be accounted for. They are:

- the effect of vertical tail aspect ratio A_v and wing aspect ratio $\mathcal{AR}$ for several wing positions on the K_{W_v} interference factor;
- the effect of a longitudinal translation of the horizontal stabilizer on the K_{H_v} interference factor;
- the effect of horizontal tail size with respect to the vertical tail size on the K_{H_v} interference factor.

A.1 On the effects of vertical tailplane and wing aspect ratio

Figure A.1 shows the effects of vertical tail aspect ratio A_v and wing aspect ratio $\mathcal{AR}$ on the wing interference factor K_{W_v} for three wing positions. The original charts of Ref. [86] report the ratios of vertical tail sideforce coefficients C_{Y_v}, instead of yawing moment coefficient derivatives $C_{N_{\beta_v}}$, for different configurations, in this case the wing - fuselage - vertical tail (WFV) combination versus the fuselage - vertical tail (FV) combination. These charts are referred to CFD simulations with the straight fuselage after-body $z_{ftc}/r_f = 1.0$, the upper configuration of Figure 5.9.

Data show that the effect of vertical tail aspect ratio on the aerodynamic interference due to the wing is negligible. For this reason, the curves in

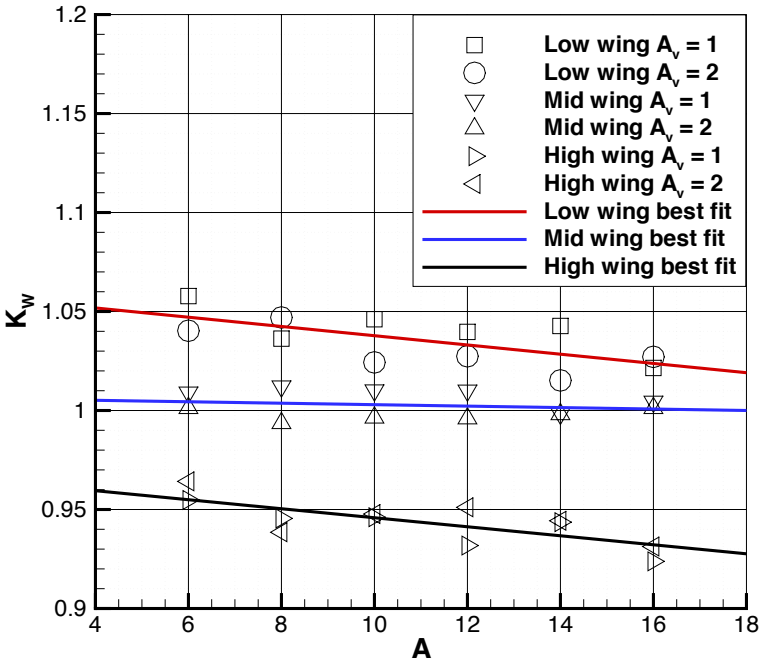

FIGURE A.1: Effects of vertical tail and wing aspect ratio. Fuselage tail-cone with $z_{ftc}/r_f = 1.0$. Reproduced from Ref. [86].

Section 5.5 are referred to a vertical tail with aspect ratio $A_v = 1.5$. Also, the effect of an increasing wing aspect ratio $\mathcal{AR}$ is to reduce the wing amplification factor for the high and low wing position in fuselage, whereas this effect on the mid wing seems negligible for the configurations investigated. On the contrary, as reported in Equation 3.11, USAF DATCOM provides an increasing *sidewash* (hence, an increasing sideforce derivative C_{Y_β}, see Equation 3.10) with wing aspect ratio, although the effect of wing position in fuselage is predominant.

For the investigated configurations, as shown in Figure A.1, the effect of the vertical tail aspect ratio A_v is negligible, whereas the effect of the wing aspect ratio $\mathcal{AR}$ is confined within 2 % of the sideforce derivatives ratio, although the combined effect of wing position and aspect ratio is less than 6 %. This reduced variation made the author choose the values $\mathcal{AR} = 6$, 10, and 14 to proceed with CFD simulations for the other fuselage tail-cones, as reported in Section 5.5.

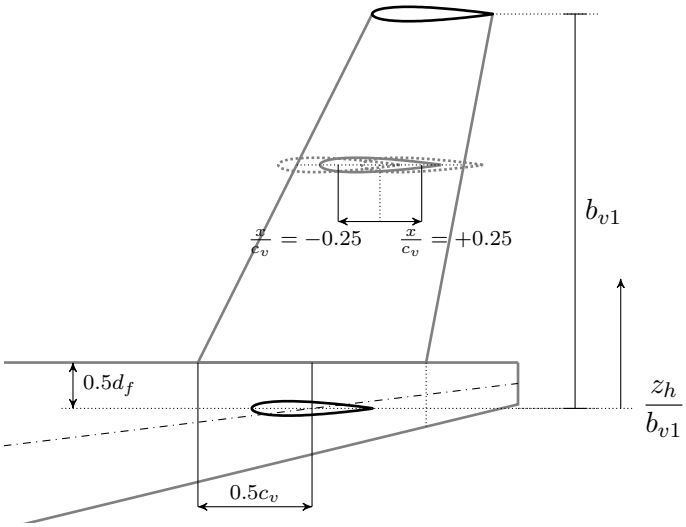

FIGURE A.2: Reference system for the horizontal tail position. Reproduced from Ref. [86].

A.2 On the effects of horizontal tailplane position and size

The results of Section 5.6 are intended for a horizontal stabilizer centered on the local chord of the vertical tailplane. Considering the possibility to move the former along the local chord of the latter, as shown in Figure A.2, the effect of such a longitudinal translation are reported in Figure A.3 for the vertical stabilizer with $A_v = 2.0$ and the fuselage with the straight fuselage after-body $z_{ftc}/r_f = 1.0$.

It can be stated that moving the horizontal stabilizer along a vertical tail chord has a negligible effect for all the configurations investigated, except for the forward translation of the body-mounted tailplane, which can decrease the horizontal tail interference factor by up to 6 %.

The effect of horizontal tail size with respect to vertical tail size is reported in Figure A.4. It is apparent that this effect changes the derivatives ratio up to 6 %, even for a horizontal stabilizer that has twice (or half) the planform area of the vertical tailplane. Usually, the ratio S_h/S_v is close to unity, hence the effect is negligible, especially if compared with the magnitude of the K_{H_v} term reported in Section 5.6.

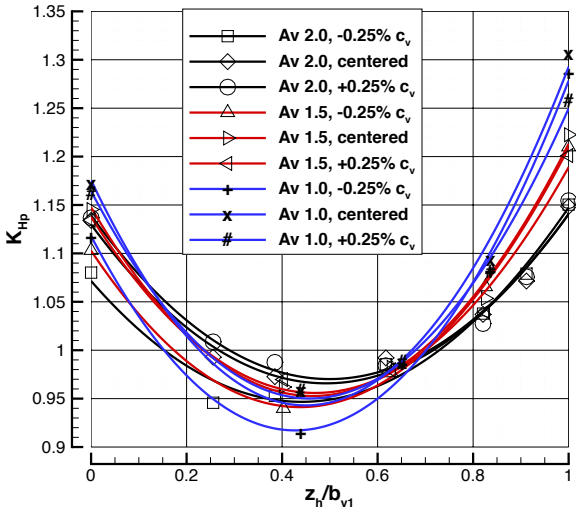

FIGURE A.3: Effects of horizontal tail position. Reproduced from Ref. [86].

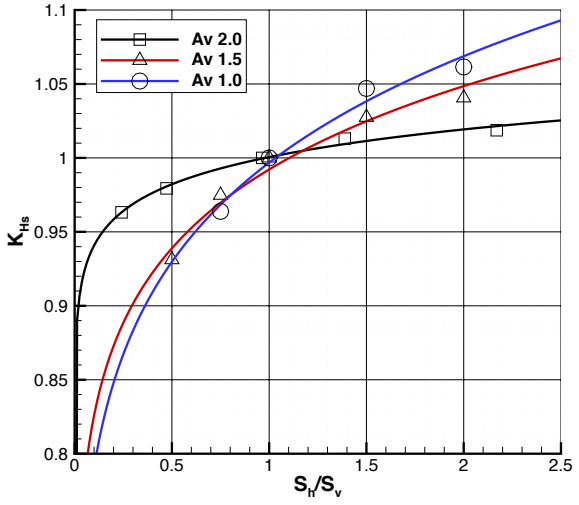

FIGURE A.4: Effects of horizontal tail size. Reproduced from Ref. [86].

Appendix B

CAD drawings

The following drawings of the CAD model are reported:

1. Model 3-view
2. Exploded view
3. Fuselage nose
4. Fuselage cabin
5. Fuselage tail-cone
6. Vertical tail
7. Vertical tail web
8. Load cell attach plate
9. Vertical tail attach plate
10. Wind tunnel balance interface plate
11. Horizontal tail spar
12. Sheet covering tail-cone
13. Sheet covering cabin

Items 1 and 2 show the assembly. Items from 3 to 6 are made from polyurethane machinable slabs. Last items are made from aluminum.

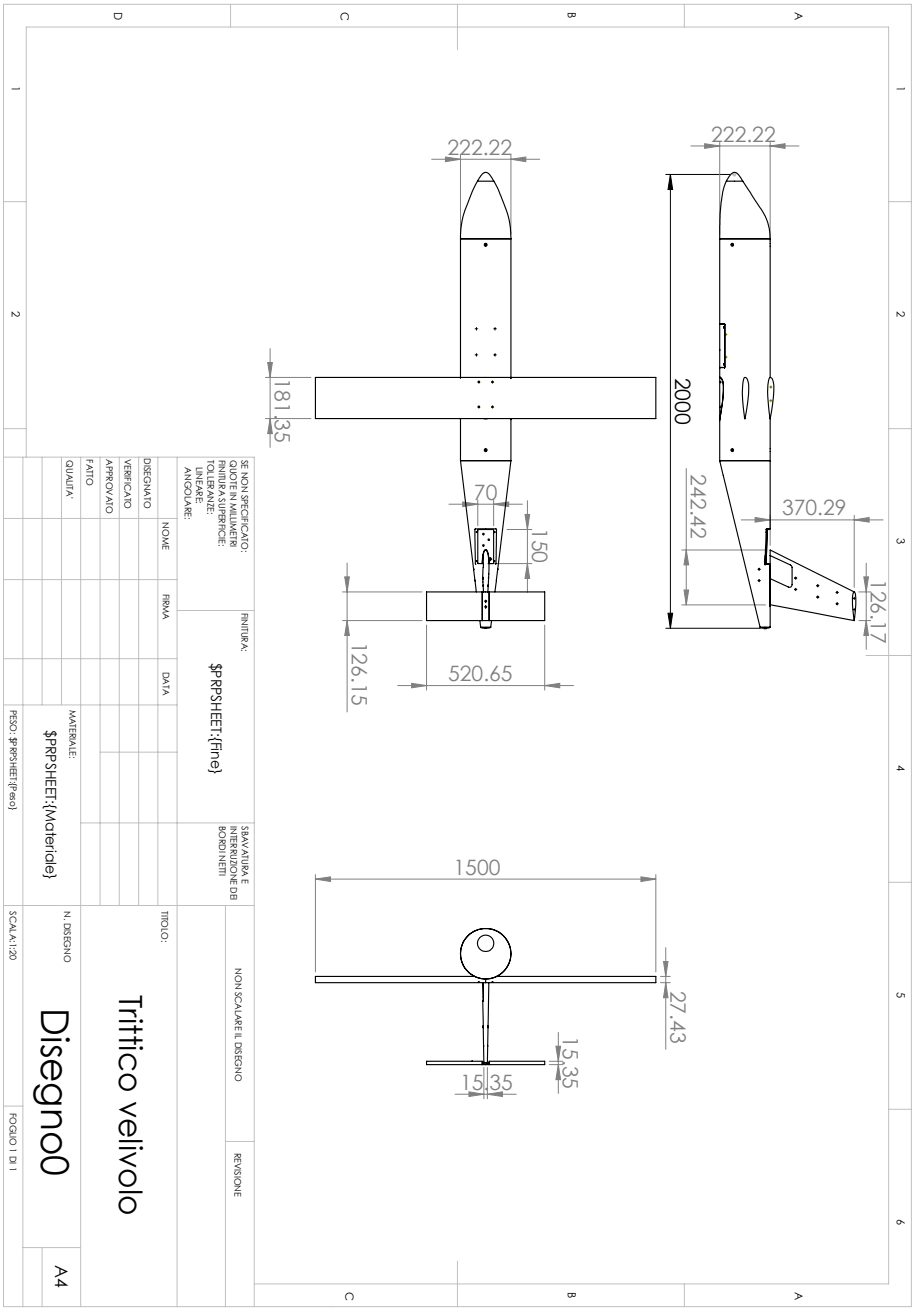
222.22
222.22
2000
181.35
70
150
242.42
370.29
126.17
126.15
520.65
1500
27.43
15.35
15.35
SE NON SPECIFICATO:
QUOTE IN MILLIMETRI
FINITURA SUPERFICIE:
TOLLERANZE:
LINEARE:
ANGOLARE:
FINITURA:
$PRPSHEET:{Finish}
SBAVATURA E INTERRUZIONE DEI BORDI NETTI
NOME
FIRMA
DATA
DISEGNATO
VERIFICATO
APPROVATO
FATTO
QUALITA'
MATERIALE:
$PRPSHEET:{Materiale}
PESO: $PRPSHEET:{Peso}
TITOLO:
Trittico velivolo
N. DISEGNO
Disegno0
A4
NON SCALARE IL DISEGNO
REVISIONE
SCALA:1:20
FOGLIO 1 DI 1

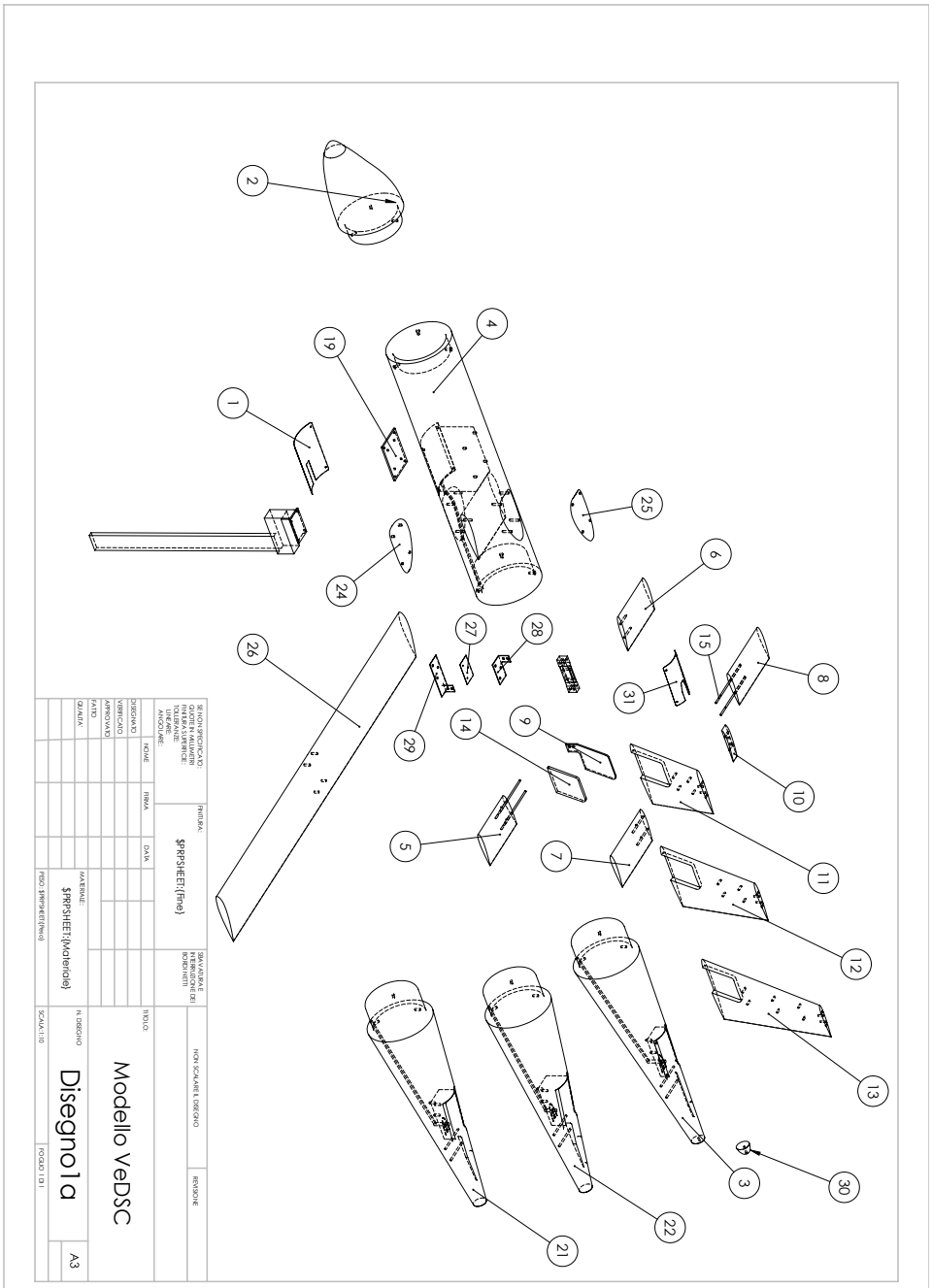
Modello VeDSC
Disegno1a
A3
$PRPSHEET:{Material}
$PRPSHEET:{Finish}
SCALA 1:10
FOGLIO 1 DI 1
NON SCALARE IL DISEGNO
REVISIONE
TITOLO:
N. DISEGNO
MATERIALE:
PROVA:
DATA:
FIRMA:
NOME:
DISEGNATO
VERIFICATO
APPROVATO
PESO: $PRPSHEET{Mass}
SMUSSI E RACCORDI NON INDICATI
SALVO DIVERSA INDICAZIONE
SE NON SPECIFICATO:
QUOTE IN MILLIMETRI
TOLLERANZE LINEARI:
TOLLERANZE ANGOLARI:
1
2
3
4
5
6
7
8
9
10
11
12
13
14
15
19
21
22
24
25
26
27
28
29
30
31

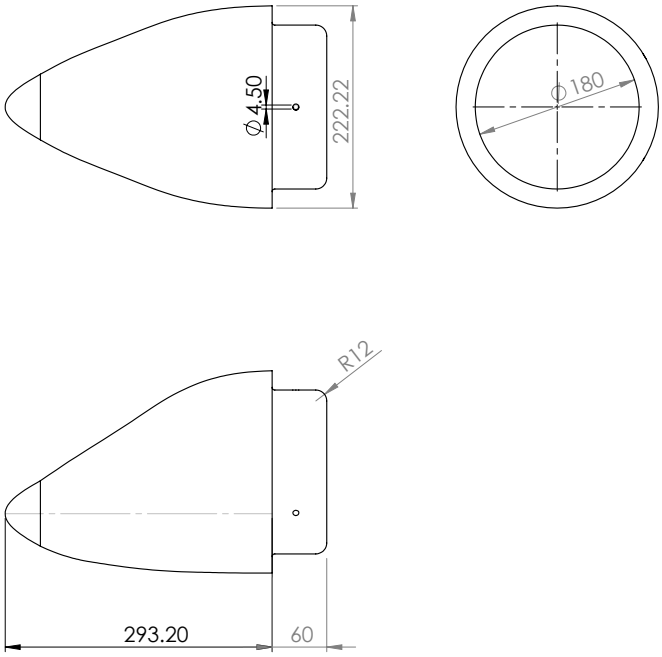

SE NON SPECIFICATO: QUOTE IN MILLIMETRI FINITURA SUPERFICIE: TOLLERANZE: LINEARE: ANGOLARE:	FINITURA: $PRPSHEET:{Fine}			SBAVATURA E INTERRUZIONE DEI BORDI NETTI	NON SCALARE IL DISEGNO	REVISIONE
	NOME	FIRMA	DATA		TITOLO:	
DISEGNATO					Muso fusoliera	
VERIFICATO						
APPROVATO						
FATTO						
QUALITA'				MATERIALE: $PRPSHEET:{Materiale}	N. DISEGNO Disegno2	A4
				PESO: $PRPSHEET:{Peso}	SCALA:1:5	FOGLIO 1 DI 1

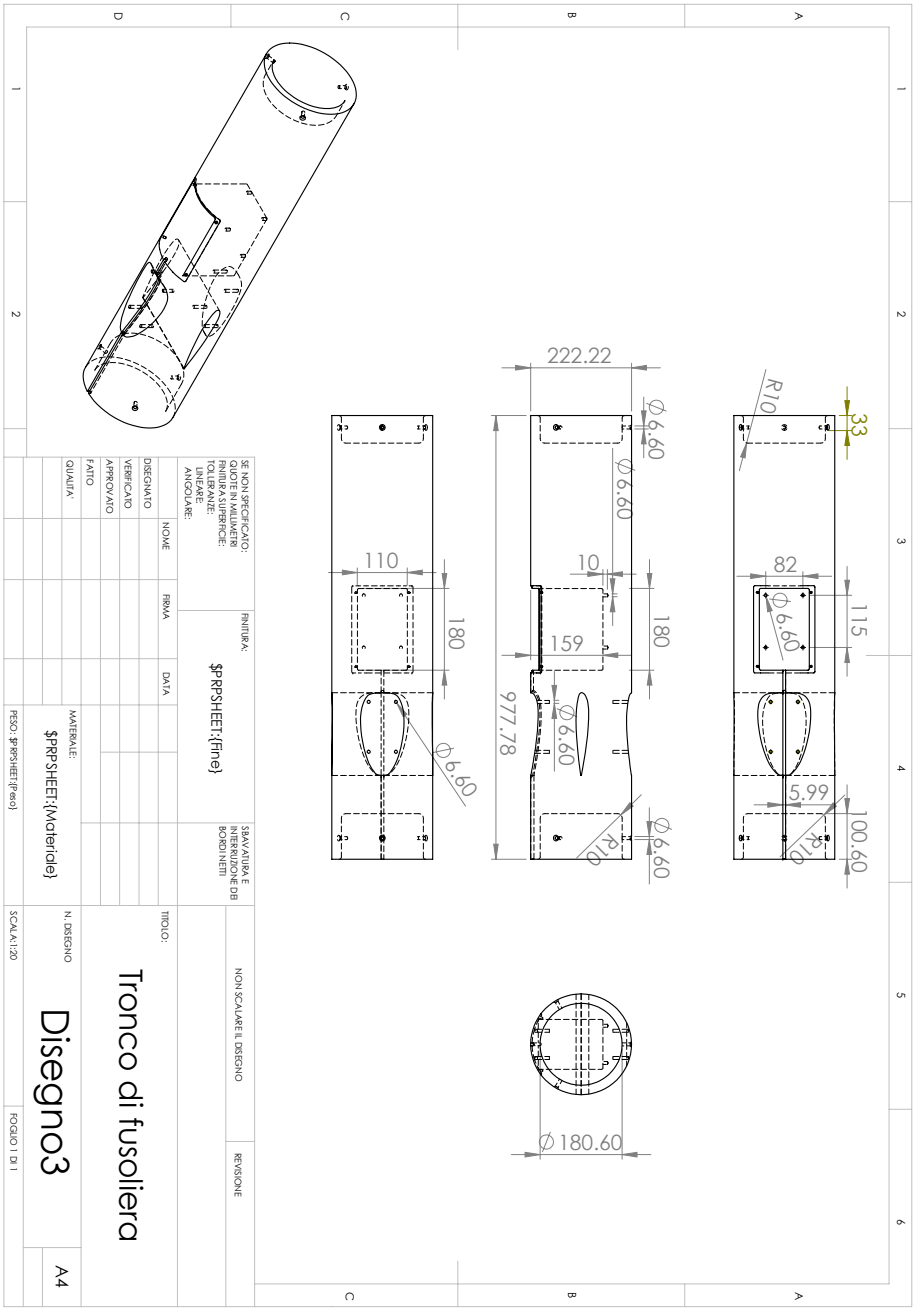
33
R10
82
115
Ø6.60
5.99
100.60
15°
222.22
Ø6.60
Ø6.60
10
180
159
977.78
Ø6.60
R10
Ø6.60
110
180
Ø6.60
Ø180.60
SE NON SPECIFICATO:
QUOTE IN MILLIMETRI
RUGOSITÀ SUPERFICIE:
TOLLERANZE:
LINEARE:
ANGOLARE:
FINITURA:
$PRPSHEET:{Finish}
SBAVATURA E INTERRUZIONE DEI BORDI NETTI
NOME
FIRMA
DATA
DISEGNATO
VERIFICATO
APPROVATO
FATTO
QUALITÀ
MATERIALE:
$PRPSHEET:{Material}
PESO: $PRPSHEET:{Weight}
NON SCALARE IL DISEGNO
REVISIONE
TITOLO:
Tronco di fusoliera
N. DISEGNO
Disegno3
A4
SCALA: 1:20
FOGLIO 1 DI 1

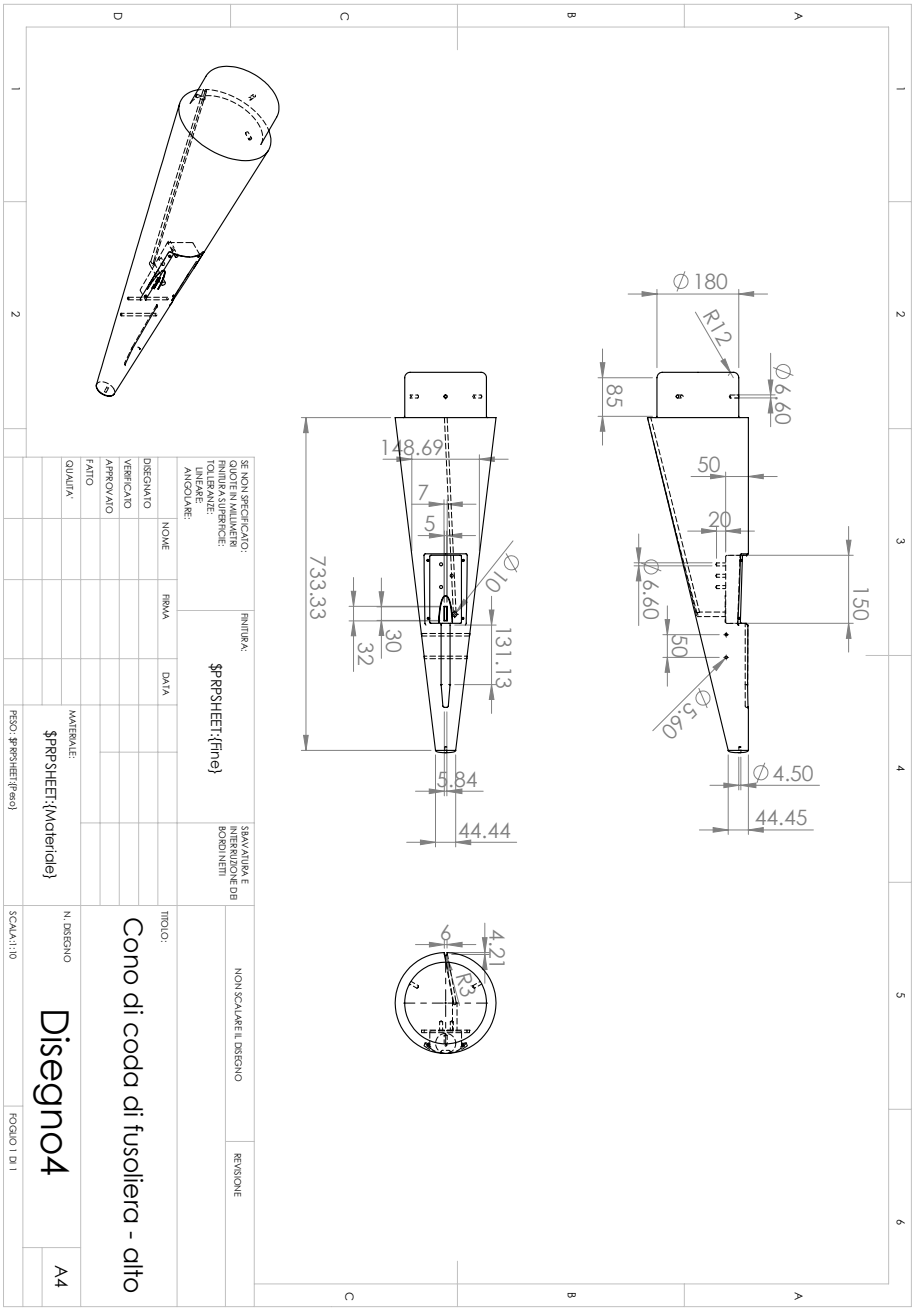
∅180
R12
∅6.60
85
50
20
150
∅6.60
50
∅5.60
∅4.50
44.45
148.67
7
5
733.33
∅10
131.13
30
32
5.84
44.44
6
4.21
R3
SE NON SPECIFICATO:
QUOTE IN MILLIMETRI
FINITURA SUPERFICIE:
TOLLERANZA LINEARE:
ANGOLARE:
NOME
FIRMA
DATA
DISEGNATO
VERIFICATO
APPROVATO
FATTO
QUALITÀ
FINITURA:
$PRPSHEET:{Fine}
MATERIALE:
$PRPSHEET:{Materiale}
PESO: $PRPSHEET:{Peso}
SBAVATURA E INTERRUZIONE DEI BORDI NETTI
NON SCALARE IL DISEGNO
REVISIONE
TITOLO:
Cono di coda di fusoliera - alto
N. DISEGNO
Disegno4
A4
SCALA:1:10
FOGLIO 1 DI 1

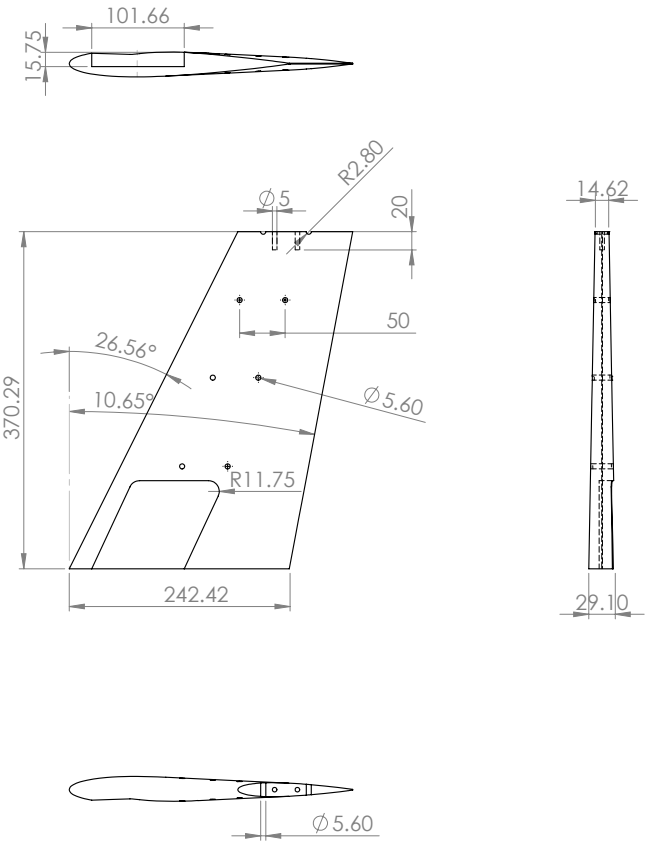

SE NON SPECIFICATO: QUOTE IN MILLIMETRI FINITURA SUPERFICIE: TOLLERANZE: LINEARE: ANGOLARE:	FINITURA: $PRPSHEET:{Fine}			SBAVATURA E INTERRUZIONE DEI BORDI NETTI	NON SCALARE IL DISEGNO	REVISIONE
	NOME	FIRMA	DATA		TITOLO: Piano verticale AR 2.0	
DISEGNATO						
VERIFICATO						
APPROVATO						
FATTO						
QUALITA'				MATERIALE: $PRPSHEET:{Materiale}	N. DISEGNO Disegno5	A4
				PESO: $PRPSHEET:{Peso}	SCALA:1:5	FOGLIO 1 DI 1

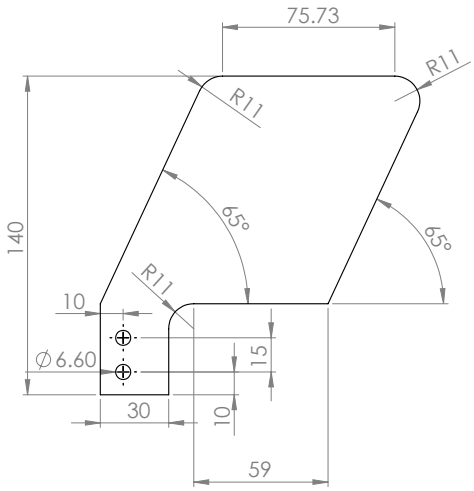

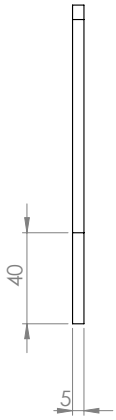

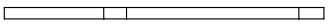

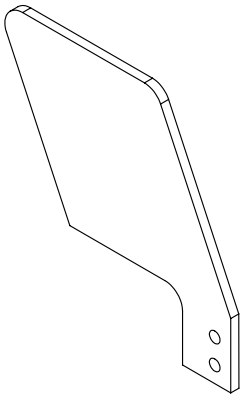

SE NON SPECIFICATO: QUOTE IN MILLIMETRI FINITURA SUPERFICIE: TOLLERANZE: LINEARE: ANGOLARE:		FINITURA: $PRPSHEET:{Fine}		SBAVATURA E INTERRUZIONE DEI BORDI NETTI		NON SCALARE IL DISEGNO	REVISIONE
	NOME	FIRMA	DATA			TITOLO: Piastra piano verticale	
DISEGNATO							
VERIFICATO							
APPROVATO							
FATTO							
QUALITA'				MATERIALE: $PRPSHEET:{Materiale}		N. DISEGNO Disegno6	A4
				PESO: $PRPSHEET:{Peso}		SCALA:1:2	FOGLIO 1 DI 1

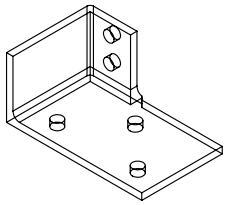

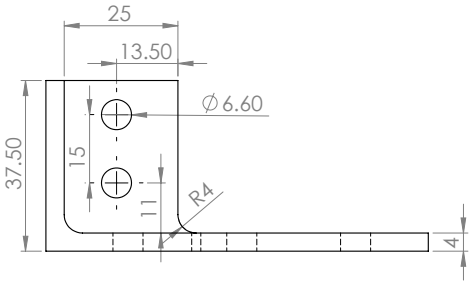

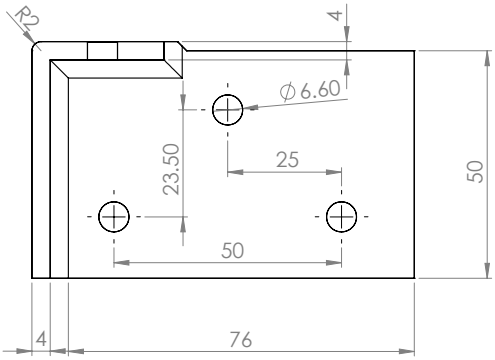

SE NON SPECIFICATO: QUOTE IN MILLIMETRI FINITURA SUPERFICIE: TOLLERANZE: LINEARE: ANGOLARE:	FINITURA: $PRPSHEET:{Fine}			SBAVATURA E INTERRUZIONE DEI BORDI NETTI	NON SCALARE IL DISEGNO	REVISIONE
	NOME	FIRMA	DATA		TITOLO: Piastra sostegna cella di carico	
DISEGNATO						
VERIFICATO						
APPROVATO						
FATTO						
QUALITA'				MATERIALE: $PRPSHEET:{Materiale}	N. DISEGNO Disegno7	A4
				PESO: $PRPSHEET:{Peso}	SCALA:1:1	FOGLIO 1 DI 1

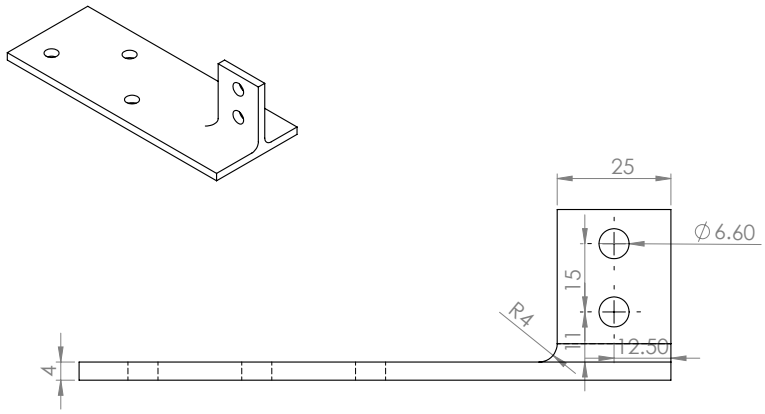

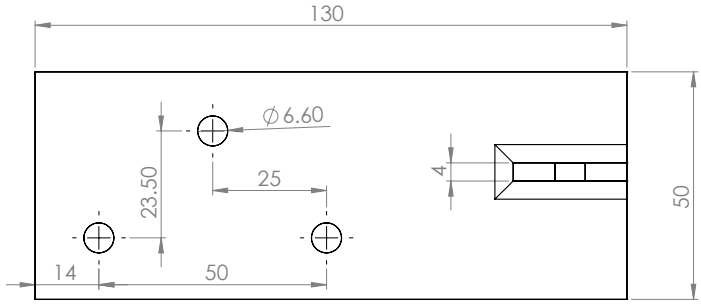

SE NON SPECIFICATO: QUOTE IN MILLIMETRI FINITURA SUPERFICIE: TOLLERANZE: LINEARE: ANGOLARE:		FINITURA: $PRPSHEET:{Fine}		SBAVATURA E INTERRUZIONE DEI BORDI NETTI	NON SCALARE IL DISEGNO	REVISIONE
	NOME	FIRMA	DATA		TITOLO: Piastra sostegno PV	
DISEGNATO						
VERIFICATO						
APPROVATO						
FATTO						
QUALITA'				MATERIALE: $PRPSHEET:{Materiale}	N. DISEGNO Disegno8	A4
				PESO: $PRPSHEET:{Peso}	SCALA:1:1	FOGLIO 1 DI 1

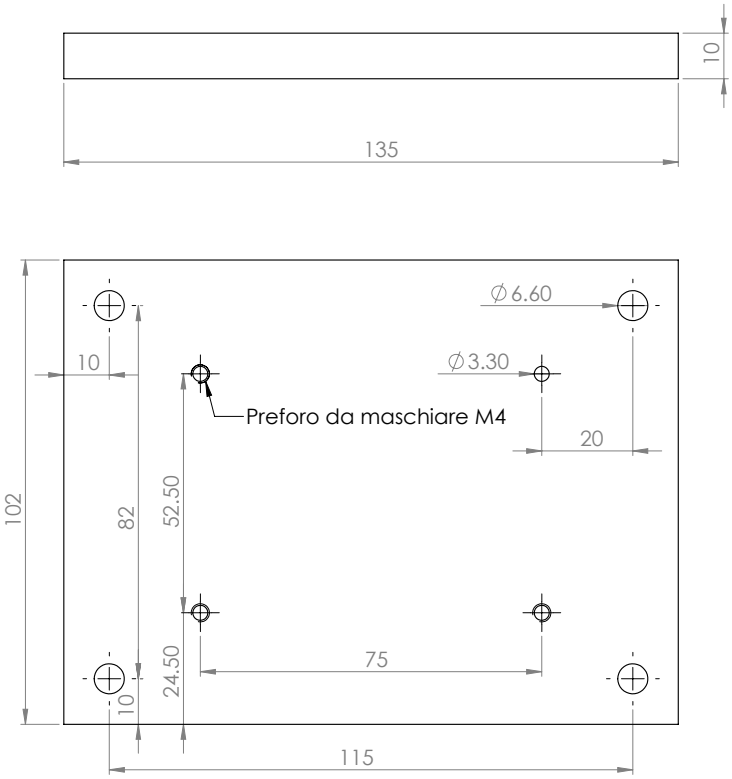

SE NON SPECIFICATO: QUOTE IN MILLIMETRI FINITURA SUPERFICIE: TOLLERANZE: LINEARE: ANGOLARE:	FINITURA: $PRPSHEET:{Fine}				SBAVATURA E INTERRUZIONE DEI BORDI NETTI	NON SCALARE IL DISEGNO	REVISIONE
	NOME	FIRMA	DATA			TITOLO:	
DISEGNATO						Piastra bilancia di galleria	
VERIFICATO							
APPROVATO							
FATTO							
QUALITA'				MATERIALE: $PRPSHEET:{Materiale}		N. DISEGNO Disegno9	A4
				PESO: $PRPSHEET:{Peso}		SCALA:1:1	FOGLIO 1 DI 1

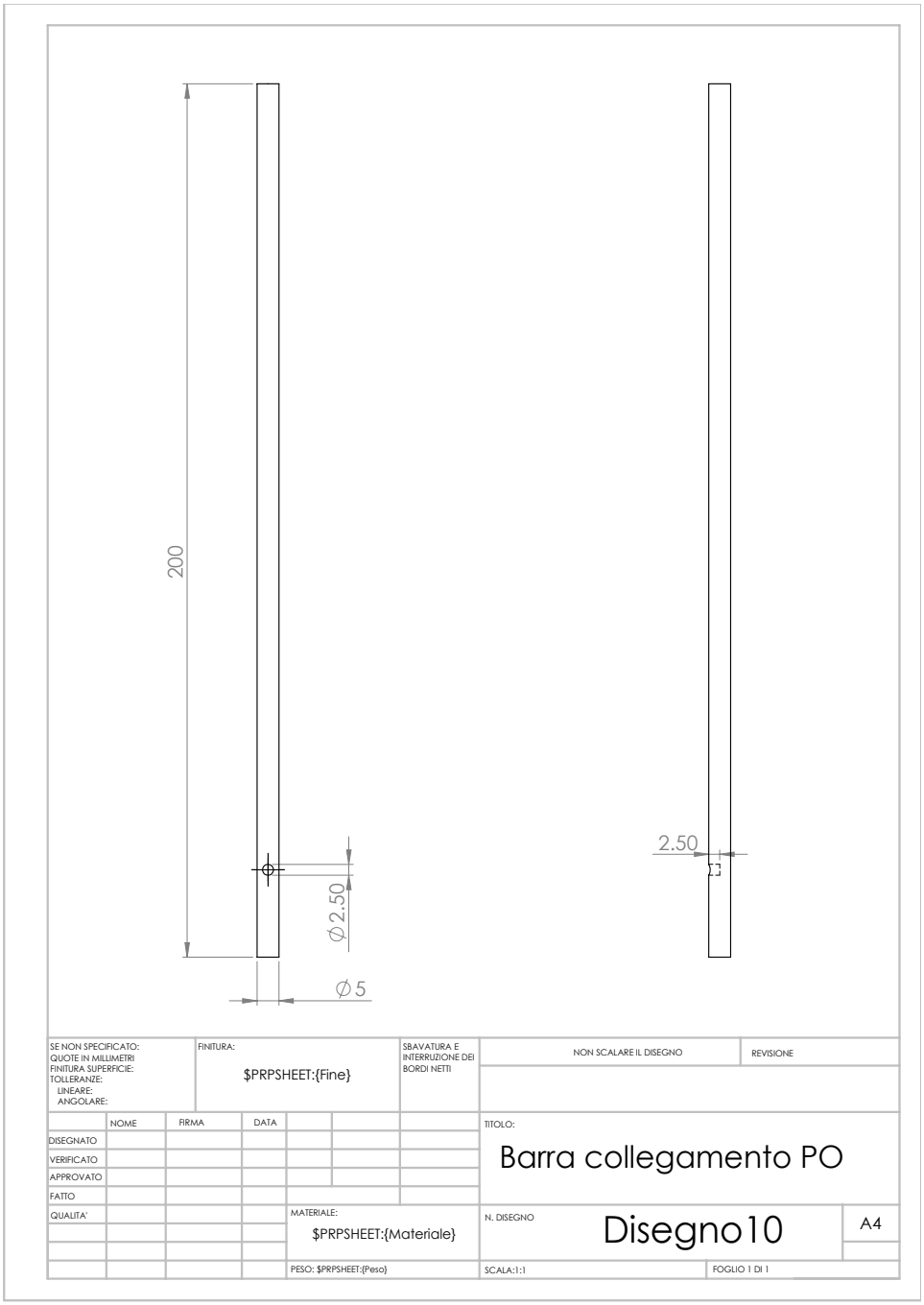
200
∅2.50
∅5
2.50
SE NON SPECIFICATO:
QUOTE IN MILLIMETRI
FINITURA SUPERFICIE:
TOLLERANZE:
LINEARE:
ANGOLARE:
FINITURA:
$PRPSHEET:{Fine}
SBAVATURA E INTERRUZIONE DEI BORDI NETTI
NON SCALARE IL DISEGNO
REVISIONE
NOME
FIRMA
DATA
DISEGNATO
VERIFICATO
APPROVATO
FATTO
QUALITA'
TITOLO:
Barra collegamento PO
MATERIALE:
$PRPSHEET:{Materiale}
N. DISEGNO
Disegno10
A4
PESO: $PRPSHEET:{Peso}
SCALA:1:1
FOGLIO 1 DI 1

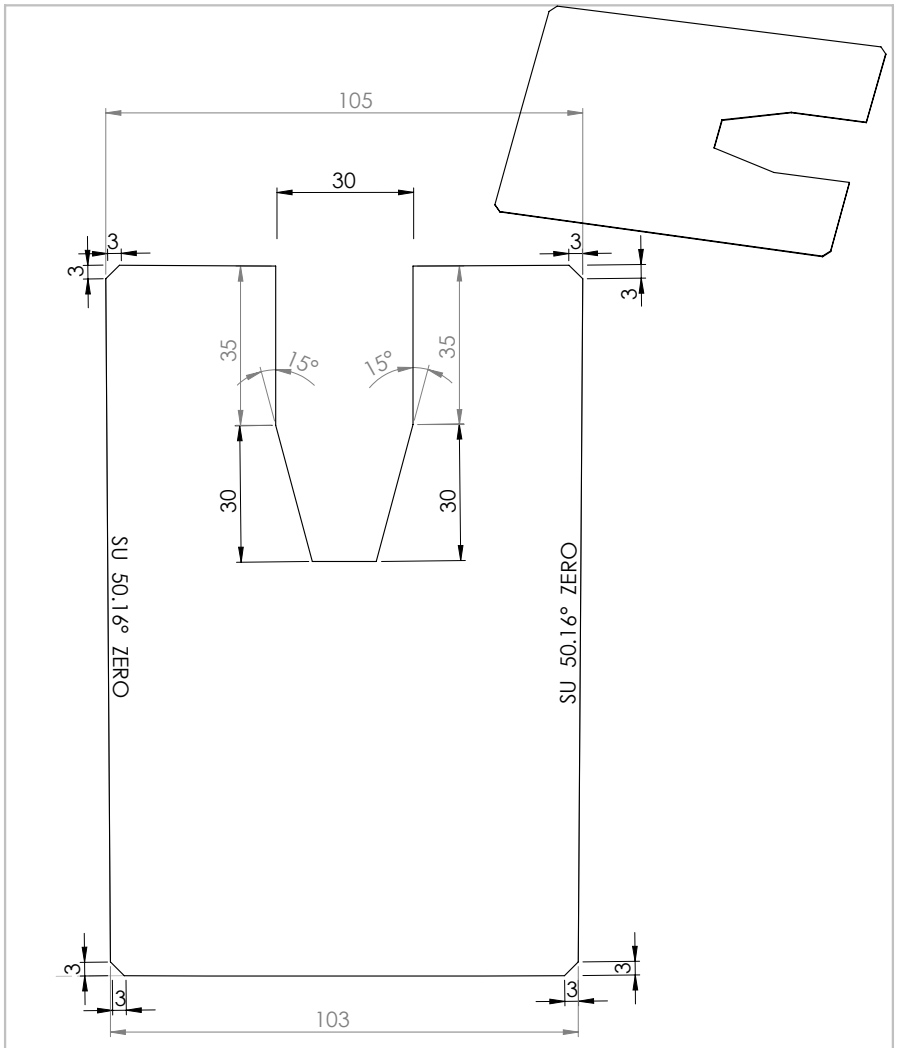

SE NON SPECIFICATO: QUOTE IN MILLIMETRI FINITURA SUPERFICIE: TOLLERANZE: LINEARE: ANGOLARE:	FINITURA: $PRPSHEET:{Fine}	SBAVATURA E INTERRUZIONE DEI BORDI NETTI	NON SCALARE IL DISEGNO	REVISIONE	
	NOME	FIRMA	DATA	TITOLO: Lamierino cono coda fusoliera	
DISEGNATO					
VERIFICATO					
APPROVATO					
FATTO					
QUALITA'	MATERIALE: Alluminio			N. DISEGNO Disegno11	A4
	PESO: $PRPSHEET:{Peso}			SCALA:1:1	FOGLIO 1 DI 1

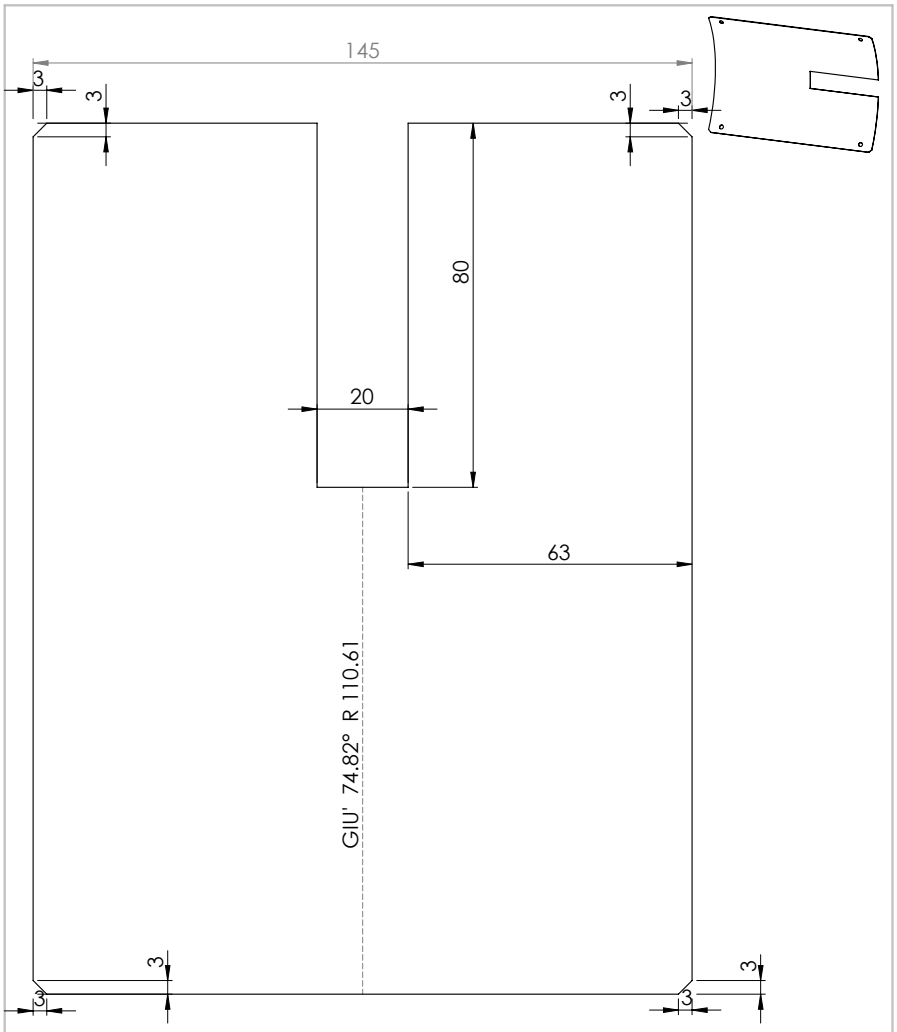

SE NON SPECIFICATO: QUOTE IN MILLIMETRI FINITURA SUPERFICIE: TOLLERANZE: LINEARE: ANGOLARE:	FINITURA: $PRPSHEET:{Fine}			SBAVATURA E INTERRUZIONE DEI BORDI NETTI	NON SCALARE IL DISEGNO	REVISIONE
	NOME	FIRMA	DATA		TITOLO: Lamierino scavo tronco fusoliera	
DISEGNATO						
VERIFICATO						
APPROVATO						
FATTO						
QUALITA'				MATERIALE: Alluminio	N. DISEGNO Disegno12	A4
				PESO: $PRPSHEET:{Peso}	SCALA:1:1	FOGLIO 1 DI 1

Appendix C

Lateral-directional static stability derivatives from wind tunnel tests

The nomenclature is as follows.

Aircraft components IDs are separated by underscores _

Body is indicated by two letters (Figure 6.38)

- **BH** body high
- **BM** body mid
- **BL** body low

Wing (if present) is indicated by two letters (Figure 6.40)

- **WH** wing high
- **WM** wing mid
- **WL** wing low

Vertical tail (if present) is indicated by a letter and two digits (Figure 6.39)

- **V10** $A_v = 1.0$
- **V15** $A_v = 1.5$
- **V20** $A_v = 2.0$

Horizontal tail (if present) is indicated by a letter and a digit (Figure 6.41)

H1 body-mounted horizontal tail

H2 low cruciform horizontal tail

H3 mid cruciform horizontal tail

H4 high cruciform horizontal tail

H5 T-tail configuration

Example: `BH_WH_V15_H4` indicates the configuration with high fuselage afterbody (tail-cone), high wing, vertical tail with aspect ratio $A_v = 1.5$ and a high cruciform empennage configuration.

The following table resumes the results of wind tunnel tests. Stability derivatives have been evaluated between $-6°$ and $6°$ sideslip angle. All results are in /deg.

TABLE C.1: Wind tunnel results for the the fuselage BH. Derivatives are in /deg.

Configuration	C_{N_β}	$C_{\mathcal{L}_\beta}$	$C_{N_{\beta_v}}$
V10	0.0000	0.0000	0.0026
V15	0.0000	0.0000	0.0043
V20	0.0000	0.0000	0.0061
BH	−0.0030	0.0003	0.0000
BH_WH	−0.0031	−0.0006	0.0000
BH_WM	−0.0029	0.0006	0.0000
BH_WL	−0.0029	0.0017	0.0000
BH_V10	0.0005	−0.0007	0.0031
BH_V15	0.0026	−0.0014	0.0052
BH_V20	0.0045	−0.0029	0.0069
BH_V10_H1	0.0012	−0.0006	0.0037
BH_V10_H3	0.0006	−0.0008	0.0031
BH_V10_H4	0.0010	−0.0010	0.0035
BH_V10_H5	0.0017	−0.0013	0.0042
BH_V15_H1	0.0037	−0.0014	0.0060
BH_V15_H3	0.0025	−0.0023	0.0051
BH_V15_H4	0.0029	−0.0018	0.0054
BH_V15_H5	0.0040	−0.0022	0.0064
BH_V20_H1	0.0055	−0.0032	0.0079

Continued...

Configuration	C_{N_β}	$C_{\mathcal{L}_\beta}$	$C_{N_{\beta_v}}$
BH_V20_H2	0.0043	−0.0022	0.0068
BH_V20_H3	0.0044	−0.0024	0.0069
BH_V20_H4	0.0040	−0.0027	0.0066
BH_V20_H5	0.0052	−0.0032	0.0077
BH_WH_V10	0.0002	−0.0014	0.0031
BH_WH_V10_H1	0.0010	−0.0013	0.0036
BH_WH_V10_H3	0.0001	−0.0015	0.0030
BH_WH_V10_H4	0.0005	−0.0017	0.0034
BH_WH_V10_H5	0.0012	−0.0020	0.0041
BH_WH_V15	0.0021	−0.0020	0.0050
BH_WH_V15_H1	0.0034	−0.0025	0.0059
BH_WH_V15_H3	0.0022	−0.0021	0.0051
BH_WH_V15_H4	0.0017	−0.0020	0.0045
BH_WH_V15_H5	0.0035	−0.0029	0.0064
BH_WH_V20	0.0040	−0.0034	0.0069
BH_WH_V20_H1	0.0055	−0.0036	0.0080
BH_WH_V20_H2	0.0039	−0.0030	0.0067
BH_WH_V20_H3	0.0039	−0.0035	0.0068
BH_WH_V20_H4	0.0043	−0.0035	0.0072
BH_WH_V20_H5	0.0051	−0.0043	0.0080
BH_WM_V10	0.0008	−0.0003	0.0033
BH_WM_V10_H1	0.0015	−0.0003	0.0038
BH_WM_V10_H3	0.0008	−0.0004	0.0032
BH_WM_V10_H4	0.0012	−0.0006	0.0035
BH_WM_V10_H5	0.0020	−0.0009	0.0043
BH_WM_V15	0.0028	−0.0010	0.0053
BH_WM_V15_H1	0.0038	−0.0015	0.0060
BH_WM_V15_H3	0.0028	−0.0012	0.0051
BH_WM_V15_H4	0.0030	−0.0017	0.0054
BH_WM_V15_H5	0.0036	−0.0015	0.0059
BH_WM_V20	0.0048	−0.0024	0.0072
BH_WM_V20_H1	0.0058	−0.0022	0.0080
BH_WM_V20_H2	0.0046	−0.0026	0.0070
BH_WM_V20_H3	0.0046	−0.0021	0.0070

Continued...

Configuration	C_{N_β}	$C_{\mathcal{L}_\beta}$	$C_{N_{\beta_v}}$
BH_WM_V20_H4	0.0042	−0.0019	0.0066
BH_WM_V20_H5	0.0057	−0.0030	0.0080
BH_WL_V10	0.0009	0.0008	0.0033
BH_WL_V10_H1	0.0016	0.0008	0.0038
BH_WL_V10_H3	0.0010	0.0006	0.0032
BH_WL_V10_H4	0.0014	0.0004	0.0037
BH_WL_V10_H5	0.0021	0.0005	0.0044
BH_WL_V15	0.0030	−0.0004	0.0053
BH_WL_V15_H1	0.0041	−0.0001	0.0062
BH_WL_V15_H3	0.0031	−0.0003	0.0053
BH_WL_V15_H4	0.0033	−0.0002	0.0056
BH_WL_V15_H5	0.0044	−0.0015	0.0066
BH_WL_V20	0.0051	−0.0013	0.0074
BH_WL_V20_H1	0.0062	−0.0020	0.0083
BH_WL_V20_H2	0.0049	−0.0018	0.0072
BH_WL_V20_H3	0.0051	−0.0012	0.0073
BH_WL_V20_H4	0.0048	−0.0018	0.0071
BH_WL_V20_H5	0.0066	−0.0027	0.0087

TABLE C.2: Wind tunnel results for the the fuselage BM. Derivatives are in /deg.

Configuration	C_{N_β}	$C_{\mathcal{L}_\beta}$	$C_{N_{\beta_v}}$
BM	−0.0032	0.0001	0.0000
BM_V10	−0.0002	−0.0005	0.0027
BM_V15	0.0019	−0.0011	0.0046
BM_V20	0.0037	−0.0018	0.0064
BM_WH_V10	−0.0004	−0.0011	0.0026
BM_WH_V10_H1	0.0003	−0.0010	0.0030
BM_WH_V10_H3	−0.0005	−0.0012	0.0025
BM_WH_V10_H4	−0.0002	−0.0013	0.0028
BM_WH_V10_H5	0.0004	−0.0015	0.0033
BM_WH_V15	0.0014	−0.0017	0.0044
BM_WH_V15_H1	0.0023	−0.0016	0.0050
BM_WH_V15_H3	0.0012	−0.0017	0.0042

Continued...

Configuration	C_{N_β}	$C_{\mathcal{L}_\beta}$	$C_{N_{\beta_v}}$
BM_WH_V15_H4	0.0015	−0.0019	0.0044
BM_WH_V15_H5	0.0023	−0.0026	0.0053
BM_WH_V20	0.0032	−0.0027	0.0062
BM_WH_V20_H1	0.0042	−0.0024	0.0068
BM_WH_V20_H2	0.0031	−0.0024	0.0061
BM_WH_V20_H3	0.0030	−0.0029	0.0059
BM_WH_V20_H4	0.0031	−0.0027	0.0060
BM_WH_V20_H5	0.0039	−0.0031	0.0068
BM_WM_V10	0.0000	−0.0002	0.0027
BM_WM_V10_H1	0.0006	−0.0001	0.0030
BM_WM_V10_H3	0.0001	−0.0001	0.0026
BM_WM_V10_H4	0.0004	−0.0003	0.0030
BM_WM_V10_H5	0.0011	−0.0006	0.0036
BM_WM_V15	0.0021	−0.0008	0.0046
BM_WM_V15_H1	0.0028	−0.0012	0.0052
BM_WM_V15_H3	0.0021	−0.0009	0.0046
BM_WM_V15_H4	0.0024	−0.0010	0.0049
BM_WM_V15_H5	0.0031	−0.0013	0.0055
BM_WM_V20	0.0039	−0.0021	0.0064
BM_WM_V20_H1	0.0048	−0.0022	0.0071
BM_WM_V20_H2	0.0038	−0.0014	0.0063
BM_WM_V20_H3	0.0038	−0.0015	0.0062
BM_WM_V20_H4	0.0042	−0.0019	0.0066
BM_WM_V20_H5	0.0045	−0.0025	0.0070
BM_WL_V10	0.0004	0.0009	0.0029
BM_WL_V10_H1	0.0009	0.0011	0.0033
BM_WL_V10_H3	0.0004	0.0009	0.0028
BM_WL_V10_H4	0.0008	0.0008	0.0032
BM_WL_V10_H5	0.0017	0.0004	0.0040
BM_WL_V15	0.0024	0.0002	0.0049
BM_WL_V15_H1	0.0031	0.0003	0.0054
BM_WL_V15_H3	0.0022	0.0003	0.0046
BM_WL_V15_H4	0.0026	−0.0003	0.0050
BM_WL_V15_H5	0.0035	−0.0004	0.0059

Continued...

Configuration	C_{N_β}	$C_{\mathcal{L}_\beta}$	$C_{N_{\beta_v}}$
BM_WL_V20	0.0042	−0.0007	0.0066
BM_WL_V20_H1	0.0050	−0.0007	0.0073
BM_WL_V20_H2	0.0042	−0.0005	0.0066
BM_WL_V20_H3	0.0036	−0.0004	0.0060
BM_WL_V20_H4	0.0043	−0.0010	0.0067
BM_WL_V20_H5	0.0050	−0.0015	0.0074

TABLE C.3: Wind tunnel results for the the fuselage BL. Derivatives are in /deg.

Configuration	C_{N_β}	$C_{\mathcal{L}_\beta}$	$C_{N_{\beta_v}}$
BL	−0.0032	0.0002	0.0000
BL_WH	−0.0032	−0.0006	0.0000
BL_WM	−0.0030	0.0005	0.0000
BL_WL	−0.0032	0.0015	0.0000
BL_V10	−0.0004	−0.0004	0.0024
BL_V15	0.0015	−0.0009	0.0042
BL_V20	0.0034	−0.0017	0.0061
BL_WH_V10	−0.0007	−0.0011	0.0022
BL_WH_V10_H1	−0.0003	−0.0012	0.0025
BL_WH_V10_H3	−0.0008	−0.0011	0.0021
BL_WH_V10_H4	−0.0005	−0.0012	0.0024
BL_WH_V10_H5	0.0002	−0.0015	0.0030
BL_WH_V15	0.0011	−0.0016	0.0040
BL_WH_V15_H1	0.0018	−0.0015	0.0044
BL_WH_V15_H3	0.0010	−0.0017	0.0039
BL_WH_V15_H4	0.0013	−0.0021	0.0041
BL_WH_V15_H5	0.0021	−0.0028	0.0050
BL_WH_V20	0.0028	−0.0030	0.0058
BL_WH_V20_H1	0.0038	−0.0022	0.0063
BL_WH_V20_H2	0.0029	−0.0022	0.0058
BL_WH_V20_H3	0.0028	−0.0025	0.0056
BL_WH_V20_H4	0.0032	−0.0025	0.0060
BL_WH_V20_H5	0.0038	−0.0028	0.0065
BL_WM_V10	−0.0003	−0.0002	0.0024

Continued...

Configuration	C_{N_β}	$C_{\mathcal{L}_\beta}$	$C_{N_{\beta_v}}$
BL_WM_V10_H1	0.0002	0.0000	0.0027
BL_WM_V10_H3	−0.0003	−0.0001	0.0023
BL_WM_V10_H4	−0.0002	−0.0002	0.0024
BL_WM_V10_H5	0.0002	−0.0004	0.0028
BL_WM_V15	0.0018	−0.0005	0.0044
BL_WM_V15_H1	0.0024	−0.0005	0.0048
BL_WM_V15_H3	0.0017	−0.0006	0.0042
BL_WM_V15_H4	0.0021	−0.0008	0.0046
BL_WM_V15_H5	0.0029	−0.0012	0.0054
BL_WM_V20	0.0036	−0.0013	0.0061
BL_WM_V20_H1	0.0043	−0.0012	0.0067
BL_WM_V20_H2	0.0035	−0.0013	0.0060
BL_WM_V20_H3	0.0035	−0.0013	0.0060
BL_WM_V20_H4	0.0038	−0.0016	0.0063
BL_WM_V20_H5	0.0044	−0.0018	0.0069
BL_WL_V10	−0.0002	0.0011	0.0025
BL_WL_V10_H1	0.0001	0.0011	0.0027
BL_WL_V10_H3	−0.0002	0.0010	0.0024
BL_WL_V10_H4	0.0002	0.0008	0.0027
BL_WL_V10_H5	0.0008	0.0006	0.0033
BL_WL_V15	0.0018	0.0006	0.0044
BL_WL_V15_H1	0.0021	−0.0004	0.0047
BL_WL_V15_H3	0.0017	0.0004	0.0042
BL_WL_V15_H4	0.0020	0.0002	0.0046
BL_WL_V15_H5	0.0029	−0.0001	0.0054
BL_WL_V20	0.0037	−0.0001	0.0063
BL_WL_V20_H1	0.0043	−0.0004	0.0068
BL_WL_V20_H2	0.0036	−0.0002	0.0061
BL_WL_V20_H3	0.0036	−0.0003	0.0061
BL_WL_V20_H4	0.0038	−0.0004	0.0063
BL_WL_V20_H5	0.0046	−0.0008	0.0071

Bibliography

[1] *Worldwide market forecast 2015–2034*. Japan Aircraft Development Corporation. 2015.

[2] *Regional turboprops market outlook 2014-2033*. ATR. 2014.

[3] *Market forecast 2015–2034*. Bombardier Commercial Aircraft. 2015.

[4] *GDP*. http://www.wolframalpha.com/input/?i=gdp. 2015.

[5] *Ontario's long-term report on the economy. Chapter 2 Long-term Ontario economic projection*. http://www.fin.gov.on.ca/en/economy/ltr/2014/ch2.html. 2015.

[6] *World air transport and GDP*. http://www.wolframalpha.com/input/?i=air+travel+vs+gdp. 2015.

[7] *Air travel vs GDP*. http://www.wolframalpha.com/input/?i=world+air+transport+and+gdp. 2015.

[8] *The market for regional transport aircraft 2014–2023*. Forecast International. 2014.

[9] Della Vecchia, P. "Development of Methodologies for the Aerodynamic Design and Optimization of New Regional Turboprop Aircraft". PhD thesis. Università degli Studi di Napoli "Federico II", 2013.

[10] St. Ives Westerham Ltd, ed. *The Jet Engine*. 65 Buckingham Gate, London: Rolls-Royce, 2005.

[11] *ATR-72-500 sample report*. https://www.aircraftcostcalculator.com/. 2015.

[12] Raymer, D. P. *Aircraft design: a conceptual approach*. 5th edition. AIAA education series. Reston, VA: American Institute of Aeronautics and Astronautics, 2012. ISBN: 9781600869112.

[13] Gudmundsson, S. *General aviation aircraft design: applied methods and procedures*. Butterworth-Heinemann, 2013.

[14] Torenbeek, E. *Synthesis of subsonic airplane design: an introduction to the preliminary design, of subsonic general aviation and transport aircraft, with emphasis on layout, aerodynamic design, propulsion, and performance*. Delft: Delft University Press, 1982. ISBN: 9024727243.

[15] Kroo, I. and Alonso, J. *Tail design and sizing*. http://adg.stanford.edu/aa241/stability/taildesign.html. Stanford University, 2012.

[16] Perkins, C. D. and Hage, R. E. *Airplane performance stability and control*. New York: Wiley, 1949.

[17] Obert, E. et al. *Aerodynamic design of transport aircraft*. Amsterdam, The Netherlands: Ios Press, 2009. ISBN: 9781586039707.

[18] EASA. *Acceptable Means of Compliance for Large Aeroplanes CS-25*. Tech. Rep. Amendment 17. European Aviation Safety Agency, 2015.

[19] FAA. *Federal Aviation Regulations*. Tech. rep. Federal Aviation Authorities, 2015.

[20] Horlings, H. "Control and Performance During Asymmetrical Powered Flight". In: *Change* 2013 (2012), pp. 08–15.

[21] Jenkinson, L. R., Simpkin, P., and Rhodes, D. *Civil jet aircraft design*. Reston, VA: American Insitute of Aeronautics and Astronautics, 1999. ISBN: 156347350X (alk. paper). URL: http://www.loc.gov/catdir/toc/fy034/99022190.html.

[22] Kaufmann, M. "Cost/weight optimization of aircraft structures". PhD thesis. KTH Engineering Sciences, 2008.

[23] Dubois, T. *ATR Targets 100-Aircraft Annual Production Rate*. http://www.ainonline.com/aviation-news/aerospace/2015-01-21/atr-targets-100-aircraft-annual-production-rate. 2015.

[24] Roskam, J. *Airplane design*. Lawrence, Kan: DARcorporation, 2000. ISBN: 188488542X (pt. 1).

[25] *Lab 8 notes – Basic aircraft design rules*. http://ocw.mit.edu/courses/aeronautics-and-astronautics/16-01-unified-engineering-i-ii-iii-iv-fall-2005-spring-2006/systems-labs-06/spl8.pdf. Massachusetts Institute of Technology, 2006.

[26] Finck, R. D. *USAF Stability and Control DATCOM*. AFWAL-TR 83-3048. Wright-Patterson Air Force Base, Ohio: McDonnell Douglas Corporation, 1978.

[27] Nicolosi, F., Della Vecchia, P., and Ciliberti, D. "Aerodynamic interference issues in aircraft directional control". In: *Journal of Aerospace Engineering* (2014).

[28] Hoggard, H. P. *Wind-tunnel Investigation of Fuselage Stability in Yaw with Various Arrangements of Fins.* Technical Report 785. National Advisory Committee for Aeronautics, 1940.

[29] Thompson, F. and Gilruth, R. R. *Notes on the stalling of vertical tail surfaces and on fin design.* Technical Note 778. National Advisory Committee for Aeronautics, 1940.

[30] Allen, E. T. and Schairer, G. S. *Aircraft empennage.* United States Patent Office 2,356,139. 1944.

[31] Gale, L. J. and Jones Jr., I. P. *Effects of Antispin Fillets and Dorsal Fins on the Spin and Recovery Characteristics of Airplanes as Determined From Free-Spinning-Tunnel Tests.* Technical Note 1779. National Advisory Committee for Aeronautics, 1948.

[32] Barua, P., Sousa, T., and Scholz, D. *Empennage statistics and sizing methods for dorsal fins.* Technical Note. Hamburg, Germany: Aircraft Design, Systems Group (AERO), Department of Automotive, and Aeronautical Engineering, Hamburg University of Applied Sciences, 2013.

[33] Jacobs, E. N. and Ward, K. E. *Interferences of wing and fuselage from tests of 209 combinations in the NACA variable-density wind tunnel.* Technical Report 540. National Advisory Committee for Aeronautics, 1935.

[34] House, R. O. and Wallace, A. R. *Wind-tunnel investigation of effect of interference on lateral-stability characteristics of four NACA 23012 wings, an elliptical and circular fuselage and vertical fins.* Technical Report 705. National Advisory Committee for Aeronautics, 1940.

[35] Bamber, R. J. and House, R. O. *Wind-tunnel investigation of effect of yaw on lateral-stability characteristics. II – Rectangular NACA 23012 wing with a circular fuselage and a fin.* Technical Report 730. National Advisory Committee for Aeronautics, 1939.

[36] Queijo, M. J. and Wolhart, W. D. *Experimental investigation of the effect of the vertical-tail size and length and of fuselage shape and length on the static lateral stability characteristics of a model with* 45° *sweptback wing and tail surfaces.* Technical Report 1049. National Advisory Committee for Aeronautics, 1950.

[37] Brewer, J. D. and Lichtenstein, J. H. *Effect of horizontal tail on low-speed static lateral stability characteristics of a model having* 45° *sweptback wing and tail surfaces.* Technical Note 2010. National Advisory Committee for Aeronautics, 1950.

[38] Recant, I. and Wallace, A. *Wind-tunnel Investigation of the Effect of Vertical Position of the Wing on the Side Flow in the Region of the Vertical Tail.* Technical Note 804. National Advisory Committee for Aeronautics, 1941.

[39] Michael Jr, W. H. *Investigation of Mutual Interference Effects of Several Vertical-tail-fuselage Configurations in Sideslip.* Technical Note 3135. National Advisory Committee for Aeronautics, 1954.

[40] Katzoff, S. and Mutterperl, W. *The end-plate effect of a horizontal-tail surface on a vertical-tail surface.* Technical Note 797. National Advisory Committee for Aeronautics, 1941.

[41] Murray, H. E. *Wind-tunnel investigation of end-plate effects of horizontal tails on a vertical tail compared with available theory.* Technical Note 1050. National Advisory Committee for Aeronautics, 1946.

[42] Riley, D. R. *Effect of horizontal-tail span and vertical location on the aerodynamic characteristics of an unswept tail assembly in sideslip.* Technical Report 1170. National Advisory Committee for Aeronautics, 1953.

[43] Gilbey, R. W. *Contribution of fin to sideforce, yawing moment and rolling moment derivatives due to sideslip,* $(Y_v)_F$, $(N_v)_F$, $(L_v)_F$, *in the presence of body, wing and tailplane.* Item 82010. Engineering Science Data Unit, 1982.

[44] Weber, J. and Hawk, A. C. *Theoretical load distributions on fin-body-tailplane arrangements in a side-wind.* Reports and Memoranda No. 2992. London, UK: Ministry of Supply, 1954.

[45] Schlichting, H. T. and Truckenbrodt, E. A. *Aerodynamics of the Airplane.* McGraw-Hill Companies, 1979.

[46] Hoerner, S. F. *Fluid-dynamic drag: practical information on aerodynamic drag and hydrodynamic resistance*. Midland Park, NJ: Published by the author, 1965.

[47] Munk, M. M. *The aerodynamic forces on airship hulls*. Technical Report 184. National Advisory Committee for Aeronautics, 1924.

[48] Multhopp, H. *Aerodynamics of the Fuselage*. Technical Memorandum 1036. National Advisory Committee for Aeronautics, 1942.

[49] Lamb, H. *The inertia coefficients of an ellipsoid moving in fluid*. Reports and Memoranda 623. British Aeronautical Research Commitee, 1918.

[50] Abbott, I. H. *Fuselage-drag tests in the variable-density wind tunnel: streamline bodies of revolution, fineness ratio of 5*. Technical Note 614. National Advisory Committee for Aeronautics, 1937.

[51] Gilruth, R. R. and White, M. D. *Analysis and prediction of longitudinal stability of airplanes*. Technical Report 711. National Advisory Committee for Aeronautics, 1941.

[52] Hall, S. *How big the tail*. `http://www.eaa62.org/technotes/tail.htm`. 2002.

[53] Ciliberti, D. et al. "Conceptual design of a 90 pax regional turboprop". Workgroup for the aircraft design class at the University of Naples "Federico II". 2011.

[54] Diederich, F. *A plan-form parameter for correlating certain aerodynamic characteristics of swept wings*. Technical Note 2335. National Advisory Committee for Aeronautics, 1951.

[55] Chappell, P. D. and Gilbey, R. W. *Lift-curve slope and aerodynamic centre position of wings in inviscid subsonic flow*. Item 70011. Engineering Science Data Unit, 1970.

[56] Cusati, V. "Development of a new methodology for the prediction of aircraft fuselage aerodynamic characteristics". MA thesis. Università degli Studi di Napoli "Federico II", 2013.

[57] Vos, J. B. et al. "Navier-Stokes solvers in European aircraft design". In: *Progress in Aerospace Sciences* 38.8 (2002), pp. 601–697.

[58] Smith, W. G. and Ball, L. H. *Static Lateral-Directional Stability Characteristics of Five Contemporary Airplane Models From Wind-Tunnel Tests at High Subsonic and Supersonic Speeds*. Research Memorandum. National Advisory Committee for Aeronautics, 1956.

[59] Lan, C. E. *Calculation of Lateral-Directional Stability Derivatives for Wing-Body Combinations with and without Jet-Interaction Effects*. Contractor Report 145251. National Aeronautics and Space Administration, 1977.

[60] Hall, R. M. et al. *Computational Methods for Stability and Control (COMSAC): the time has come*. Tech. rep. 6121. American Institute of Aeronautics and Astronautics, 2005.

[61] Erickson, L. L. *Panel methods: An introduction*. Vol. 2995. National Aeronautics, Space Administration, Office of Management, Scientific, and Technical Information Division, 1990.

[62] Terzi, A. and Chiu, T. W. "Modern panel method techniques for modeling wake body interference". In: *AIAA Paper* 97.1829 (1997).

[63] Obert, E. *Tail design*. Report H-0-93. Amsterdam (Netherlands): Fokker Aircraft B.V, 1992.

[64] Hucho, W. *Aerodynamics of Road Vehicles: From Fluid Mechanics to Vehicle Engineering*. Elsevier Science, 2013. ISBN: 9781483102078. URL: `https://books.google.it/books?id=psP8BAAAQBAJ`.

[65] Dutt, H. and Rajeswari, S. "Wing-body interference using a hybrid panel method". In: *Acta mechanica* 106.3-4 (1994), pp. 111–126.

[66] Lamb, M., Sawyer, W. C., and Thomas, J. L. *Experimental and theoretical supersonic lateral-directional stability characteristics of a simplified wing-body configuration with a series of vertical-tail arrangements*. Technical Paper 1878. National Aeronautics and Space Administration, 1981.

[67] Park, M. A. et al. "Determination of stability and control derivatives using computational fluid dynamics and automatic differentiation". In: *Proceedings of the 17th AIAA Applied Aerodynamics Conference*. 1999.

[68] Johnson, F. T., Tinoco, E. N., and Yu, N. J. "Thirty years of development and application of CFD at Boeing Commercial Airplanes, Seattle". In: *Computers & Fluids* 34.10 (2005), pp. 1115–1151.

[69] Shang, J. S. "Three decades of accomplishments in computational fluid dynamics". In: *Progress in Aerospace Sciences* 40.3 (2004), pp. 173–197.

[70] Fujii, K. "Progress and future prospects of CFD in aerospace – Wind tunnel and beyond". In: *Progress in Aerospace Sciences* 41.6 (2005), pp. 455–470.

[71] Anderson, J. D. *Computational fluid dynamics: the basics with applications*. Mcgraw-Hill, 1995.

[72] O'Neill, C. R. *Determination of flight stability coefficients using a finite element CFD*. Tech. rep. 74077. Stillwater, Oklahoma: Department of Mechanical and Aerospace Engineering, Oklahoma State University, 2000.

[73] Papa, R., de Mattos, B. S., and de Castro Santos, L. C. "Considerations about forward fuselage aerodynamic design of a transport aircraft". In: *AIAA Paper* (2004).

[74] Rivers, M. B. and Dittberner, A. "Experimental investigations of the NASA common research model in the NASA Langley national transonic facility and NASA Ames 11-ft transonic wind tunnel". In: *AIAA Paper* 1126 (2011), p. 2011.

[75] Rudnik, R., Huber, K., and Melber-Wilkending, S. "EUROLIFT Test Case Description for the 2nd High Lift Prediction Workshop". In: *30th AIAA Applied Aerodynamics Conference*. 2012, pp. 25–28.

[76] Rumsey, C. L. et al. "Summary of the first AIAA CFD high-lift prediction workshop". In: *Journal of Aircraft* 48.6 (2011), pp. 2068–2079.

[77] Levy, D. W. et al. "Summary of data from the fifth AIAA CFD drag prediction workshop". In: *AIAA Paper* (2013).

[78] Spalart, P. R. and Allmaras, S. R. "A one equation turbulence model for aerodinamic flows". In: *AIAA Journal* 94 (1992).

[79] Della Vecchia, P. and Ciliberti, D. "Numerical aerodynamic analysis on a trapezoidal wing with high lift devices: a comparison with experimental data". In: *22th AIDAA Conference*. Associazione Italiana di Aeronautica e Astronautica, 2013.

[80] Nicolosi, F., Della Vecchia, P., and Corcione, S. "Design and aerodynamic analysis of a twin-engine commuter aircraft". In: *Aerospace Science and Technology* 40 (2015), pp. 1–16.

[81] Della Vecchia, P. and Nicolosi, F. "Aerodynamic guidelines in the design and optimization of new regional turboprop aircraft". In: *Aerospace Science and Technology* 38 (2014), pp. 88–104.

[82] Nicolosi, F., Corcione, S., and Della Vecchia, P. "Commuter aircraft aerodynamic design: wind-tunnel tests and CFD analysis Commuter aircraft aerodynamic design: wind-tunnel tests and CFD analysis Commuter aircraft aerodynamic design: wind-tunnel tests and CFD analysis". In: *ICAS 2014 Proceedings*. International Council of the Aeronautical Sciences. Optimage Ltd., 2014.

[83] Nicolosi, F., Della Vecchia, P., and Corcione, S. "Aerodynamic analysis and design of a twin engine commuter aircraft". In: *ICAS 2012 Proceedings*. Vol. 1316000327. International Council of the Aeronautical Sciences. Optimage Ltd., 2012, pp. 23–28.

[84] Nicolosi, F., Della Vecchia, P., and Ciliberti, D. "An investigation on vertical tailplane contribution to aircraft sideforce". In: *Aerospace Science and Technology* 28.1 (2013), pp. 401–416.

[85] Nicolosi, F. et al. "Development of new preliminary design methodologies for regional turboprop aircraft by CFD analyses". In: *ICAS 2014 Proceedings*. International Council of the Aeronautical Sciences. Optimage Ltd., 2014.

[86] Ciliberti, D., Nicolosi, F., and Della Vecchia, P. "A new approach in aircraft vertical tailplane design". In: *22th AIDAA Conference*. Associazione Italiana di Aeronautica e Astronautica, 2013.

[87] Della Vecchia, P., Nicolosi, F., and Ciliberti, D. "Aircraft directional stability prediction method by CFD". In: *33rd AIAA Applied Aerodynamics Conference*. 2015.

[88] Nicolosi, F. et al. "Fuselage aerodynamic prediction methods". In: *33rd AIAA Applied Aerodynamics Conference*. 2015.

[89] *SCoPE*. `http://scope.unina.it/`. 2012.

[90] *STAR-CCM+*. 9.06. CD-adapco. Melville, NY, 2014.

[91] Antunes, A. P., da Silva, R. G., and Azevedo, J. F. L. "On the effects of turbulence modeling and grid refinement on high lift configuration aerodynamic simulations". In: *ICAS 2012 Proceedings*. Vol. 23. International Council of Aeronautics and Astronautics. Optimage Ltd., 2012, p. 28.

[92] Hansen, H. et al. "Overview about the European high lift research programme EUROLIFT". In: *AIAA Paper* 767 (2004).

[93] Corcione, S. "Design Guidelines, Experimental Investigation and Numerical Analysis of a New Twin Engine Commuter Aircraft". PhD thesis. Università degli Studi di Napoli "Federico II", 2015.

[94] Melber-Wilkending, S. et al. "Verification of MEGAFLOW – Software for high lift applications". In: *MEGAFLOW-Numerical Flow Simulation for Aircraft Design*. Springer, 2005, pp. 163–178.

[95] Barlow, J. B., Rae, W. H., and Pope, A. *Low-speed wind tunnel testing*. 3rd ed. New York: Wiley, 1999. ISBN: 0471557749 (cloth : alk. paper). URL: `http://www.loc.gov/catdir/bios/wiley041/98028891.html`.